UNIVERSIDAD DE CONCEPCIÓN
DIRECCIÓN DE POSTGRADO

MULTI-SCALE DESIGN OF DEEP EUTECTIC SOLVENTS TO RECOVER FLUORINATED GREENHOUSE GASES

POR

Bastian Ignacio Gonzalez Barramuno

Tesis presentada a la Dirección de Postgrado de la Universidad de Concepción para optar al grado académico de Doctorado en Ciencias de la Ingeniería con Mención en Ingeniería Química

Profesor guía

Prof. José Matías GARRIDO
Universidad de Concepción

Profesor co-guía

Prof. Héctor QUINTEROS-LAMA
Universidad de Talca

Comité de Evaluación

Prof. Alejandro KARELOVIC
Universidad de Concepción

Prof. Andrés MEJÍA
Universidad de Concepción

Prof. Ana B. PEREIRO
Universidade de Lisboa

Prof. Santiago APARICIO
Universidad de Burgos

julio 2026
Concepción (Chile)

AGRADECIMIENTOS

Nada de lo que se encuentra plasmado en este escrito habría sido posible sin la guía conjunta de mis tutores José Matías Garrido y Héctor Quinteros Lama. Particularmente, agradezco a José Matías por su constante disponibilidad para discutir resultados y artículos, entre tantas otras tareas propias de este proceso. A su vez, doy las gracias a Héctor, por su guía a la distancia desde Curicó, y por sus *city tours* y discusiones en Tarragona y Barcelona.

Agradezco a los Profesores Fèlix Llovell y Belén Rodriguez Reartes, con quienes desarrollé una parte importante de los resultados aquí presentados, y con quienes tuve el gusto de poder encontrarme en más de una ocasión durante estos años. Tampoco puedo dejar de mencionar a Luan, tanto por la colaboración académica como por su extroversión, que hizo mucho más especial mi estadía en Tarragona y los congresos que tuve la suerte de compartir con él.

También quiero agradecer al Profesor Gonzalo Guillén Gosálbez por recibirme en SUPERLab, dándome la oportunidad de aprender mucho más de lo que esperaba durante mi estancia en Zúrich. Entre los miembros de este grupo, agradecer a Lucas, Javi, Georgios, Fabian, y Richard, con quienes más pude compartir durante estos mesees. La disposición y conocimientos de todos, junto con la dedicación de Lucas, convirtieron mi estadía en una experiencia que siempre tendré presente.

Es imposible no reconocer a los miembros del Nanolab (ahora Thermolab). Comenzando con reconocer a Esteban, cuyas contribuciones en más que unas cuantas dimensiones de la vida hicieron posible, en gran medida, este trabajo. A Elvis, por creer constantemente en mi más de lo que creí posible o, en momentos, merecido. A Maidelys, por estar siempre disponible, tanto ella como su departamento, para cualquier panorama del grupo. A Jorge, por sus recomendaciones de libros y por siempre sumarse a ir por un café cuando ya no quedaba nada más por hacer. A Joaquín, por todo el arte, música y cine que me hizo descubrir, y especialmente por su visita durante mi estancia en Zúrich. A Paula y Seba, cuyo paso algo más corto por el Nanolab no impidió que sigan siendo personas tan presentes hasta hoy. A las nuevas adiciones del Nanolab, por estar ahí durante este semestre final que se hizo increíblemente corto.

Sin duda, agradezco también a mi familia, en especial a mis papás, abuela, hermanos y tíos, con quienes sé que siempre podré encontrar un apoyo incondicional y un lugar de paz fuera del caos del entorno académico. A mis amigos, que han estado presentes ahora y siempre, y son ya tantos que no puedo llegar a nombrar en esta corta página. Por último, pero no menos importante, gracias totales a Belén, quien, con su compañía y apoyo, tanto en este proceso como en la vida misma, ha sido una fuente inagotable de tranquilidad, alegría y motivación.

Resumen

La creciente preocupación ambiental asociada a hidrofluorocarbonos (HFC) de alto potencial de calentamiento global ha impulsado acuerdos internacionales para su eliminación progresiva. Dado su amplio uso en sistemas refrigerantes, diversas estrategias se han ideado para su recuperación. Entre ellas, la destilación extractiva es una alternativa prometedora, pues permite recuperar componentes refrigerantes para usos alternativos. En este contexto, los líquidos iónicos y los solventes eutécticos han despertado interés como solventes de arrastre debido a sus propiedades termofísicas y versatilidad molecular. Sin embargo, el vasto espacio químico y complejos fenómenos físicos asociados a estos dificultan su diseño racional, resaltando la necesidad de enfoques teóricos predictivos que fundamenten la toma de decisiones en torno a nuevas tecnologías de separación.

El modelo de solvatación COSMO-RS y las simulaciones por dinámica molecular proveen un marco robusto para estudiar el efecto de características microscópicas sobre el comportamiento termofísico de solventes eutécticos fluorados. Estos enfoques demuestran que la solubilidad de HFCs es influenciada por interacciones localizadas soluto–solvente y por la disrupción de aglomeraciones de soluto en la fase líquida. La información molecular obtenida permite identificar criterios específicos para el desarrollo de solventes avanzados destinados a la recuperación de HFCs.

En una escala más amplia, ecuaciones de estado basadas en SAFT proporcionan modelos robustos para caracterizar equilibrios de fases relevantes para la absorbción de HFCs. Los modelos termodinámicos empleados permiten evaluar líquidos iónicos basados en fosfonio y solventes de eutéctico profundo de tipo III como solventes de arrastre para mezclas refrigerantes en un amplio rango de condiciones operacionales. Su desempeño, cuantificado en torno a métricas de selectividad, permite identificar candidatos para la recuperación de HFCs desde mezclas comerciales.

Los modelos termodinámicos generados son integrados en simulaciones de proceso y análisis de ciclo de vida para evaluar su desempeño ambiental en la recuperación de mezclas refrigerantes mediante destilación extractiva. Este proceso constituye una alternativa viable a las rutas de tratamiento basadas en destrucción química, siempre que la demanda por compuestos recuperados permita reemplazar su producción virgen. La evaluación de cadenas de suministro destaca la importancia de adoptar tempranamente esta tecnología, con tal de reducir la huella de carbono asociada a futuros escenarios de eliminación de HFCs.

En conjunto, la integración multiescala de enfoques computacionales constituye una metodología efectiva para el desarrollo de tecnologías basadas en solventes avanzados orientadas al tratamiento sostenible de gases fluorados.

Abstract

The increasing environmental concern associated with high-GWP hydrofluorocarbons (HFCs) has propelled international agreements for their progressive phase-out. Given the widespread use of these compounds in refrigeration applications, considerable efforts have been devoted to the development of strategies for their recovery. Extractive distillation has emerged as a promising route, as it enables the recovery of refrigerant constituents for their use in alternative applications. In this context, ionic liquids and eutectic solvents have attracted growing interest as entrainers due to their suitable thermophysical properties and molecular tunability. However, the vast chemical space and complex physical phenomena associated with these solvents hinder their rational design, highlighting the need for predictive theoretical approaches aimed at supporting decision-making in the implementation of novel separation technologies.

The COSMO-RS solvation model and molecular dynamics simulations provide a powerful framework to study the effect of microscopic features in the thermophysical behavior of fluorinated eutectic solvents. These approaches demonstrate that HFC solubility is strongly influenced by localized solute–solvent interactions and disruption of solute clustering in the liquid phase. The obtained molecular-level insights highlight specific design criteria for the development of advanced solvents for HFC recovery.

At a broader scale, SAFT-based equations of state provide robust mathematical models to characterize phase equilibria in systems relevant to HFC absorption. The employed thermodynamic models allow to evaluate phosphonium-based ionic liquids and type III deep eutectic solvents as entrainers for refrigerant blends over a wide range of operational conditions. The performance of these solvents, quantified through selectivity metrics, is assessed to identify promising candidates for the recovery of HFCs from commercial mixtures.

The generated thermodynamic models are integrated into process simulation and life cycle assessment frameworks to evaluate their environmental performance in the reclamation of refrigerant blends. HFC recovery based on extractive distillation provides a viable alternative to destruction-oriented management routes, subjected to the extent to which recovered components displace fresh production. Furthermore, supply chain assessments highlight the importance of early deployment of this technology in reducing the carbon footprint of phase-out scenarios for HFCs.

Overall, the multiscale integration of computational approaches provides an effective framework for the development of technologies based on advanced solvents aimed at the sustainable management of fluorinated gases.

Contents

List of Figures

List of Tables

List of Abbreviations

Abbreviation	Definition
AARD	Average Absolute Relative Deviation
ASC	Apparent Surface Charge
ADD	Angle-distance Distribution
BAU	Business-as-usual
CFC	Chlorofluorocarbon
[Ch]Cl	Choline Chloride
COSMO	Conductor-like Screening Model
COSMO-RS	Conductor-like Screening Model for Realistic Solvents
CSM	Continuum Solvation Model
[C_2mim][HDFS]	1-ethyl-3-methylimidazolium heptadecafluorooctane-1-sulfonate
DES	Deep Eutectic Solvent
DFT	Density Functional Theory
EG	Ethylene Glycol
EoS	Equation of State
ES	Eutectic Solvent
EQ	Ecosystem Quality
FEP	Free Energy Perturbation
FES	Fluorinated Eutectic Solvent
FFP	Fossil Fuel Potential
FU	Functional Unit
FVT	Free Volume Theory
F-gas	Fluorinated gas
GBA	Generalized Born Approximation
GHG	Greenhouse gas
GL	Glycerol
GWP	Global Warming Potential

HBA	Hydrogen Bond Acceptor
HBD	Hydrogen Bond Donor
HCFC	Hydrochlorofluorocarbon
HFC	Hydrofluorocarbon
HH	Human Health
HREX	Hamiltonian Replica Exchange
HS	Hard-Sphere
HTP	Human Toxicity Potential
IL	Ionic Liquid
KA	Kigali Amendment
LCA	Life Cycle Assessment
LCI	Life Cycle Inventory
LCIA	Life Cycle Impact Assessment
LINCS	Linear Constraint Solver
LJ	Lennard-Jones
MBAR	Multistate Benett Acceptance Ratio
MD	Molecular Dynamics
MPE	Multipole Expansion
NEMD	Non-Equilibrium Molecular Dynamics
NR	Natural Resources
[N_{1111}]Cl	Tetramethylammonium chloride
[N_{4444}][NFS]	Tetrabutylammonium nonafluorobutane-1-sulfonate
ODP	Ozone Depleting Potential
OPLS	Optimized Potential for Liquid Simulations
PC-SAFT	Perturbed Chain - Statistical Associating Fluid Theory
PCM	Polarizable Continuum Model
PFPA	Perfluoropentanoic acid
PME	Particle-Mesh Ewald
[P_{4444}]Br	Tetrabutylphosphonium bromide
[$P_{666,14}$]Cl	Trihexyl(tetradecyl)phosphonium chloride
[$P_{666,14}$][GLY]	Trihexyl(tetradecyl)phosphonium glycinate
[$P_{666,14}$][TMPP]	Trihexyl(tetradecyl)phosphonium bis(2,4,4-trimethylpentyl)phosphinate
RDF	Radial Distribution Function
R125	Pentafluoroethane
R1234yf	2,3,3,3-tetrafluoropropene
R1234ze(E)	Trans-1,3,3,3-tetrafluoropropene

R134a	1,1,1,2-tetrafluoroethane
R143a	1,1,1-trifluoroethane
R32	Difluoromethane
RMSD	Root-Mean-Square-Deviations
SAFT	Statistical Associating Fluid Theory
SCD	Screening Charge Density
SW	Square-Well
TAP	Terrestrial Acidification Potential
TPD	Tangent Plane Distance
TPT1	First-Order Thermodynamic Perturbation Theory
QC	Quantum Chemistry
VLE	Vapor-Liquid Equilibrium
WCP	Water Consumption Potential

List of Symbols

Symbol	Definition
$\tilde{a}^{\text{assoc}}$	SAFT association Helmholtz energy contribution
$\tilde{a}^{\text{chain}}$	SAFT chain Helmholtz energy contribution
$\tilde{a}^{\text{disp}}$	SAFT dispersion Helmholtz energy contribution
$\tilde{a}^{\text{hc}}$	SAFT hard-chain Helmholtz energy contribution
$\tilde{a}^{\text{hs}}$	SAFT hard-sphere Helmholtz energy contribution
$\tilde{a}^{\text{res}}$	SAFT residual Helmholtz energy contribution
a_{eff}	Effective contact area between COSMO surface segments
A	Helmholtz energy
$\underline{\underline{\boldsymbol{\mathcal{A}}}}$	LCA technology matrix
B	FVT overlap parameter
$\underline{\underline{\boldsymbol{\mathcal{B}}}}$	LCA intervention matrix
d_i	Temperature-dependent segment diameter of species i
e_{HB}	COSMO-RS hydrogen-bonding energy contribution
e_{misfit}	COSMO-RS misfit energy contribution
E	Energy
E_{CA}	Cation–anion interaction energy
E_{COSMO}	COSMO energy
E_{vdW}	COSMO-RS van der Waals energy contribution
f_{pol}	COSMO polarization correction factor
$\hat{f}_i$	Fugacity
$\underline{\mathbf{F}}$	Force vector
g	Radial distribution function
$\underline{\boldsymbol{g}}$	LCA vector of environmental interventions
$\underline{\boldsymbol{h}}$	LCA impact vector
$\mathcal{H}$	Hamiltonian

$\tilde{H}^{\text{res}}$	Residual molar enthalpy
k_{ij}	SAFT binary interaction parameter between components i and j
L_v	Length FVT parameter
L_x	Simulation box length in the x-direction
L_y	Simulation box length in the y-direction
L_z	Simulation box length in the z-direction
$m_{s,i}$	Number of spherical segments constituting species i in SAFT
m_i	Mass of particle i
$\bar{m}$	Mean segment number
M_w	Molecular weight
$\underline{\boldsymbol{n}}$	Normal vector to a given surface
n_b	Number of flows allocated to the biosphere
n_c	Number of components
n_{el}	Number of chemical elements
n_f	Number of flows
n_p	Number of environmental impact categories
n_q	Number of surface segments in the COSMO cavity
$n_{q,M}$	Number of point charges in the charge distribution of the solute
n_s	Number of process vectors
n_t	Number of flows allocated to the technosphere
n_λ	Number of intermediate alchemical states
n_σ	Number of contacts between COSMO surface segments
N	Number of particles
$p_S(\sigma)$	COSMO σ-profile
p_ξ	Momentum
P	Pressure
P^{sat}	Saturation pressure
P_i^{sat}	Saturation pressure of species i
P_{xx}	Diagonal component of pressure in the x direction
P_{yy}	Diagonal component of pressure in the y direction
P_{zz}	Diagonal component of pressure in the z direction
$\underline{\underline{\boldsymbol{\mathcal{P}}}}$	LCA process matrix
q	Atomic point charge
q_M	Atomic point charge of solute
$\underline{\underline{\boldsymbol{\mathcal{Q}}}}$	LCA characterization matrix
r	Radial distance

r_{CA}	Cation–anion distance
r_{cut}	Cut-off distance for interaction calculation
r_{list}	Cut-off distance for the short-range neighbor list
$\underline{\mathbf{r}}$	Position vector
$\underline{\mathbf{s}}$	Position vector on a closed surface
$\underline{\boldsymbol{s}}$	LCA vector of scaling factors
S^{A_i}	Number of association sites of type A in species i
$S_{i/j}$	Selectivity of species i over component j
S_{vdW}	COSMO surface area
$S_{v,i}$	Area of COSMO surface segment i
t	Time
T	Absolute temperature
u	Pair potential
u_{ii}^{LJ}	Lennard-Jones potential of species i
u_{ii}^{mSW}	Modified square well potential of species i
U	Potential energy
U_{angles}	Angles energy contribution to potential energy
U_{bonds}	Bonds energy contribution to potential energy
$U_{\mathrm{non\text{-}bonded}}$	Non-bonded energy contribution to potential energy
U_{torsion}	Torsion energy contribution to potential energy
$\tilde{v}$	Molar volume
$\underline{\mathbf{v}}$	Particle velocity
V	Volume
x_i	Mole fraction of species i
$\underline{\mathbf{x}}$	Mole fraction vector
X^{A_i}	Fraction of molecules of species i unbonded at site A
Z	Compressibility factor
α	FVT energy barrier parameter
$\alpha'_{\mathrm{misfit}}$	COSMO-RS misfit constant
γ_i	Activity coefficient of species i
γ_i^{∞}	Activity coefficient at infinite dilution of species i
γ	Surface tension
$\Delta^{A_iB_i}$	SAFT association strength between sites A and B of species i
ΔE_{int}	Difference in interaction energy
Δt	Time interval
$\Delta\eta$	FVT dense fluid contribution to dynamic viscosity

ϵ	Electrical permittivity
ε	Depth of potential energy well
$\varepsilon^{A_iB_i}$	SAFT association energy between sites A and B in species i
ε_{ii}	SAFT dispersion energy of species i
ε_{ij}	SAFT cross-dispersion energy between components i and j
η	Dynamic viscosity
η^{L}	Liquid shear viscosity
η_0	FVT dilute gas dynamic viscosity
η_0^{mix}	FVT dilute-gas viscosity of a mixture
κ_T	Isothermal compressibility
$\kappa^{A_iB_i}$	SAFT association volume between sites A and B in species i
λ_i	Parametric value of alchemical state i
$\lambda_{\sigma,ii}$	Reduced well width in the modified SW pair potential of species i
Λ_i	Thermal de Broglie wavelength of species i
μ_i	Chemical potential of species i
μ_i^{res}	Residual chemical potential of species i
μ_i^0	Chemical potential of species i in its pure state
π	Number of phases in equilibrium
ρ	Number density
$\hat{\rho}$	Mass density
$\tilde{\rho}$	Molar density
$\hat{\rho}^{\mathrm{L}}$	Liquid mass density
ϱ_M	Electronic charge density of the solute
σ	Screening charge density
σ_{ii}	SAFT segment diameter of species i
σ_{ij}	SAFT cross-segment diameter between components i and j
τ_P	Time constant for barostat
τ_T	Time constant for thermostat
Υ	Solute cavity surface
$\hat{\phi}_i$	Fugacity coefficient of species i
Φ	Reaction field potential
χ_{comb}	COSMO-RS combinatorial contribution to chemical potential
Ω	Possible SAFT association sites in a set
$\Omega^{(2,2)}$	FVT collision integral

1. Introduction

Hydrofluorocarbons (HFCs) have been widely adopted in the refrigeration industry as replacements for ozone-depleting substances, yet their high global warming potentials have triggered their phase-out under the Kigali Amendment to the Montreal Protocol. This problem has posed the need for effective HFC phase-out strategies, in order to facilitate the transition toward next-generation refrigerants. Among the available alternatives, the selective recovery of HFC-based blends through extractive distillation represents a promising route to support a circular economy framework. In this context, ionic liquids and eutectic solvents have emerged as attractive entrainers due to their tunable physicochemical properties. Nevertheless, the vast chemical space and molecular complexity associated with these compounds demands the use of theoretical approaches rooted in microscopic physical phenomena to support the decision-making toward their implementation.

Anthropogenic impacts on environment have evolved from a primarily scientific concern to one of the defining challenges of the 21st century [1, 2]. Their significance lies in the magnitude of their effects on Earth's ecological balance, including the increased frequency of heatwaves [3], ocean acidification [4], biodiversity loss [5], and accelerated cryospheric melting [6]. The diversity of these phenomena, distinct in their underlying mechanisms, motivated the development of the planetary boundaries assessment [7]. This framework defines nine Earth-system processes, whose disruption beyond critical thresholds may lead to changes beyond the planet's self-regulating capacity. These processes are: climate change, rate of biodiversity loss, disruption of nutrient (nitrogen and phosphorus) cycles, stratospheric ozone depletion, ocean acidification, global freshwater use, change in land use, atmospheric aerosol loading, and chemical pollution.

Since the planetary boundaries framework was first proposed, several of these thresholds have already been transgressed [8, 9], with ocean acidification recently exceeding its safe boundary [10]. As expected from Earth-system processes, these boundaries are tightly coupled [7], meaning that the disruption of one process can compromise the stability of others. Among them, anthropogenic emission of greenhouse gases (GHGs) is the primary driver of global warming, *i.e.*, the ongoing increase in global average temperature, and therefore a paramount driver of climate change [11]. The importance of greenhouse forcing is reflected in the international treaties established over the past decades, most notably the United Nations Framework Convention on Climate Change [12],

followed by the Kyoto Protocol [13], and the Paris Agreement [14]. Despite substantial international efforts aimed at reducing GHG emissions, atmospheric concentrations of these compounds have continued to rise [2], accompanied by increasing global temperatures. Moreover, recent evidence further suggests that the 1.5°C target established in the Paris Agreement may already been temporarily exceeded [15].

Regarding atmospheric concentrations, the most relevant GHGs are carbon dioxide, nitrous oxide, and methane [2], and most mitigation strategies have historically focused at these compounds [16]. However, fluorinated gases (F-gases), despite accounting for less than 3% of total GHG emissions [17], are a particularly concerning class of compounds due to their exceptionally high global warming potentials (GWPs). Owing to the high stability of the carbon–fluorine bond, these compounds exhibit low reactivity and thus long atmospheric lifetimes. Furthermore, the strong infrared absorption associated with fluorinated functional groups further increases their radiative forcing. As a result, F-gases can exhibit GWPs several orders of magnitude above those of conventional GHGs [18]. Among F-gases, hydrofluorocarbons (HFCs) constitute the most important family from an industrial perspective. These compounds were conceived as alternatives to chlorofluorocarbons (CFCs) and hydrochlorofluorocarbons (HCFCs) as working fluids for refrigeration systems [19]. Their adoption was largely driven by the phase-out of CFCs and HCFCs under the Montreal Protocol on Substances That Deplete the Ozone Layer [20], following the demonstration of their ozone-depleting effects [21, 22].

At present, HFCs, also referred to as third-generation refrigerants, remain among the most used compounds in refrigeration and air-conditioning equipment [19], creating a particularly concerning combination with their high GWPs [23]. Examples of this are difluoromethane (R32), 1,1,1,-trifluoroethane (R143a), 1,1,1,2-tetrafluoroethane (R134a), and pentafluoroethane (R125), with reported GWPs of 677, 4800, 1300, and 3170, respectively [11]. Details on the nomenclature system for these compounds can be found elsewhere [19]. The widespread use of HFCs generates a positive feedback mechanism, in which increasing global temperatures intensify the demand for cooling technologies, subsequently increasing the potential release of high-GWP refrigerants through equipment leakage and inadequate end-of-life management [23]. In the absence of effective control measures, projections indicate a significant contribution of HFCs to climate forcing, with global emissions reaching up to 5.3 $GtCO_2e{\cdot}yr^{-1}$ by 2050 [18, 24].

This issue was formally addressed through the Kigali Amendment to the Montreal Protocol [25] in 2016, which established, for the first time, a global framework to decrease HFC emissions. Relative to previously defined consumption baselines, adhering countries committed to a stepped reduction schedule, aiming at final reductions of 85% for developed countries by 2036 and 80% for developing countries by 2045. In this context, major economies such as China, the European Union, and the United States have implemented stringent HFC regulations through the National Plan on the Implementation of the Montreal Protocol [26], the European Environmental Agency [27], and the U.S. Environmental Protection Agency [28], respectively. These measures include leak prevention and repair protocols, mandatory reporting of HFC production and trade activities, and sectorial bans on high-GWP refrigeration equipment. Within this new scenario, the transition toward next-generation refrigerants has become unavoidable.

The transition to low-GWP refrigerants has been largely dominated by hydrofluoroolefins (HFOs), *i.e.*, fluorocarbons containing carbon–carbon double bonds. Compared to HFCs, the unsaturation of HFOs enhance their atmospheric reactivity, significantly reducing their atmospheric lifetimes and consequently their GWPs [19]. One of the earliest examples in this regard was the introduction of 2,3,3,3-tetrafluoropropene (R1234yf) as a replacement for R134a in automobile refrigerant systems [22]. Despite the promising environmental characteristics of HFOs, their increased reactivity has also raised concerns in terms of persistent degradation products, toxicity, and flammability. In this context, blends combining HFOs with HFCs, particularly R32 and, in some cases, R134a, have emerged as a rational compromise between GWP, operational safety, and refrigeration performance [29].

The continued incorporation of HFCs into refrigeration equipment highlights the importance of reevaluating their industrial management. While lower-GWP HFCs remain valuable as components in next-generation refrigerant blends, higher-GWP compounds, such as R143a and R125, are expected to be progressively phased-out from refrigeration equipment. However, rather than being used as pure working fluids, these compounds are commonly incorporated into commercial refrigerant blends such as R410A (50 wt.% R32 + 50 wt.% R125) and R404A (44 wt.% R125 + 52 wt.% R143a + 4 wt.% R134a) [19]. Analogously to the historical phase-out of CFCs and HCFCs, one of the most widespread strategies for eliminating high-GWP HFCs is their chemical destruction [30]. Due to the chemical inertness of fluorinated compounds, highly energy-intensive methods are usually required, with thermal oxidation representing one of the most common alternatives [31]. Although emerging technologies aim to reduce the environmental footprint of HFC destruction processes [32], the lack of dedicated infrastructure in developing regions continues to limit their implementation on a substantial scale [30].

As a less energy-intensive and more readily deployable alternative, HFC reclamation, *i.e.*, recycling and reprocessing of HFCs to meet characteristics close to virgin refrigerants, has gained increasing attention [30]. By enabling the reuse of still-permitted HFCs in refrigeration equipment, reclamation provides a pathway toward a circular economy framework for HFCs. However, business-as-usual (BAU) reclamation strategies remain severely limited in the case of refrigerant mixtures, as they are generally incapable of recovering individual HFC constituents from these systems. This limitation originates from the thermodynamic behavior targeted in refrigerant blend design, which involves small temperature glides [33], *i.e.*, small differences between dew- and bubble-point temperatures at constant pressure, or azeotropy [34], *i.e.*, identical vapor and liquid concentrations at certain temperature and pressure. Consequently, conventional distillation methods employed in BAU reclamation are generally unable to selectively separate higher-GWP HFCs from still-viable refrigerant components [35], restricting the management of these blends to destruction-based approaches.

To enable a circular economy framework for refrigerant mixtures, regardless of their composition, the selective separation of HFCs becomes a fundamental requirement. In this regard, extractive distillation is among the leading technologies for the separation of azeotropic mixtures [36]. In this process, an additional component, known as entrainer, is added to the system to modify the relative volatility of the mixture by preferentially interacting with one or more species. In a conventional extractive distillation, the entrainer is fed near the top of a distillation column, while

the mixture to be separated is incorporated a certain amount of stages below. Subsequently, the entrainer carries one or more of the species to the bottom of the equipment, while the now light key component is obtained overhead as a relatively pure distillate. Finally, the bottoms of the column are further fed to another unit operation, usually a flash vessel or second column, to separate the entrainer from the remaining components. This allows to recycle the entrainer back to the column, and to recover the absorbed volatile components, free of the distilled compound [35]. When applied to refrigerant blends, extractive distillation enables the recovery of low-GWP refrigerants, analogously to BAU reclamation, while also allowing for isolating higher-GWP components for their use in alternative applications, such as feedstock for fluoropolymer production [31, 37]. However, for the process to be technically feasible, the entrainer must meet particular characteristics, including complete miscibility with the mixture, high selectivity between components, and sufficiently low volatility to minimize losses to the vapor phase [36, 38].

Among entrainer alternatives for the separation of refrigerant blends, ionic liquids (ILs) and eutectic solvents (ESs) have been increasingly investigated as remarkable alternatives [39, 40]. ILs are salts with melting points typically below 100°C that can be tailored, by tuning cation–anion pairs, to reach properties such as negligible vapor pressure, high thermal stability, and non-flammability [41, 42]. Besides such advantageous thermophysical properties, this tunability has been used to synthesize ILs aimed at the extractive distillation of HFC-based mixtures [43], with emphasis on the role of ionic structure and functionalization [44]. From a different approach, eutectic solvents (ESs) exploit the melting point depression in binary mixtures, enabling the use of compounds that are normally solid at common operating conditions. Deep eutectic solvents (DESs), a subgroup of ESs with substantial deviations from ideal solution behavior [45], develop even wider liquidus gaps. This feature has expanded the pool of available compounds as liquid solvents, especially related to low costs, biodegradability, negligible vapor pressures, and simple preparation of their mixtures [46]. Historically, these deviations from ideality were attributed to hydrogen bonding, which motivates the classification of the components of an ES as hydrogen bond acceptor (HBA) and donor (HBD) [47]. Like ILs, ESs offer broad molecular tunability, allowing properties to be tailored for specific tasks by selecting different HBA–HBD combinations. However, their use as entrainers for HFC-based blends has not been as widely explored as for ILs, being restricted to studies on particular DESs [48].

The remarkable tunability of ILs and DESs also presents a major challenge in the identification of suitable entrainers for HFC-based blends. In the case of ILs, the wide variety of possible cation–anion combinations, together with the various possible functionalizations in each ion, renders the number of possible compounds virtually unlimited [43]. Analogously, DESs are nowadays classified into five main types depending on the nature of their comprised HBA and HBD. Type III DESs, the most extensively studied in the literature, are typically formed from quaternary ammonium salts and organic compounds such as amides, carboxylic acids, alcohols, or polyols. More recently introduced in 2019 [49], Type V DESs consist of non-ionic eutectic mixtures such as those based on phenolic compounds and monocarboxylic acids [47]. The continuously expanding chemical space associated with ILs and DESs heavily hinders a definitive experimental characterization of feasible solvents for F-gas recovery. In this context, predictive theoretical approaches, capable

of relating molecular structure and physical interactions with macroscopic thermophysical information, arise as promising tools for the rational design of these compounds for HFC absorption.

Equations of state (EoSs) constitute one of the most direct approaches to process design, as they relate the phase behavior of multicomponent mixtures with operating thermodynamic variables using explicit mathematical relations [50]. Their relevance in industry is evidenced by the extensive range of systems and thermodynamic conditions successfully modeled though these approaches. Particularly, molecular-based EoSs derived from the Statistical Associating Fluid Theory (SAFT) [51] incorporate physically meaningful parameters, associated with molecular size and intermolecular interactions [52]. The empirical fit of these parameters allow to reliably depict the thermodynamic behavior of complex fluids, while correlating this behavior with molecular-level phenomena. SAFT-based EoSs have been successfully employed to model the absorption of gaseous solutes in ILs and ESs [44, 53], providing a computationally efficient framework for predicting relevant thermophysical properties. Nevertheless, despite their rigorous statistical mechanical foundations, these approaches provide a limited physical interpretation of the mechanisms governing HFC absorption. Thus, their applicability in the search for suitable solvents for refrigerant mixtures is mostly restricted to translating experimental observations into highly predictive thermodynamic models for process design and evaluation.

A more detailed physical interpretation of HFC absorption in complex solvents can be achieved through molecular simulations. Particularly, molecular dynamics (MD) simulations constitute a fundamental tool for understanding the microscopic phenomena underlying the macroscopic behavior of condensed systems, as they derive macroscopic thermophysical properties directly from the statistical averaging of molecular trajectories [54]. Despite their high computational cost relative to SAFT-based approaches, MD simulations have become an important complement to empirical observations and thermodynamic modeling [55]. In the context of F-gas absorption, this is evidenced by studies characterizing the effect of intermolecular interactions, solvation environments, and liquid structure in the thermodynamic performance of novel solvents [56]. Furthermore, the development of increasingly transferable models for MD simulation has substantially improved the predictive capability of this approach for complex solvents [57–59], where new insights can provide information on desirable molecular features for entrainers.

Within a predictive framework, quantum chemical (QC) methods provide access to molecular electronic structure from first principles, allowing to characterize intermolecular interactions directly from chemical structure [60]. Among these approaches, the conductor-like screening model for realistic solvents (COSMO-RS), rooted in continuum solvation theory, has gained considerable attention due to its ability to connect electronic structure calculations with fluid-phase thermodynamics [61]. This model is also characterized by its efficiency, requiring the computationally demanding QC calculations to be performed only once per compound. Consequently, COSMO-RS has enabled the exploration of large chemical spaces with minimum dependence on empirical parameterizations [62]. In the search for suitable entrainers for HFC-based blends, COSMO-RS has been used in the evaluation of ILs and ESs in terms of Henry's law constants, excess thermodynamic properties, and phase equilibria [63, 64]. Although the resulting predictions are generally qualitative in nature, the highly predictive character of COSMO-RS makes it a valuable screening tool for identifying promising solvents for a further, more detailed, analysis.

The conjunction of above computational approaches defines a powerful framework for the study and design of solvents for HFC absorption and recovery processes. Nevertheless, a comprehensive assessment of such technologies requires a broader perspective than an evaluation of their feasibility in terms of material and energy requirements [65]. In this regard, the decision-making around the deployment of IL- or ES-based processes can be supported through methods of life cycle assessment (LCA). By quantifying environmental impact indicators across multiple areas of protection for sustainable development, LCA offers a valuable insight of the feasibility of novel solvents beyond their thermodynamic performance [66, 67]. This is especially relevant for ESs, which are frequently coined as green alternatives to conventional solvents and ILs [68], despite such claims often neglecting the environmental burdens of the supply chain that yields to their synthesis [45]. In this regard, the holistic perspective of LCA, capable of encompassing stages from raw material extraction to end-of-life management, offers an essential contribution to the development of sustainable solvent-based technologies for HFC recovery and separation.

1.1. Hypothesis

A computational strategy comprising reliable thermodynamic models allows to define a set of environmentally feasible solvents to separate and recover F-gases. The characterization of these solvents can be studied by understanding its behavior at a molecular level, with aims to holistically extend this approach to process design and life cycle assessment.

1. It is possible to find a selection of appropriate eutectic solvents according to the required objective, enhancing the life cycle of the process either from an environmental, economic, or energetic perspective.
2. It is possible to reduce the environmental impact of separation processes of F-gases by finding alternative solvents to traditional compounds.
3. The characterization of ESs can be studied and enhanced though the understanding of their behavior at a molecular level with aims to the macroscale. Molecular modeling tools are nowadays ready to grant key information to be used in the search for the most appropriate solvent.

1.2. Main Objective

Provide a holistic theoretical framework, based on a methodology combining molecular modeling techniques with process simulation, to evaluate new absorption units for the recycling of F-gases using eutectic solvents.

Specific objectives

- Analyze the performance of COSMO-RS as a predictive model for the selection of solvents in the capture of F-gases, evaluating their absorption capabilities through the characterization of their phase equilibrium and relating predicted molecular features with macroscopic observables.
- Characterize the behavior of systems formed by F-gases and eutectic solvents by SAFT-based equations of state and MD simulations, evaluating the impact of solvent structure and intermolecular interactions in the thermophysical behavior of the system.
- Study the feasibility of selected solvents based on criteria of selectivity and regeneration performance for their use in the proposed reclamation process by extractive distillation.
- Evaluate the performance of the extractive distillation of refrigerant blends using eutectic solvents by means of process-related parameters, such as purity of recovered gases, and environmental markers relative to current phase-out strategies.

2. Fundamentals of COSMO-RS

This chapter presents the fundamental theoretical background of the continuum solvation model for realistic solvents (COSMO-RS). Based on continuum solvation models, the development of COSMO provided a stable, accurate, and simple numerical approach to characterize solvation phenomena. However, the further development of COSMO-RS triggered its wide use due to its remarkable predictive qualities for thermophysical characterization. Relying on statistical thermodynamics applied to electronic distributions, COSMO-RS provides access to a wide variety of thermodynamic properties. Thus, its use in the screening and predictive evaluation of novel solvents serves as a promising tool to assess DESs for HFC absorption.

2.1. Introduction

Understanding and predicting the behavior of complex fluid mixtures is a central concern in chemical thermodynamics. In this regard, the availability of experimental data serves as the foundation for model development, while also enabling the validation of existing theories related to thermophysical characterization. However, as increasingly complex compounds are proposed to address current technological and environmental challenges [69, 70], the accessible chemical compound space continues to expand [71]. With an increased pool of available compounds, comprehensive experimental characterization is hindered [72], thus challenging the traditional paradigm of thermodynamic model development [71, 73].

This shift motivated, among other approaches, the elaboration of *ab initio*-based methods. Instead of relying on system-specific parameterizations, quantum chemistry (QC) methods describe compounds in terms of their molecular structure to characterize their electronic behavior [60]. In this context, continuum solvation models (CSMs) have gained wide acceptance by incorporating solvent effects into molecular calculations, which are known to strongly influence molecular behavior [74]. Within these models, the solvent environment of a given molecule is simplified to a dielectric medium, reducing the degrees of freedom of the problem while providing a realistic description of solvation effects. This approach has proven successful in describing various concepts such as

conformational changes, reaction mechanisms, and association equilibria [75]. However, macroscopic thermodynamics lies out of the scope of these methods, resulting in a breach with concepts essential for engineering applications [62].

The conductor-like screening model for realistic solvents (COSMO-RS) provides a framework to bridge this gap, establishing a pathway from quantum chemistry to thermophysical properties [61]. Within this formalism, molecules are represented by their surface screening charge density distribution, and their interactions are evaluated through a statistical thermodynamic treatment of pairwise surface contacts [76]. This method enables the prediction of thermophysical properties with minimal reliance on experimental data, making it suitable for exploring large and continuously expanding chemical compound spaces. The success of COSMO-RS also lies in its computational efficiency, as the most demanding step of molecular structure optimization must be performed only once per compound [77]. Thus, both pure and multicomponent systems, formed by various sets of chemical species, can be readily defined to construct phase equilibrium diagrams, screen novel solvents, and compute partition coefficients, among other applications [61].

In this chapter, the theoretical foundations of COSMO-RS are introduced, and the methodology adopted in this work is described. The chapter begins with a conceptual overview of the COSMO approach, followed by the statistical thermodynamic formulation of COSMO-RS, and concludes with the methodological details employed throughout this thesis.

2.2. Theoretical background

COSMO belongs to the more general CSMs, which find their basis on the Onsager reaction field model [78]. Here, a single solute molecule is immersed in an infinite solvent reservoir, represented as an unstructured dielectric continuum with electrical permittivity ϵ. The segregation between solute and solvent is done by defining a void cavity surrounding the solute. Two characteristics are assumed for this cavity: it physically excludes the solvent medium and the entire electronic charge distribution of the solute, ϱ_M, lies within it [75].

The size and shape of this solute cavity must be selected in a physical consistent manner, excluding the least amount of solute–solvent charge distribution overlap while retaining a size that doesn't conflict with the exclusion of the solvent. The most implemented definition consists on superposed atomic spheres with radii near their van der Waals values [75]. Radii proposed by Pauling [79], Bondi [80], and Klamt et al. [81] are commonly employed to ensure a coherent compromise between physical consistency and computational efficiency [75].

Once the method for the construction of the solute cavity is defined, the foremost problem of CSMs is tackled. Here, ϱ_M polarizes the dielectric continuum, which in turn polarizes ϱ_M. This problem, electrostatic in nature, is formalized by applying the Poisson equation to the so called reaction field potential, Φ [75]. This is shown in Eq. 2.1,

$$-\nabla^2\Phi\left(\underline{\mathbf{r}}\right) = \begin{cases} 4\pi\varrho_M\left(\underline{\mathbf{r}}\right) & \text{within solute cavity}\,, \\ 0 & \text{outside solute cavity}\,, \end{cases} \tag{2.1}$$

where $\underline{\mathbf{r}}$ is vector of spatial coordinates, and Φ is the sum of the potentials generated by ϱ_M, Φ_{M}, and by the polarization of the dielectric medium, Φ_{R}, as shown in Eq. 2.2,

$$\Phi = \Phi_{\mathrm{M}} + \Phi_{\mathrm{R}}\,, \tag{2.2}$$

where Φ_{R} is also denoted as reaction potential. Although Φ_{M} is directly obtained by knowing ϱ, the reaction potential is *a priori* unknown, as it depends on the response of the dielectric environment to the solute electronic field. Moreover, said response modifies ϱ, demanding a self-consistent process to obtain a correct characterization of the solute in the solvent environment. Numerous approaches have been proposed in the literature to solve this problem, including apparent surface charge (ASC), multipole expansion (MPE), and generalized Born approximation (GBA) [74].

COSMO belongs to the ASC methods. These are characterized by defining an auxiliary variable, such that its integration over the solute cavity surface, Y, yields Φ_{R}. This auxiliary variable is commonly expressed as a surface charge density, σ, which takes non-zero values only in the set of coordinates $\underline{\mathbf{s}} \in \mathrm{Y}$. Thus, the reaction potential can be obtained following Eq. 2.3,

$$\Phi_{\mathrm{R}}\left(\underline{\mathbf{r}}\right) = \int_{\mathrm{Y}} \frac{\sigma\left(\underline{\mathbf{s}}\right)}{\left\|\underline{\mathbf{r}} - \underline{\mathbf{s}}\right\|} d^2 s\,. \tag{2.3}$$

As seen from Eq. 2.3, the advantage of ASC methods lies in that the problem of characterizing the response of the infinite dielectric medium is reduced to the more simple problem of integrating σ over a closed surface. This calculation is more commonly performed by approximating Y as a set of n_q finite elements. Following this, the integration of $\sigma\left(\underline{\mathbf{s}}\right)$ over Y is simplified to the sum over all n_q elements as shown in Eq. 2.4,

$$\Phi_{\mathrm{R}}\left(\underline{\mathbf{r}}\right) \approx \sum_{i=1}^{n_q} \frac{\sigma_i S_{v,i}}{\left\|\underline{\mathbf{r}} - \underline{\mathbf{s}}_i\right\|} = \sum_{i=1}^{n_q} \frac{q_i}{\left\|\underline{\mathbf{r}} - \underline{\mathbf{s}}_i\right\|}\,, \tag{2.4}$$

where σ_i is the surface charge density of element i, $S_{v,i}$ its area, and q_i its associated point charge. The only remaining problem is the computation of σ, such that the boundary conditions of the electrostatic problem are reproduced. Following the original ASC method, the polarizable continuum model (PCM) [82], $\sigma\left(\underline{\mathbf{s}}\right)$ is directly calculated from the polarization condition on the cavity surface, following Eq. 2.5,

$$\sigma\left(\underline{\mathbf{s}}\right) = \frac{\epsilon - 1}{4\pi} \left(\frac{\partial \Phi}{\partial \underline{\boldsymbol{n}}}\right)_{\mathrm{in}} \Bigg|_{\underline{\mathbf{s}}}\,, \tag{2.5}$$

where $\underline{\boldsymbol{n}}$ is the unit vector normal to the cavity surface and pointing outward, and the subindex in the potential derivative indicates that the differentiation is performed at the inside limit of the cavity.

In the above scheme, the local values $\Phi(\underline{\mathbf{s}})$, required to define $\sigma(\underline{\mathbf{s}})$, also depend on the whole set of surface charge densities. Thus, an iterative procedure can be applied to yield a self-consistent solution for ϱ_M and σ. Although straightforward, this approach increases the computational cost of quantum chemical calculations, which are already iterative.

Considering this, COSMO was proposed to yield an approximate solution of Eq. 2.5 by adopting an ideal conductor boundary condition [83]. Here, the dielectric constant of the medium is replaced by that of a conductor, i.e., $\epsilon \to \infty$. Under this condition, the solute experiences a perfect screening from the conductor environment, thus conceptually replacing the discretized surface charge densities, σ_i, by screening charge densities (SCDs). The SCDs exactly compensate for the electronic contribution of the solute, such that the reaction field potential to vanish at Y according to Eq. 2.6,

$$\Phi(\underline{\mathbf{s}}) = 0\,. \tag{2.6}$$

The boundary condition supplied in Eq. 2.6, when applied to all SCDs in vector $\underline{\boldsymbol{\sigma}} \in \mathbb{R}^{n_q}$, generate a system of linear equations that relate interactions of segments with ϱ_M and between each other. The shape of the Y surface must be taken into account, and COSMO utilizes a formalism based on Green's functions to solve the electrostatic problem for arbitrarily shaped cavity surfaces. Finally, the solution to this problem is summarized by the calculation of the set of point charges in the cavity surface, $\underline{\boldsymbol{q}} \in \mathbb{R}^{n_q}$, by solving Eq. 2.7,

$$\underline{\boldsymbol{q}} = -\underline{\underline{\boldsymbol{A}}}^{-1}\underline{\underline{\boldsymbol{B}}}\,\underline{\boldsymbol{q}}_M\,, \tag{2.7}$$

where $\underline{\underline{\boldsymbol{A}}} \in \mathbb{R}^{n_q \times n_q}$ represents the electrostatic potential between surface segments, $\underline{\underline{\boldsymbol{B}}} \in \mathbb{R}^{n_{q,M} \times n_q}$ represents the electrostatic interaction between the solute charge distribution and the surface segments, and $\underline{\boldsymbol{q}}_M \in \mathbb{R}^{n_{q,M}}$ is the vector containing the $n_{q,M}$ charges from the solute charge distribution. Expressions for matrices $\underline{\underline{\boldsymbol{A}}}$ and $\underline{\underline{\boldsymbol{B}}}$ are given in Eqs. 2.8,

$$\frac{A_{ij}}{4\pi\epsilon_0} = \begin{cases} \|\underline{\mathbf{s}}_i - \underline{\mathbf{s}}_j\|^{-1} & i \neq j\,, \\ 1.07\sqrt{4\pi}\, S_{v,i}^{-1/2} & i = j\,, \end{cases} \tag{2.8a}$$

$$\frac{B_{ij}}{4\pi\epsilon_0} = \|\underline{\mathbf{s}}_i - \underline{\mathbf{r}}_j\|^{-1}\,. \tag{2.8b}$$

where $\underline{\mathbf{r}}_j$ represents the position of point charge $q_{M,j}$, and ϵ_0 is the electrical permittivity in the vacuum. Furthermore, to recover the effects of a finite dielectric constant, computed SCDs are multiplied by a factor of $(\epsilon - 1) \cdot (\epsilon + 0.5)^{-1}$.

The solution of Eq. 2.7 provides a direct solution of the set of SCDs within the molecular calculations for the solute. This allows the computation of solvation energies and molecular equilibrium geometries through a stable, accurate and simple numerical approach, given the simplicity of the

operators $\underline{\underline{\boldsymbol{A}}}$ and $\underline{\underline{\boldsymbol{B}}}$. This has ensured the presence of COSMO in a wide variety of quantum chemical packages [62]. The COSMO cavity construction is represented in Figures 2.14a and 2.14b for an ethanol molecule. Here, the QC calculation yields both an equilibrium geometry under solvation conditions and a cavity surface characterized by SCDs σ representing the response of the conductor medium.

Despite its remarkable contribution, the most noticeable impact of COSMO is the development of COSMO-RS [76, 81], which links the quantum chemical output of COSMO with the computation of thermodynamic properties. For an arbitrary system composed by an arbitrary number of species, this is achieved by first characterizing its interaction energy difference with respect to a reference COSMO state, ΔE_{int}. In the initial state of the system, each molecule is represented by its solute cavity surrounded by an infinite conductor medium. Thus, their SCDs and conformation energies can be precisely obtained from a COSMO calculation. Subsequently, an ensemble of molecules can be generated by placing the respective COSMO cavities separated by conductor surfaces. As these dividing surfaces serve as a perfect conductor, they perfectly screen all cavity surfaces, thereby canceling any electrostatic difference with respect to the previous step. Finally, to approach the real system, the hypothetical conductor surfaces must be removed. This further generates a contact between cavity surface segments, characterized by an effective contact area, a_{eff}, assumed constant across the ensemble.

To model the contact of two surface segment with SCDs of σ and σ', an equivalent segment with a SCD of $-\left(\sigma+\sigma'\right)$ is added to the system. Then, the energy difference due to the generation of the segment contact is obtained by computing the self-energy of the inserted segment [81], given by Eq. 2.9,

$$e_{\text{misfit}}\left(\sigma,\sigma'\right) = f_{\text{pol}}\,\alpha'_{\text{misfit}}\,\frac{\left(\sigma+\sigma'\right)^2}{2}\,, \tag{2.9}$$

where f_{pol} is the polarizability correction factor, arising from the adjustment of the wavefunction of molecules due to the change in their electrostatic medium, *i.e.*, the removal of the conductor surface. Considering typical electronic polarization values for organic solvents, a value of $f_{\text{pol}} = 0.6$ is commonly assumed [81]. Moreover, in Eq. 2.9, the α'_{misfit} constant is given by Eq. 2.10,

$$\alpha'_{\text{misfit}} = \frac{0.3}{\epsilon_0} a_{\text{eff}}^{1/2}\,. \tag{2.10}$$

Eq. 2.9 is commonly coined as misfit energy, as it arises from the deviation from the ideal contact of SCDs, *i.e.*, the case where $\sigma = -\sigma'$. In addition to this energy correction, COSMO-RS includes the formation of hydrogen bonds between segment pairs with a sufficient polarity difference. Thus, the energy contribution from the hydrogen bonding between two segments with SCDs of σ and σ' is computed using Eq. 2.11,

$$e_{\text{HB}}\left(\sigma,\sigma'\right) = c_{\text{HB}}\,\min\left(0,\,\sigma\sigma' - \sigma_{\text{HB}}^2\right)\,, \tag{2.11}$$

where c_{HB} is a temperature-dependent coefficient that accounts for the entropy loss due to the formation of the hydrogen bond [61], and the threshold value σ_{HB} limits the accounting for e_{HB} only between sufficiently polar surface segments [62]. Considering this, the problem of characterizing ΔE_{int} from all molecules in the system is replaced by finding the interaction energy among all n_σ surface contact interactions. Thus, the interaction energy difference, compared to the reference COSMO state, is computed following Eq. 2.12,

$$\Delta E_{\mathrm{int}} = a_{\mathrm{eff}} \sum_{i=1}^{n_\sigma} e_{\mathrm{int}} \left(\sigma_i, \sigma_i'\right) = a_{\mathrm{eff}} \sum_{i=1}^{n_\sigma} \left[e_{\mathrm{misfit}} \left(\sigma_i, \sigma_i'\right) + e_{\mathrm{HB}} \left(\sigma_i, \sigma_i'\right)\right] . \tag{2.12}$$

To obtain the total energy of the system, this quantity is added to the reference energy, which encompasses two contributions that are independent from individual surface contacts. The first one is the energy from the initial screened state, E_{COSMO}, which is directly obtained from COSMO calculations. The second one is the contribution due to the attractive dispersion interactions, E_{vdW}, which, as done in other CSMs [75], is computed as a first order expression as shown in Eq. 2.13,

$$E_{\mathrm{vdW}} = \sum_{i=1}^{n_{\mathrm{el}}} \tau_{\mathrm{vdW},i} \, S_{\mathrm{vdW},i} \, , \tag{2.13}$$

where n_{el} is the number of elements in the system, $\tau_{\mathrm{vdW},i}$ is an element-specific adjustable parameter for atom i, and $S_{\mathrm{vdW},i}$ its corresponding COSMO surface area.

Considering the fluctuating nature of fluid phases, Eq. 2.12 can be treated by calculating instead the ensemble average of the total energy of the system from a statistical thermodynamic approach. Thus, an integration of the surface contact-dependent energy must be carried out to characterize the thermodynamic properties of the system. However, this demands knowledge on all surface contacts i occurring in the ensemble, which translates into the need of all possible mutual arrangements among molecules, generating prohibitive calculations when trying a proper thermodynamic sampling [62].

To treat this scenario, COSMO-RS introduces a fundamental approximation: geometrical constraints in Eq. 2.12 can be decoupled from the analysis, and only the information on all interacting $\sigma_i - \sigma_i'$ pairs is required. It is assumed that all patches form pairs, thus representing a condensed medium where no free surface exists in the bulk. From this, the initial ensemble of molecules is replaced by the corresponding ensemble of pairwise interacting surface segments [62].

Since each patch can be uniquely described by their corresponding SCD, the new ensemble is sufficiently characterized by the distribution function $p_S(\sigma)$, commonly referred to as σ-profile. This profile describes the probability of finding, within a given molecule, a surface segment with a mean SCD of σ [81]. σ-profiles constitute the central molecular descriptors in COSMO-RS, encoding the surface charge density distribution of a molecule and allowing their treatment from a statistical thermodynamic perspective. Moreover, they serve as a common basis to recognize the chemical nature of compounds. As schematized in Figure 2.1c for ethanol, regions given by $\sigma < 0$ are correlated with electrophilic trends, characterized by a hydrogen bond donor nature. In turn, $\sigma > 0$

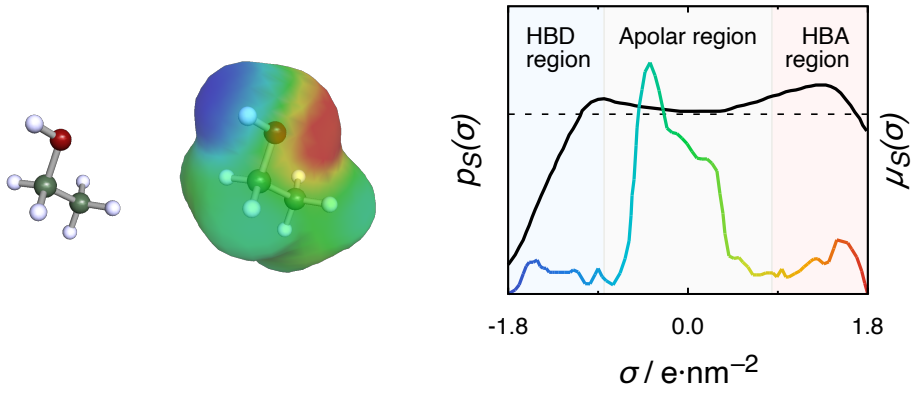

FIGURE 2.1: Schematic representation of the COSMO-RS workflow for ethanol. (a) Optimized molecular geometry within the COSMO boundary conditions. (b) COSMO cavity generated and colored according to the local SCD σ. (c) Corresponding σ-profile, $p_S(\sigma)$, (left axis, colored solid line) and σ-potential, $\mu_S(\sigma)$, (right axis, black solid line) employed in COSMO-RS. The $\mu_S(\sigma) = 0$ line is included (right axis, dashed line).

values represent nucleophilic and hydrogen bond acceptor trends. Regions around $\sigma = 0$, such as alkyl groups, are related to a low polarity.

A pure system of species i is characterized the σ-profile of a single molecule of this species, $p_{S,i}(\sigma)$. In turn, in a system of n_c components, the net σ-profile is given by Eq. 2.14,

$$p_S(\sigma) = \sum_{i=1}^{n_c} x_i \, p_{S,i}(\sigma) \, , \tag{2.14}$$

where x_i denotes the mole fraction of component i.

From the above change, the problem of characterizing the ensemble average is equivalent to finding the chemical potential of an additional patch with a SCD of σ in one mole of patches, $\mu_S(\sigma)$, which can be computed by solving the self-consistent relation given in Eq. 2.15,

$$\mu_S(\sigma) = -\frac{k_B T}{a_{\text{eff}}} \ln \int p_S(\sigma') \exp\left[-\frac{a_{\text{eff}}}{k_B T}\left(e_{\text{int}}(\sigma,\sigma') - \mu_S(\sigma')\right)\right] d\sigma' \, , \tag{2.15}$$

where the integration is carried out over all neighboring $\sigma - \sigma'$ pairs [61]. This chemical potential is more commonly referred to as the σ-potential of the system, and serves as an indicator of interaction preferences with surface segments of polarity σ. Thus, as schematized in Figure 2.1c, $\mu_S(\sigma) < 0$ values in the $\sigma < 0$ region represent preferential interactions with hydrogen bond-donor

compounds, while $\mu_S(\sigma) < 0$ values in the $\sigma > 0$ region represent preferential interactions with hydrogen bond acceptor compounds.

For non-Gaussian σ-profiles, Eq. 2.15 must be solved iteratively, commonly considering an initial value of $\mu_S(\sigma') = 0$ on the right-hand side, which ensures a rapid convergence [76]. Then, the chemical potential of compound i, μ_i, can be obtained by integrating $\mu_S(\sigma)$ over the surface of said compound [62], as shown in Eq. 2.16,

$$\mu_i = \int p_{S,i}(\sigma)\,\mu_S(\sigma)\,d\sigma + k_B T \ln\left(x_i + \chi_{\text{comb},i}\right) . \tag{2.16}$$

The first term of the right-hand side of Eq. 2.16 arises from the direct solute-solvent interactions, namely the residual part of the total chemical potential. The second term incorporates the trivial $k_B T \ln x_i$ term, as well as the combinatorial contribution, $\chi_{\text{comb},i}$, which describes the solute size dependence. This is incorporated in the COSMO-RS formalism by using the molecular surface areas and volumes, computed from the previous COSMO calculation [61].

Eq. 2.16 is the central equation in COSMO-RS. It provides the energetic characterization of an arbitrary solute, and extends the solvation foundings of the model by giving access to almost the entire fluid phase equilibrium thermodynamics [61]. This is done in the basis of computing the activity coefficient of component i in the mixture, γ_i, directly computed from Eq. 2.17,

$$\ln \gamma_i = \frac{\mu_i - \mu_i^0}{RT} , \tag{2.17}$$

where μ_i^0 is the chemical potential of species i in its pure state, and R is the ideal gas constant.

2.3. Implementation of COSMO-RS

The COSMO-RS implementation available in the BIOVIA COSMOtherm package [84] was employed for all phase equilibrium calculations. Here, a geometry optimization of the molecular structure, considering the COSMO solvation model is used as the starting point to generate the molecule cavity with its SCD. The TURBOMOLE package [85] is employed to perform the required QC calculations. The results of geometry optimizations are summarized in a `.cosmo` file, containing the molecular geometry, the discretized molecular cavity, the σ values associated to each surface segment, and the COSMO energy of the molecule. Subsequently, SCDs contained in the `.cosmo` file are used to construct the corresponding $p_S(\sigma)$ of the molecule, allowing the computation of $\mu_S(\sigma)$ through Eq. 2.15. Furthermore, a `.energy` file, containing the gas-phase energy of the molecule, is obtained by the above procedure.

The BP-TZVP parameterization (version BP_TZVP_2024) of the COSMO-RS empirical parameters was employed for all calculations. In this parameterization, DFT calculations at the BP86/def-TZVP level of theory are used to optimize the molecular geometry of the studied species.

A wide variety of calculations related to phase equilibrium can be performed. However, for the evaluation of absorption of gaseous solutes in non-volatile solvents, two main concepts are considered. In the first place, the equilibrium pressure of the system, P^{sat}, which characterizes solubility isotherms, is computed following Eq. 2.18,

$$P^{\text{sat}} = \sum_{i=1}^{n_c} P_i^{\text{sat}} x_i \gamma_i \,, \tag{2.18}$$

where P_i^{sat} is the saturation pressure of species i. As COSMO-RS does not directly compute thermophysical properties in the gas phase, complementary alternatives must be supplied for the estimation of P_i^{sat}. The employed approach consists on its estimation using the gas-phase energy provided in the `.energy` file.

Finally, effective Henry's constants [86] of species i in the mixture, $K_{\text{H},i}^{\text{eff}}$, is computed assuming an incompressible liquid phase, thus following Eq. 2.19,

$$K_{\text{H},i}^{\text{eff}} = \gamma_i^{\infty} P_i^0 \,, \tag{2.19}$$

where γ_i^{∞} is the activity coefficient of species i at the limit of infinite dilution.

3. Fundamentals and computational methods of molecular dynamics

This chapter describes the essential theoretical background of molecular dynamics (MD). With robust statistical mechanics foundations, MD simulations offer a powerful framework to understand the influence of microscopic phenomena on thermophysical behavior. When applied to the systems of interest, MD simulations enable the study of solvation characteristics related to the performance of novel solvents for HFC absorption.

3.1. Introduction

Molecular simulation has become a powerful computational tool for understanding and predicting the behavior of molecular systems [54, 87]. It provides insights into molecular-level phenomena that are often inaccessible to experimental techniques. Using statistical mechanics principles, molecular simulation bridges the gap between microscopic phenomena and macroscopic behavior, facilitating the study of thermodynamic, structural, and transport properties [87]. Since its conception several decades ago, molecular simulation has become an indispensable tool in molecular science [88]. During this period, advances in computational hardware and algorithms have significantly expanded the scope and efficiency of simulations, making it possible to study increasingly complex systems with remarkable accuracy and detail.

Among the most widely used molecular simulation techniques is molecular dynamics (MD), a computational method that relies on mechanical principles derived from Newton's laws of motion, where the future state of the system can be predicted based on its current state [55]. In MD, atoms are represented as mass points that interact through a specified force field. These force fields simplify the calculations by ignoring the movement of electrons and instead treating the energy of a system solely as a function of nuclear positions. By neglecting electron motion, MD simulations compute results in much shorter time scales than quantum mechanics methods while still achieving high accuracy when adequately calibrated.

This chapter introduces the core concepts and methodologies central to MD simulations, aiming to provide a clear understanding of the foundational principles and practical steps involved. Key

elements such as potential energy functions, force fields, and thermodynamic ensembles are discussed to establish the theoretical framework. In addition, the methodology used in MD simulations is introduced, including system initialization, application of periodic boundary conditions, and execution of the production phase. Methodologies for calculating viscosity, diffusivity are included, and computation of free energies, of paramount importance in the characterization of solvation behavior, is discussed.

3.2. Fundamental principles in molecular dynamics

3.2.1. Potential energy functions and force fields

MD simulation relies on statistical thermodynamics to predict molecular geometry, energy, and other properties based on physical interactions. To do so, molecules are represented as systems of particles (e.g., atoms) connected by bonds and interacting through intramolecular and intermolecular forces. Force fields (FFs) are the explicit representations of these interactions, and are defined by mathematical expressions involving the particle positions of the system. This formalism considers bonded interactions, such as variations in bond lengths and angles, as well as non-bonded interactions like van der Waals forces and electrostatics. These interactions govern the dynamics of the system, including rotation, vibration, and translation, resulting in energetically favorable conformations.

The typical potential energy in MD, $u\left(\underline{\mathbf{r}}_1, \underline{\mathbf{r}}_2, \ldots, \underline{\mathbf{r}}_N\right)$, can be expressed as a sum of energy contributions, as shown in Eq. 3.1,

$$u\left(\underline{\mathbf{r}}_1, \underline{\mathbf{r}}_2, \ldots, \underline{\mathbf{r}}_N\right) = \sum u_{\text{bonds}} + \sum u_{\text{angles}} + \sum u_{\text{torsion}} + \sum u_{\text{non-bonded}}\,, \tag{3.1}$$

which depends on the positions $\underline{\mathbf{r}}_i$ for the N particles in the system. In the right-hand side of Eq. 3.1, the first term models the interaction between bonded atom pairs and how they stretch or compress relative to a reference equilibrium state. The second term represents the energy caused by the angle motion formed between three adjacent atoms. The third term is a torsional potential, which models how the energy changes as the bond rotates. The fourth term represents the contribution of the non-bonded or intermolecular interactions, calculated between all pairs of atoms across all molecules. This last term typically uses the Coulomb potential for electrostatic interactions and the Lennard-Jones (LJ) potential for van der Waals interactions.

Force fields such as OPLS [89], CHARMM [90], and AMBER [91] parameterize these interactions using empirical or quantum mechanical data to ensure accurate representations of molecular systems. The choice of force field depends on the specific system under study, with each force field optimized for particular types of molecules, such as proteins, small organic compounds, or polymers.

MD simulations can adopt different levels of resolution to represent molecules with a particular force field, ranging from all-atom models to coarse-grained approaches [54]:

- **All-atom models**: These models explicitly represent every atom in the system, including hydrogen atoms, providing the highest level of detail. They are widely used for systems where precise interactions, such as hydrogen bonding and detailed electrostatics, are critical. However, the high level of detail makes all-atom models computationally expensive, especially for large systems or long simulation times.
- **United-atom models**: In these models, groups of atoms, such as CH_3, CH_2, or CH, are treated as single interaction sites [92]. This simplification reduces computational cost compared to all-atom models while still capturing essential molecular features. United-atom models are commonly used to simulate hydrocarbons, lipids, and other systems in which hydrogen atoms have a minimal impact on overall properties.
- **Coarse-grained models**: Coarse-graining further simplifies the system by grouping multiple atoms into a single particle or "bead". These models are particularly useful for studying large-scale phenomena, such as protein folding, membrane dynamics, or polymer aggregation, where fine atomic details are less critical. The MARTINI force field is a popular example of a coarse-grained model [93, 94], optimized for biomolecular and material simulations. Coarse-grained approaches enable simulations of much larger systems over longer time scales but sacrifice some accuracy in representing molecular interactions.

The choice of model resolution (all-atom, united-atom, or coarse-grained) depends on the research question and the balance between computational efficiency and the level of detail required. Combining these approaches in multiscale simulations can provide insights across different spatial and temporal scales.

3.2.2. Finite difference methods and integration algorithms

Under the influence of continuous potentials such as Lennard-Jones, Coulomb, or Mie, the motion of particles in MD simulations is inherently coupled, resulting in a highly complex system of equations. Analytical solutions for these equations are rarely possible, necessitating numerical approaches. The finite-difference method is widely used for integrating the equations of motion in MD simulations. The central idea of this approach is to discretize time into small intervals of fixed length, Δt, typically on the order of femtoseconds (10^{-15} s). At each time step, the total force acting on a particle is computed as the sum of the interactions with all other particles in the system. From this force, the acceleration is determined using Newton's second law of motion. The positions and velocities of the particles at the next time step, $t + \Delta t$, are then calculated from their values at time t, assuming that the force remains constant within the time step.

Various integration algorithms have been developed to solve the equations of motion in MD simulations. These algorithms are based on the Taylor series expansion of positions, velocities, or accelerations over time, which aim to balance computational efficiency, accuracy, and physical fidelity. To ensure successful simulations, a desirable integration algorithm should [87]:

- Be computationally efficient, requiring minimal memory.
- Permit the use of sufficiently long time steps, Δt, without sacrificing accuracy.

- Accurately reproduce the classical trajectory of the particles.
- Conserve key physical quantities, such as energy and momentum, ensuring time-reversibility.
- Be simple to implement and robust in application.

The Verlet algorithm [95] is perhaps the most widely known integration method in MD due to its simplicity and numerical stability. It works by discretizing time into fixed steps, Δt, and iteratively calculates new positions, $\underline{\mathbf{r}}$, and velocities, $\mathbf{v}$, using acceleration, $\mathbf{a}$. This is done following the formulation of equations for the integration of the equations of motion over a single timestep from t to $t + \Delta t$, as shown in Eqs. 3.2,

$$\mathbf{v}\left(t + \frac{1}{2}\Delta t\right) = \mathbf{v}(t) + \frac{1}{2}\Delta t\mathbf{a}(t)\,, \tag{3.2a}$$

$$\underline{\mathbf{r}}(t + \Delta t) = \underline{\mathbf{r}}(t) + \Delta t\mathbf{v}\left(t + \frac{1}{2}\Delta t\right)\,, \tag{3.2b}$$

$$\mathbf{v}(t + \Delta t) = \mathbf{v}\left(t + \frac{1}{2}\Delta t\right) + \frac{1}{2}\Delta t\mathbf{a}(t + \Delta t)\,. \tag{3.2c}$$

In the first step (3.2a), the velocities are "half-advanced" to an intermediate time $t + \frac{1}{2}\Delta t$ using the accelerations at time t. These intermediate velocities are then used in step (3.2b) to propagate the particle coordinates from t to $t + \Delta t$. Finally, the accelerations at the new positions are computed, allowing the velocities to be fully updated in step (3.2c).

Other variations and improvements have been developed from this algorithm. A commonly used algorithm is Leapfrog [96], which estimates velocities at half-time steps $\left(t + \frac{1}{2}\Delta t\right)$ using the relations shown in Eqs. 3.3,

$$\underline{\mathbf{r}}(t + \Delta t) = \underline{\mathbf{r}}(t) + \Delta t\mathbf{v}(t + \frac{1}{2}\Delta t)\,, \tag{3.3a}$$

$$\mathbf{v}(t + \frac{1}{2}\Delta t) = \mathbf{v}(t - \frac{1}{2}\Delta t) + \Delta t\mathbf{a}(t)\,. \tag{3.3b}$$

The only difference between the Leapfrog algorithm and the Verlet algorithm is that the velocities are not calculated at the same time as positions.

3.2.3. Constraint algorithms

In MD simulations, modeling some molecules requires maintaining fixed specific bond lengths and angles, especially those involving hydrogen atoms, which have high frequencies and thus require a small integration time step for correct sampling. Using constraint algorithms allows for larger integration time steps, thereby improving computational efficiency.

The SHAKE algorithm, introduced by Ryckaert et al. [97], is a widely used method. Operating within the Verlet integration algorithm, SHAKE iteratively adjusts atomic positions to satisfy bond length constraints. Initially, the algorithm computes unconstrained positions; it then applies corrections based on constraint forces to ensure that the bond lengths stick to the specified values. This iterative process continues until all constraints satisfy a predefined tolerance. However, SHAKE's convergence can slow with increasing molecular complexity as the number of iterations required increases with the number of constraints.

For systems involving water molecules, the SETTLE algorithm offers a more efficient alternative [98]. Explicitly designed for rigid water models, SETTLE provides an analytical solution to the constraints, allowing for quick and accurate enforcement of bond lengths and angles within water molecules. This efficiency makes SETTLE particularly advantageous in simulations in which water constitutes a significant portion of the system.

Another notable method is the Linear Constraint Solver (LINCS) algorithm [99], which resets bond lengths after an unconstrained update. LINCS is non-iterative and generally more stable and faster than SHAKE, but it can only be used with bond and isolated angle constraints. Because of its stability, LINCS is especially useful for large molecules.

3.2.4. Periodic boundary conditions

Periodic boundary conditions allow simulations to be performed using a relatively small number of particles, letting them experience forces as if in the bulk of the fluid. Replicating a cubic box that contains particles in all directions creates a periodic arrangement. Figure 3.1 illustrates a two-dimensional example, where each box is surrounded by eight identical boxes (a three-dimensional box would have 26). The figure shows how molecules enter or leave the box through any of its faces.

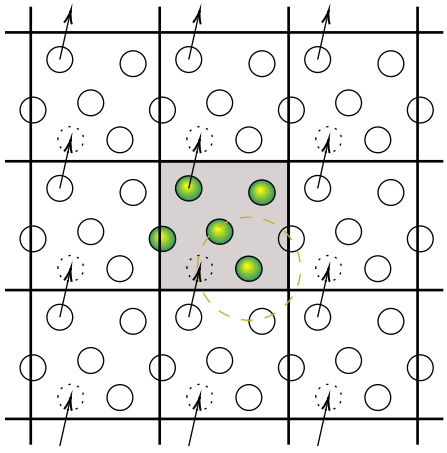

FIGURE 3.1: Two-dimensional representation of periodic boundary conditions.

As long as the potential is short-ranged, the minimum image convention can be adopted, where each atom interacts with the nearest image in the periodic arrangement. Therefore, if a particle

leaves the box during a simulation, it is replaced by its image entering from the opposite face of the box, as illustrated in Figure 3.1. This keeps the number of particles in the central box constant. Care must be taken with long-range potentials, such as those for charged or dipolar systems, to prevent molecules from interacting with themselves.

3.2.5. Neighbor searching

Calculating non-bonded interactions for interatomic forces in MD simulations involves many calculations: each atom i interacts with every atom j, meaning that the separation r_{ij} must be computed. If short-range interactions are considered with a cutoff radius r_{cut}, particles with $r_{ij} > r_{\text{cut}}$ can be omitted from the calculation, reducing the computational cost. However, examining all pair separations for a system with N particles is proportional to the number of distinct pairs, $\frac{1}{2}N(N-1)$, and for each pair, at least r_{ij}^2 must be computed, which is still computationally expensive.

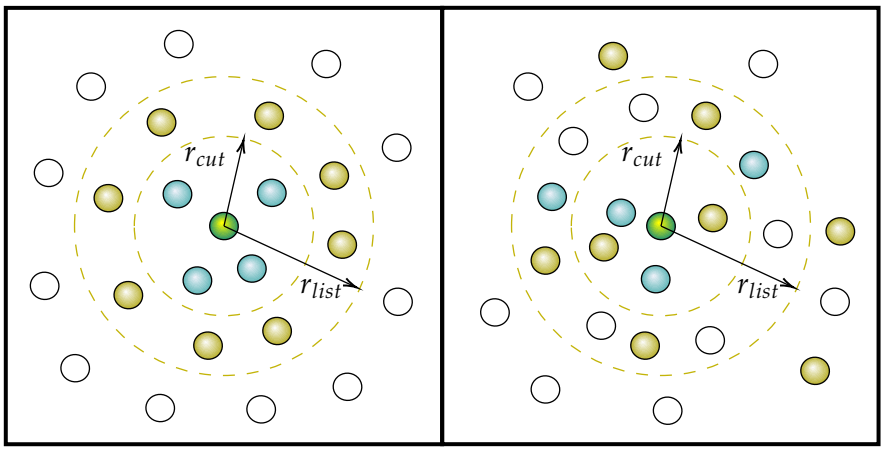

FIGURE 3.2: Two-dimensional representation of the Verlet neighbor list in two different snapshots: at the moment the list was created and several steps later.

A more efficient computational strategy is to use a list of the nearest atom pairs. Verlet proposed this technique in 1967 to improve program speed, known as the Verlet neighbor list [100]. In this technique, a cutoff sphere of radius r_{cut} around a particle is surrounded by a shell of radius r_{list}, as shown in Figure 3.2. At the first simulation step, a list is constructed and stored for each atom, indicating all neighbors within a separation of r_{list}. In subsequent iterations, force calculations are only performed for atom pairs in the list, and the list is reconstructed periodically. The choice of r_{list} affects performance: longer lists need less frequent reconstruction but do not reduce computational time as effectively as shorter lists.

3.2.6. Thermodynamic ensembles

Thermodynamic ensembles originate from the statistical mechanics theory, which serves as the molecular foundation of thermodynamics. An ensemble is the set of all possible states and microstates consistent with the constraints that characterize the macroscopic system. There are three typical ensembles:

- **Microcanonical**: This ensemble consists of all states with fixed total energy E, fixed size (number of particles N), and fixed volume V. It describes an isolated system with no interaction with the surroundings.
- **Canonical**: This ensemble consists of all microstates with a fixed number of particles N and fixed volume V. The energy can fluctuate; however, the system remains in equilibrium while being in contact with a heat bath at a fixed temperature T.
- **Grand Canonical**: This ensemble describes a system with a variable composition (allowing the exchange of particles with the surroundings) that is in chemical and thermal equilibrium with a thermodynamic reservoir. This reservoir has a fixed temperature T and a fixed chemical potential μ for various particle types at constant volume V.

3.2.7. Simulation controls: thermostats and barostats

MD simulations are traditionally performed in the microcanonical ensemble (NVE). However, many applications require simulations in the canonical ensemble (NVT), which maintains a constant temperature, or the isothermal-isobaric ensemble (NPT), which maintains constant temperature and pressure. Depending on the purpose of the simulation, it may or may not be necessary to generate the exact ensemble and to understand its characteristics rigorously. The following sections describe methods for controlling temperature and/or pressure during simulations using a thermostat and/or a barostat, respectively.

Berendsen thermostat

The Berendsen thermostat [101] assumes that the system is immersed in a heat bath that maintains the temperature at a constant value, with energy exchange occurring gradually between the system and the bath. The instantaneous temperature T_i is gradually brought to the desired temperature T, with the rate of change of the instantaneous temperature proportional to the temperature difference, given by Eq. 3.4.

$$\frac{dT_i}{dt} = \frac{T - T_i}{\tau_T} \tag{3.4}$$

In this temperature relaxation process, the velocity $\mathbf{v}$ of each particle is scaled at every step by a factor λ, which is defined by Eq. 3.5,

$$\lambda = \left[1 + \frac{\Delta t}{\tau_T}\left(\frac{T}{T_i} - 1\right)\right]^{1/2} \tag{3.5}$$

where Δt is the integration time step, and τ_T is a time constant that determines the time scale to reach the desired temperature T. The coupling strength between the heat bath and the system is controlled by τ_T. A smaller τ_T value indicates stronger coupling and faster convergence to the desired temperature, while a larger τ_T value results in weaker coupling.

Velocity rescaling thermostat

From the Berendsen thermostat (Eq. 3.5), two important cases for τ_T can be noted. In the first case, if $\tau_T = \Delta t$, the Berendsen thermostat is reduced to Eq. 3.6.

$$\lambda = \sqrt{\frac{T}{T_i}} \tag{3.6}$$

This equation corresponds to the velocity rescaling method [102], the most straightforward and most commonly used approach to maintain constant temperature. In the second case, if τ_T is very large, then $\lambda = 1$ decouples the system from the heat bath and reproduces the microcanonical (NVE) ensemble.

Nosé-Hoover Thermostat

The Nosé-Hoover thermostat was proposed by Nosé [103] and later modified by Hoover [104]. This method modifies the system's Hamiltonian ($\mathcal{H}$) by introducing a heat reservoir and a friction term into the equations of motion. The frictional force is proportional to the product of the velocity of the particle and a friction parameter ξ. This parameter, a dynamic variable of the heat bath, has its own momentum p_ξ and equation of motion.

The particle equations of motion are modified as shown in Eq. 3.7,

$$\frac{d^2\underline{\mathbf{r}}_i(t)}{dt^2} = \frac{\mathbf{F}_i}{m_i} - \frac{p_\xi}{Q}\frac{d\underline{\mathbf{r}}_i}{dt} \tag{3.7}$$

where m_i and $\mathbf{F}_i$ are the mass and force applied to the particle, and the heat bath motion ξ is governed by a first-order differential equation, given by Eq. 3.8.

$$\frac{dp_\xi}{dt} = (T - T_0) \tag{3.8}$$

Here, T_0 is the reference temperature, and T is the instantaneous temperature of the system. The coupling strength is determined by the parameter Q, often referred to as the mass parameter of the reservoir, in combination with the reference temperature.

The extended Hamiltonian produced by the Nosé-Hoover thermostat is expressed by Eq. 3.9,

$$\mathcal{H} = \sum_{i=1}^{N} \frac{\mathbf{p}_i^2}{2m_i} + U(r_1, r_2, \ldots, r_N) + \frac{p_\xi^2}{2Q} + N_f k_B T \xi \tag{3.9}$$

where N_f is the number of degrees of freedom.

Berendsen Barostat

Similarly to the Berendsen thermostat, the Berendsen barostat [101] rescales the box vectors at each step to maintain a constant pressure P_0. A first-order coupling constant τ_P controls the simulation pressure P, as shown in Eq. 3.10.

$$\frac{dP}{dt} = \frac{P_0 - P}{\tau_P} \tag{3.10}$$

For isotropic scaling, the factor μ by which the coordinates and box dimensions are scaled by Eq. 3.11,

$$\mu = 1 - \frac{\kappa_T \Delta t}{3\tau_P}(P_0 - P) \tag{3.11}$$

where κ_T is the isothermal compressibility of the system, and Δt is the integration time step.

This scaling ensures that the system's volume changes in response to the pressure difference, facilitating the exponential pressure relaxation towards the reference value. These equations enable the Berendsen barostat to effectively control system pressure by modulating volume. However, it's important to note that this method does not generate a correct statistical mechanical ensemble and may not accurately reproduce pressure fluctuations.

Parrinello-Rahman Barostat

Unlike the Berendsen barostat, the Parrinello-Rahman barostat [105, 106] accounts for system fluctuations to provide a better sampling of the isothermal-isobaric ensemble. It uses a scheme similar to the Nosé-Hoover thermostat, where the box vector lengths are governed by the Eq. 3.12,

$$\frac{d^2 b}{dt^2} = \frac{V}{Wb'}(P_0 - P) \tag{3.12}$$

where V is the box volume, b is the box vectors, and W is the matrix that determines the coupling strength of the barostat.

3.3. Simulation methodology

MD simulations begin with the creation of an initial configuration, where particles are arranged within a simulation box. The first step is to define the number of molecules and the dimensions of the simulation box. A cubic box is typically used for homogeneous systems, with dimensions at least twice the cut-off distance for molecular interactions to prevent self-interaction. An estimation of the density of the system can be used either to calculate the number of molecules based on the volume of the simulation box or to determine the box volume based on the number of molecules to be inserted. Molecules are then placed randomly within the box, but care must be taken to avoid

overlaps that can result in unrealistic, high-energy configurations, which is particularly challenging for complex systems. PACKMOL software [107] is often used to generate the initial configuration by packing molecules into defined spatial regions while ensuring minimal overlap to avoid short-range repulsive interaction. Once the molecular positions are determined, initial velocities are assigned according to a Maxwell-Boltzmann distribution at the desired temperature.

Once the initial configuration is prepared, the system needs to be energy minimized. This step reduces the potential energy of the system by adjusting the atomic positions to resolve any physically unrealistic configurations, such as overlapping atoms or excessive bond distortions. Energy minimization ensures mechanical stability and prevents numerical instabilities in subsequent simulation steps. For this purpose, algorithms like the steepest descent method or the more efficient conjugate gradient method are commonly used. The result is a configuration with minimized potential energy that provides a stable starting point for dynamic simulations.

Following energy minimization, the system enters the equilibration phase, which prepares it to represent the desired thermodynamic state, such as a specific temperature or pressure. This phase consists of thermal equilibration and, if necessary, pressure equilibration. The Berendsen thermostat and barostat are excellent tools for quickly equilibrating systems to a desired temperature or pressure. However, they do not accurately generate the correct thermodynamic ensembles, and the data from this process should not be used for further analysis. Throughout this process, properties such as temperature, pressure, and energy are monitored until they stabilize, indicating that the system is equilibrated.

The final phase of an MD simulation is the production run, during which the equilibrated system is simulated over time to generate data for analysis. In this phase, the system evolves according to Newton's equations of motion, with minimal external interference, allowing the natural dynamics of the system to unfold. Temperature and pressure can be controlled using the Nosé-Hoover thermostat and the Parrinello-Rahman barostat, respectively. Both methods are more accurate for ensemble generation, while the desired temperature and pressure are kept constant. Long simulation times are often required during production to ensure that the results are representative of the system's equilibrium state and that the calculated properties converge statistically.

There are slight differences in the simulation methodology when performing non-equilibrium molecular dynamics (NEMD) simulations to calculate viscosity. The details of these differences are discussed in the following sections.

3.3.1. Calculation of transport properties

For the viscosity calculation, the same methodology described previously can be applied. The only distinction arises when using the NEMD approach, where an external force is periodically applied during the production phase, typically in the x-direction [108]. Although the liquid phase is homogeneous and isotropic, the Cartesian coordinate system is used to define the direction of the applied force and to resolve the resulting velocity field. This force induces a flow in the fluid, from which the viscosity can be determined. To ensure consistency with periodic boundary conditions and to minimize local shear rates, both the acceleration and velocity profiles must be smooth and periodic [108]. Therefore, Eq. 3.13 is typically chosen to provide the external force $a_x(z)$:

$$a_x(z) = \mathcal{A}\cos\left(\frac{2\pi}{L_z}z\right) \tag{3.13}$$

In this case, according to the Navier–Stokes equation, the generated velocity profile at equilibrium is given by Eq. 3.14:

$$v_x(z) = \mathcal{A}\frac{\hat{\rho}^{\mathrm{L}}}{\eta^{\mathrm{L}}}\left(\frac{L_z}{2\pi}\right)^2\cos\left(\frac{2\pi}{L_z}z\right) \tag{3.14}$$

In Eqs. 3.13 and 3.14, $\mathcal{A}$ is the acceleration amplitude, which indicates the magnitude of the applied force, $\hat{\rho}^{\mathrm{L}}$ is the liquid mass density, η^{L} is the liquid viscosity, and L_z is the box length in the z-direction. As shown in Eq. 3.14, the velocity amplitude is proportional to the acceleration amplitude, and both are related to the viscosity of the system. Furthermore, this procedure should be repeated at different $\mathcal{A}$ values, ranging from 0.08 to 0.20 $\mathrm{nm/ps^2}$, to extrapolate the viscosity to zero acceleration amplitude and obtain a more accurate estimate under equilibrium conditions.

Equilibrium MD simulations can be used to compute self-diffusivity of species i, $\mathcal{D}_i$, which make use of the autocorrelation function formalism [87]. In the first place, system-size corrections are recommended to be included [109], considering the expression proposed by Yeh and Hummer [110], as shown in Eq. 3.15,

$$\mathcal{D}_i = \frac{k_B T \xi}{6\pi\,\eta^{\mathrm{L}}\,L_x} + \mathcal{D}_{\mathrm{PBC},i}\,, \tag{3.15}$$

where L_x is the length of the cubic simulation box, $\xi = 2.837297$, and $\mathcal{D}_{\mathrm{PBC},i}$ is the self-diffusion of i in a simulation with periodic boundary conditions. This term can be computed via the Einstein's equation following Eq. 3.16,

$$\mathcal{D}_{\mathrm{PBC},i} = \frac{1}{6}\lim_{t\to\infty}\frac{d}{dt}\langle\,[\underline{\mathbf{r}}_i(t) - \underline{\mathbf{r}}_1(0)]^2\,\rangle\,, \tag{3.16}$$

where $[\underline{\mathbf{r}}_i(t) - \underline{\mathbf{r}}_1(0)]^2$ is the mean-squared displacement (MSD) of i, which can be directly obtained from available MD simulation software. Thus, $\mathcal{D}_i$ is finally obtained as the slope of a linear fit for MSD, performed at a sufficiently long simulation time, depending on the analyzed system.

3.3.2. Free energy calculations

Free energy calculations enable the determination of free energy differences associated with numerous physical processes [111]. Particularly for homogeneous fluid phases, they allow the characterization of solvation through the calculation of the excess chemical potential of species i in a mixture, μ_i^{ex}.

Among the routes to compute free energy differences from MD simulations, free energy perturbation (FEP) formalism is the oldest and one of the most versatile approaches [111]. As in all

applications of perturbation theory, FEP represents the system of interest with respect to an initial, unperturbed, state. Thus, the solvation of species i can be characterized by the free energy difference between systems containing and not containing this species. In the case of considering a single molecule of species i, this free energy difference yields μ_i^{ex}.

Despite this direct approach, free energy differences are highly dependent on the phase-space overlap between both systems. Thus, the consideration of only two states will yield inconclusive and inefficient energy differences [112]. Both states can be formally bridged using alchemical free energy calculations. This formalism establishes n_λ intermediate states through the parametric variable $\lambda \in [0, 1]$. The initial and final states are represented by values of λ of 0 and 1, respectively, while all intermediate states lie within both limits. This parameterization is applied to the FF of the target molecule by scaling its non-bonded parameters as a function of λ. Thus, the gradual decoupling of the molecule from the system is modeled through a continuous pathway connecting the fully interacting and decoupled states. Conversely, the coupling of the molecule can be characterized following the reverse path.

Using the above approach, μ_i^{ex} is evaluated from differences in the Hamiltonian of the system $\mathcal{H}$, between different alchemical states. This is exemplified by Eq. 3.17 [111, 113],

$$\frac{\mu_i^{\text{ex}}}{k_B T} = -\sum_{j=1}^{n_\lambda - 1} \ln \left\langle \exp\left[-\frac{\mathcal{H}(\lambda_{j+1}) - \mathcal{H}(\lambda_j)}{k_B T} \right] \right\rangle_j , \tag{3.17}$$

where $\langle \dots \rangle_j$ denotes the ensemble average over configurations sampled over alchemical state j.

Eq. 3.17, also referred to as Zwanzig relationship [114], is the basic free energy estimator, and computes μ_i^{ex} through ensemble averages of Hamiltonian differences between neighboring states. More recent estimators have been defined to yield a higher statistical efficiency. This is the case for the Bennett acceptance ratio (BAR) estimator [115], which draws data from two different states to compute free energy differences while minimizing the variance of the estimation. A further extension of this method was achieved with the multistate Bennett acceptance ratio (MBAR) estimator [116]. Here, samples from all thermodynamic states are simultaneously considered to yield the free energy estimation, also providing a direct computation of uncertainties. Provided that sufficient alchemical states are considered, the MBAR estimator has shown better statistical performance and lower bias than other FEP-based estimators [117, 118], thus representing one of the most widely applied estimators in free energy calculations.

A defining factor in obtaining reliable free energy estimates is the phase-space overlap between states, *i.e.*, the degree to which an energetically favorable configuration can be observed in two states [117]. For species with complex chemical structures, maintaining sufficient phase-space overlap is computationally expensive due to the need of longer simulation runs, required to obtain a comprehensive sample of each alchemical state. To tackle this problem, the Hamiltonian replica exchange (HREX) method [119] serves as a powerful sample accelerator. Within this approach, all alchemical states are simulated in parallel. At regular time intervals, the configurations of two states, or replicas, are exchanged if the exchange acceptance probability, determined from both Hamiltonians, satisfies the Metropolis criterion [120].

4. Molecular-based equations of state

This chapter describes the fundamental framework of the Statistical Associating Fluid Theory (SAFT) and two of its variations, namely the soft-SAFT and PC-SAFT equations of sate. The robust statistical thermodynamic framework of these models gives them a particularly predictive character for complex solvents where strongly directional interactions appear. Applied to the assessment of HFC absorption, SAFT-based formalisms yield a reliable assessment of novel solvents.

4.1. Introduction

Prediction and modeling of thermophysical properties, such as phase equilibria and transport properties, are essential for the development and evaluation of chemical processes [121]. Reliable process design requires thermodynamic models capable of describing the behavior of complex fluids over wide ranges of operation conditions in an accurate and computationally efficient manner [50].

Equations of state (EoSs), *i.e.*, mathematical models that describe the relationship between thermodynamic properties such as pressure, volume, and temperature, represent one of the most influential approaches to this problem. Their origin can be traced back to the seminal work of Johannes Diderik van der Waals, who in 1873 introduced a framework to describe real fluids by incorporating the effect of finite molecular size and intermolecular attraction [122]. This formulation constituted a significant improvement over the ideal gas law, providing the first theoretical basis for describing vapor–liquid equilibrium through a simple cubic expression in molar volume. This equation laid the foundation for the refinement of numerous cubic EoSs to better reproduce experimental data [123], with the most industrially prominent being the Redlich-Kwong EoS [124], its further modification by Soave [125], and the Peng-Robinson EoS [126]. At the same time, van der Waals' EoS motivated the development of more advanced models aimed at describing more complex fluids, where molecular structure and specific interactions lead to deviations from the behavior predicted by classical cubic EoSs [127].

Chemical association differs from dispersion interactions due to its highly directional nature, leading to specific phenomena such as hydrogen bonding and formation of clusters and dimers [128].

To explicitly include these complex effects in fluid phase calculations, the Statistical Associating Fluid Theory (SAFT) [51, 129–131] arguably represents the most successful approach [52]. While SAFT relies on more computationally demanding formulations than cubic EoSs, it improves the description of complex fluids by incorporating a physically meaningful parameterization. Starting from a reference fluid, molecules are represented as chains of spherical segments, and their interactions are decomposed into distinct contributions, including dispersion, chain formation, and association. The first SAFT-based EoS was proposed by Chapman et al. [51, 131], who incorporated Wertheim's first-order thermodynamic perturbation theory (TPT1) [132–135] to describe directional interactions. This formulation proved highly suitable in modeling both simple and complex systems, for pure substances and mixtures, and established the basis for further developments. Since its introduction, several SAFT-based EoSs have been proposed, mainly differing in the choice of the interaction potential used to describe the reference fluid. Particular examples include SAFT-VR-SW [136, 137], SAFT-VR-Mie [138], soft-SAFT [139, 140], and PC-SAFT [141, 142]. Several reviews in the literature provide detailed descriptions of each of these versions, highlighting their advantages and limitations [52, 143–145].

In this chapter, the theoretical foundations of the SAFT framework are presented. As both the soft-SAFT and PC-SAFT models were employed in this thesis, details of their specific formulations are provided. Additionally, parameterization strategies for pure fluids and mixtures are introduced, followed by the procedures for the calculation of thermodynamic properties and the formulation of the phase equilibrium problem within the SAFT framework.

4.2. SAFT-based molecular models

Within the SAFT formalism, fluids are initially modeled as a collection of equal-sized spheres (or segments) to represent repulsive interactions, usually via a hard-sphere (HS) model. Attractive forces are then incorporated by including a dispersive potential, commonly a square-well (SW) or LJ potential. Molecular structure is accounted for via a coarse grained framework, where segments are connected by covalent bonds to form chains. Finally, specific interaction sites are introduced along the chains to represent directional interactions, typically modeled using SW association potentials. Each of these contributions (reference repulsion, dispersion, chain formation, and association) adds a corresponding term to the residual Helmholtz free energy of the fluid, $\tilde{a}^{\text{res}}$, as shown in Eq. 4.1,

$$\tilde{a}^{\text{res}} = \tilde{a} - \tilde{a}^{\text{id}} = \tilde{a}^{\text{seg}} + \tilde{a}^{\text{chain}} + \tilde{a}^{\text{assoc}}\,, \tag{4.1}$$

where $\tilde{a}^{\text{seg}}$ is the segment contribution to the Helmholtz free energy, including both the HS reference and dispersion terms; $\tilde{a}^{\text{chain}}$ is the energy contribution due to chain formation; and $\tilde{a}^{\text{assoc}}$ is the contribution from chemical association. Additionally, $\tilde{a}$ refers to the reduced molar Helmholtz energy of the system, *i.e.*, the Helmholtz free energy of the system divided by a factor of RT, where R is the ideal gas constant and T the absolute temperature. Moreover, $\tilde{a}^{\text{id}}$ represents the contribution of the ideal gas, which, for a system consisting on n_c components, can be expressed through Eq. 4.2,

$$\tilde{a}^{\mathrm{id}} = \sum_{i=1}^{n_c} [x_i \ln x_i] + \ln\left(\rho\Lambda^3\right) - 1\,, \tag{4.2}$$

where x_i is the mole fraction of component i, ρ is the number density of the system, and $\Lambda = 2\pi\hbar \cdot (m_e k_B T)^{-\frac{1}{2}}$ is the thermal de Broglie wavelength, with $\hbar$ being the reduced Planck constant and m_e the mass of the electron.

The most distinguishable feature of all SAFT-based EoSs is the association term, $\tilde{a}^{\mathrm{assoc}}$, from Eq. 4.1. This contribution, derived from Wertheim's TPT1 [132–135], enables the accurate representation of associating fluids by describing the specific interactions between molecules at association sites. The contribution of the association term to the Helmholtz free energy, which reflects these interactions, is given by Eq. 4.3,

$$\tilde{a}^{\mathrm{assoc}} = \sum_{i=1}^{n_c} x_i \sum_{A\in\Omega}^{|\Omega|} S^{Ai} \left[\ln X^{Ai} - \frac{X^{Ai}}{2} + \frac{1}{2}\right]\,. \tag{4.3}$$

Here, the sum is performed over the n_c components in the mixture and their respective $|\Omega|$ possible association sites in a set Ω of different kinds of site. S^{Ai} denotes the number of association sites of type A on each molecule of component i, while X^{Ai} represents the fraction of molecules of component i that remain unbonded at site A.

For every molecule in the mixture, S^{Ai} should be known according to the defined association scheme, while X^{Ai} changes according to the thermodynamic conditions of the system and can be obtained by solving the mass balance shown in Eq. 4.4 [146],

$$X^{Ai} = \left[1 + \rho_m \sum_{k=1}^{n_c} x_k \sum_{B\in\Omega, B\neq A}^{|\Omega|} S^{Bi} X^{Bj} \Delta^{A_i B_j}\right]^{-1}\,. \tag{4.4}$$

Here, $\Delta^{A_i B_j}$ is the association strength between the site type A in component i and the site type B in component j, whose expression is derived depending on the utilized SAFT variation. Its general functional form is given by Eq. 4.5,

$$\Delta^{A_i B_j} \propto \kappa^{A_i B_j} \left[\exp\left(\frac{\varepsilon^{A_i B_j}}{k_B T}\right) - 1\right]\,, \tag{4.5}$$

where $\kappa^{A_i B_j}$, the association volume, is a measure of the volume available for bonding between a site of type A in component i and a site of type B in component j, and $\varepsilon^{A_i B_j}$, the association energy, is the well depth of the site–site interaction potential. If the association occurs within the same molecule, it is referred to as self-association; otherwise, it is a case of cross-association. The association interaction is symmetrical, which means $\varepsilon^{A_i B_j} = \varepsilon^{B_j A_i}$. In the case where the association site type A cannot associate with site type B, $\varepsilon^{A_i B_j} = 0$, which means $\Delta^{A_i B_j} = 0$ by using Eq. 4.5.

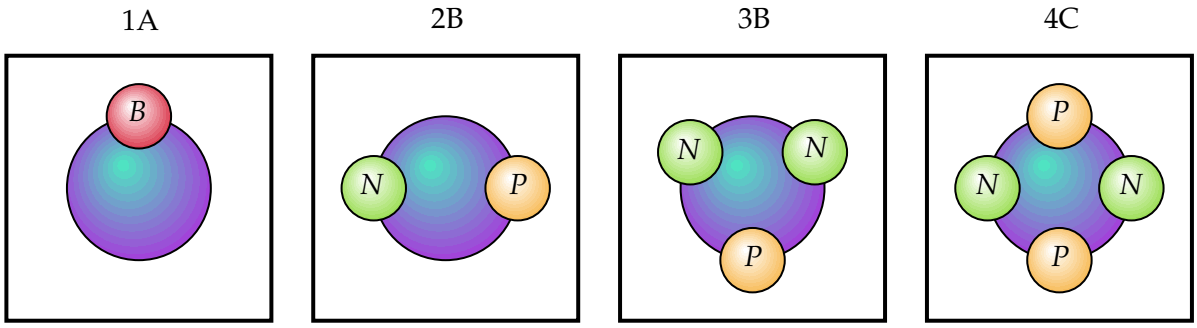

FIGURE 4.1: Examples of association schemes based on the Huang and Radosz notation [148], considering three different types of sites: Bivalent (B), Positive (P), and Negative (N).

Otherwise, the parameters for cross-association can be obtained using the mixing rules proposed by Wolbach and Sandler [147], as given by Eqs. 4.6.

$$\varepsilon^{A_iB_j} = \frac{1}{2}\left(\varepsilon^{A_iB_i} + \varepsilon^{A_jB_j}\right), \tag{4.6a}$$

$$\kappa^{A_iB_j} = \sqrt{\kappa^{A_iB_i}\kappa^{A_jB_j}}\left(\frac{\sqrt{\sigma_i\sigma_j}}{\sigma_{ij}}\right)^3. \tag{4.6b}$$

Association schemes are used to represent or visualize how association occurs between molecules. The association schemes used throughout the literature were originally proposed by Huang and Radosz [148]. In general, these schemes are simplified by recognizing that there are three types of association sites: positive electron-accepting sites, negative electron-donating sites, and bipolar (or bivalent) sites. Positive sites interact with both negative and bipolar sites, negative sites interact with both positive and bipolar sites, and bipolar sites interact with all sites. Examples of association schemes following this notation are shown in Figure 4.1.

By defining proper association schemes and thus the solution of the bonding type, SAFT-based EoSs directly incorporate highly directional interactions in the thermodynamic behavior of the system. The remaining contributions to the overall Helmholtz free energy are obtained depending on the utilized SAFT-based EoS.

4.2.1. The soft-SAFT equation of state

In the soft-SAFT EoS [139, 140], a given species i is modeled as a homonuclear chain of segments, whose repulsive and attractive interactions are modeled through a Lennard-Jones (LJ) potential, as shown in Eq. 4.7,

$$u_{ii}^{\mathrm{LJ}}(r) = 4\varepsilon_{ii}\left[\left(\frac{\sigma_{ii}}{r}\right)^{12} - \left(\frac{\sigma_{ii}}{r}\right)^{6}\right], \tag{4.7}$$

where u_{ii}^{LJ} is the pair potential, r is the radial distance between two segments, and σ_{ii} and ε_{ii} are the collision diameter and depth of the potential well of species i, respectively.

For a mixture of n_c components, analytical expressions developed for pure LJ fluids are extended though the definition of a pseudofluid with collision diameter σ_m and depth of the potential well ε_m. This hypothetical fluid represents the multicomponent system by weighting the contribution of each independent species. Within the soft-SAFT approach, these required parameters are computed using the van der Waals one-fluid theory [149] as shown in Eqs. 4.8,

$$\sigma_m^3 = \frac{\sum_{i=1}^{n_c}\sum_{j=1}^{n_c} m_i m_j x_i x_j \sigma_{ij}^3}{\sum_{i=1}^{n_c}\sum_{j=1}^{n_c} m_i m_j x_i x_j}, \tag{4.8a}$$

$$\epsilon_m \sigma_m^3 = \frac{\sum_{i=1}^{n_c}\sum_{j=1}^{n_c} x_i x_j \epsilon_{ij} \sigma_{ij}^3}{\sum_{i=1}^{n_c}\sum_{j=1}^{n_c} m_i m_j x_i x_j}, \tag{4.8b}$$

where σ_{ij} and ε_{ij} are the crossed collision diameter and well depth between species i and j, which are computed using the Lorentz-Berthelot mixing rules [150, 151] following Eqs. 4.9,

$$\sigma_{ij} = \left(1 - l_{ij}\right) \frac{\sigma_{ii} + \sigma_{jj}}{2}, \tag{4.9a}$$

$$\epsilon_{ij} = \left(1 - k_{ij}\right) \sqrt{\epsilon_{ii}\epsilon_{jj}}, \tag{4.9b}$$

where the binary parameters l_{ij} and k_{ij} can be fit to empirical data to enhance the thermodynamic description of multicomponent mixtures.

The contribution of LJ segments, $\tilde{a}^{\mathrm{seg}}$, is obtained using the EoS proposed by Johnson, Zollweg and Gubbins [152]. This equation was fit to molecular simulation data, developed to model the thermodynamic behavior of the LJ fluid in a wide range of temperatures and densities. This is achieved by the temperature-dependent set of parameters $\boldsymbol{a}^{\mathrm{JZG}}$ and $\boldsymbol{b}^{\mathrm{JZG}}$, and the density-dependent set of parameters $\boldsymbol{G}^{\mathrm{JZG}}$. Thus, the segment contribution to the Helmholtz free energy is expressed as in Eq. 4.10,

$$a^{\mathrm{seg}} = \sum_{i=1}^{8} \frac{a_i^{\mathrm{JZG}}}{i} \left(\rho \sigma_m^3\right)^i + \sum_{i=1}^{6} b_i^{\mathrm{JZG}} G_i^{\mathrm{JZG}}. \tag{4.10}$$

The expressions of parameters $\boldsymbol{a}^{\mathrm{JZG}}$, $\boldsymbol{b}^{\mathrm{JZG}}$, and $\boldsymbol{G}^{\mathrm{JZG}}$ are provided in the original work by the authors [152].

The energy contribution due to chain formation, a^{chain}, is based on the expression independently derived by Wertheim [153, 154] and Chapman et al. [129, 130] Here, a system of chain molecules is obtained from a system of spherical segments with compatible association sites. By setting the fraction of monomers equal to zero, *i.e.*, in the limit of complete polymerization, the total energy of formation of chains is obtained. For a system of Lennard-Jones segments, this is quantified in Eq. 4.11,

$$a^{\mathrm{chain}} = \sum_{i=1}^{n_c} x_i \left(1 - m_i\right) \ln g_m^{\mathrm{LJ}}\left(\sigma_m\right) , \tag{4.11}$$

where the general expression is constrained by setting the bond lengths between adjacent segments equal to the LJ collision diameter of the pseudofluid, σ_m. The pair distribution function required in Eq. 4.11 is simplified to the pair distribution function between non-bonded LJ segments of the pseudofluid defined by Eqs. 4.8, evaluated at its collision diameter, $g_m^{LJ}\left(\sigma_m\right)$. Similarly to a^{seg}, an empirical function, fit from molecular simulations of the Lennard-Jones fluid [155], is applied to obtain this otherwise unavailable analytical function. Thus, a polynomial expansion on density and temperature is applied, as shown in Eq. 4.12,

$$g_m^{\mathrm{LJ}}(\sigma_m) = 1 + \sum_{i=1}^{5}\sum_{j=1}^{5} \mathrm{C}_{ij}^{\mathrm{JZG}} \left(\rho\sigma_m^3\right)^i \left(\frac{k_B T}{\varepsilon_m}\right)^{1-j} , \tag{4.12}$$

where the set of fit parameters $\boldsymbol{C}^{\mathrm{JZG}}$ is available in the original work by the authors [155].

Within the soft-SAFT formalism, association in a species i is modeled by incorporating a SW potential inside the LJ sphere of one of its segments. This potential has a collision diameter of $\sigma^{\mathrm{SW}} = 0.2\sigma_{ii}$, and its origin is located at a distance of $0.2\sigma^{\mathrm{SW}}$ from the origin of the LJ potential of the segment. Subsequently, the association strength between sites A and B in species i and j, respectively, is evaluated through Eq. 4.13,

$$\Delta^{A_i B_j} = 4\pi\kappa^{A_i B_j} \left[\exp\left(\frac{\varepsilon^{A_i B_j}}{k_B T}\right) - 1\right] \mathcal{I}^{\mathrm{SW}} , \tag{4.13}$$

where $\mathcal{I}^{\mathrm{SW}}$ is a dimensionless integral defining the non-zero site–site associations for the introduced SW potential, obtained from Eq. 4.14,

$$\mathcal{I}^{\mathrm{SW}} = \frac{1}{3.84 \cdot 10^4} \sum_{i=0}^{4}\sum_{j=0}^{4} a_{ij}^{\mathrm{MG}} \left(\rho\sigma_m^3\right)^i \left(\frac{k_B T}{\varepsilon_m}\right)^j , \tag{4.14}$$

where the set of parameters $\boldsymbol{a}^{\mathrm{MG}}$ is provided in the original work of the derivation of $\mathcal{I}^{\mathrm{SW}}$ [156].

4.2.2. The PC-SAFT equation of state

In the PC-SAFT framework, unlike most SAFT versions, dispersive interactions are incorporated into the chain contribution rather than the HS reference term. For a species i, the pair potential between segments in a chain is described using a modified SW potential, u_{ii}^{mSW}, as defined in Eq. 4.15 [157],

$$u_{ii}^{\mathrm{mSW}}(r) = \begin{cases} \infty & r < (\sigma_{ii} - 0.12\sigma_{ii})\,, \\ 3\varepsilon_{ii} & (\sigma_{ii} - 0.12\sigma_{ii}) \leq r < \sigma_{ii}\,, \\ -\varepsilon_{ii} & \sigma_{ii} \leq r < \lambda_{\sigma,ii}\sigma_{ii}\,, \\ 0 & r \geq \lambda_{\sigma,ii}\sigma_{ii}\,. \end{cases} \tag{4.15}$$

Here, r is the radial distance between two segments, σ_{ii} is the temperature-independent segment diameter, ε_{ii} indicates the depth of the potential well, and $\lambda_{\sigma,ii}$ is the reduced well width.

Based on the modified SW potential defined in Eq. 4.15 and employing perturbation theory, the PC-SAFT EoS is described as a sum of energetic contributions to the reduced residual Helmholtz energy, as shown in Eq. 4.16,

$$\tilde{a}^{\mathrm{res}} = \tilde{a} - \tilde{a}^{\mathrm{id}} = \tilde{a}^{\mathrm{hc}} + \tilde{a}^{\mathrm{disp}} + \tilde{a}^{\mathrm{assoc}} \tag{4.16}$$

where $\tilde{a}^{\mathrm{hc}}$ is the reduced Helmholtz energy contribution of the hard-chain reference fluid, and $\tilde{a}^{\mathrm{disp}}$ represents the contribution of the dispersive interactions.

The hard-chain reference term in Eq. 4.16 consists of two contributions: the HS contribution ($\tilde{a}^{\mathrm{hs}}$), which comes from the number of spherical segments in each molecule ($m_{s,i}$), and the chain contribution ($\tilde{a}^{\mathrm{chain}}$), which results from the bonding of these segments within each molecule. This is shown in Eq. 4.17:

$$\tilde{a}^{\mathrm{hc}} = \bar{m}_s \tilde{a}^{\mathrm{hs}} + \tilde{a}^{\mathrm{chain}}\,. \tag{4.17}$$

Here, $\bar{m}_s$ is the mean segment number in the mixture, as given by Eq. 4.18,

$$\bar{m}_s = \sum_{i=1}^{n_c} x_i m_{s,i}\,. \tag{4.18}$$

The HS term is given by the expression developed by Boublík [158] and Mansoori et al. [159], which reduces to the formulation proposed by Carnahan and Starling [160] for pure fluids. This is shown in Eq. 4.19,

$$\tilde{a}^{\mathrm{hs}} = \frac{1}{\xi_0(1-\xi_3)}\left[3\xi_1\xi_2 + \frac{\xi_2^3}{\xi_3(1-\xi_3)^2} + \left(\frac{\xi_2^3}{\xi_3^2} - \xi_0\right)\ln(1-\xi_3)\right], \tag{4.19}$$

where ξ_n is defined by the number density of molecules, ρ, in Eq. 4.20,

$$\xi_n = \frac{\pi\rho}{6}\sum_{i=1}^{n_c} x_i m_{s,i} d_i^n\,, \quad n \in \{0,1,2,3\}\,, \tag{4.20}$$

where d_i represents the temperature-dependent segment diameter of a component i, given by Eq. 4.21,

$$d_i = \sigma_{ii}\left[1 - 0.12\exp\left(-3\frac{\varepsilon_{ii}}{k_B T}\right)\right]\,. \tag{4.21}$$

For the chain formation contribution, it is assumed that the segments are tangentially bonded at a distance $r = \sigma_{ii}$, resulting in the expression given in Eq. 4.22,

$$\tilde{a}^{\text{chain}} = \sum_{i=1}^{n_c} x_i(1 - m_{s,i})\ln g_{ii}^{\text{hs}}(\sigma_{ii})\,. \tag{4.22}$$

Here, $g_{ii}^{\text{hs}}(\sigma_{ii})$ is the zero-order RDF, as determined by the Boublík [158] and Mansoori et al. [159] expression for a HS segment, as shown in Eq. 4.23,

$$g_{ij}^{\text{hs}}(\sigma_{ij}) = \frac{1}{(1-\xi_3)} + \left(\frac{d_i d_j}{d_i + d_j}\right)\frac{3\xi_2}{(1-\xi_3)^2} + \left(\frac{d_i d_j}{d_i + d_j}\right)^2 \frac{2\xi_2^2}{(1-\xi_3)^3}\,. \tag{4.23}$$

After the hard-chain reference fluid has been defined, the perturbation theory developed by Barker and Henderson [161, 162] is applied to account for the attractive part of the chain interactions. This second-order perturbation theory expresses the Helmholtz free energy as the sum of first- and second-order contributions, as shown in Eq. 4.24,

$$\tilde{a}^{\text{disp}} = \tilde{a}_1 + \tilde{a}_2\,. \tag{4.24}$$

Each contribution can be written in a simplified form, as shown in Eqs. 4.25 [141],

$$\tilde{a}_1 = -2\pi\rho\bar{I}_1(\eta,\bar{m})\overline{m^2\epsilon\sigma^3}\,, \tag{4.25a}$$

$$\tilde{a}_2 = -\pi\rho\bar{m}C_1\bar{I}_2(\eta,\bar{m})\overline{m^2\epsilon^2\sigma^3}\,. \tag{4.25b}$$

Here, $\bar{I}_1(\eta,\bar{m})$ and $\bar{I}_2(\eta,\bar{m})$ are integrals over the intermolecular potential defined in Eq.4.15 and the radial distribution function between segments. The analytical solution is approximated using power series expansions in the reduced segment density (commonly referred to as the packing fraction, η, which is equal to ξ_3 as defined in Eq.4.20), as given by Eqs. 4.26 [141],

$$\bar{I}_1\left(\eta,\bar{m}\right)=\sum_{i=0}^{6}a_i\left(\bar{m}\right)\eta^i\,, \tag{4.26a}$$

$$\bar{I}_2\left(\eta,\bar{m}\right)=\sum_{i=0}^{6}b_i\left(\bar{m}\right)\eta^i\,, \tag{4.26b}$$

where the coefficients a_i and b_i are given by Eqs. 4.27.

$$a_i\left(\bar{m}\right)=a_{0i}+\frac{\bar{m}-1}{\bar{m}}a_{1i}+\frac{\bar{m}-1}{\bar{m}}\frac{\bar{m}-2}{\bar{m}}a_{2i}\,, \tag{4.27a}$$

$$b_i\left(\bar{m}\right)=b_{0i}+\frac{\bar{m}-1}{\bar{m}}b_{1i}+\frac{\bar{m}-1}{\bar{m}}\frac{\bar{m}-2}{\bar{m}}b_{2i}\,. \tag{4.27b}$$

The model constants introduced in these series (a_{ij} and b_{ij}) were fitted to the properties of pure *n*-alkanes (vapor pressure and volumetric data) and can be found in the original publication [141].

In Eq. 4.25, C_1 is an analytical expression related to the compressibility factor and can be calculated using Eq. 4.28,

$$C_1=\left(1+\bar{m}\frac{8\eta-2\eta^2}{\left(1-\eta\right)^4}+\left(1-\bar{m}\right)\frac{20\eta-27\eta^2+12\eta^3-2\eta^4}{\left[\left(1-\eta\right)\left(2-\eta\right)\right]^2}\right)^{-1}\,. \tag{4.28}$$

The terms $\overline{m^2\epsilon\sigma^3}$ and $\overline{m^2\epsilon^2\sigma^3}$ arise from applying the van der Waals one-fluid mixing rules to the perturbation terms, resulting in Eqs. 4.29,

$$\overline{m^2\epsilon\sigma^3}=\sum_{i=1}^{n_c}\sum_{j=1}^{n_c}x_ix_jm_im_j\left(\frac{\varepsilon_{ij}}{k_BT}\right)\sigma_{ij}^3\,, \tag{4.29a}$$

$$\overline{m^2\epsilon^2\sigma^3}=\sum_{i=1}^{n_c}\sum_{j=1}^{n_c}x_ix_jm_im_j\left(\frac{\varepsilon_{ij}}{k_BT}\right)^2\sigma_{ij}^3\,. \tag{4.29b}$$

The parameters for unlike segments are obtained using the conventional Lorentz-Berthelot combining rules [150, 151], as shown in Eqs. 4.9.

Finally, the association strength is computed following Eq. 4.30

$$\Delta^{A_iB_j}=\sigma_{ij}^3g_{ij}^{hs}(\sigma_{ij})\kappa^{A_iB_j}\left[\exp\left(\frac{\varepsilon^{A_iB_j}}{k_BT}\right)-1\right]\,. \tag{4.30}$$

It is important to note that, while the PC-SAFT EoS defines the association volume, $\kappa^{A_iB_j}$, as a dimensionless quantity, the soft-SAFT EoS defines this parameter in units of volume, as inferred from Eq. 4.13.

4.3. SAFT parametrization

Summarizing the discussion on individual contributions of SAFT-based EoSs, reduced Helmholtz free energy relies on at least three molecular parameters for each species i: the effective number of segments forming the molecular chain, $m_{s,i}$, the segment diameter, σ_{ii}, and the dispersive energy between segments, ε_{ii}. For species containing association sites, two additional parameters are required: the association energy, $\varepsilon^{A_iB_i}$, and the association volume, $\kappa^{A_iB_j}$. These parameters are illustrated in Figure 4.2.

The typical parametrization used for cubic EoS is usually not applied in SAFT-type EoS as these models tend to overpredict the critical point. This limitation arises because SAFT models, like other mean-field theories, cannot accurately account for long-wavelength density fluctuations unless a crossover term is explicitly introduced [163–166]. Instead, it is common practice to perform a regression to fit experimental data on density and vapor pressure, without considering data around the critical point. This procedure results effective in the modeling of gaseous solutes such as CO_2 and F-gases, easily characterized through their vapor-liquid coexistence curves. However, species that are solid under atmospheric conditions or have a negligible volatility, such as ILs and precursors for ESs, demand alternative procedures for a reliable fit of their molecular parameters. A direct approach for species with negligible volatility is the fit to liquid density data, as this is an easily accessible property for most solvents. However, it can rapidly lead to parameter degeneracy, due to the fit of five different molecular parameters to a single thermodynamic property. Thus, alternative approaches considering additional properties or mixture data can be applied. For species that remain solid at room temperature and pressure, the regression of molecular parameters to mixture data, such as aqueous density and osmotic pressure, is a widely employed approach [167, 168].

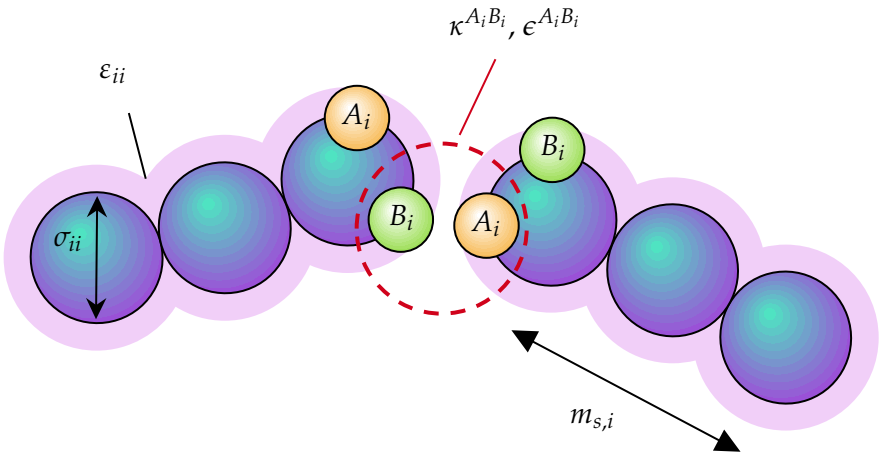

FIGURE 4.2: Illustration of SAFT molecular parameters for pure compounds, including the effective number of segments ($m_{s,i}$), segment diameter (σ_{ii}), dispersive energy (ε_{ii}), and association parameters for molecules with association sites ($\kappa^{A_iB_i}$ and $\varepsilon^{A_iB_i}$).

4.4. Calculation of thermodynamic properties

The Helmholtz energy is the key thermodynamic potential in SAFT-type EoSs, and its derivatives provide access to various thermodynamic properties. For instance, the first derivative of the Helmholtz energy with respect to density is related to the pressure, while its derivative with respect to temperature is related to the entropy. Additionally, second derivatives are useful for calculating response functions such as isothermal compressibility and heat capacities. Thus, by taking appropriate derivatives of the Helmholtz energy, a wide range of thermodynamic properties can be obtained.

In the following, the expressions for the most commonly used properties are presented using the reduced Helmholtz energy as a function of absolute temperature T, molar density $\tilde{\rho}$, and the mole fraction vector $\underline{\mathbf{x}}$.

4.4.1. Pressure and density

The pressure, P, can be obtained using Eq. 4.31,

$$P\left(T,\tilde{\rho},\underline{\mathbf{x}}\right) = RT\tilde{\rho}^2\left(\frac{\partial\tilde{a}}{\partial\tilde{\rho}}\right)_{T,x_i}. \tag{4.31}$$

Additionally, the molar density at a target condition, $\left(P_{\text{target}},T,\underline{\mathbf{x}}\right)$, can be determined by solving the nonlinear equation $P\left(T,\tilde{\rho},\underline{\mathbf{x}}\right) - P_{\text{target}} = 0$, where P is calculated using Eq. 4.31.

The compressibility factor, Z, can be obtained using a similar derivative, as shown in Eq. 4.32.

$$Z = 1 + \tilde{\rho}\left(\frac{\partial \tilde{a}^{res}}{\partial \tilde{\rho}}\right)_{T,x_i} . \tag{4.32}$$

4.4.2. Chemical potential and fugacity coefficient

The chemical potential of a component i in a mixture, μ_i, can be obtained using Eq. 4.33,

$$\frac{\mu_i}{RT} = \tilde{a} + Z + \left(\frac{\partial \tilde{a}}{\partial x_i}\right)_{T,\tilde{\rho},x_{j\neq i}} - \sum_{j=1}^{n_c} x_j \left(\frac{\partial \tilde{a}}{\partial x_j}\right)_{T,\tilde{\rho},x_{k\neq i}} . \tag{4.33}$$

The fugacity coefficient of a component i in a mixture, $\hat{\varphi}_i$, can be obtained using Eq. 4.34,

$$\ln \hat{\phi}_i\left(T, P, \underline{\mathbf{x}}\right) = \tilde{a}^{\mathrm{res}} + (Z-1) + \left(\frac{\partial \tilde{a}^{\mathrm{res}}}{\partial x_i}\right)_{T,\tilde{\rho},x_{j\neq i}} - \sum_{j=1}^{n_c} x_j \left(\frac{\partial \tilde{a}^{\mathrm{res}}}{\partial x_j}\right)_{T,\tilde{\rho},x_{k\neq i}} . \tag{4.34}$$

The activity coefficient of a component i in a mixture, γ_i, can be obtained using Eq. 4.35,

$$\gamma_i\left(T, P, \underline{\mathbf{x}}\right) = \frac{\hat{\phi}_i\left(T, P, \underline{\mathbf{x}}\right)}{\hat{\phi}_i\left(T, P, x_i = 1\right)} . \tag{4.35}$$

4.4.3. Enthalpy

The residual molar enthalpy, $\tilde{H}^{\mathrm{res}}$, can be obtained using Eq. 4.36,

$$\frac{\tilde{H}^{\mathrm{res}}}{RT} = -T\left(\frac{\partial \tilde{a}^{res}}{\partial T}\right)_{\tilde{\rho},x_i} + (Z-1) . \tag{4.36}$$

4.4.4. Entropy

The residual molar entropy, $\tilde{S}^{\mathrm{res}}$, can be obtained, under conditions of constant temperature and pressure, using Eq. 4.37,

$$\frac{\tilde{S}^{\mathrm{res}}}{R} = -T\left(\frac{\partial \tilde{a}^{res}}{\partial T}\right)_{\tilde{\rho},x_i} - \tilde{a}^{\mathrm{res}} + \ln Z . \tag{4.37}$$

4.5. Calculation of phase equilibrium

A mixture of chemical compounds can be distributed across multiple phases (solid, liquid, vapor), with the exchange of components continuing until phase equilibrium is established [121]. At equilibrium, intensive properties, such as temperature, pressure, density, and composition, remain

constant in all coexisting phases. Intensive properties are independent of the size, mass, or shape of each phase. Equilibrium thermodynamics provides a mathematical framework to quantitatively describe the relationships between these variables and the state of the system.

Phase equilibrium conditions are derived by applying a differential entropy balance within a closed system [169]. Thus, for π phases in equilibrium, thermal, mechanical, and chemical equilibrium conditions should satisfy the set of Eqs. 4.38,

$$T^I = T^{II} = ... = T^\pi \,, \tag{4.38a}$$

$$P^I = P^{II} = ... = P^\pi \,, \tag{4.38b}$$

$$\mu_i^I = \mu_i^{II} = ... = \mu_i^\pi \quad ; \quad i = 1, ..., n_c \,. \tag{4.38c}$$

The chemical potential condition, Eq. 4.38, ensures that there is no net mass transfer between phases. The chemical potential, μ_i, can be related to the fugacity, $\hat{f}_i$, a thermodynamic property that accounts for deviations from ideal behavior in real systems. The relationship between the chemical potential and the fugacity of the component i can be expressed by Eq. 4.39,

$$\mu_i = \mu_i^0 - RT \ln\left(\hat{f}_i^0\right) + RT \ln\left(\hat{f}_i\right) = \Gamma^0 + RT \ln\left(x_i \hat{\varphi}_i P\right) \,, \tag{4.39}$$

where μ_i^{ref} and $\hat{f}_i^{\text{ref}}$ are the reference chemical potential and fugacity, respectively. At equilibrium, the fugacities of each component must be equal across all phases,which can be written using the fugacity coefficient by Eq 4.40.

$$x_i^I \hat{\varphi}_i^I = x_i^{II} \hat{\varphi}_i^{II} = \cdots = x_i^\pi \hat{\varphi}_i^\pi \quad ; \quad i = 1, ..., n_c \,. \tag{4.40}$$

This equality of fugacities across phases provides a practical way to calculate phase equilibrium in real systems, particularly for non-ideal mixtures. By using EoS or activity coefficient models, fugacities can be computed and used to evaluate equilibrium conditions.

4.5.1. Phase stability analysis

A stability analysis in phase equilibrium is a method used to determine whether a system at a given thermodynamic condition will remain in a single phase or split into multiple phases. The purpose of the test is to assess the stability of a homogeneous phase by checking if the Gibbs energy can be reduced by splitting the phase into two or more different phases. The tangent plane distance (TPD) method, developed by Michelsen [170], is frequently used for this analysis. In this method, the TPD function, F_{TPD}, is defined as the distance between the Gibbs energy surface of the mixture at a global concentration $\underline{\mathbf{z}}$ and that of a hypothetical mixture with concentration $\underline{\mathbf{w}}$, which, in terms of fugacity coefficients, is expressed in Eq. 4.41,

$$F_{\mathrm{TPD}}(\underline{\mathbf{w}}) = \sum_{i=1}^{n_c} w_i \left(\ln w_i + \ln \hat{\varphi}_i(w) - \ln z_i - \ln \hat{\varphi}_i(z) \right) . \tag{4.41}$$

This function is minimized with respect to the phase composition $\underline{\mathbf{w}}$. If the value of F_{TPD} at the global minimum is negative, it implies that the phase is unstable at a global composition $\underline{\mathbf{z}}$ and should split into additional phases.

4.5.2. Characterization of solubility

Besides the computation of solubility isotherms directly from the VLE of a solute–solvent system, other parameters are useful in characterizing solubility. The thermodynamic excess property related to extensive property $\tilde{M}$, $\tilde{M}^{\mathrm{ex}}$, can be computed following Eq. 4.42,

$$\tilde{M}^{\mathrm{ex}} = \tilde{M}^{\mathrm{res}} - \sum_{i=1}^{n_c} \tilde{M}_i^{\mathrm{res}} , \tag{4.42}$$

$\tilde{M}_i^{\mathrm{res}}$ denotes the residual molar property of pure compound i.

The effective Henry's constant [86] of species i, $K_{\mathrm{H}}^{\mathrm{eff}}$, can be computed following the phase equilibrium at infinite dilution conditions [171], as shown in Eq. 4.43,

$$K_{\mathrm{H},i}^{\mathrm{eff}} = \lim_{x_i \to 0} \left(\frac{y_i P^{\mathrm{sat}} \hat{\varphi}_i^{\mathrm{V}}}{x_i} \right) , \tag{4.43}$$

where P^{sat} denotes the saturation pressure of the system, y_i the mole fraction of i in the vapor phase, and $\hat{\varphi}_i^{\mathrm{V}}$ its vapor-phase fugacity coefficient.

Computing effective Henry's constants for various species enables the computation of ideal selectivity of species i over species j in a given liquid phase, $\alpha_{i/j}$, given by Eq. 4.44,

$$\alpha_{i/j} = \frac{K_{\mathrm{H},j}^{\mathrm{eff}}}{K_{\mathrm{H},i}^{\mathrm{eff}}} , \tag{4.44}$$

which, as can be seen, is valid at conditions of infinite dilution of species i and j. A further assessment can be made by computing competitive selectivity of i over j, $S_{i/j}$, given by Eq. 4.45,

$$S_{i/j} = \frac{y_j}{y_i} \frac{x_i}{x_j} , \tag{4.45}$$

which demands the computation of the VLE for the multicomponent system, rather than the diluted conditions considered for $\alpha_{i/j}$. Thus, $S_{i/j}$ allows to assess selectivity in a system when considering the interaction between species i and j.

Finally, dissolution enthalpy, $\Delta\tilde{H}^{\text{dis}}$, offers information concerning the strength of solute–solvent interactions [172], and can be computed through the Clausius-Clapeyron expression following Eq. 4.46,

$$\Delta\tilde{H}^{\text{dis}} = -RT^2 \left(\frac{\partial \ln P^{\text{sat}}}{\partial T} \right)_{\tilde{\rho}, x_i} . \tag{4.46}$$

4.6. Calculation of viscosity using Free Volume Theory

Transport properties cannot be directly derived from an EoS, because they primarily describe the thermodynamic equilibrium properties of an homogeneous system. However, EoSs can be integrated into additional theoretical frameworks to estimate these properties. For example, viscosity can be estimated using Free Volume Theory (FVT), where the EoS provides the necessary molecular parameters as well as the dependence of molar density on thermodynamic conditions.

FVT was first proposed by Allal et al. [173] to model the viscosity of Newtonian fluids. The main feature of FVT, compared to other viscosity models, lies in its incorporation of the free volume concept, in conjunction with molecular diffusion models—specifically, the microscopic friction factor [173]. This approach has gained significant attention in the scientific community due to its ability to accurately model the viscosity of both low-density fluids (e.g., gases) and high-density fluids (e.g., liquids) [174].

According to FVT, the dynamic viscosity of a fluid, η, can be expressed as the sum of two contributions, as shown in Eq. 4.47,

$$\eta = \eta_0 + \Delta\eta \, , \tag{4.47}$$

where η_0 represents the viscosity of the dilute gas, and $\Delta\eta$ accounts for the contribution from the dense fluid.

For hard-sphere molecules of a pure component, the dilute-gas viscosity, η_0, is accurately described by kinetic theory, as formulated by Chapman and Enskog [175]. This theory considers the intermolecular forces influencing molecular behavior in low-density conditions. Chung [176] later extended this model to encompass molecules of varying shapes and anisotropic molecular forces, providing a more generalized expression for η_0, given by Eq. 4.48,

$$\eta_0 = \frac{5}{16} \frac{\sqrt{M_W k_B T/(N_A \pi)}}{\sigma^2 \Omega^{(2,2)}} F_c \, . \tag{4.48}$$

In this equation, N_A is the Avogadro's number, M_w represents the molecular weight, σ is the collision diameter, $\Omega^{(2,2)}$ is the collision integral, and F_c is the correction factor accounting for the effects of chain bonding, hydrogen bonding, and polarity. $\Omega^{(2,2)}$ can be calculated by the empirical equation proposed by Neufeld et al. [177], given by Eq. 4.49,

$$\Omega^{(2,2)} = \left(\frac{A}{T_{\text{ad}}B}\right) + \frac{C}{\exp(DT_{\text{ad}})} + \frac{E}{\exp(FT_{\text{ad}})} + GT_{\text{ad}}^{B}\sin\left(S\left[\frac{k_BT}{\varepsilon}\right]^{W} - H\right), \tag{4.49}$$

where $A = 1.16145$, $B = 0.14874$, $C = 0.52487$, $D = 0.77320$, $E = 2.16178$, $F = 2.43787$, $G = -6.435 \cdot 10^{-4}$, $H = 7.27371$, $S = 18.0323$, and $W = -0.76830$.

The dilute-gas viscosity of a mixture, η_0^{mix}, is typically calculated using the dilute-gas viscosities of its n_c components. A widely used mixing rule, proposed by Wilke [178], is shown in Eq. 4.50,

$$\eta_0^{\text{mix}} = \sum_{i=1}^{n_c} \frac{\eta_0^i}{1 + \frac{1}{x_i}\sum_{j=1, j\neq i}^{n_c} x_j\phi_{ij}}. \tag{4.50}$$

In this expression, η_0^i is the dilute-gas viscosity of component i, and ϕ_{ij}, is a function of the interaction between components i and j as a correction due to different molecular weight, given by Eq. 4.51,

$$\phi_{ij} = \frac{\left[1 + \left(\frac{\eta_0^i}{\eta_0^j}\right)^{\frac{1}{2}}\left(\frac{M_w^i}{M_w^j}\right)^{\frac{1}{4}}\right]^2}{\left(\frac{4}{\sqrt{2}}\right)\left(1 + \frac{M_w^i}{M_w^j}\right)^{\frac{1}{2}}}. \tag{4.51}$$

In this work, the dilute-gas term is neglected, as its contribution is negligible for liquids [178].

The dense fluid viscosity of a Newtonian pure fluid can be calculated through Eq. 4.52,

$$\Delta\eta = L_v(P + \alpha\tilde{\rho}^2M_w)\sqrt{\frac{M_w}{3RT}}\exp\left[B\left(\frac{P + \alpha\tilde{\rho}^2M_w}{\tilde{\rho}RT}\right)^{\frac{3}{2}}\right], \tag{4.52}$$

where L_v is an adjustable length parameter, P is the absolute pressure, α is an adjustable parameter associated with the barrier energy that molecules must overcome to diffuse, $\tilde{\rho}$ is the molar density, and B is characteristic of the free-volume overlap, which is also an adjustable parameter. These parameters can be fitted to the viscosity data of a pure component.

In this work, the dense fluid viscosity for a mixture of n_c components was calculated using the same model described earlier. The approach follows that of other authors [173, 174] for the mixing rule of FVT parameters, employing a simple mixing rule as shown in Eqs. 4.53,

$$\alpha^{\text{mix}} = \sum_{i=1}^{n_c} \alpha_i x_i \,, \tag{4.53a}$$

$$B^{\text{mix}} = \sum_{i=1}^{n_c} B_i x_i \,, \tag{4.53b}$$

$$L_v^{\text{mix}} = \sum_{i=1}^{n_c} L_{v,i} x_i \,. \tag{4.53c}$$

It is important to note that only the parameters of the pure components are used to calculate the viscosity of mixtures, which indicates that the model is predictive for mixtures.

5. Theoretical and methodological framework of life cycle assessment

This chapter presents the general theoretical background and methodological implementation of life cycle assessment (LCA). Within the dimension of environmental assessment, this method allows to compare different alternatives from an environmental perspective. Moreover, it permeates into the decision-making level by evaluating the environmental capabilities of the proposed DES-based processes. Within the evaluation of processes using novel chemicals, LCA enables a holistic view in their evaluation.

5.1. Introduction

Sustainable development was defined in 1987 by the United Nations' World Commission on Environment and Development as a development that meets the needs of the present without compromising the ability of future generations to meet their own needs [179]. This concept is supported by environmental, economic, and social pillars, which have been further articulated through the establishment of the 2015 Sustainable Development Goals [1]. Within the framework of Chemical Engineering, the design and implementation of chemical processes within a sustainable framework is a key factor in achieving these objectives [65]. In this regard, a wide variety of chemical compounds and technologies have been proposed to deploy new processes or improve existing ones, often claiming an enhanced operational performance together with improved sustainability [69, 180, 181].

However, the development of such technologies rarely extends beyond process design [65], and their environmental performance is often inferred from previous studies. Alternatively, environmental impacts can be assessed based on isolated indicators, such as energy consumption or direct emissions. While useful as quantitative measures, these metrics do not account for the broader chain of activities associated with a given process, including upstream resource extraction and downstream processing [182]. Thus, decisions aimed at advancing toward sustainability require a holistic approach, capable of evaluating environmental impacts across different scenarios and interconnected activities.

Life cycle assessment (LCA) is a methodology capable of generating such comprehensive environmental evaluations. It was initially conceived in the 1960s, where it emerged as an approach for material and energy accounting, focusing on inventorying energy and resource use, emissions, and waste generation across the industrial processes characteristic of the life cycle of products [183]. Since the late 1990s, LCA has evolved into a standardized and harmonized framework, used to quantify the impact potentials associated to complex process chains. LCA evaluates the environmental load of a product or process in a holistic manner, encompassing all stages from raw material extraction to end-of-life treatment [184]. From an environmental perspective, this provides a basis for identifying critical stages, as well as for contrasting alternative scenarios within a consistent framework [182]. In this sense, LCA is inherently a comparative methodology, as its results are only truly meaningful when used to compare alternative products, processes, or scenarios, rather than as absolute measures of sustainability [185].

In this chapter, the theoretical foundations and methodological framework of LCA are presented. The chapter begins with an overview of the mathematical formulation of LCA, and follows with its general implementation structure, including goal and scope definition, inventory analysis, and impact assessment.

5.2. Theoretical background

The LCA framework is essentially divided into two steps. First, the life cycle inventory (LCI) is performed, where the considered product or process is modeled by the aggregation of all unit processes involved in its realization. This set of interconnected unit processes is defined as the product system [185]. Subsequently, the impact potential of the product system is assessed by translating all process exchanges into a manageable set of environmental impact categories. This process is denoted as the life cycle impact assessment (LCIA), and provides a simplified and practical representation of the overall environmental burden, which can be further used to compare alternative product systems.

As process exchanges span widely different natures depending on their associated unit processes, *e.g.*, materials, wastes, substances, and energy, a consistent method is required to represent the LCI within an unified framework among different LCAs. Moreover, in product systems involving multiple interconnected unit processes, the quantification of the various process exchanges becomes complex. Given these considerations, the LCI is formulated as a multidimensional linear problem [186]. Here, a unit process is represented by a n_f-dimensional vector in a linear space. The basis of this space consists on the n_f flows that act as inputs or outputs for each unit process. Thus, a product system is represented by its process matrix, $\underline{\underline{\boldsymbol{\mathcal{P}}}} \in \mathbb{R}^{n_f \times n_s}$, obtained by the juxtaposition of the n_s unit process vectors. As a convention, negative and positive values for each element $\mathcal{P}_{ij}$ indicate an input or output of flow i from process j, respectively.

Within the LCA framework, processes are conceptually divided into two domains: the technosphere and the ecosphere. The technosphere contains all human-made processes, such as production of substances and disposal of equipments, while the ecosphere represents all exchanges with the natural environment, such as emissions and resource extractions. In the mathematical

formulation, each flow i of process j, $\mathcal{P}_{ij}$, represents either an exchange between unit processes or an exchange between a unit process and the environment. Consequently, $\underline{\underline{\boldsymbol{\mathcal{P}}}}$ is partitioned into the technology matrix, which describes exchanges within the technosphere, and the intervention matrix, which accounts for exchanges with the ecosphere. This partition is shown in Eq. 5.1,

$$\underline{\underline{\boldsymbol{\mathcal{P}}}} = \begin{pmatrix} \underline{\underline{\boldsymbol{\mathcal{A}}}} \\ \underline{\underline{\boldsymbol{\mathcal{B}}}} \end{pmatrix} , \tag{5.1}$$

where $\underline{\underline{\boldsymbol{\mathcal{A}}}} \in \mathbb{R}^{n_t \times n_s}$ and $\underline{\underline{\boldsymbol{\mathcal{B}}}} \in \mathbb{R}^{n_b \times n_s}$ represent the technology and intervention matrices, respectively. Accordingly, n_t and n_b represent the number of flows allocated to the technosphere and ecosphere, respectively.

Additionally, an integral part of the LCI is the definition of the system boundaries, which determine the process flows contained within the product system, and thus the numbers n_f and n_s. The definition of the system boundary is directly related to the stages of the product life cycle considered in the assessment [182]. Three key stages are usually distinguished: the cradle, which represents the extraction of natural resources for the manufacturing of the reference product; the gate, which corresponds to the point at which the reference product leaves the production system; and the grave, which encompasses the end-of-life activities [187]. Several system boundaries can be established by the conjunction of these stages, including:

- **Cradle-to-gate**, which encompasses all processes from raw material extraction to production of the reference product.
- **Gate-to-grave**, which includes the use-phase and end-of-life management of the reference product.
- **Cradle-to-grave**, which represents the most comprehensive type of LCA, as it covers the complete life cycle of the product system, from resource extraction to end-of-life.

The outcome of the LCI is controlled by the definition of the functional unit (FU). The FU is one of the key concepts within the LCI, as it provides a quantitative description of the function delivered by the product system. It is generally represented by the r^{th} flow, corresponding to the activity to be finally assessed. Within the LCI linear formalism, the final demand vector, $\underline{\boldsymbol{y}} \in \mathbb{R}^{n_t}$, is used to express the FU by having the reference flow y_r as its only non-zero element.

The LCI problem consists in determining the amount of each unit process j required to yield the FU. This is achieved by computing the set of scaling factors, $\underline{\boldsymbol{s}} \in \mathbb{R}^{n_s}$, for which the unit processes in $\underline{\underline{\boldsymbol{\mathcal{A}}}}$ satisfy the final demand vector. In this formulation, it is assumed that each process j is a linear technology, such that their output scale proportionally with the increase or decrease of their associated flows. Thus, the LCI inventory problem is expressed as a system of linear equations, which can be solved as shown in Eq. 5.2,

$$\underline{\boldsymbol{s}} = \underline{\underline{\boldsymbol{\mathcal{A}}}}^{-1} \underline{\boldsymbol{y}} . \tag{5.2}$$

The effect of scaling the technology matrix by the vector $\underline{s}$ must be assessed in the intervention matrix. From the assumption of linear technologies, the exchanges with the ecosphere are computed in an analogous manner, as expressed by Eq. 5.3,

$$\underline{g} = \underline{\underline{\mathcal{B}}}\,\underline{s}\,, \tag{5.3}$$

where $\underline{g} \in \mathbb{R}^{n_b}$ is the vector of environmental interventions, whose elements represent the aggregated flows exchanged with the biosphere across the product system.

The formalism of Eq. 5.2 is only valid when $\underline{\underline{\mathcal{A}}}$ is square and invertible. That is, a unique correspondence between technosphere unit processes and flows is assumed. However, this is not the general case, where multifunctional processes, recycling loops, or co-products can be present in the product system. Different approaches, such as partitioning and substitution methods, can be applied to yield an invertible technology matrix [186]. Irrespective of the applied method, Eq. 5.2 can be solved to quantify the configuration of the product system in order to supply the flow, and its quantity, given by the FU.

Once the LCI problem is solved, the LCIA can be performed. To translate the above results into environmental impact indicators, the LCIA is based on characterization factors that quantify the contribution of a given environmental intervention to a specific environmental impact category. Assuming that n_p environmental impact categories are selected, the impact vector $\underline{h} \in \mathbb{R}^{n_p}$ is defined to represent the environmental performance of the product system. This vector is computed following Eq. 5.4,

$$\underline{h} = \underline{\underline{\mathcal{Q}}}\,\underline{g}\,, \tag{5.4}$$

where $\underline{\underline{\mathcal{Q}}} \in \mathbb{R}^{n_p \times n_b}$ denotes the characterization matrix, such that $\mathcal{Q}_{ij}$ quantifies the contribution of environmental intervention j to impact category i.

The computation of $\underline{h}$ is the starting point of the cause–effect chain in LCA, which represents the pathway from the raw elements of $\underline{g}$ to impact scores understandable for decision making. The resulting impact scores are referred to as midpoint impact indicators. These indicators aggregate the different environmental interventions into groups representing a specific environmental problem. Furthermore, a higher level of aggregation can be achieved by using endpoint indicators, which translate midpoint indicators into more general classifications, such as human health and ecosystem quality. These generalized groups are related to areas of protection, of interest in the decision making around the product system.

Several methodologies have been developed to establish the cause–effect chain, as various possibilities exist around the definition of characterization factors and impact categories. Consequently, a variety of LCIA methodologies are currently available, including CML 2001 [188], IMPACT 2002+ [189], and ReCiPe 2016 [190].

5.3. Methodology

To ensure a standardized methodology and compatibility among studies, the ISO 14040 standard [191] establishes the general framework that every LCA must follow.

In the first step, the goal and scope definition, the product system is defined in terms of the system boundaries and the FU [182]. Moreover, the scope of the environmental impacts of importance for the study can also be defined, before being formally defined in further steps. Furthermore, the perspective to apply in the study is also decided, *i.e.*, the definition of an attributional or consequential LCA. In the first perspective, the environmental burdens associated with the product system are assessed. The second perspective offers a broader scope for the study, assessing the expected consequences of choosing the product system.

Once the above terms are defined, the second step of a LCA consists of solving the LCI problem of Eq. 5.2. Thus, all unit process vectors in the $\underline{\underline{\mathcal{P}}}$ matrix must be known. The dimension and elements associated to these vectors must be obtained from comprehensive databases, comprising process exchanges within the technosphere and ecosphere as detailed as possible. Several available databases can be implemented for the LCI, with ecoinvent [192], GaBi, and SimaPro [193] being among the most widely used sources of inventory data.

In the third step, the LCIA assessment is performed by solving Eq. 5.4. Analogously to the requirement of process exchanges in the LCI, the LCIA requires a comprehensive coverage of the characterization factors in the $\underline{\underline{\mathcal{Q}}}$ matrix. Among the different LCIA methods, ReCiPe 2016 [194] offers a comprehensive list of characterization factors, defining a total of 18 midpoint and 3 endpoint impact indicators. Moreover, this approach also considers different perspectives in the assumptions used for environmental impact calculation, *i.e.*, the individualistic, hierarchist, and egalitarian approaches. The individualistic approach is based on short-term interest, with optimistic assumptions regarding technology on human adaptation. The hierarchist perspective represents a baseline time horizon, considering plausibility of impact mechanisms. Finally, the egalitarian approach takes into account the longest time frame and all impact pathways for which data is available [190].

Within the development of this thesis, the ReCiPe 2016 method using the hierarchist approach was considered. The midpoint impact indicators of interest are presented in Table 5.1. Furthermore, within the hierarchist approach, endpoint indicators are derived from these quantities and grouped into the categories of ecosystem quality (EQ), human health (HH), and use of natural resources (NR), each one with units of species·yr, DALYs, and USD_{2013}, respectively.

Once the LCIA is performed, the last step in the LCA is the interpretation of the results, aimed at evaluating the significance of the results with respect to the defined goals. Depending of the objective of the performed LCA, the main drivers of environmental impact can be identified.

TABLE 5.1: Overview of the considered midpoint impact categories from the ReCiPe 2016 LCIA methodology [194].

Impact category	**Indicator**	**Midpoint characterization factor**	**Unit**
Climate change	Infra-red radiative forcing increase	Global warming potential (GWP)	[kg_{CO_2e}]
Terrestrial acidification	Proton increase in natural soils	Terrestrial acidification potential (TAP)	[kg_{SO_2e}]
Human toxicity	Risk increase of non-cancer disease incidence	Human toxicity potential (HTP)	[$kg_{1,4\text{-}DCBe}$]
Ozone depletion	Stratospheric ozone decrease	Ozone depletion potential (ODP)	[kg_{CFC11e}]
Water use	Increase of water consumed	Water consumption potential (WCP)	[m^3]
Fossil resource scarcity	Upper heating value	Fossil fuel potential (FFP)	[kg_{oil}]

6. Unveiling Molecular Features Controlling the Solubility of Hydrofluorocarbons in Fluorine-Based Eutectic Solvents

In this chapter, the solubility and solvation mechanisms of HFCs in fluorine-based eutectic solvents (FESs) is investigated using COSMO-RS and MD simulations. Three FESs based on perfluoropentanoic acid (PFPA) as the hydrogen bond donor were evaluated to understand how ionic and molecular hydrogen bond acceptors influence the absorption of R32, R134a, and R125. Results for solubility isotherms, structural features, and interaction energy show that solubility can be enhanced by disrupting the HFC cluster formation in the liquid phase. This effect is less marked for fluorinated ethanes, related to a lower free volume and lesser van der Waals interactions in solvents with non-voluminous components. Results from this approach suggest the importance of localized interactions in the solubility of HFCs, and provides a rational basis for designing advanced solvents for the recovery of HFCs.[*]

6.1. Introduction

Molecular tailoring of ILs and IL-based DESs has enabled the study of solvents with highly specific thermophysical properties. This can be primarily exemplified by fluorinated ionic liquids (FILs), *i.e.*, ILs bearing perfluorinated alkyl chains containing four or more carbon atoms. FILs nanosegregate into polar, apolar, and fluorinated domains [195], a feature that has been associated with enhanced solubilization of fluorinated solutes, particularly HFCs [196, 197]. Sosa et al. [198] reported the absorption of R32, R134a, and R125 in FILs, showing that fluorinated alkyl chains in the anion reduce Henry's constants compared to conventional ILs, suggesting increased solubilities at lower pressures. The authors attributed this behavior to the larger free volume and potential F–H interactions provided by fluorinated domains. In parallel, quaternary phosphonium-based

[*]This chapter is adapted with permission from:
B. González-Barramuño, E. Cea-Klapp, N.F. Gajardo-Parra, R.I. Canales, H. Quinteros-Lama, and J.M. Garrido, "Unveiling Molecular Features Controlling the Solubility of Hydrofluorocarbons in Fluorine-Based Eutectic Solvents", Industrial & Engineering Chemistry Research **64**, 46, 22400-22412 (2025).

ionic liquids (PILs) have emerged as promising candidates for HFC absorption. Compared with ammonium-based ILs, PILs exhibit higher thermal stability [199] and enhanced robustness under nucleophilic or basic conditions [200]. Although they remain less studied, recent experimental studies have reported promising HFC absorption capabilities in selected PILs [44, 201].

Despite the favorable absorption properties of FILs, the incorporation of C–F bonds in their chemical structure may increase their melting temperatures beyond typical absorption operating conditions [202]. To overcome this limitation, Castro et al. [203] mixed FILs with perfluorinated acids to synthesize fluorinated eutectic solvents (FESs). By measuring the absorption of R32, R134a, and R125 in these mixtures, the authors reported remarkable solubilities, reaching HFC liquid mole fractions of up to 0.6 under the studied conditions for R32, R134a, and R125. The formation of these FESs establishes cooperative effects between its constituents, where free volume and strong electrostatic interactions may enhance the solubility of HFCs. On the other hand, quaternary phosphonium-based DESs have demonstrated promising gas absorption capabilities for compounds such as CO_2 [204] and SO_2 [205]. In particular, tetrabutylphosphonium bromide ([P_{4444}]Br) forms DESs with several acids and glycols [206–208], which have been predominantly investigated for extraction and absorption processes [204, 208]. However, despite the growing interest in PIL-based ESs, their application to HFC absorption has not yet been systematically studied.

To understand how the molecular architecture of FIL- and PIL-based ESs influence HFC solubility, predictive theoretical tools are required to feasibly characterize their thermophysical behavior. In this chapter, COSMO-RS and MD simulations are employed to study three FESs based on perfluoropentanoic acid (PFPA) as the HBD. The first and second FESs, already experimentally synthesized [203], comprise 1-ethyl-3-methylimidazolium heptadecafluorooctanesulfonate ([C_2mim][HDFS]) and tetrabutylammonium nonafluorobutanesulfonate ([N_{4444}][NFS]) as HBAs. Furthermore, motivated by the potential of PILs for HFC capture, [P_{4444}]Br was selected as the HBA for a third FES due to its simplicity and current use as a precursor in DES synthesis. Since the eutectic behavior of [P_{4444}]Br:PFPA has not been experimentally validated, an initial assessment was performed by analyzing the deviation of activity coefficients from ideality. After effectively confirming the non-ideal character of these systems through the employed computational approach, HFC absorption was characterized by computing solubility isotherms and transport properties. Finally, MD simulations provided molecular-level insights into solvation environments and their relationship with HFC solubility.

6.2. Molecular modeling

A collaborative approach of COSMO-RS and MD simulations was used to assess the absorption of HFCs in [C_2mim][HDFS]:PFPA, [N_{4444}][NFS]:PFPA, and [P_{4444}]Br:PFPA. The chemical structures of the compounds comprising all studied solvents are presented in Table 6.1.

TABLE 6.1: Molecular structure of the compounds forming the considered solvents.

Name	Structure	Abbreviation
1-ethyl-3-methylimidazolium heptadecafluorooctane-1-sulfonate	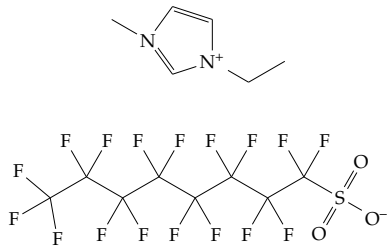	$[C_2mim][HDFS]$
tetra-n-butylammonium nonafluorobutane-1-sulfonate	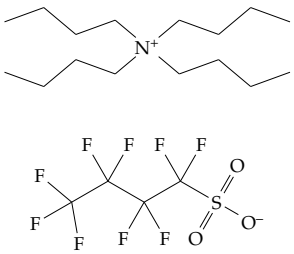	$[N_{4444}][NFS]$
tetra-n-butylphosphonium bromide	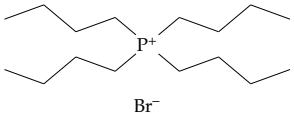	$[P_{4444}]Br$
perfluoropentanoic acid	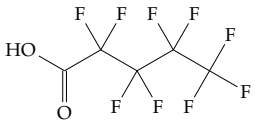	PFPA

6.2.1. COSMO-RS modeling

COSMO-RS [81] was employed to corroborate the non-ideal behavior of the considered FESs, and to compare their performance in the absorption of R32, R134a, and R125. The COSMOTherm package [84], with the BP-TZVP parameterization (see Section 2.3), was utilized to model all species and to perform thermodynamic equilibrium calculations. To model the ILs serving as HBAs in each solvent, the independent-ion, or C+A, approach was adopted. Here, the cation and anion are treated as two distinct species within the mixture, thereby defining the FES as a ternary system, where both ionic species are present in an equimolar ratio. Given the molecular complexity of the considered ions, this approach was preferred over the combined CA approach, in which both ionic species are combined in a unique optimized structure, requiring a more computationally demanding conformational sampling and joint optimization.

Once the σ-profiles, $p_S(\sigma)$, of each species were obtained, their σ-potentials, $\mu_S(\sigma)$, were computed for all studied FESs to analyze the predicted nature of their absorption mechanisms. Moreover, deviations from ideal solution behavior were studied by computing the activity coefficient of PFPA, γ_{HBD}, in $[C_2mim][HDFS]$:PFPA, $[N_{4444}][NFS]$:PFPA, and $[P_{4444}]Br$:PFPA as a function of the liquid

mole fraction of HBA, x_{HBA}, at 303.15 K and 1 bar. A range of x_{HBA} covering the HBA:HBD mole ratios of 1:2, 1:1, and 2:1, previously assessed as eutectic concentrations for [N_{4444}][NFS]:PFPA and [C_2mim][HDFS]:PFPA [203], was considered for all studied FESs. Once the deviations from ideal solution behavior were quantified, effective Henry's constants [86] and solubility isotherms for R32, R134a, and R125 were computed in each solvent.

6.2.2. MD simulations details

MD simulations were performed to study the capability of molecular mechanics models to predict non-ideal behavior in the considered FESs, along with characterizing the absorption of HFCs in them. All MD simulations were carried out using the GROMACS (version 2022.1) suite [209], considering homogeneous systems of FES and HFC + FES.

Molecular mechanics force fields

To model the chemical structures presented in Table 6.1, all-atoms FFs were employed. The CL&P FF [57], based on the optimized potentials for liquid simulations (OPLS) [89], was chosen to represent the HBAs comprising the FESs. This FF was developed to model families of ILs, rather than specific cation–anion combinations, allowing to assemble ILs from any available parameterization. Thus, its transferability to the studied HBA ILs is regarded suitable for the considered approach. Among the ionic species of interest, $[N_{4444}]^+$, $[C_2mim]^+$, $[P_{4444}]^+$, Br^-, and $[NFS]^-$ count with available parameters from the CL&P FF [210–213]. Only $[HDFS]^-$ has not been previously parameterized, and both bonded and non-bonded parameters were directly transferred from the parameterization for $[NFS]^-$ [213].

The remaining species, *i.e.*, PFPA, R32, R134a, and R125, were modeled using available parameters based on the OPLS FF. For PFPA, parameters from OPLS-based FFs for perfluoroalkylated substances [214] were directly transferred. On the other hand, for HFCs, proper models for R32 and R134a have already been reported in the literature [215, 216] and were directly applied in this work. In the case of R125, where no OPLS-based parametrization is available, a FF model was developed analogously to the work of Peguin et al. for R134a [216]. Details regarding the implementation and validation of this approach are presented in Appendix A, where results for the computed VLE of R125 show acceptable correspondence with available experimental data.

Consistently with the OPLS methodology [89], 1–2 and 1–3 non-bonded interactions were excluded, while 1–4 interactions were scaled by a factor of 0.5 for LJ and electrostatic interactions. Long-range electrostatic interactions were treated using the fast-smooth particle mesh Ewald method [217], and analytical dispersion corrections were applied to the LJ potential for the computation of energy and pressure, provided that all considered systems were simulated as homogeneous phases. A cutoff radius of 1.2 nm was used in all cases for LJ and short-range Coulomb interactions. Neighbor lists were constructed using the Verlet scheme [100] with a tolerance of 10^{-4} kJ·mol^{-1}·ps^{-1} and a neighbor cutoff radius of 1.2 nm. Periodic boundary conditions were implemented in all directions. During all production and equilibration runs, bonds involving hydrogen atoms were constrained using the LINCS algorithm [99], whereas all bonds were constrained during energy minimization runs.

To handle polarization effects, point charges for ionic species were scaled by a factor of 0.8 to enhance the gas diffusivity in the liquid phase and obtain faster dynamics [218]. It is worth noting that, to represent this effect more explicitly, more sophisticated approaches are available [219]. Particularly, the CL&P FF has already been extended to account for polarization, which has been used to compute effective Henry's constants of F-gases in ILs [56]. Although with better results regarding dynamics, these models, based on classical Drude oscillators [220], rely on a substantially high computational cost. As free energy calculations performed in this work depended on parallelization to achieve a correct sampling and reliable results, the inclusion of these novel models was considered prohibitive for the studied systems. Thus, the scaling of point charges was considered as a reasonable compromise between computational cost and accuracy of results.

FFs for species comprising the studied FESs were validated by comparing the predicted liquid mass density, $\hat{\rho}^{\mathrm{L}}$, with available experimental data for PFPA [221], [C_2mim][HDFS]:PFPA [203], and [N_{4444}][NFS]:PFPA [203]. Details and results of MD simulations in each case are presented in Appendix B. In the case of PFPA, results showed an appreciable overestimation of $\hat{\rho}^{\mathrm{L}}$. Thus, following a previously validated procedure [222], LJ parameters for PFPA were scaled to minimize deviations with respect to experimental density. In this case, the collision diameter and dispersion energy for all sites in the molecule were scaled by 1.04 and 0.89, respectively. As shown in Figure B.1, deviations from experimental data were reduced, thus validating the scaled model of PFPA for its use in liquid phase computations. For [C_2mim][HDFS]:PFPA, a similar procedure was required to refine the modeling of $\hat{\rho}^{\mathrm{L}}$. Considering [HDFS]$^-$ was parameterized by merely transferring the parameters of [NFS]$^-$, its LJ parameters were modified analogously to PFPA. Thus, collision diameter and dispersion energy of every site of [HDFS]$^-$ were scaled by 1.04 and 0.97, respectively. As shown in Figure B.2, the small shift in these parameters allow for a better correspondence with experimental data. Moreover, Figure B.2 also provides results for [N_{4444}][NFS]:PFPA, which didn't require any modification to achieve acceptable correspondence with experimental data.

MD simulations of FESs

Deviations from ideal solution behavior were studied using MD simulations by computing γ_{HBD} at different HBA:HBD mole ratios. This activity coefficient was obtained following the expression proposed by Hempel et al. [223], as shown in Eq. 6.1,

$$\gamma_i = \exp\left(\frac{\mu_i^{\mathrm{ex}} - \mu_i^{\mathrm{ex},0}}{RT}\right)\frac{\tilde{\rho}}{\tilde{\rho}^0}\,, \tag{6.1}$$

where μ_i^{ex} is the excess chemical potential of component i in the mixture, and $\tilde{\rho}$ is the mole density of the system. The superscript 0 stands for properties at the pure state of component i.

Eq. 6.1 requires the computation of $\mu_{\mathrm{HBD}}^{\mathrm{ex}}$, from simulations for both pure PFPA and FESs. In this work, this was achieved through free energy calculations using the FEP method. The MBAR estimator, incorporated in the Alchemlyb software [224, 225], was used to compute free energy differences across the different states. Considering the structural complexity of the studied solvents, the HREX method was employed as a sample accelerator to overcome the deterioration of

energetic sampling due to slow dynamics or insufficient simulation time. Further details can be found in Section 3.3.2.

NPT HREX MD simulations were performed to compute $\hat{\rho}^{\mathrm{L}}$ and γ_{HBD} at 303.15 K and 1 bar. Since PFPA is the only FES precursor that remains liquid at these conditions, the HBA:HBD mole ratios were selected such that all simulated systems stayed in the liquid phase. Thus, HBA:HBD mole ratios of 1:9, 1:6, 1:4, 1:3, and 1:2, were considered, respectively covering concentrations ranging from near-pure PFPA to one of the experimentally reported concentrations of the FESs [203]. Accordingly, 100 ionic liquid pairs were inserted into each simulation box, in addition to 900, 600, 400, 300, or 200 molecules of PFPA, for each respective mole ratio. Initial configurations were generated by randomly inserting the desired molecules using the PACKMOL software [107]. An energy minimization was first run on every configuration to ensure the absence of overlaps between atoms. The steepest descent algorithm was utilized in all cases, applying a tolerance of 10 kJ·mol^{-1}·nm^{-1}. Upon reaching a minimum energy configuration, systems were subjected to two successive *NPT* equilibration runs. First, a 0.25 ns run was performed using the Berendsen barostat [101], with a time constant of 2 ps, to bring the system to the desired pressure. Then, a 10 ns run was performed, using a Parrinello-Rahman barostat [105] with a time constant of 2 ps and a liquid compressibility of $4.5{\cdot}10^{-5}$ bar^{-1}. For both simulations, a timestep of 1 fs was used, and equations of motion were integrated using the stochastic dynamics Leapfrog integrator [226], coupled with a Langevin thermostat [227] with a time constant of 1 ps. Once the systems were equilibrated at the desired conditions, the FEP was performed by decoupling the interactions of one PFPA molecule in the course of 24 intermediate states, attempting exchanges between replicas every 2000 steps. Each simulation was run for 50 ns, and all configurations related to their controllers were considered equivalent to the ones of the second equilibration run. Finally, $\mu^{\mathrm{ex}}_{\mathrm{HBD}}$ was computed considering the last 30 ns of each one of the 24 runs. Moreover, an analogous simulation of 1000 PFPA molecules was performed to compute the required $\mu_i^{\mathrm{ex},0}$ and $\tilde{\rho}^0$.

MD simulations of HFC + FES systems

Solubility isotherms of HFCs in each FES were obtained at 303.15 K following the expression proposed by Wang et al. [228], shown in Eq. 6.2,

$$\frac{\mu_i^{ex}}{k_B T} - \ln \frac{q_s\,(T)\ \langle V \rangle_t}{\Lambda_i^3 N_i^L} = -\ln \frac{q_s k_B T}{\Lambda_i^3 P_0} + \ln \frac{P}{P_0} + \ln \hat{\varphi}_i^{\mathrm{V}}\,, \tag{6.2}$$

where $q_s(T)$ is the single-molecule ideal-gas partition function, $\langle V \rangle_t$ is the mean volume of the system along the simulation time, Λ_i is the thermal de Broglie wavelength for component i, N_i^{L} is the number of molecules of component i in the liquid phase, P_0 is a reference pressure, P is the equilibrium pressure of the system, and $\hat{\varphi}_i^{\mathrm{V}}$ is the vapor-phase fugacity coefficient for i. Considering the inherent low volatility of the studied FESs, $\hat{\varphi}_i^{\mathrm{V}}$ was computed as the pure fugacity coefficient of each HFC, rather than considering its VLE with the solvent. Thus, the dependence of $\hat{\varphi}_i^{\mathrm{V}}$ on T and P was accounted for by using the soft-SAFT EoS. Previously optimized parameters for R32, R134a, and R125 [229, 230] were directly applied to obtain their fugacity coefficients, and the applied molecular parameters are presented in Table 6.2.

TABLE 6.2: Molecular weight and soft-SAFT molecular parameters for the considered HFCs. The notation of Huang and Radosz [148] is used to denote the association scheme in each case.

Compound	M_w [g·mol^{-1}]	$m_{s,i}$	σ_{ii} [Å]	ε_{ii}/k_B [K]	$\varepsilon^{A_iB_i}/k_B$ [K]	$k^{A_iB_i}$ [Å^3]	Assoc. scheme	Source
R32	52.00	1.321	3.529	144.40	1708	24050	2B	[229]
R134a	102.03	1.392	4.166	166.60	1862	24050	2B	[230]
R125	120.02	1.392	4.242	148.80	1685	24050	2B	[229]

The excess chemical potentials of R32, R134a, and R125 in the studied FESs were computed via NPT HREX MD simulations at 303.15 K and 1 bar as the reference pressure. Considering the obtained results for non-ideality of the considered solvents (see Section 6.3.2), only the solubility of HFCs in FESs with an HBA:HBD mole ratio of 1:2 was studied. Therefore, 250 ionic liquid pairs and 500 PFPA molecules were inserted into simulation boxes. Different amounts of HFC were added to the system based on their desired mole fraction in the liquid phase, x_{HFC}. Thus, 133, 322, and 614 HFC molecules were included to ensure x_{HFC} values of 0.15, 0.30, and 0.45, respectively. Then, the same procedure applied to the computation of $\mu^{\mathrm{ex}}_{\mathrm{HBD}}$ was performed, considering the decoupling molecule to one molecule of R32, R134a, or R125, depending on the case. Effective Henry's constants of HFCs into the analyzed solvents were estimated by fitting the computed solubility curves to a corresponding polynomial function and extrapolating its slope to $x_{\mathrm{HFC}} = 0$.

Molecular insights for the absorption of HFCs in FESs were also obtained from MD simulations, which were conducted at 303.15 K and at the previously computed equilibrium pressures. The same configurations as the ones for absorption isotherm simulations, *i.e.*, 250 ionic liquid pairs, 500 PFPA molecules, and 133, 322, or 614 HFC molecules, were utilized in this case. Upon inserting the required molecules using the PACKMOL software [107], an energy minimization by steepest descent with a tolerance of 10 kJ·mol^{-1}·nm^{-1} was run. Then, a NPT equilibration run, analogous to the first equilibration run for the computation of μ^{ex}_i, was performed to rapidly achieve the desired pressure. A subsequent 30 ns NPT equilibration was run, using the Berendsen thermostat [101] and the Parrinello-Rahman barostat [105] with time constants of 1 ps and 2 ps, respectively. Finally, a 20 ns NPT production run was performed to extract the required structural information. A Nosé-Hoover thermostat [104] and a Parrinello-Rahman barostat [105], with time constants of 1.5 ps and 3.5 ps, respectively, were used to generate the ensemble. The liquid compressibility for all the implemented barostats was chosen as $4.5{\cdot}10^{-5}$ bar^{-1}. In all cases, a 1 fs timestep was used, and, except for the first equilibration run, equations of motion were integrated using the Leapfrog algorithm [231]. Finally, radial distribution functions (RDFs) between the centers of mass (COMs) of HFCs and the different species of the FESs were computed using the last 18 ns of the production run. Additionally, spatial distribution functions (SDFs) and angle-distance distributions (ADDs) were computed from the same time interval using the TRAVIS software [232, 233]. Furthermore, an interaction energy analysis was performed in the same time interval to quantify the Coulomb and LJ contributions to the overall internal energy.

Transport properties in HFC + FES systems, at 303.15 K, were studied given their industrial importance in the implementation of ESs as absorbent agents. Shear liquid viscosity, η^{L} was computed from NEMD simulations (see Section 3.3.1) at $x_{\mathrm{HFC}} = 0$ and $x_{\mathrm{HFC}} = 0.45$. MD simulations at amplitudes of $\mathcal{A} \in \{0.05, 0.10, 0.15, 0.20, 0.25, 0.30, 0.40, 0.50\}$ were considered for each viscosity calculation. An initial configuration was defined for each one of the eight runs by extracting different frames from the 30 ns NPT equilibration run from the molecular insights MD simulations. Snapshots were extracted from the trajectory every 500 ps, starting from the last frame. To ensure that every amplitude run had the same volume, the dimensions of the extracted configurations were rescaled to meet the mean volume of the system, computed from the last 15 ns of the above equilibration run. Following this approach, η^{L} could be computed close to VLE by the obtained solubility isotherms. To stabilize the systems to their new volumes, these were subjected to an energy minimization, analogous to the previously done, and a NVT equilibration run of 1 ns, using a Nosé-Hoover thermostat [104] with a time constant of 1.5 ps. Then NVT NEMD simulations were run for 20 ns at their corresponding $\mathcal{A}$ values, using the same thermostat. All simulations were run using a 1 fs timestep, and equations of motion were integrated using the Leapfrog algorithm [231]. Viscosity values were extracted from the last 18 ns of the trajectory.

Self-diffusivity of HFCs in the HFC + FES systems, $\mathcal{D}_{\mathrm{HFC}}$, was analyzed at $x_{\mathrm{HFC}} = 0.45$, in order to relate its results with η^{L}. Computations were done using Einstein's equation with system-size corrections (see Section 3.3.1). Analogously to previous NEMD simulations, four runs were performed for each measured value of $\mathcal{D}_{\mathrm{HFC}}$ to reduce the uncertainty of results. These runs were also obtained by extracting and scaling different snapshots from the aforementioned NPT equilibration run. After a minimization and an NVT equilibration run, analogous to the ones performed for the computation of η^{L}, a 30 ns NVT production run was done using the same thermostat. MSD data was extracted at the entire trajectory, and $\mathcal{D}_{\mathrm{HFC}}$ was obtained as the slope of a linear fit performed for a time interval from the 10 ns to 25 ns of simulation time.

6.3. Results and Discussion

6.3.1. HFC absorption insights from COSMO-RS

Figure 6.1a presents the computed $p_S(\sigma)$ for the studied FESs at 303.15 K, 1 bar, and a fixed HBA:HBD mole ratio of 1:2. As can be seen, all FESs present a widely spread charge distribution, roughly ranging from –2.5 e·nm^{-2} to 2.0 e·nm^{-2}. A marked region in the neutral-charge region is observed, which is associated to the presence of carbon atoms. Moreover, this central peak extends to the positively charged region ($\sigma < 0$) for all three FESs. Given the stronger presence of hydrogen atoms in [N_{4444}][NFS]:PFPA (1:2) and [P_{4444}]Br:PFPA (1:2), these FESs are characterized by a marked left shoulder in their $p_S(\sigma)$, compared to [C_2mim][HDFS]:PFPA (1:2). For the negatively charged region ($\sigma > 0$), [N_{4444}][NFS]:PFPA (1:2) and [C_2mim][HDFS]:PFPA (1:2) yield similar σ-profiles, given by the structural similarity in their anions. However, [P_{4444}]Br:PFPA (1:2) displays a different behavior in this region, characterized by a narrow peak at about 1.8 e·nm^{-2}, due to its atomic Br^- anion with a highly localized charge.

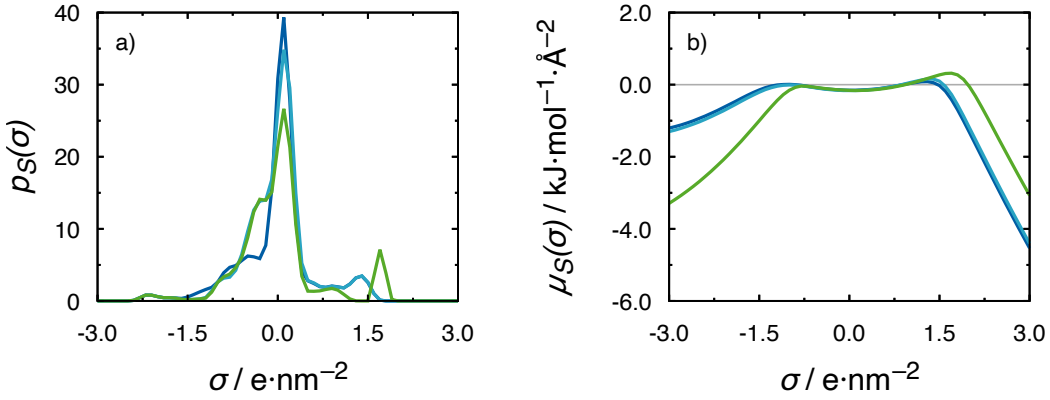

FIGURE 6.1: σ-profiles, $p_S(\sigma)$, (a) and σ-potentials, $\mu_S(\sigma)$, at 303.15 K (b), obtained using COSMO-RS at the BP-TZVP parameterization, for [C_2mim][HDFS]:PFPA (1:2) (—), [N_{4444}][NFS]:PFPA (1:2) (—), and [P_{4444}]Br:PFPA (1:2) (—). The $y = 0$ line is included in (b) (—) for guiding purposes.

To relate the above structural characteristics with the preferential absorption of solutes, $\mu_S(\sigma)$ were computed and are shown in Figure 6.1b. [N_{4444}][NFS]:PFPA (1:2) and [C_2mim][HDFS]:PFPA (1:2) present virtually equal $\mu_S(\sigma)$, characterized by markedly negative values at both negative and positive regions of σ. This suggests solvation preferences toward both electrophilic and nucleophilic solutes, respectively [234], with a stronger preference for the latter due to more negative $\mu_S(\sigma)$ at $\sigma > 0$. A different behavior is observed for [P_{4444}]Br:PFPA (1:2), with much more negative $\mu_S(\sigma)$ values in the $\sigma < 0$ region. At the same time, a lower affinity for nucleophilic solutes, compared to the above FESs, is developed, with more positive values for $\mu_S(\sigma)$ at the $\sigma > 0$ region. This can be related to the Br^- anion, which concedes the solvent a stronger affinity for electrophilic solutes though its more localized negative charge. Considering this, [P_{4444}]Br:PFPA should present a different solvation behavior than [N_{4444}][NFS]:PFPA and [C_2mim][HDFS]:PFPA, oriented toward the acceptance of hydrogen atoms from the solute.

Energetic characteristics of the solvation of HFCs were studied by computing thermodynamic excess properties. Figure 6.2 presents the excess Gibbs energy, $\tilde{G}^{ex}$, and excess enthalpy, $\tilde{H}^{ex}$, for HFC + FES mixtures at $x_{HFC} = 0.15$. As can be seen, [P_{4444}]Br:PFPA (1:2) provides more negative values of $\tilde{G}^{ex}$ for all considered HFCs, suggesting a more favorable absorption of these gases. This can be attributed to the more nucleophilic nature of the FES, as assessed from its $\mu_S(\sigma)$. When comparing[N_{4444}][NFS]:PFPA (1:2) and [C_2mim][HDFS]:PFPA (1:2), both FESs show a similar absorption behavior, with the former presenting more favorable interactions in all cases.

A more detailed understanding of the solvation mechanism was obtained by analyzing the individual contributions to the total excess enthalpy, *i.e.*, van der Waals ($\tilde{H}^{ex}_{vdW}$), hydrogen bonding ($\tilde{H}^{ex}_{hb}$), and electrostatic misfit ($\tilde{H}^{ex}_{mf}$) interactions. As shown, van der Waals contributions are consistently negligible or slightly positive, indicating weak or unfavorable dispersion interactions across all systems. In contrast, electrostatic interactions dominate enthalpic stabilization

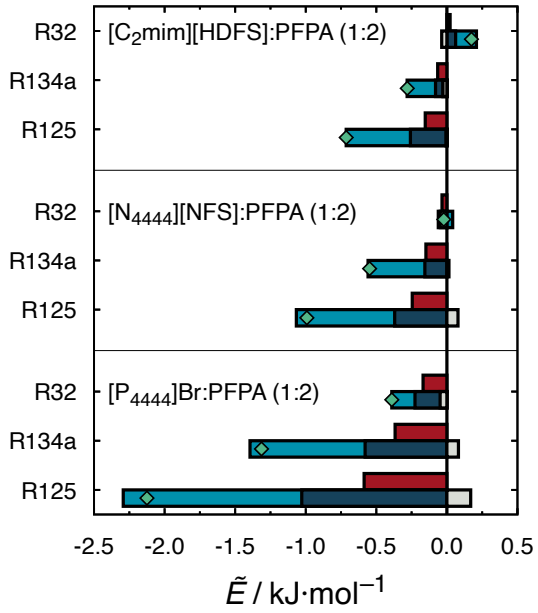

FIGURE 6.2: Excess Gibbs energy, $\tilde{G}^{ex}$ (■), and enthalpy, $\tilde{H}^{ex}$ (◆) for HFC + FES mixtures at 303.15 K and $x_{HFC} = 0.15$, obtained using COSMO-RS at the BP-TZVP parameterization. Detailed contributions to excess enthalpy, namely $\tilde{H}^{ex}_{vdW}$ (□), $\tilde{H}^{ex}_{hb}$ (■), and $\tilde{H}^{ex}_{mf}$ (■), are included.

in [C_2mim][HDFS]:PFPA (1:2) and [N_{4444}][NFS]:PFPA (1:2) for all studied HFCs. This effect is less pronounced in [P_{4444}]Br:PFPA (1:2), where hydrogen bonding is more relevant. Overall, these results highlight the importance of electrostatic interactions in the studied solvents, with hydrogen bonding providing better affinities between HFCs and [P_{4444}]Br:PFPA (1:2). This is especially marked for R125, whose single hydrogen atom creates a highly localized HBD ($\sigma < 0$) region with a strong affinity toward the bromide-containing solvent.

6.3.2. Thermodynamic and transport properties assessed from COSMO-RS and MD simulations

To validate the feasibility of COSMO-RS and the implemented FFs in the description of the studied FESs, $\hat{\rho}^{L}$ and γ_{HBD} were computed. Results are presented in Figure 6.3 as a function of x_{HBA}, at 303.15 K and 1 bar. Compared with experimental data [203], the utilized FFs yield reliable liquid densities at all analyzed HBA:HBD mole ratios, only generating an appreciable deviation for [C_2mim][HDFS]:PFPA at its highest x_{HBA} value. Results for $\hat{\rho}^{L}$ at other temperatures, presented in Figure B.2 also yield good correspondence with available data.

Results for γ_{HBD} from MD simulations and COSMO-RS predictions are presented in Figure 6.3b. As can be seen, its depression at higher values of x_{HBA} agrees with the expected negative deviations from ideal solution behavior ($\gamma_{HBD} = 1$). Moreover, results between both approaches qualitatively

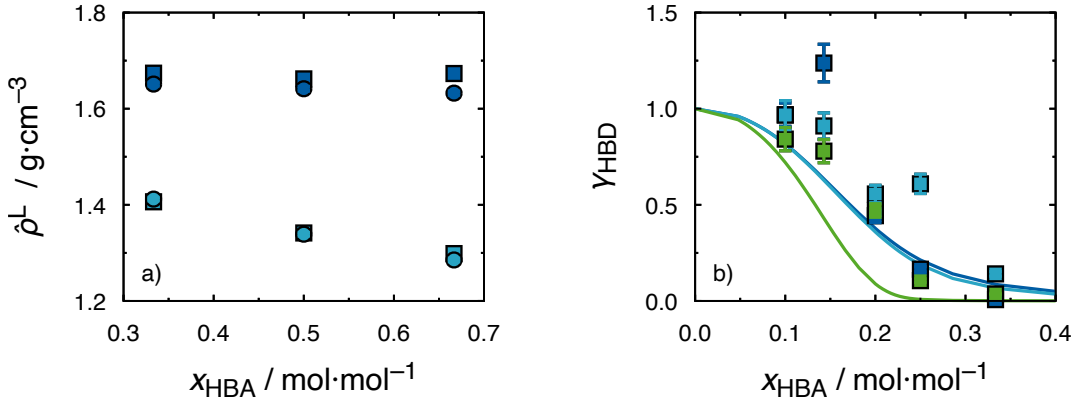

FIGURE 6.3: Liquid mass density, $\hat{\rho}^{L}$, (a) and activity coefficient of PFPA, γ_{HBD}, (b) in [C_2mim][HDFS]:PFPA (—), [N_{4444}][NFS]:PFPA (—), and [P_{4444}]Br:PFPA (—) at 303.15 K, 1 bar, and different liquid mole fractions of HBA, x_{HBA}. Results from COSMO-RS (—) and MD simulations (□) are shown and compared with available experimental data (○) [203]. Error bars are included for MD simulations results.

agree, showing a more pronounced decay of γ_{HBD} for [P_{4444}]Br:PFPA. This strong non-ideality suggests a significant depression of the melting point with respect to the pure HBD, consistent with the formation of a stable liquid at the studied composition, as typically observed in eutectic systems. For MD simulations results, γ_{HBD} show a less reliable behavior when approaching to the pure HBD, even showing positive deviations from ideality. This was associated to the increasing module of the error in the computation of μ^{ex}_{HBD}, where an increase in the size of the system may be necessary to get more consistent results.

Overall, the combined evidence from COSMO-RS and MD supports that all three mixtures should remain liquid at the experimentally available HBA:HBD ratio of 1:2. This includes [P_{4444}]Br:PFPA, for which experimental validation is not yet available. Considering this, along with a reliable modeling of liquid density, the prediction of HFC absorption was assessed using a fixed mole HBA:HBD ratio of 1:2 for all considered FESs.

Figure 6.4 presents the results for effective Henry's constants, K^{eff}_{H}, and solubility isotherms for R32, R134a, and R125 in the studied FESs. COSMO-RS results for K^{eff}_{H} show good agreement with available experimental data [203] for [C_2mim][HDFS]:PFPA (1:2) and [N_{4444}][NFS]:PFPA (1:2), confirming that its predictive features [235] are well fit for the studied systems. In all cases, R32 exhibits the highest K^{eff}_{H} values, and thus the lowest solubilities at diluted conditions, consistent with above results regarding its lower affinity for the studied FESs. For the screened solvent, [P_{4444}]Br:PFPA (1:2), COSMO-RS predicts significatively lower K^{eff}_{H} values for all studied HFCs, and thus higher solubilities at diluted conditions. This is more clearly shown in the computed solubility isotherms, where this solvent develops the highest HFC absorption through all the analyzed concentration range, consistently with the analyzed excess properties in Figure 6.2. Moreover, comparison with experimental data [203] yields good agreement with solubility isotherms of [C_2mim][HDFS]:PFPA

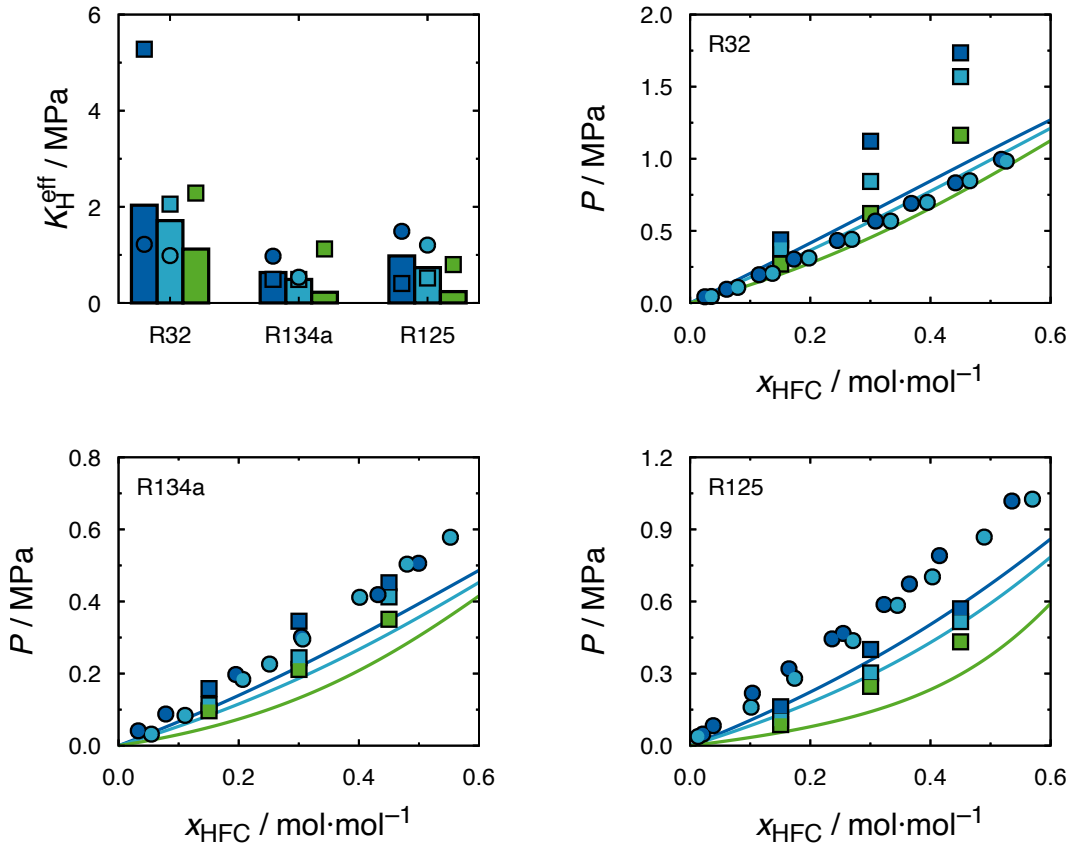

FIGURE 6.4: Effective Henry's constants, K_H^{eff}, and solubility isotherms for different HFCs in [C_2mim][HDFS]:PFPA (1:2) (—), [N_{4444}][NFS]:PFPA (1:2) (—), and [P_{4444}]Br:PFPA (1:2) (—) at 303.15 K. Results from COSMO-RS at the BP-TZVP parameterization (■ , —) and MD simulations (□) are shown and compared with available experimental data [203] (○).

(1:2) and [N_{4444}][NFS]:PFPA (1:2). Larger deviations are observed at higher values of liquid HFC mole fraction, x_{HFC}, consistently with the limitations of COSMO-RS at non-diluted conditions. These deviations are more pronounced for R125, suggesting that its affinity for the solvents, although reasonably predicted at lower x_{HFC} values, is overestimated at higher HFC concentration. Still, COSMO-RS reproduces the reported solubility trends with satisfactory accuracy, supporting its use in the screening and design of fluorinated solvents for HFC absorption.

K_H^{eff} values computed from MD simulations agree with COSMO-RS predictions for R134a and R125 in [C_2mim][HDFS]:PFPA (1:2) and [N_{4444}][NFS]:PFPA (1:2). However, an opposed behavior is observed for [P_{4444}]Br:PFPA (1:2), where all HFCs show similar or higher K_H^{eff} values, relative to the other two FESs. Additionally, K_H^{eff} for R32 in [C_2mim][HDFS]:PFPA (1:2) is clearly overpredicted, reflecting its underestimated solubility shown in Figure 6.4. Although [N_{4444}][NFS]:PFPA (1:2)

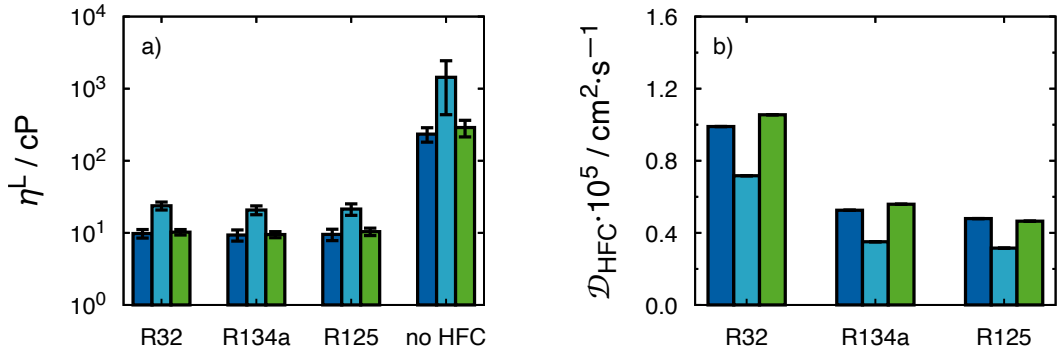

FIGURE 6.5: Shear liquid viscosity, η^L, (a) and HFC diffusivity, $\mathcal{D}_{HFC}$, (b) for HFC + FES mixtures, computed from MD simulations at 303.15 K and $x_{HFC} = 0.45$ for [C_2mim][HDFS]:PFPA (1:2) ( ), [N_{4444}][NFS]:PFPA (1:2) ( ), and [P_{4444}]Br:PFPA (1:2) ( ).

presents a comparable overestimation, this deviation is less pronounced due to its less steep solubility at lower x_{HFC} values, obtained from the fitting of the computed solubilities. Higher agreement with experimental data [203] is observed for solubility isotherms of R134a and R125.

Despite the observed deviations, MD simulations results reproduce the qualitative behavior of experimental data for [C_2mim][HDFS]:PFPA (1:2) and [N_{4444}][NFS]:PFPA (1:2), displaying similar solubilities for all HFCs in them. Consistent with COSMO-RS, HFC solubilities in [P_{4444}]Br:PFPA (1:2) are invariably enhanced in all cases, most notoriously for R32. These results suggest that the employed molecular mechanics models are feasible to study these systems in deeper detail, particularly regarding the interactions governing HFC solvation. This allows for a qualitative comparison among the three considered FESs, aligned with previous observations that solubility trends of F-gases in ionic solvents can be assessed from a qualitative standpoint using MD simulations [56]. Numerical values of saturation pressures computed from MD simulations are presented in Table 6.3.

Figure 6.5 presents results for η^L and $\mathcal{D}_{HFC}$ from MD simulations. In the absence of HFC absorption, [N_{4444}][NFS]:PFPA (1:2) displays the highest viscosities from the three considered FESs, surpassing η^L values of 1000 cP. In the case of [C_2mim][HDFS]:PFPA (1:2) and [P_{4444}]Br:PFPA (1:2), both solvents show nearly equal viscosities within the estimated error. However, at concentrations of $x_{HFC} = 0.45$, MD simulations predict a sharp decrease in η^L, reaching roughly 10 cP for all FESs. This decrease is proportional to pure solvent viscosities, proven by the generally higher viscosities in the HFC + [N_{4444}][NFS]:PFPA (1:2) system. On the other hand, $\mathcal{D}_{R32}$ yields higher values for all FESs compared to R134a and R125, as expected from its lesser steric impediments. This generally agrees with results for η^L, where a higher viscosity is related to a lower diffusion of solute within the estimated uncertainty. As the considered molecular mechanics models yield qualitative results

TABLE 6.3: Saturation pressures (in MPa), computed from MD simulations at 303.15 K, for the different studied HFC + FES mixtures.[a]

	[C_2mim][HDFS]:PFPA (1:2)	[N_{4444}][NFS]:PFPA (1:2)	[P_{4444}]Br:PFPA (1:2)
		$x_{HFC} = 0.15$	
R32	0.437(8)	0.376(6)	0.270(4)
R134a	0.158(4)	0.113(2)	0.096(2)
R125	0.162(4)	0.107(3)	0.088(2)
		$x_{HFC} = 0.30$	
R32	1.21(2)	0.84(1)	0.620(9)
R134a	0.345(8)	0.244(5)	0.211(5)
R125	0.40(1)	0.303(7)	0.247(6)
		$x_{HFC} = 0.45$	
R32	1.73(3)	1.56(3)	1.16(2)
R134a	0.45(1)	0.412(9)	0.351(7)
R125	0.57(1)	0.52(1)	0.432(9)

[a]The values in parenthesis denote the accuracy of the last decimal, *i.e.*, 0.437(8) denotes 0.437±0.008.

for these systems, it is expected that the obtained insights may guide the design of separation processes utilizing the studied FESs. Particularly, the use of [N_{4444}][NFS]:PFPA (1:2) for the capture of HFCs seem restrictive, due to its higher viscosity in comparison with the studied alternatives.

6.3.3. Molecular insights from MD simulations

To analyze the solvation of HFCs in the different FESs, molecular insights were obtained from MD simulations at 303.15 K, $x_{HFC} = 0.45$, and the corresponding saturation pressures from solubility calculations. Results are presented in Figure 6.6, where COM–COM RDFs between HFCs and ionic components of the FESs are shown. Moreover, Figure 6.6 also presents COM–COM self-RDFs for HFCs in the liquid phase. As can be seen, [N_{4444}][NFS]:PFPA (1:2) and [C_2mim][HDFS]:PFPA (1:2) exhibit similar solvation behavior, with comparable first peaks in their HFC–anion RDFs. Likewise, [P_{4444}]Br:PFPA (1:2) and [N_{4444}][NFS]:PFPA (1:2) show analogous HFC–cation RDFs, with first peaks appearing closely after those of their corresponding anions. In contrast, the [C_2mim]$^+$ cation displays a wide first peak, appearing along with the first peak of the HFC–HFC RDF and extending beyond the first solvation shell of other components, thus suggesting a delocalized HFC-[C_2mim]$^+$ interaction.

As observed from the HFC-HFC RDFs, marked peaks before distances of 0.5 nm suggest the formation of HFC clusters in the liquid phase, which are slightly more marked for R32. Said interactions

show to be more correlated than the interactions between HFCs and the ionic species from the FESs, as seen from the less marked first peaks in the HFC–[X] RDFs. However, this is not the case for the HFC–Br^- RDFs, which show a highly localized interaction between both molecules, surpassing the maximum value observed for the HFC–HFC RDFs. This is more marked for R32, and suggests that Br^- disturbs the formation of HFC clusters in the liquid phase, enhancing solute–solvent interactions and thus their solubility. This can be directly attributed to the smaller size of this anion, compared to the bulkier structures of $[NFS]^-$ and $[HDFS]^-$, which allows closer interactions with the hydrogen atoms of the HFCs without steric impediments. Accordingly, results also show that $[P_{4444}]$Br:PFPA (1:2) slightly weakens the HFC–HFC correlation, as evidenced by the slightly lower first peak of their RDFs.

For R134a, the above behavior is less marked than for R32 and R125. As shown in Figure 6.6, the first peak of the R134a–Br^- RDF is only moderately more prominent than the rest of components, and also less marked than the first peak of the R134a–R134a RDF. This shows an opposed behavior than the R32– and R125–Br^- RDFs, suggesting that the Br^- anion yields a less important interaction with R134a when compared to R32. This can be explained purely on the chemical structure of R134a, where both the presence of steric effects, due to the CF_3 group, and two hydrogen atoms, able to interact with Br^-, hinder the solvation mechanism of $[P_{4444}]$Br:PFPA (1:2). Although R134a and R125 are structurally similar, a sharper first peak in the R125–Br^- RDF is observed, suggesting a more localized interaction analogously to R32. This agrees with the presence of a single hydrogen atom in R125, allowing for a higher affinity with the Br^- anion, as also concluded from Figure 6.2. Moreover, this cluster disruption is achieved to a lesser extent than for R32, highlighting the presence of steric impediments in R125 in a similar way than for R134a.

To further understand the degree of localization of the different molecular interactions, SDFs were also computed. Considering that $[C_2mim]$[HDFS]:PFPA (1:2) and $[N_{4444}]$[NFS]:PFPA (1:2) display similar solubilities and correlation functions for all analyzed HFCs, only the results for the former FES, along with $[P_{4444}]$Br:PFPA (1:2), are herein presented. This is also justified in the higher viscosities predicted for $[N_{4444}]$[NFS]:PFPA (1:2), which make this FES a less desirable solvent for HFC absorption. Results for SDFs are shown in Figure 6.7, where SDFs for cations, anions, PFPA and HFC are compared within each selected FES. At first glance, a clear distinction is observed in the loci where the cation, anion and PFPA exert their influence on the HFCs. As can be seen, HFC–cation interactions are invariably set toward the more fluorinated zone of the solute. Oppositely, both anions and PFPA orient toward the hydrogen atoms of the HFC. This is an expected behavior, given the strong Coulomb interactions arising from the higher charge difference between the anion's functional groups and the hydrogen atoms in the HFC. Moreover, SDFs suggest that electrostatic interactions between anions and PFPA produce a similar locus of solvation. Additionally, PFPA only acts at higher distances from the HFCs when compared with both anions. This suggests that, compared to the ionic components of the FESs, the PFPA contributes more as a solvent environment than in the direct solubilization of HFCs.

From R32–R32 SDFs, a clear distinction is seen between both FESs. For $[C_2mim]$[HDFS]:PFPA (1:2), the R32–$[HDFS]^-$ SDF clearly positions at a higher distance from the COM of the HFC, compared to the R32–R32 SDF. Thus, a marked R32 clustering is observed between the R32 molecule and the rest of SDFs, suggesting a hindered interaction with the components of the FES. On the other

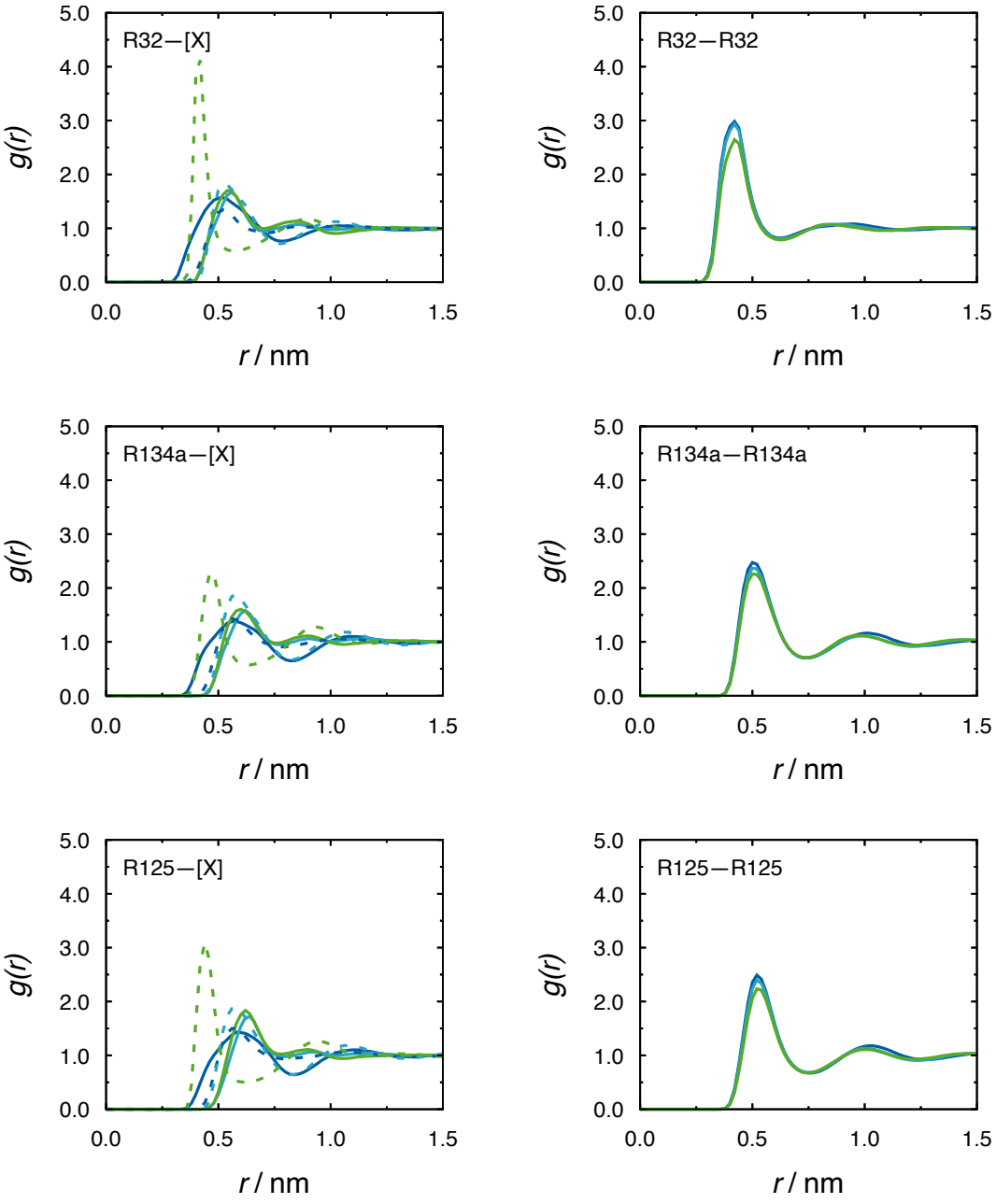

FIGURE 6.6: COM-COM RDFs, g, of HFCs in HFC + FES mixtures, computed from MD simulations at 303.15 K, $x_{\mathrm{HFC}} = 0.45$, and the corresponding saturation pressure. Results shown for [C_2mim][HDFS]:PFPA (1:2) (—), [N_{4444}][NFS]:PFPA (1:2) (—), and [P_{4444}]Br:PFPA (1:2) (—). Functions for cations (—) and anions (- - -) are displayed for HFC-[X] systems.

hand, for [P_{4444}]Br:PFPA (1:2), a different behavior is shown. In this case, the R32–Br^- SDF forms at a closer distance from the HFC molecule, weakening the R32–R32 SDF. Again, this confirms that Br^- is able to penetrate more closely into the solvation environment of the HFC, disturbing the formation of R32 clusters. Considering that R32 solubilities for this FES were the highest, results suggest that a more localized Coulomb interaction, achieved through less voluminous anions, can enhance its solubility.

The same effect of the Br^- anion regarding cluster interruption is observed for R134a and R125. However, this effect shows little impact in the solubilities of these HFCs in [P_{4444}]Br:PFPA (1:2), as presented in Figure 6.4. In this regard, steric hindrance, due to the presence of two fluoroalkyl groups in the solute, may hinder the interactions with the solvent, even when HFC clustering is interrupted by the Br^- anion. Thus, results suggest that the formation of R134a and R125 clusters in the liquid phase is not as detrimental for solubility as for R32. Moreover, SDFs of these HFCs with cations and PFPA are slightly more marked in the case of [C_2mim][HDFS]:PFPA (1:2), suggesting the role of structure and free volume in the liquid phase in the absorption of R134a and R125. Indeed, the atomic structure of the Br^- anion hinders the occurrence of van der Waals interactions with the FES, which has shown to be an important part in the general solvation mechanism of F-gases [56].

The importance of energetic interactions in the solvation of HFCs was further assessed by an interaction energy analysis. Results are shown in Figure 6.8. Here, Lennard-Jones interaction energies correlate well with the predicted solubility trends, showing similar values between R134a and R125, and less negative values for R32. Furthermore, [P_{4444}]Br:PFPA (1:2) consistently displays more positive Lennard-Jones interactions, suggesting hindered interactions with the HFCs. Its lower free volume, due to its lack of a voluminous anion, can be seen as a counter effect for its capability of strong directional interactions. Thus, this lack of structure within the liquid phase may offset the enhanced interactions from the Br^- anion, specially in fluorinated ethanes such as R134a and R125, where said interactions contribute less to the overall internal energy. Moreover, the fact that R32 interacts more strongly with polar regions of the solvent agrees with previously reported observations in other ILs [218]. This also suggests that a better treatment of charges in the molecular mechanics model for the HBAs, such as polarizable models [236], would enhance solubility predictions for this HFC.

Finally, to study HFC–anion interactions in deeper detail, normalized ADDs were computed for the HFC–anion pairs in [C_2mim][HDFS]:PFPA (1:2) and [P_{4444}]Br:PFPA (1:2). To select the involved atoms in the analysis, it was assumed that they acted through a similar interaction than that of hydrogen bonding. Thus, hydrogen donor and acceptor atoms, D and A, respectively, were defined for each HFC–anion pair, defining the D–A distance, $r_{D–A}$, and the H–D–A angle, $\theta_{H–D–A}$. For R32, D was defined as the central carbon atom, while for R134a and R125 the carbon atom containing hydrogen was selected, labeling it in both cases as C1. The acceptor atom, A, was defined as one of the oxygen atoms of the SO_3 functional group of the $[HDFS]^-$ anion, O1, or as Br^-, depending on the case. Results are presented in Figure 6.9, where the hydrogen atom involved in the interaction, H1, represents any of the hydrogen atoms present in the HFC.

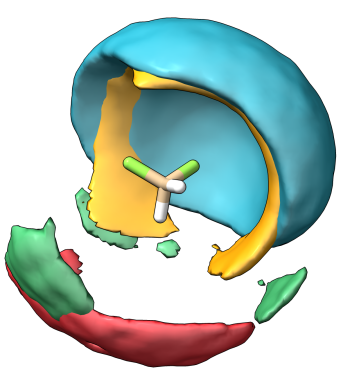

R32 + [C_2mim][HDFS]:PFPA (1:2)

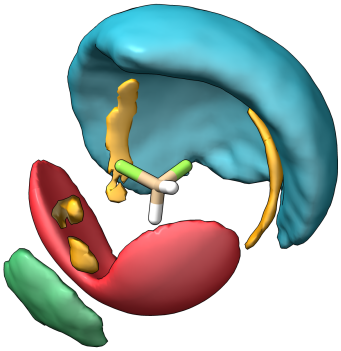

R32 + [P_{4444}]Br:PFPA (1:2)

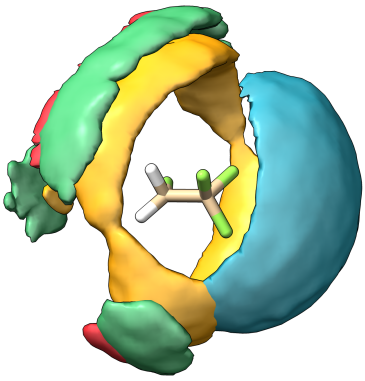

R134a + [C_2mim][HDFS]:PFPA (1:2)

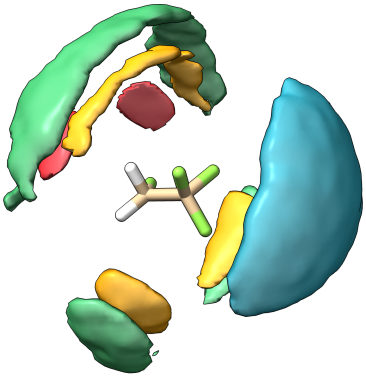

R134a + [P_{4444}]Br:PFPA (1:2)

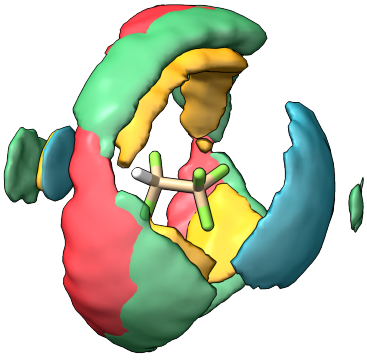

R125 + [C_2mim][HDFS]:PFPA (1:2)

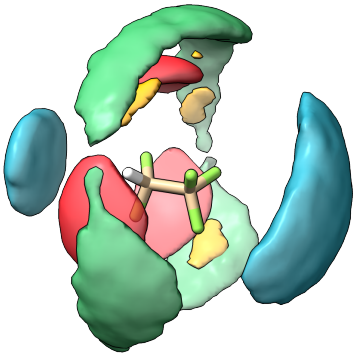

R125 + [P_{4444}]Br:PFPA (1:2)

FIGURE 6.7: SDFs of HFCs in HFC + FES mixtures, computed from MD simulations at 303.15 K, $x_{HFC} = 0.45$, and the corresponding saturation pressure. Functions between HFC and cations ( ), anions ( ), PFPA ( ), and HFC ( ) are shown.

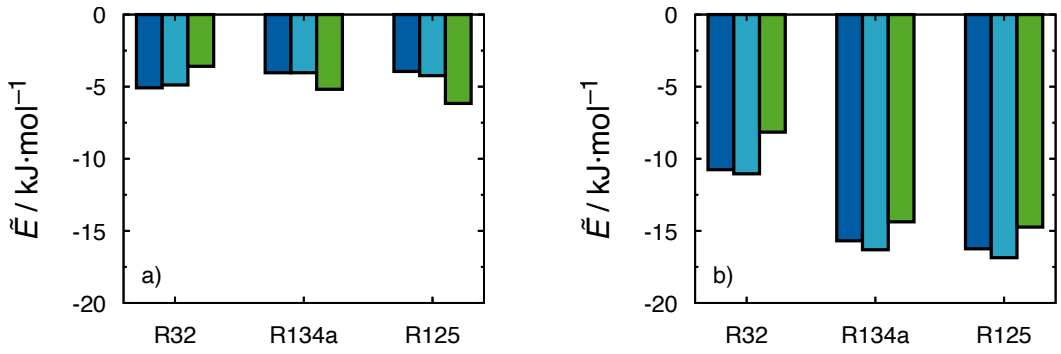

FIGURE 6.8: Coulomb (a) and Lennard-Jones (b) interaction energies for HFC + FES mixtures, computed from MD simulations at 303.15 K, $x_{HFC} = 0.45$, and the corresponding saturation pressure. Results shown for [C_2mim][HDFS]:PFPA (1:2) ( ), [N_{4444}][NFS]:PFPA (1:2) ( ), and [P_{4444}]Br:PFPA (1:2) ( ).

For all HFCs, ADDs are characterized by a strongly localized probability region, ranging between 0.3 nm and 0.4 nm for $r_{C1–O1}$. Interactions with the [HDFS]$^-$ anion are less centered than for Br$^-$, as seen by a generally homogeneous ADD at a wide portion of the considered space. Moreover, HFC–[HDFS]$^-$ ADDs are characterized by a marked probability at $r_{C1–O1} \approx 0.6$ nm, associated to the other two oxygen atoms in the SO_3 functional group. ADDs for R134a show a generally higher homogeneity than for R32, given the presence of steric effects that prohibit both anions to access the hydrogen atoms of R134a from a narrower variety of angles and distances. For R125, ADDs present considerable probabilities at more constrained distance–angle combinations, compared to R32 and R134a. This is due to its single hydrogen atom, which restricts its directional interaction with the anions to a smaller set of the considered space. It is worth noting that the HFC–[HDFS]$^-$ ADD does not meet the common hydrogen bonding criteria of distances and angles [237], *i.e.*, $r_{D–A} < 0.35$ nm and $\theta_{H–D–A} < 30°$. Thus, according to MD simulations results, hydrogen bonding can be discarded as part of the solvation mechanism of HFCs in this FES.

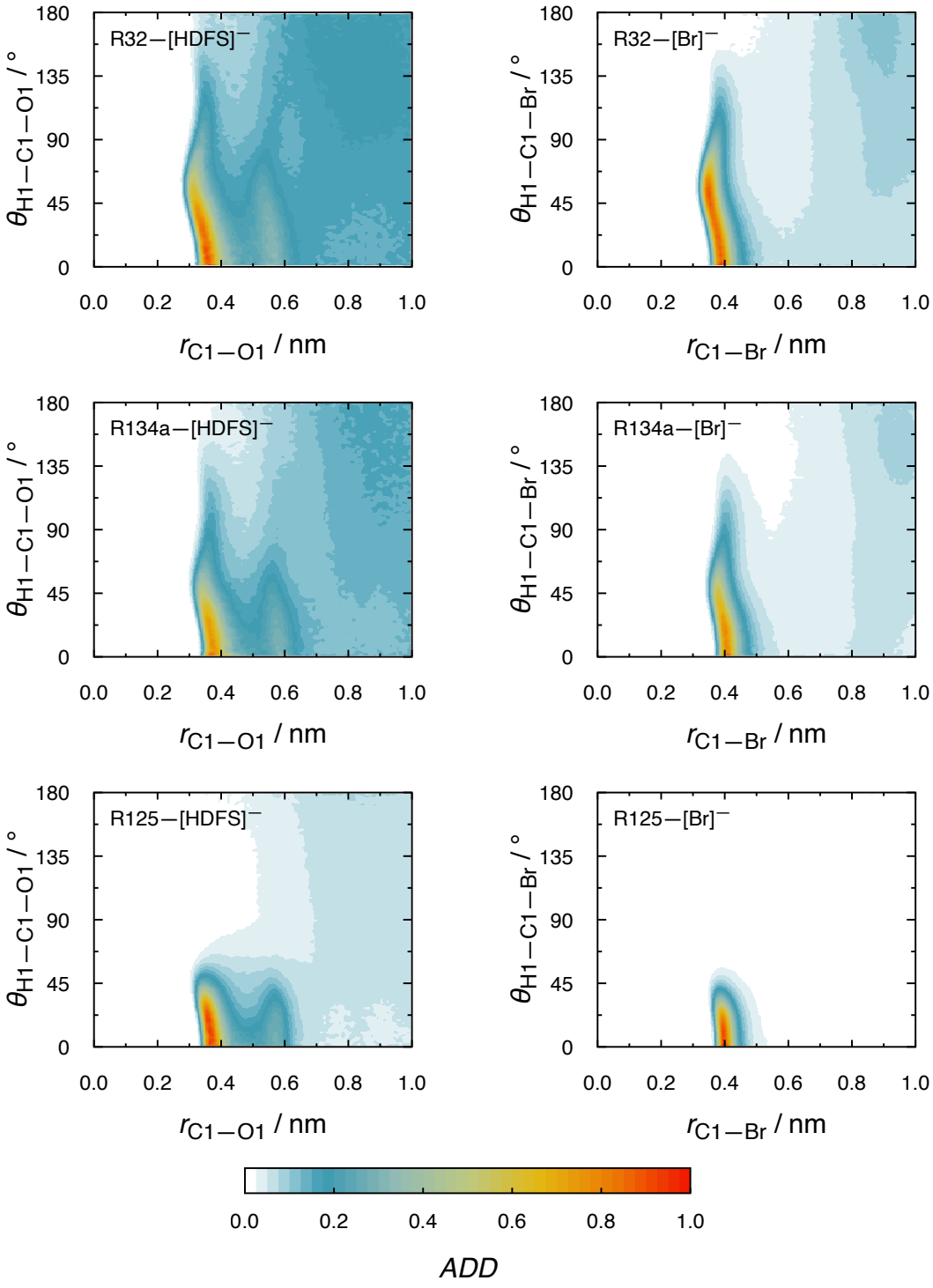

FIGURE 6.9: Normalized ADDs of HFCs in HFC + FES mixtures, computed from MD simulations at 303.15 K, $x_{\mathrm{HFC}} = 0.45$, and the corresponding saturation pressure.

6.4. Conclusions

COSMO-RS and MD simulations were employed to investigate the absorption of HFCs in three FESs: [C_2mim][HDFS]:PFPA, [N_{4444}][NFS]:PFPA, and [P_{4444}]Br:PFPA. First, the thermophysical behavior of these solvents was assessed by computing the PFPA activity coefficient in each solvent using both approaches. In all cases, strong negative deviations from ideal solution behavior were observed, suggesting significant melting point depressions relative to their precursors. These findings agree with previous data for [C_2mim][HDFS]:PFPA and [N_{4444}][NFS]:PFPA, and further suggest a similar behavior for [P_{4444}]Br:PFPA, for which no experimental validation is yet available.

Following this validation, the solubility of R32, R134a, and R125 in the considered FESs was computed and compared with available experimental data. COSMO-RS yield reliable results in the computation of solubility isotherms for the selected systems, despite its common limitations associated with non-diluted mixtures. For MD simulations, deviations from trends in Henry's constants were observed, and solubility of R32 was underestimated. However, the reproduced trends of solubility isotherms for all considered HFCs showed a qualitative agreement within all studied approaches, suggesting that R32, R134a, and R125 exhibit increased solubility in [P_{4444}]Br:PFPA (1:2). MD simulations were also performed to compute HFC diffusivity and viscosity of the FESs. Results regarded [N_{4444}][NFS]:PFPA (1:2) as the least feasible solvent for its use as an absorber medium, due to its high viscosities and lower HFC diffusivities.

To explain the observed trends in solubilities from MD simulations, molecular insights were obtained from radial and spatial distribution functions, and complemented by an interaction energy analysis. HFC–Br^- interactions were the most prominent, showing stronger correlations than HFC–HFC distribution functions. These interactions were related to the feature of Br^- disrupting the formation of HFC clusters in the liquid phase, which may be a contributing factor in enhancing its solubility. The aforementioned behavior was observed for R32, but showed a less marked effect on R134a and R125, related to the lower free volume and structured liquid phase of [P_{4444}]Br:PFPA, given by its non-voluminous anion compared to [C_2mim][HDFS]:PFPA and [N_{4444}][NFS]:PFPA. Results from this analysis suggest the importance of localized interactions in the solubility of fluorinated methanes, along with the need for free volume and cavities in the solvent in the case of fluorinated ethanes.

7. Selective Recovery of Fluorinated Gases from Commercial Refrigerants Using Phosphonium-Based Ionic Liquids

In this chapter, the absorption of six F-gases in three quaternary phosphonium-based ILs is studied for the first time using the soft-SAFT EoS. COSMO-RS is employed to analyze charge distributions and guide the description of cation–anion association within the SAFT framework. The resulting model is used to assess solubilities and predict Henry's constants, enthalpy of dissolution, and ideal and competitive selectivities. Competitive absorption from four commercial refrigerant blends is further assessed over a range of temperatures and pressures. Among the examined ILs, [$P_{666,14}$][TMPP] shows potential as an entrainer for R410A, whereas [$P_{666,14}$]Cl provides a viable separation route for the R451A blend.[*]

7.1. Introduction

Although quaternary phosphonium-based ionic liquids (PILs) remain less explored as other structurally tailored IL families, they exhibit a significant potential as entrainers for the separation of HFC-based blends. Besides their high thermal stability compared to their ammonium- and imidazolium- based counterparts [199, 238], PILs can be tailored to develop, compared to other ILs, lower regeneration energy, high gas solubilities, and lower viscosities [239]. These properties have propelled their use as gas absorbents and entrainers [200], making PILs a considerable alternative in the phase-out of refrigerant blends. Moreover, the use of PIL-based DESs in extraction and absorption processes [204, 208] suggests an unexplored potential in the design of novel DESs.

[*]This chapter is adapted with permission from:
B. González-Barramuño, H. Quinteros-Lama, J.M. Garrido, F. Llovell, and S.B. Rodriguez-Reartes, "Selective Recovery of Fluorinated Gases from Commercial Refrigerants Using Phosphonium-Based Ionic Liquids", Industrial & Engineering Chemistry Research (2026). Copyright 2026 American Chemical Society

Indeed, the potential of PILs as entrainers for refrigerant blends has been experimentally assessed in the literature. Baca et al. [240] studied the separation of the R410A blend using various ILs, regarding trihexyl(tetradecyl)phosphonium chloride ([$P_{666,14}$]Cl) as a promising candidate. Further experimental assessments have shown the potential of this same PIL [201] and of trihexyl(tetradecyl)phosphonium bis(2,4,4-trimethylpentyl)phosphinate ([$P_{666,14}$][TMPP]) [241, 242] in the absorption of HFCs and HFOs and the separation of their blends.

In order to reduce experimental efforts in the characterization of PILs, different theoretical approaches have been employed in the literature. In a variety of contributions, experimental studies have been complemented with DFT calculations to predict intermolecular interactions and molecular geometries [243, 244]. On the other hand, COSMO-RS has been used as a screening tool for the solubilization of F-gases using PILs. In this regard, Sosa et al. [235] assessed trihexyl(tetradecyl)phosphonium glycinate ([$P_{666,14}$][GLY]) with notable absorption capabilities of R32 and R134a, compared to a wide variety of other screened ILs.

The numerical and versatile advantages of SAFT-based EoSs have been used in the study of PILs. The PC-SAFT EoS [141] has been used to describe the solubility of CO_2 in some of these ILs [245, 246]. Moreover, the electrolytic extension of this model, the ePC-SAFT EoS [247, 248], has been used to study PILs based on the trihexyl(tetradecyl)phosphonium cation ([$P_{666,14}$]$^+$) [249]. In this regard, the soft-SAFT EoS stands out in its consistent use in the assessment of HFC absorption in ILs [44]. Despite having been used to study the absorption of CO_2 and SO_2 in PILs [250, 251], this EoS haven't been implemented to asses the absorption F-gases in these solvents.

To assess the capabilities of PILs as selective solvents for F-gases, the development of EoS models for the design of extractive processes is a key step. The complex chemical structures in these systems mandate a holistic approach, in order to capture key physical information that can be translated to reliable thermophysical properties. Particularly, previous work applying soft-SAFT models to PILs develops a combined strategy with COSMO-RS [250, 251], allowing the transfer of detailed chemical interactions to simplified coarse grained models. In this chapter, new soft-SAFT molecular models for [$P_{666,14}$]Cl, [$P_{666,14}$][GLY], and [$P_{666,14}$][TMPP] are generated. Since these PILs are modeled for the first time using the soft-SAFT EoS, a quantum chemical modeling method based on DFT calculations is used as a complementary tool to optimize association parameters. [$P_{666,14}$]Cl was considered as a benchmark for comparison purposes, using the molecular parameters fit from previous work [250]. Following this parameterization, the solubility of HFCs and HFOs is assessed from binary and ternary mixtures, finally examining their performance to separate commercial refrigerant blends.

7.2. Molecular modeling

The absorption of HFCs and HFOs in [$P_{666,14}$]Cl, [$P_{666,14}$][GLY], and [$P_{666,14}$][TMPP] was assessed using the soft-SAFT EoS. The chemical structures of the studied PILs are presented in Table 7.1.

TABLE 7.1: Molecular structures of the species conforming the studied PILs.

Name	Structure	Abbreviation
trihexyl(tetradecyl)phosphonium	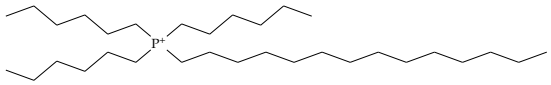	$[P_{666,14}]^+$
glycinate	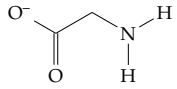	$[GLY]^-$
bis(2,4,4-trimethylpentyl)phosphinate	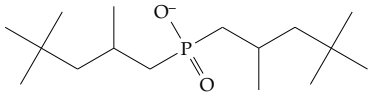	$[TMPP]^-$

7.2.1. Procedure to define soft-SAFT molecular models for PILs

To generate proper molecular parameters for the studied PILs, first a specific association scheme and chemical association parameters must be defined from a coherent approach. The association schemes for $[P_{666,14}][GLY]$ and $[P_{666,14}][TMPP]$ were determined using COSMO-RS [81]. For this purpose, the COSMOTherm package [84] with the BP-TZVP parameterization was used to optimize the molecular structures and generate the corresponding $p_S(\sigma)$.

Figure 7.1 presents the $p_S(\sigma)$ for the cation and anion in each analyzed PIL. As can be seen, the $[P_{666,14}]^+$ cation is characterized by a wide charge distribution around the $\sigma = 0$ region. This suggest that most of the molecule's surface is neutrally charged, something expected given the large presence of alkyl chains in its structure. Moreover, a subtle peak, extending into the $\sigma < 0$ region, indicates a trend toward a positive net charge, caused by a localized charge around the P atom. The computed $p_S(\sigma)$ agrees with previously published results for $[P_{666,14}]Cl$ [250]. On the other hand, all considered anions show a clear charge population in the $\sigma > 0$ region. Cl^- develops a highly localized peak, characteristic of monoatomic species. As for $[GLY]^-$ and $[TMPP]^-$ anions, wide peaks extend through the $\sigma > 0$ region, showing charge delocalization in the IL. $[TMPP]^-$ concentrates an important part of its charge distribution around neutral values of σ, meaning that part of this species does not contribute to the cation–anion interaction.

Considering the above, $[P_{666,14}][GLY]$ and $[P_{666,14}][TMPP]$ were modeled with two association sites, D and N. The former is dual-like site, also present in the model of $[P_{666,14}]Cl$, and represents the main cation–anion interactions. The latter site is added to account for the negative charge delocalization. Within the deifned association scheme, D–D and D–N interactions are allowed, while N–N interactions are forbidden, *i.e.*, $\Delta^{D_iD_i} \neq 0$, $\Delta^{D_iN_i} \neq 0$, and $\Delta^{N_iN_i} = 0$. Moreover, D and N are assumed to have the same association energy and volume, reflecting that electronic density is delocalized across all sites.

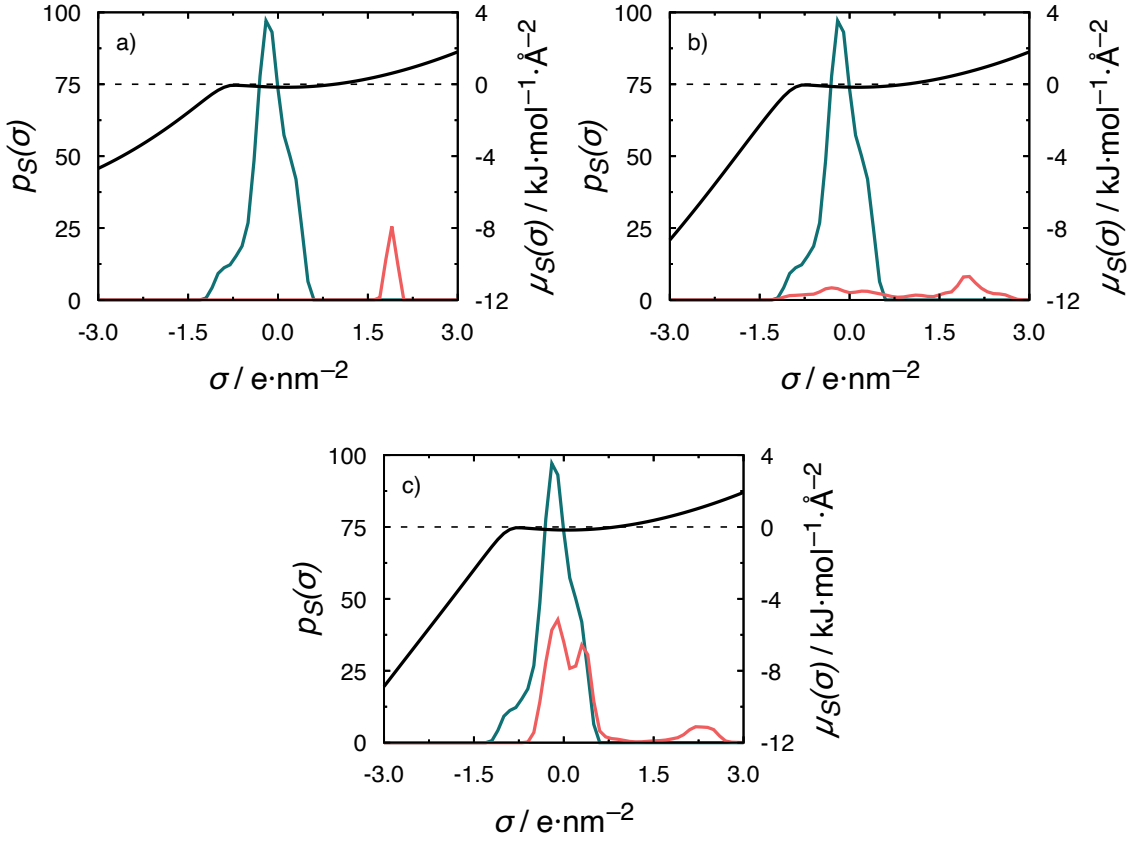

FIGURE 7.1: σ-profiles, $p_S(\sigma)$, (left axis) and σ-potentials, $\mu_S(\sigma)$, at 303.15 K (—, right axis) obtained using COSMO-RS at the BP-TZVP parameterization, for $[P_{666,14}]Cl$ (a), $[P_{666,14}][GLY]$ (b) and $[P_{666,14}][TMPP]$ (c). Profiles for the $[P_{666,14}]^+$ cation (—) and the respective anions (—) are shown. The $y = 0$ line is included in the secondary axis (- - -) for guiding purposes.

The values for association energy, $\varepsilon^{A_iB_i}$, and volume, $\kappa^{A_iB_i}$, for $[P_{666,14}][GLY]$ and $[P_{666,14}][TMPP]$ were elucidated following a previously defined methodology [250], selected to reduce the number of adjustable parameters while keeping the physical significance of the model. Thus, DFT-D3 [252] calculations were done for each PIL at the B3LYP/def2-TZVP level of theory using the ORCA software [253]. First, a geometry optimization was performed for all ionic species to obtain their minimum energy conformation. Subsequently, each PIL was obtaining by adding their two respective molecular structures and performing a second geometry optimization. In all cases, frequency calculations were performed to ensure that the true energy minima were reached. Additionally, to reduce the computational cost of the above calculations, the $[P_{666,14}]^+$ cation was replaced by $[P_{3333}]^+$, thus disregarding the effect of alkyl chain length in the computed association parameters.

Once the minimum energy chemical structures were obtained for each PIL, cation–anion interaction energy, E_{CA}, and distance, r_{CA}, were computed to respectively estimate $\varepsilon^{A_iB_i}$ and $\kappa^{A_iB_i}$. To

handle the basis set superposition error [254], E_{int} were obtained using the counterpoise correction [255] as shown in Eq.

$$E_{\text{CA}} = E_{\text{IL}}^{\text{IL}}(\text{IL}) - E_{\text{C}}^{\text{C}}(\text{C}) - E_{\text{A}}^{\text{A}}(\text{A}) - \left(E_{\text{C}}^{\text{IL}}(\text{IL}) - E_{\text{C}}^{\text{IL}}(\text{C}) + E_{\text{A}}^{\text{IL}}(\text{IL}) - E_{\text{A}}^{\text{IL}}(\text{A})\right), \tag{7.1}$$

where $E_{\text{X}}^{\text{Y}}(\text{Z})$ denotes the single-point energy of species X, evaluated at the optimized geometry Y, and using the Z basis set. Additionally, r_{CA}, was defined as the distance between the P atom in the $[\text{P}_{3333}]^+$ cation and the center of mass of the functional group of the anion. Once cation–anion interaction energy and distance was computed for each PIL, their respective $\varepsilon^{A_iB_i}$ and $\kappa^{A_iB_i}$ were obtained by linearly scaling the association parameters of $[\text{P}_{3333}]\text{Cl}$, assumed equal to those of $[\text{P}_{666,14}]\text{Cl}$, by the same E_{CA} and r_{CA} ratios.

soft-SAFT molecular models for HFCs and HFOs were directly transferred from previous contributions [229, 230]. For all F-gases, the dipole moment is mimicked by using two association sites, P and N, that interact with each other. Thus, for each F-gas molecule, a site of type N, of the same nature as the one defined in the PILs, and a site of type P are defined. Only N–P interactions are allowed, *i.e.*, $\Delta^{N_iP_i} \neq 0$ and $\Delta^{P_iP_i} = 0$.

7.3. Results and Discussion

7.3.1. Preliminary molecular insights from COSMO-RS

In addition to granting insights into association schemes, COSMO-RS was used as a screening tool to assess the nature of interactions between F-gases and the studied PILs. The σ-potential, $\mu_S(\sigma)$, for each solvent was computed at 303.15 K, and is included in Figure 7.1 besides $p_S(\sigma)$. In all cases, positive $\mu_S(\sigma)$ are obtained in the $\sigma > 1$ e·nm^{-2}, indicating low affinity for solutes with a hydrogen-bond acceptor character [234]. In the intermediate charge region, *i.e.*, -1 e·nm^{-2} $< \sigma <$ 1 e·nm^{-2}, all $\mu_S(\sigma)$ become slightly negative, suggesting a moderate affinity for apolar and hydrophobic solutes, attributable to the long alkyl chains of the $[\text{P}_{666,14}]^+$ cation. Finally, in the $\sigma <$ 1 e·nm^{-2} region, σ-potentials sharply drop to more negative values, with $[\text{P}_{666,14}]\text{Cl}$ showing the least pronounced decay. This suggests an increased affinity for hydrogen-bond donor solutes, particularly for $[\text{P}_{666,14}]$[GLY] and $[\text{P}_{666,14}]$[TMPP], due to the marked charge delocalization observed in their σ-profiles.

To assess the affinity of the studied F-gases in the above PILs, a similar analysis involving $p_S(\sigma)$ and $\mu_S(\sigma)$ was performed for selected HFCs and HFOs. Results are shown in Figure C.1, where all compounds exhibit a similar σ-profile, with prominent peaks in the central region and charge delocalization toward negative σ values. In addition, all F-gases display a negative $\mu_S(\sigma)$ in the apolar region, suggesting some affinity for apolar solvents. However, they generally show positive $\mu_S(\sigma)$ in both polar regions, implying weak interactions with solvents characterized by charge delocalization. Interestingly, R125 behaves differently: it exhibits a negative $\mu_S(\sigma)$ in the $\sigma > 1$ e·nm^{-2} region, indicating a favorable interaction with negatively delocalized solvents. This behavior may be attributed to its unique hydrogen atom, which enhances its ability to engage in specific hydrogen bonding interactions. Thus, although this hydrogen does not lead to a visible charge

TABLE 7.2: Cation–anion interaction energy, E_{CA}, and distances, r_{CA}, computed from DFT-D3 single-point calculations at the B3LYP/def2-TZVP level of theory, and soft-SAFT association parameters for the considered PILs.

PIL	E_{CA} [kcal·mol^{-1}]	r_{CA} [Å]	$\varepsilon^{A_iB_i}/k_B$ [K]	$\kappa^{A_iB_i}$ [Å^3]
[P_{3333}]Cl[a]	–93.426	3.374	3500	2000
[P_{3333}][GLY]	–94.552	3.415	3500	2000
[P_{3333}][TMPP]	–96.577	3.688	3600	2200

[a] Association parameters taken from [250]

delocalization in its $p_S(\sigma)$, it may still play a significant role in shaping the molecule's interaction profile with solvents.

7.3.2. Fit of soft-SAFT molecular models for PILs

Association parameters obtained from DFT calculations are presented in Table 7.2. As similar cation–anion interaction energies and distances were obtained for all PILs, their corresponding $\varepsilon^{A_iB_i}/k_B$ and $\kappa^{A_iB_i}$ do not deviate from the reference values of [P_{3333}]Cl. Only E_{CA} for [P_{3333}][TMPP] presents a notably higher value, which can be attributed to steric effects from the larger structure of the [TMPP]$^-$ anion.

Once the association scheme and parameters were defined for each PIL, non-associating parameters were fit to available liquid density data, as typically done with ILs [256]. The soft-SAFT parameters for all studied PILs are presented in Table 7.3. As shown in Figure 7.2, the employed parameterization for [$P_{666,14}$][GLY] and [$P_{666,14}$][TMPP] results in an acceptable description of their liquid densities, obtaining average absolute deviations (AADs) of 0.23% and 0.77%, respectively. Moreover, the considered F-gases were selected based on the availability of experimental solubility data, and are also included in Table 7.3.

7.3.3. HFC and HFO solubility in PILs assessed from the soft-SAFT EoS

The HFC and HFO absorption capacity of the considered PILs was modeled using the soft-SAFT EoS. Given the deviations from classic Lorentz-Berthelot mixing rules in the considered binary systems, F-gas–PIL binary interaction parameters were considered. Thus, a temperature-dependent energy binary parameter was employed for specific mixtures following Eq. 7.2,

$$k_{ij} = k_{ij}^{(0)} + k_{ij}^{(1)} T \,. \tag{7.2}$$

As particular care must be taken to avoid losing the predictive character of the model, temperature dependence on k_{ij} was only considered when a clear improvement with experimental data was observed. The set of binary interaction parameters is reported in Table 7.4. A temperature-dependent

TABLE 7.3: Molecular weight and soft-SAFT molecular parameters for the considered PILs, HFCs, and HFOs.

Compound	M_w [g·mol^{-1}]	$m_{s,i}$	σ_{ii} [Å]	ε_{ii}/k_B [K]	$\varepsilon^{A_iB_i}/k_B$ [K]	$\kappa^{A_iB_i}$ [Å^3]	Assoc. sites (D, P, N)	Source
[$P_{666,14}$]Cl	519.31	11.231	4.323	386.25	3500	2000	(1, 0, 0)	[250]
[$P_{666,14}$][GLY]	557.92	11.460	4.376	375.92	3500	2000	(1, 0, 1)	This work
[$P_{666,14}$][TMPP]	773.28	13.518	4.653	379.69	3600	2200	(1, 0, 1)	This work
R32	52.00	1.321	3.529	144.40	1708	24050	(0, 1, 1)	[229]
R152a	66.05	1.392	4.007	170.90	1885	24050	(0, 1, 1)	[230]
R134a	102.03	1.392	4.166	166.60	1862	24050	(0, 1, 1)	[230]
R125	120.02	1.392	4.242	148.80	1685	24050	(0, 1, 1)	[229]
R1234yf	114.04	1.136	4.808	173.40	1909	24050	(0, 1, 1)	[230]
R1234ze(E)	114.04	1.079	4.891	186.50	1990	24050	(0, 1, 1)	[230]

k_{12} was required for [$P_{666,14}$]Cl only in its mixtures with HFOs. In contrast, [$P_{666,14}$][TMPP] required temperature-dependent k_{12} for its mixtures with all the considered HFCs. In all cases, the mean values of k_{12} exhibit values lower than zero, suggesting an underprediction of dispersion interactions in the considered systems. The accuracy of this parameterization is checked in Figures 7.3, 7.4, and 7.5, where the solubility of HFCs and HFOs is compared with available experimental data. Table 7.5 summarizes the quantitative agreement with these experimental data by presenting the AAD with soft-SAFT EoS calculations.

Figure 7.3 present the solubility isotherms of HFCs and HFOs in [$P_{666,14}$]Cl over the temperature range from 283.15 K to 343.15 K. While the soft-SAFT EoS describes the general behavior of these systems, some discrepancies can be observed, particularly for HFCs. The model overpredicts the sensitivity of solubility with temperature at higher liquid mole fractions of solute, x_1, underestimating and overestimating the saturation pressure at lower and higher temperatures, respectively. The required inclusion of the binary size parameter, l_{12}, suggests that this problem arises from a waek prediction of entropic effects. Despite these discrepancies, overall AADs remain within a reasonable 10%. Interestingly, HFO solubility in this PIL is better reproduced, with only a slight decrease in accuracy at lower temperatures and higher values of x_1. Here, it is important to recall that, for HFO + [$P_{666,14}$]Cl mixtures, a temperature-dependent k_{12} is used, while l_{12} was fixed to zero. This approach reduces AADs for solubility isotherms of R1234yf and R1234ze(E) from 11.49% and 12.00% to 5.82% and 3.13%, respectively.

Results for the solubility of R32 and R134a in [$P_{666,14}$][GLY] are presented in Figure 7.4. In this case, a better agreement is found between the soft-SAFT EoS and experimental data, offering a good description of the VLE over the available concentration range. Finally, Figure 7.5 presents the solubility isotherms of different HFCs in [$P_{666,14}$][TMPP]. For these mixtures, the soft-SAFT EoS offers a remarkable modeling of the VLE upon the consideration of a temperature-dependent k_{12}. Entropic effects are satisfactorily modeled, as can be seen by the quantitative agreement with experimental data. Consequently, AADs remain below 5% for all HFCs. It can be noted that,

TABLE 7.4: Binary interaction parameters, k_{12} and l_{12}, for the considered F-gas (1) + PIL (2) mixtures.

	R32	R152a	R134a	R125	R1234yf	R1234ze(E)
			[$P_{666,14}$]Cl			
$k_{12}^{(0)}$	–0.227	–0.295	–0.242	–0.363	–0.405	–0.423
$k_{12}^{(1)} \cdot 10^3$	0.000	0.000	0.000	0.000	0.5787	0.6385
l_{12}	–0.064	–0.018	–0.054	–0.110	0.000	0.000
			[$P_{666,14}$][GLY]			
$k_{12}^{(0)}$	–0.263	–[a]	–0.183	–	–	–
$k_{12}^{(1)} \cdot 10^3$	0.000	–	0.000	–	–	–
l_{12}	–0.096	–	–0.056	–	–	–
			[$P_{666,14}$][TMPP]			
$k_{12}^{(0)}$	–0.168	–0.348	–0.231	–0.482	–	–
$k_{12}^{(1)} \cdot 10^3$	0.4317	0.9458	0.4644	0.8837	–	–
l_{12}	0.000	0.000	0.000	0.000	–	–

[a]Not fit due to lack of experimental data for the mixture.

TABLE 7.5: Average absolute deviation, AAD%, for the solubility isotherms obtained from the soft-SAFT EoS compared to available experimental data.[a]

	R32	R152a	R134a	R125	R1234yf	R1234ze(E)
[$P_{666,14}$]Cl	11.23	12.09	10.29	7.56	5.83	3.13
[$P_{666,14}$][GLY]	9.10	–[b]	9.28	–	–	–
[$P_{666,14}$][TMPP]	3.26	3.13	1.40	4.87	–	–

[a]AAD computed as AAD $= (100/N) \sum_{i=1}^{N} \left(|P_i^{\text{exp}} - P_i^{\text{EoS}}| / P_i^{\text{exp}} \right)$.

[b]AAD not computed due to lack of experimental data for the mixture.

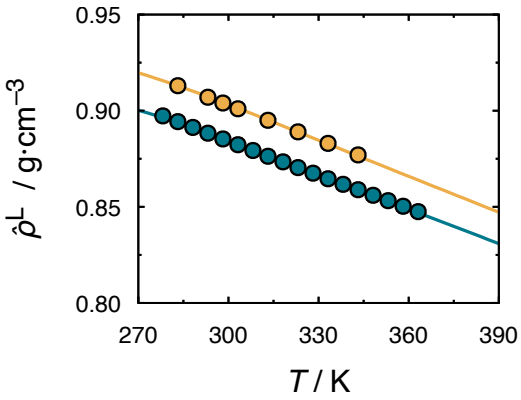

FIGURE 7.2: Liquid mass density, $\hat{\rho}^L$, of [$P_{666,14}$][GLY] (——) and [$P_{666,14}$][TMPP] (——) at 1 bar. Results from the soft-SAFT EoS (——) are shown and compared with available experimental data (○) [257, 258].

when temperature dependence of k_{12} is omitted, AADs for computed saturation pressures for R32, R152a, R134a, and R125 increase to 5.07%, 12.15%, 6.26%, and 10.39%, respectively.

To gain insights into the predicted solvation features in each analyzed mixture, excess molar enthalpy and entropy were computed following Eq. 4.42. Results are presented in Figure 7.6, where the excess Gibbs energy, $\tilde{G}^{ex} = \tilde{H}^{ex} - T\tilde{S}^{ex}$, is also included. As can be seen, [$P_{666,14}$]Cl exhibits the most favorable interactions with the studied HFCs, particularly with R152a, as indicated by its lower values for $\tilde{G}^{ex}$. In this PIL, R125, R1234yf, and R1234ze(E) show more negative values for $\tilde{H}^{ex}$ than for $\tilde{G}^{ex}$, highlighting that the energy interactions are the key drivers in the absorption of these gases. Moreover, for both HFOs, $T\tilde{S}^{ex}$ displays notoriously negative values, suggesting that spatial reordering in these systems weakens the overall affinity with the solvent. For [$P_{666,14}$][GLY], the expected behavior, *i.e.*, positive $\tilde{S}^{ex}$ and negative $\tilde{H}^{ex}$, is observed for its mixture with R32. However, for R134a, a positive $\tilde{H}^{ex}$ is present, generating a near-zero $\tilde{G}^{ex}$ and thus indicating a low affinity with the solvent. Finally, for [$P_{666,14}$][TMPP], negative $\tilde{S}^{ex}$ appear for all HFCs, as a consequence of the steric effects from the size of the $[TMPP]^-$ anion. This is partially compensated by markedly negative $\tilde{H}^{ex}$ values, especially for R125. This suggests a higher affinity for the absorption of this gas into the solvent, granted by preferable HFC–PIL interactions.

From the previous solubility results, effective Henry's constants [86] of HFCs in HFC (1) + PIL (2) mixtures were computed using Eq. 4.43. Results of this analysis are shown in Figure 7.7, where comparison with available experimental data shows that the soft-SAFT EoS satisfactorily model the slightly non-linear behavior of effective Henry's constants with temperature. This results is expected, considering the model was fit to reproduce the entire experimental range of solubility isotherms. Comparison among the considered PILs show the generally superior absorption capability, at diluted conditions, of [$P_{666,14}$]Cl over [$P_{666,14}$][TMPP], especially for R152a.

In addition to effective Henry's constants, dissolution enthalpy, $\Delta\tilde{H}^{dis}$, was computed for F-gases in F-gas (1) + PIL (2) mixtures following Eq. 4.46. A temperature of 323.15 K was considered, along

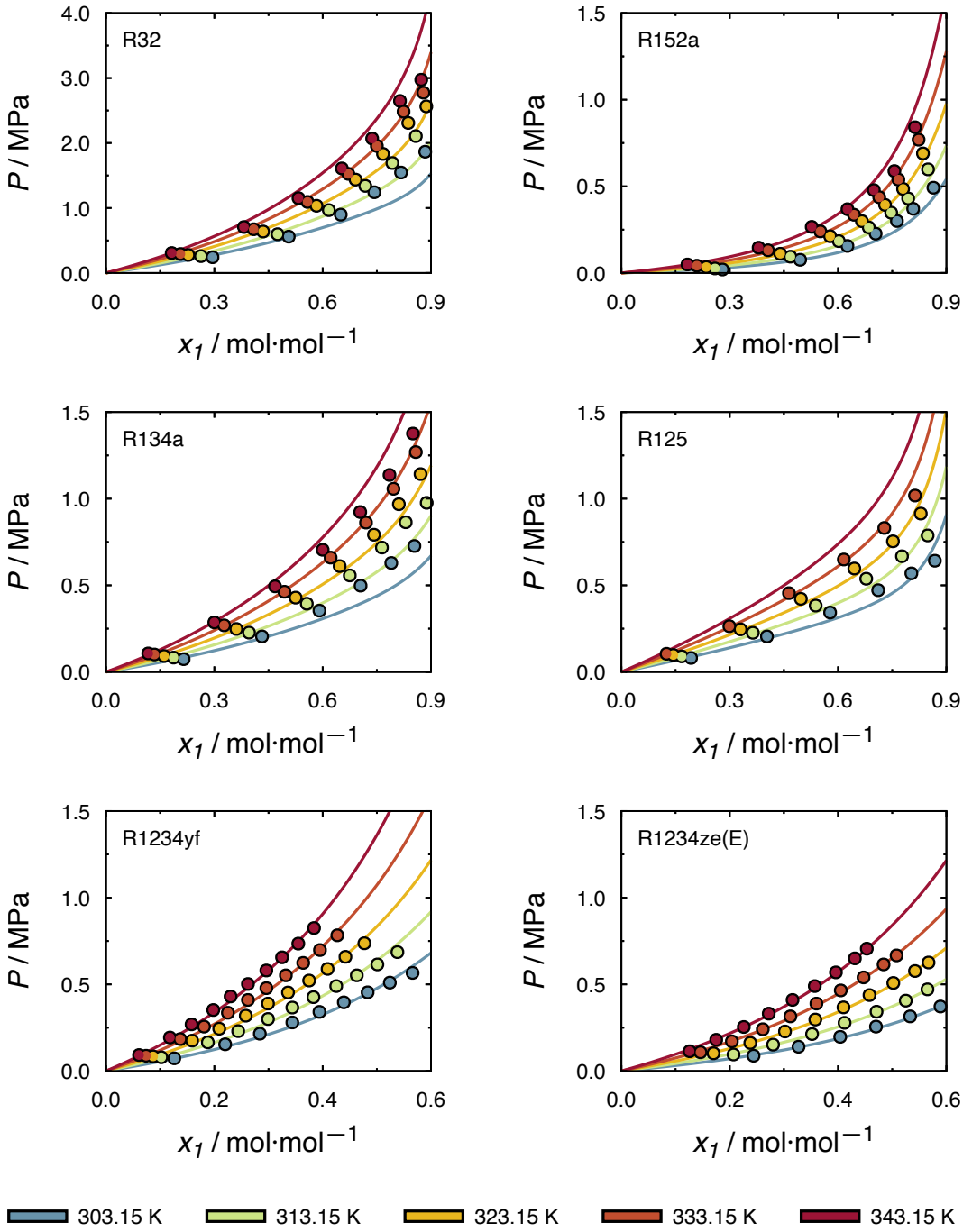

FIGURE 7.3: Solubility isotherms of F-gas (1) + $[P_{666,14}]Cl$ (2) mixtures at different temperatures. Results from the soft-SAFT EoS (—) are shown and compared with available experimental data [201, 259, 260] (○).

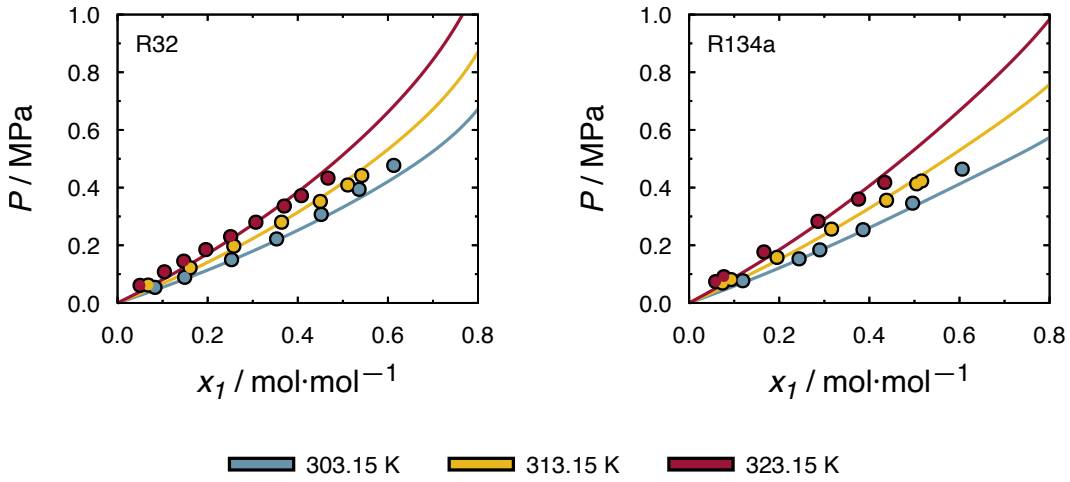

FIGURE 7.4: Solubility isotherms of HFC (1) + $[P_{666,14}]$[GLY] (2) mixtures at different temperatures. Results from the soft-SAFT EoS (—) are shown and compared with available experimental data [235] (○).

with two different F-gas liquid mole fractions to represent diluted ($x_1 = 0.001$) and concentrated ($x_1 = 0.500$) systems. Results from this analysis are shown in Table 7.6. In general, $\Delta\tilde{H}^{\text{dis}} < 0$ is observed for all studied PILs, with more negative values indicating stronger preferences of the F-gas for the solvent. Thus, for $[P_{666,14}]$Cl under diluted conditions, the most favorable interactions occur with R152a and both considered HFOs. Upon increasing x_1, a slight increase in $\Delta\tilde{H}^{\text{dis}}$ is observed for R152a and R1234ze(E), whereas a decrease is noted for the remaining F-gases. For $[P_{666,14}]$[GLY], R134a shows a more notorious decrease of $\Delta\tilde{H}^{\text{dis}}$ at concentrated conditions, compared to R32. This suggests a higher affinity for the former HFC in this PIL at higher solubility conditions. Finally, for $[P_{666,14}]$[TMPP], interactions are more favorable with R152a and R125, at both diluted and concentrated conditions, while R32 is the least favored HFC for solubilization. In summary, results for dissolution properties indicate a solvation preference for R152a in $[P_{666,14}]$Cl and $[P_{666,14}]$[TMPP], whereas $[P_{666,14}]$[GLY] exhibits similar interactions for R32 and R134a.

7.3.4. F-gas absorption competition assessed from ternary mixtures

The soft-SAFT models for binary F-gas + PIL mixtures, validated against experimental data, were further used to characterize the absorption of blends in the studied solvents. When considering systems composed of two or more F-gases, selectivity is essential to determine the feasibility of the entrainer [43, 261]. Thus, competitive selectivities of species i over species j, $S_{i/j}$ were computed following Eq. 4.45. $S_{i/j}$ allows to characterize the preferential absorption in refrigerant blends, where values deviating from unity indicate higher separation capacities for the solvent.

Considering that $[P_{666,14}]$[GLY] was parameterized for its binary mixtures with R32 and R134a, the first step in this analysis was to study the ternary VLE of PILs with both HFCs. Indeed, the

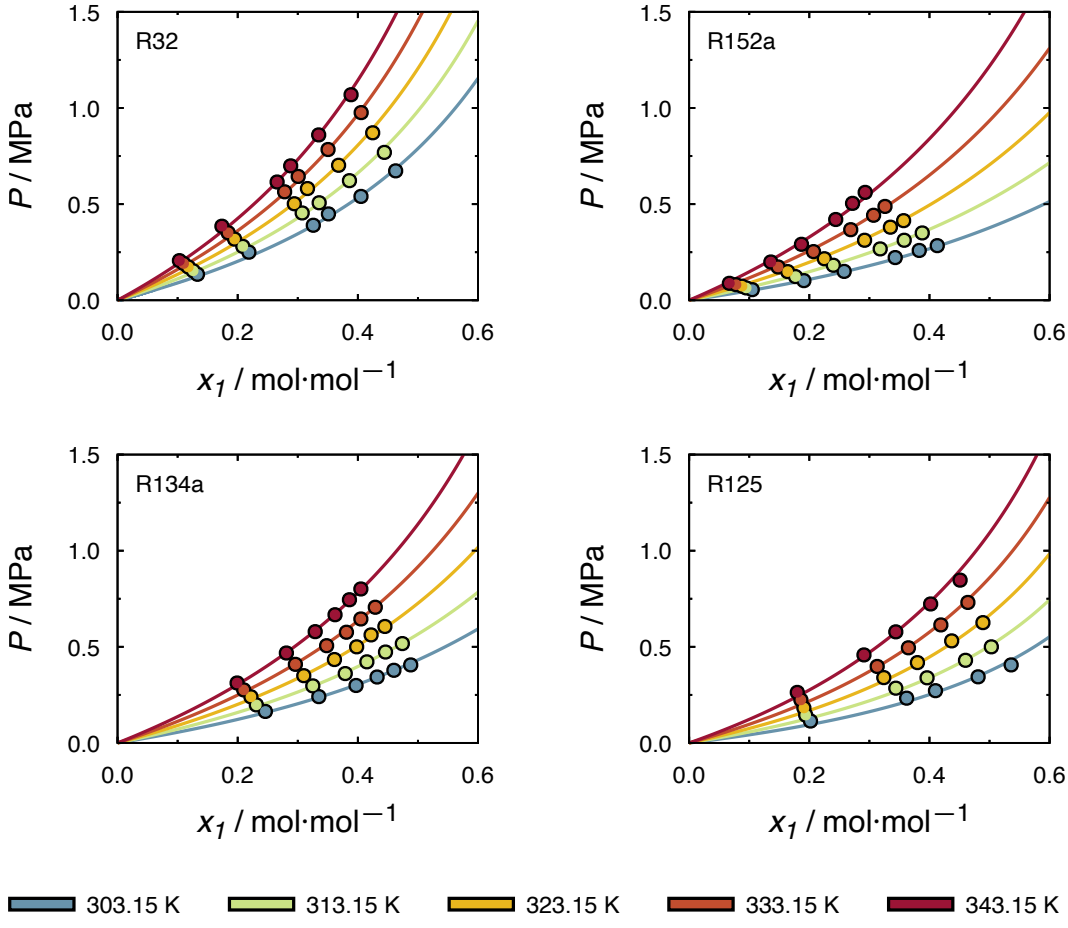

FIGURE 7.5: Solubility isotherms of HFC (1) + $[P_{666,14}][TMPP]$ (2) mixtures at different temperatures. Results from the soft-SAFT EoS (—) are shown and compared with available experimental data [241, 242] (○).

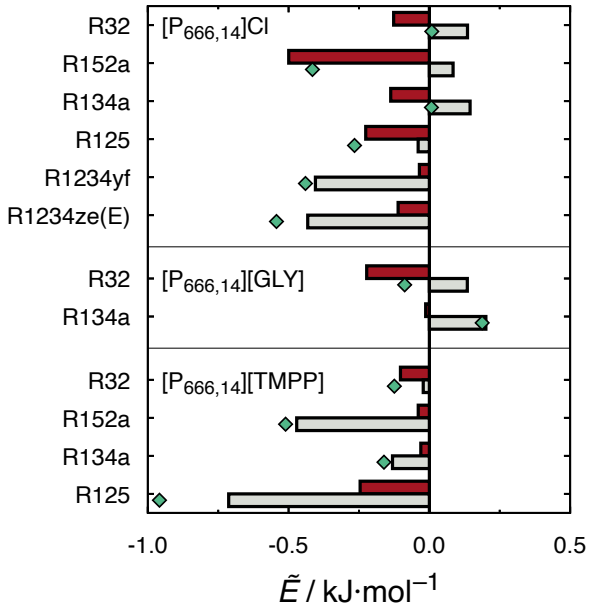

FIGURE 7.6: Excess Gibbs energy, $\tilde{G}^{ex}$ ( ), enthalpy, $\tilde{H}^{ex}$ ( ), and entropy multiplied by absolute temperature, $T\tilde{S}^{ex}$, ( ) for F-gas (1) + PIL (2) mixtures at 303.15 K and $x_1 = 0.15$, computed using the soft-SAFT EoS.

TABLE 7.6: Dissolution enthalpy, $\Delta\tilde{H}^{dis}$ (in kJ·mol^{-1}), for F-gas (1) + PIL (2) mixtures at 323.15 K, computed using the soft-SAFT EoS. Conditions of low ($x_1 = 0.001$) and high ($x_1 = 0.500$) F-gas liquid mole fraction are considered.

PIL	x_1 [mol·mol^{-1}]	R32	R152a	R134a	R125	R1234yf	R1234ze(E)
[P$_{666,14}$]Cl	0.001	–14.47	–23.21	–17.74	–16.13	–21.56	–24.31
	0.500	–16.23	–22.95	–19.30	–17.93	–22.59	–24.29
[P$_{666,14}$][GLY]	0.001	–15.57	-[a]	–15.90	-	-	-
	0.500	–17.46	-	–18.41	-	-	-
[P$_{666,14}$][TMPP]	0.001	–15.69	–23.39	–19.17	–22.90	-	-
	0.500	–16.89	–25.24	–20.87	–23.06	-	-

[a]Not computed due to lack of experimental data for the mixture.

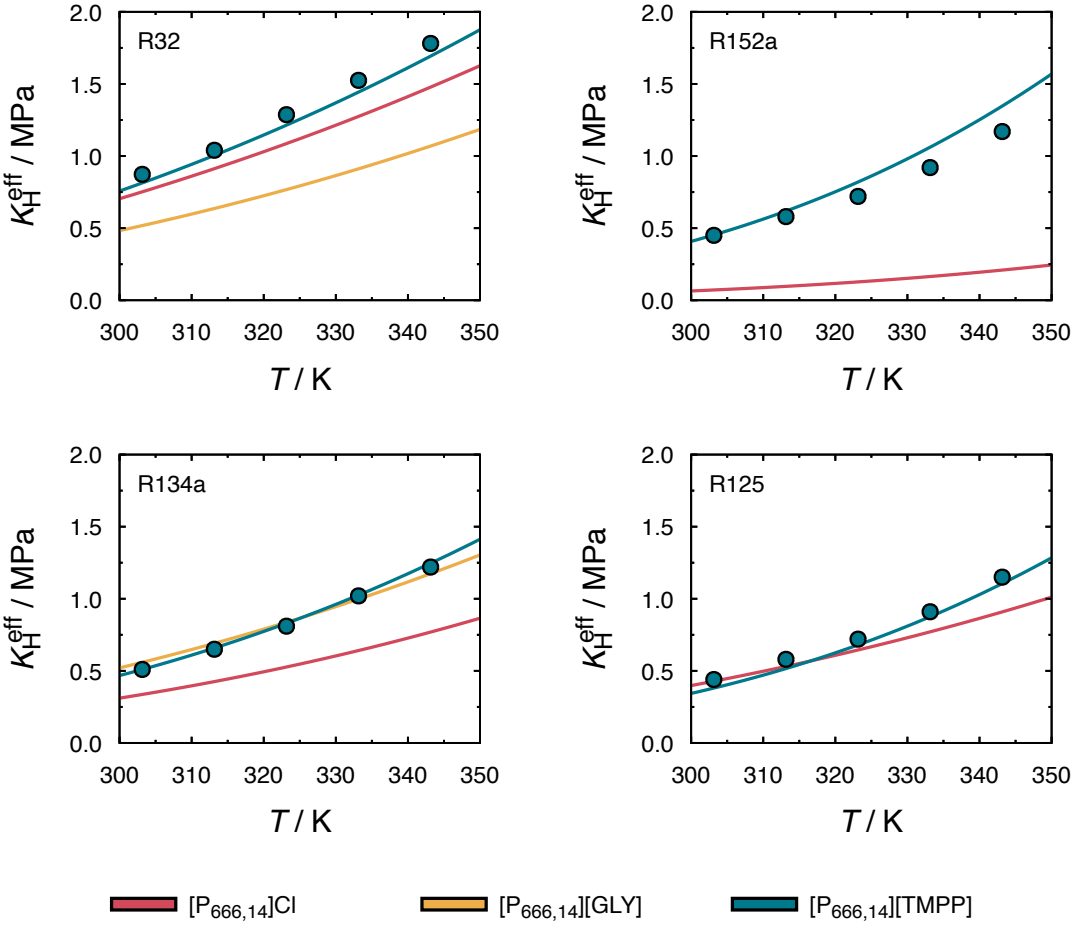

FIGURE 7.7: Effective Henry's constants, K_H, of HFCs in HFC + PIL mixtures at different temperatures. Results from the soft-SAFT EoS (——) are shown and compared with available experimental data (○) [241, 242].

separation of R32 from R134a is of interest, given that they form part of the common R407 refrigerant blends (R32 + R125 + R134a). In each case, the ternary system is characterized using the previously obtained HFC–PIL binary parameters. No binary parameters are required for the R32 + R134a mixture to yield an accurate description of its VLE, as shown in Figure C.2. Given quantitative discrepancies in the description of F-gas solubility in [$P_{666,14}$]Cl at higher pressures, the study was carried out at a moderate pressure of 0.5 MPa, considered as the upper bound to ensure reliable predictions.

Ternary VLE diagrams for the R32 (1) + R134a (2) + PIL (3) mixtures are presented in Figure 7.8, with z_i representing the global mole fraction of component i in the mixture. As expected, the VLE is characterized by a vapor phase lacking PIL regardless of the working temperature. Furthermore, the slope of the saturated liquid curves indicates the preference of the PIL to solubilize one HFC over another. In addition, the selectivity towards R134a over R32, $S_{R134a/R32}$, has been computed along the equilibrium curve for each system, and the conditions where its maximum value is reached at each temperature is pointed.

As evidenced by the slope of the saturated liquid curves, [$P_{666,14}$]Cl exhibits both the highest solubility and selectivity towards R134a, reaching a maximum value of $S_{R134a/R32} = 2.21$ at 323.15 K. Across each isotherm, $S_{R134a/R32}$ invariably increases as the global mole fraction of R134a, z_2, decreases, reaching its maximum at the limit of infinite dilution of this HFC. [$P_{666,14}$][GLY] displays a remarkable solubility for both HFCs, resulting in lower selectivities compared to [$P_{666,14}$]Cl. For this PIL, the maximum value of $S_{R134a/R32}$ occurs at lower temperatures, with R32 being the more diluted component. This behavior is reversed at temperatures above 323.15 K. Finally, [$P_{666,14}$][TMPP] shows the lowest solvent capacity, although its selectivity towards R134a is slightly higher compared to [$P_{666,14}$][GLY]. Moreover, its selectivity behavior is qualitatively analogous to that of [$P_{666,14}$]Cl. Overall, [$P_{666,14}$][GLY] is the most attractive PIL for the simultaneous absorption of R32 and R134a, while [$P_{666,14}$]Cl seems the best option for the separation of this mixture.

7.3.5. Assessment on the recovery and separation of commercial refrigerant blends

Considering the developed soft-SAFT molecular models for PILs are able to provide information on their capabilities of F-gas absorption and separation, different binary commercial refrigerant blends were studied. These blends are: R410A (50 wt.% R32 + 50 wt.% R125), R451A (10 wt.% R134a + 90 wt.% R1234yf), and R454A (35 wt.% R32 + 65 wt.% R1234yf). For the first blend, both [$P_{666,14}$]Cl and [$P_{666,14}$][TMPP] have been evaluated as potential entrainers. On the other hand, only [$P_{666,14}$]Cl was applied to HFO-based blends, as is the only PIL where the required validation for binary HFO + PIL systems has been carried out.

The soft-SAFT EoS has already been used in previous contributions to describe the solubility of the R410A blend [229]. Thus, the available binary interaction parameter $k_{R32,R125} = 0.045$ was directly transferred to the corresponding systems. Similarly, the R134a + R1234yf blend has been previously modeled at the specific concentration of the R513A blend (44 wt.% R134a + 56 wt.% R1234yf), incorporating a binary parameter of $k_{R134a,R1234yf} = 0.040$ [262]. Binary parameters for the rest of studied blends was fit to available experimental VLE data, as depicted in... Thus, parameters of $k_{R32,R1234yf} = 0.097$ were considered. Moreover, the R134a + R1234yf mixture was evaluated over

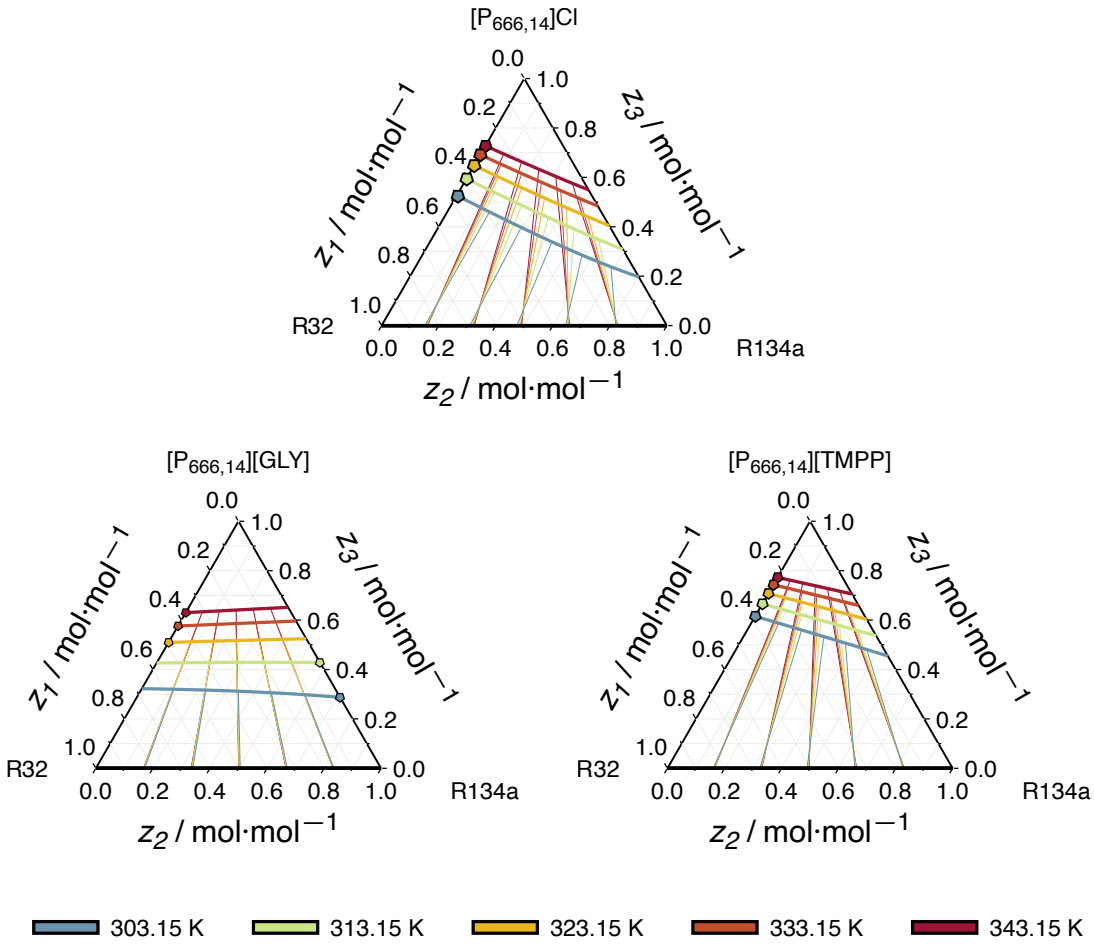

FIGURE 7.8: Ternary VLE of R32 (1) + R134a (2) + PIL (3) mixtures at 0.5 MPa and different temperatures, computed using the soft-SAFT EoS for $[P_{666,14}]Cl$, $[P_{666,14}][GLY]$, and $[P_{666,14}][TMPP]$. Thick lines depict saturated liquid curves, while thin lines correspond to vapor–liquid tie lines. Liquid-phase concentrations at which $S_{R134a/R32}$ reaches its maximum value at each temperature are also shown (⬠). Symbol sizes are scaled relative to the maximum selectivity among all systems and temperatures ($S_{R134a/R32} = 2.21$, for $[P_{666,14}]Cl$ at 323.15 K).

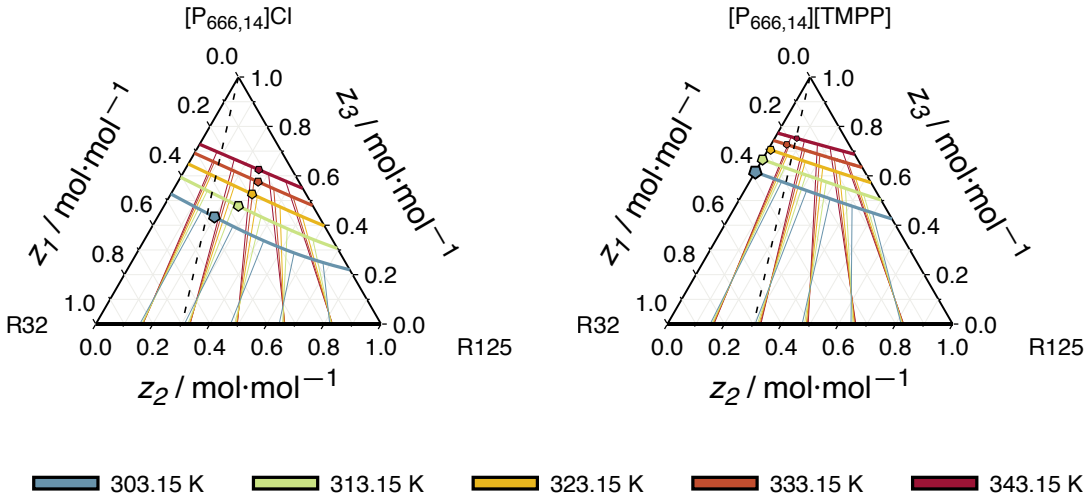

FIGURE 7.9: Ternary VLE of R32 (1) + R125 (2) + PIL (3) mixtures at 0.5 MPa and different temperatures, computed using the soft-SAFT EoS for $[P_{666,14}]Cl$ and $[P_{666,14}][TMPP]$. Thick lines depict saturated liquid curves, while thin lines correspond to vapor–liquid tie lines. The concentration curve of the R410A blend is included (- - -). Liquid-phase concentrations at which $S_{R125/R32}$ reaches its maximum value at each temperature are also shown (⬠). Symbol sizes are scaled relative to the maximum selectivity among all systems and temperatures ($S_{R125/R32} = 2.21$, for $[P_{666,14}][TMPP]$ at 303.15 K).

the entire mole fraction range to ensure the validity of the transferred binary parameter across all concentrations. Once the binary interactions among all species in the studied systems were assessed, different ternary VLE diagrams were constructed at 0.5 MPa and temperatures ranging from 303.15 K to 343.15 K.

Figure 7.9 compares the VLE of the R32 (1) + R125 (2) blend with $[P_{666,14}]Cl$ and $[P_{666,14}][TMPP]$. Results reveal that $[P_{666,14}]Cl$ yields higher solubilities for both HFCs compared to $[P_{666,14}][TMPP]$. Furthermore, both PILs exhibit a similar selectivity toward R125. While $S_{R125/R32}$ invariably decreases with temperature for both solvents, some remarkable differences have been found. For all temperatures, $[P_{666,14}]Cl$ achieves the highest R125 selectivity at intermediate concentrations. On the other hand, $[P_{666,14}][TMPP]$ reaches maximum R125 selectivities at the infinite dilution of this HFC. However, at temperatures higher than 323.15 K, this maximum selectivity displaces to intermediate concentrations of the system. Interestingly, at 343.15 K, $S_{R125/R32}$ reaches its maximum value near the global concentration of the R410A blend, suggesting an interesting feature of $[P_{666,14}][TMPP]$ as an entrainer for this refrigerant. Among both systems, and for all considered temperatures, a maximum value of $S_{R125/R32} = 2.21$ is obtained for $[P_{666,14}][TMPP]$ at 303.15 K.

Ternary VLE diagrams of the R134a + R1234ze(E), R134a + R1234yf, and R32 + R1234yf blends with $[P_{666,14}]Cl$ are presented in Figure 7.10. As can be seen, a notorious R134a selectivity is predicted from its mixture with R1234yf. Curiously, the replacement of this HFO with its isomer R1234ze(E)

yields lower R134a selectivities, as observed in Figure 7.10a. This is confirmed by the reported maximum selectivities for each system, obtaining maximum values of $S_{\text{R134a/R1234ze(E)}} = 1.29$, at 333.15 K, and $S_{\text{R134a/R1234yf}} = 2.25$, at 343.15 K. However, it is worth noting that the global concentration of the R451A blend is nearly at the minimum value of $S_{\text{R134a/R1234yf}} =$, highlighting an undesirable operating condition in this case. Although this is not the case for the R32 + R1234yf mixture, generally low selectivities are obtained for this system, with a slightly stronger affinity for R1234yf. Still, the maximum selectivity value of $S_{\text{R1234yf/R32}} = 1.41$ at 303.15 K evidences a poor separation capacity by $[P_{666,14}]Cl$.

The thermophysical information given by the above ternary VLE diagrams can be extended by studying $S_{i/j}$ at different temperatures and pressures. Thus, flash calculations were performed to compute competitive selectivities along the concentration curve of the above commercial blends. Low to moderate pressures, ranging from 0.0 MPa to 0.5 MPa, were addressed to represent absorption and desorption operating conditions. Results of this calculation are presented in Figure 7.11.

Figures 7.11a and 7.11b present $S_{\text{R125/R32}}$ at the concentration of the R410A blend for $[P_{666,14}]Cl$ and $[P_{666,14}][TMPP]$, respectively. $[P_{666,14}]Cl$ develops R125 selectivities consistently above 1.5, with a slight increase at higher pressures. In contrast $[P_{666,14}][TMPP]$ shows a negative effect of pressure and a stronger dependence on temperature, reaching selectivities up to 2.2. This aligns well with above observations on dissolution and excess properties, where R32 is the least favored HFC for absorption in this PIL. These results lie within the reported values for imidazolium-based ILs, showing ideal selectivities of approximately 2.0 and 1.8 for $[C_2mim][CF_3SO_3]$ [198] and $[C_2mim]Cl$ [263], respectively. However, these values are still below the higher selectivities of 5.0 obtained using $[C_2mim][dca]$ [264].

Figures 7.11c and 7.11d present $S_{\text{R134a/R1234yf}}$ and $S_{\text{R1234yf/R32}}$, using $[P_{666,14}]Cl$, at the concentration of the R451A and R454A blends, respectively. The highest selectivities are obtained for the R451A blend, reaching values up to 1.8 at higher temperatures and pressures. For the R454A blend, on the other hand, results show that a decrease in temperature and pressure can appreciably increase the R1234yf selectivity. This grants additional insights to the previously studied ternary VLE, showing an increased potential of $[P_{666,14}]Cl$ as an entrainer for this blend. Compared to the literature, other imidazolium-based ILs have been reported to reach higher selectivities for similar refrigerant blends. For instance, $[C_2mim][dca]$ shows consistently higher HFC/HFO ideal selectivities accross different blends [201], while $[C_2mim][SCN]$ achieves values of approximately 4.5 and 9.0 for $\alpha_{\text{R134a/R1234yf}}$ and $\alpha_{\text{R32/R1234yf}}$, respectively [44]. In addition, enhanced values of $\alpha_{\text{R134a/R1234yf}}$ have been reported for other imidazolium-based ILs [44].

It is important to note that above literature values correspond to ideal selectivity, derived from infinite dilution or Henry's constants. In contrast, the computed selectivities are obtained under finite concentration conditions. Therefore, direct quantitative comparison should be made with caution, as competitive selectivities inherently account dor non-ideal interactions and mixture effects, providing a more realistic representation of the separation performance. By explicitly capturing HFC–HFC and HFC–HFO interactions, this approach enables the identification of operating conditions under which enhanced selectivities can be achieved.

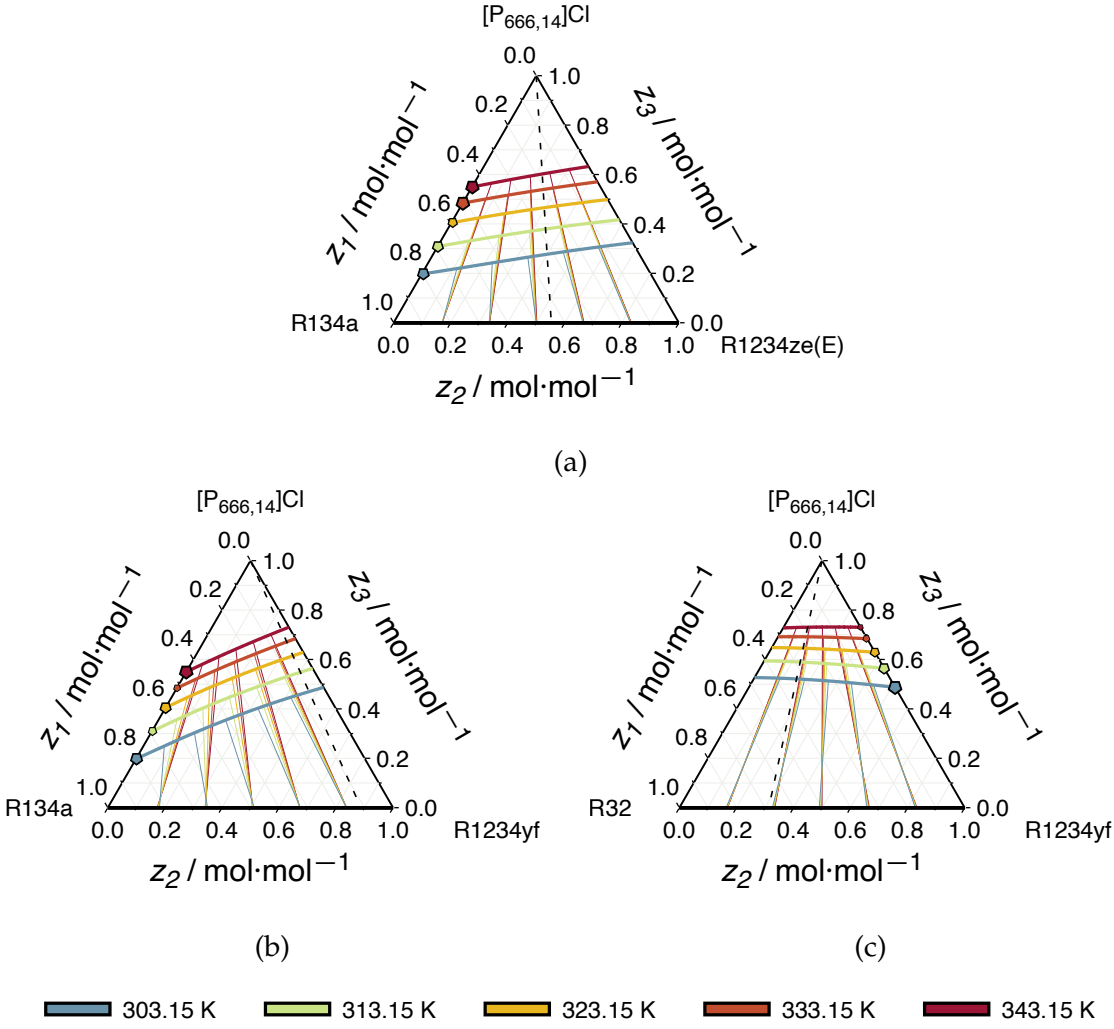

FIGURE 7.10: Ternary VLE of R134a (1) + R1234ze(E) (2) + $[P_{666,14}]Cl$ (3) (a), R134a (1) + R1234yf (2) + $[P_{666,14}]Cl$ (3) (b), and R32 (1) + R1234yf (2) + $[P_{666,14}]Cl$ (3) (c) mixtures at 0.5 MPa and different temperatures, computed using the soft-SAFT EoS. Thick lines depict saturated liquid curves, while thin lines correspond to vapor–liquid tie lines. The concentration curves of the R450A (a), R451A (b), and R454A (c) blends are included (- - -). Liquid-phase concentrations at which $S_{R134a/R1234ze(E)}$ (a), $S_{R134a/R1234yf}$ (b), and $S_{R1234yf/R32}$ (c), reach their maximum values at each temperature are also shown (⬡). Symbols sizes are scaled relative to the maximum selectivity among all temperatures for each system ($S_{R134a/R1234ze(E)} = 1.29$ at 333.15 K, $S_{R134a/R1234yf} = 2.25$ at 343.15 K, and $S_{R1234yf/R32} = 1.41$ at 303.15 K).

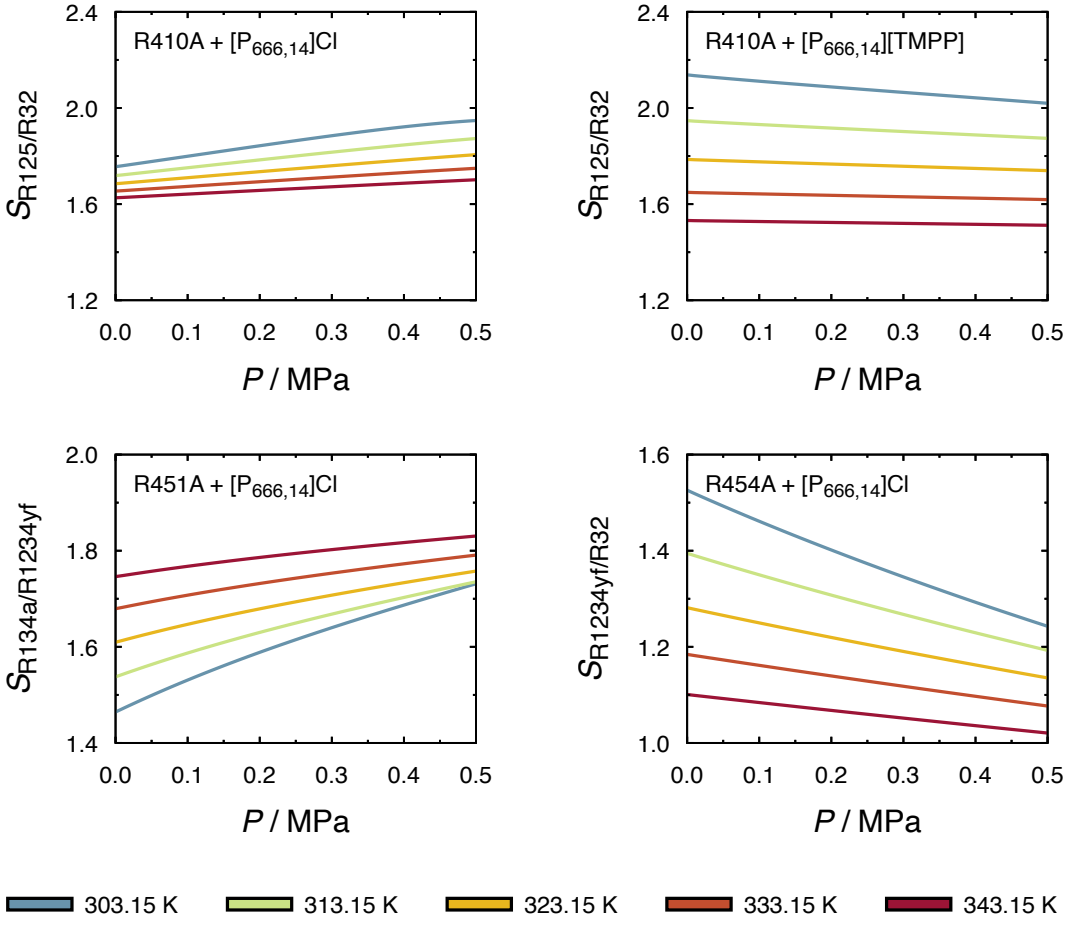

FIGURE 7.11: Competitive selectivities of compound i over j, $S_{i/j}$, in the studied mixtures of commercial refrigerant blends with PILs. Results from the soft-SAFT EoS at different temperatures (—) are shown.

7.4. Conclusions

In this work, a computational approach was used to describe the thermodynamic behavior of PILs, and to assess their capability as entrainers for refrigerant blends comprising HFCs and HFOs. To provide a physically meaningful association scheme for PILs, COSMO-RS and DFT calculations were used to define the association scheme and to compute association parameters, respectively. Subsequently, molecular models of the soft-SAFT EoS for three PILs, [$P_{666,14}$]Cl, [$P_{666,14}$][GLY], and [$P_{666,14}$][TMPP], were obtained. These models were used to describe the phase equilibrium between these PILs, HFCs, and HFOs.

For [$P_{666,14}$]Cl, results for the absorption of the HFOs R1234yf and R1234ze(E) were in reliable agreement with available experimental data, only requiring corrections for the cross-dispersive energy of the binary systems. The description of HFCs in this PIL showed higher uncertainties across the analyzed mole fraction range, although it still captured the behavior of these mixtures. Results for [$P_{666,14}$][GLY] and [$P_{666,14}$][TMPP] were accurate, describing the solubility of HFCs at different isothermal conditions in very good agreement with the available experimental data.

Based on above results, different ternary mixtures were analyzed to study the behavior of the selected PILs with refrigerant blends. Ternary VLE diagrams and selectivity calculations granted insights into the capabilities of the PILs for separating and recovering refrigerant blends. This analysis revealed insights on the behavior of selectivity along the ternary VLE, with maximum values arising from the interplay between the components in the blend and the PIL.

Finally, competitive selectivities at low to moderate pressures and different temperatures were computed from flash calculations to evaluate the performance of the PILs as entrainers for commercial refrigerant blends. Results show a high sensitivity of selectivities at lower temperatures. Notably, [$P_{666,14}$][TMPP] demonstrates a good performance in the separation of the R410A blend, achieving the highest computed selectivities among all studied systems. Additionally, [$P_{666,14}$]Cl grants a feasible separation of the R451A an R454A blends.

These findings provide the basis for further process-level analysis, required to assess the practical feasibility of the studied solvents. In particular, considerations such as transport limitations, especially under the characteristic high viscosity of ILs, must be carefully evaluated through rate-based modeling, as these effects may significantly limit mass transfer and, consequently, the overall separation performance.

8. Thermophysical Characterization of a Sustainable Hydrofluorocarbon Separation Utilizing Type III Deep Eutectic Solvents

In this chapter, the absorption and separation potential of type III DESs is investigated for selected HFCs (R32, R143a, R134a, and R125), using new experimental solubility measurements and the soft-SAFT EoS. DESs based on choline chloride ([Ch]Cl) and tetramethylammonium chloride ([N_{1111}]Cl), as HBAs, combined with ethylene glycol (EG) and glycerol (GL), as HBDs, are considered. The thermodynamic model is used to describe pure-DES density and viscosity, gas solubility, effective Henry's constants, dissolution enthalpy, and selectivity. Among the studied systems, R32 shows the highest affinity toward the DES, followed by R134a, R143a, and R125, whereas [N_{1111}]:EG exhibits the highest absorption capacity for all HFCs. In addition, [N_{1111}]:GL and [Ch]Cl:GL + 10 wt.% H_2O show promising a selectivity for separating HFC blends, particularly those containing R32, suggesting their potential application in the recovery of commercial refrigerant blends such as R410A and R407F.[*]

8.1. Introduction

Among the different DES families, type III DESs, comprised of quaternary ammonium salts as HBAs, are the most widely studied in the literature [47]. Their popularity stems from the availability of inexpensive precursors, and the large number of non-toxic organic compounds that can act as HBDs [46]. Thus, type III DESs have been used in practically all areas related to DESs, including drug solubilization, reaction media, and CO_2 capture [47, 265].

Considering their widespread application and suitable properties as entrainers, type III DESs demonstrate an important potential for the recovery of HFCs. Previous work has addressed this

[*]This chapter is adapted with permission from:
L.V.T.D. Alencar, B. González-Barramuño, S.B. Rodriguez-Reartes, H. Quinteros-Lama, J.M. Garrido, V. Codera, J.O. Pou, F.W. Tavares, R. Gonzalez-Olmos, and F. Llovell, "Thermophysical Characterization of Sustainable Pathways for Hydrofluorocarbons Separation Utilizing Deep Eutectic Solvents", *Journal of Industrial and Engineering Chemistry* **146**, 788–799 (2025). Copyright 2025 Elsevier B.V.

issue, demonstrating that DESs based on choline chloride ([Ch]Cl) exhibit promising selectivities toward commercial HFC blends [67, 266]. Thus, the evaluation of DESs comprising different common HBAs represents an attractive pathway for the further exploration of novel solvents for this application.

In this work, the absorption potential of four representative HFCs, namely R32, R143a, R134a, and R125 in selected type III DESs is evaluated. Moreover, new experimental measurements of HFC solubility are reported for DESs based on tetramethylammonium chloride ([N_{1111}]Cl). The soft-SAFT EoS was used to model the thermodynamic behavior of the considered HFC + DES mixtures, given its demonstrated capabilities in related systems [267–271]. Using the predictive capabilities of this thermodynamic model, the separation capabilities of the studies DESs were analyzed under operational conditions of interest for the extractive distillation process.

8.2. Materials and methods

A combination of experimental measurements and thermophysical modeling based on the soft-SAFT EoS was employed to study the HFC absorption in type III DESs. The chemical structures of the considered DES precursors are presented in Table 8.1.

8.2.1. Materials

Glycerol (99% purity) and ethylene glycol (99% purity) were acquired from ITW Reagents. Tetramethylammonium chloride (97% purity) was purchased from Thermo Fischer Scientific, and it was heated at 343.15 K under vacuum conditions for 15 h for further purification. The HFCs utilized in all experiments were R32, R143a, R134a, and R125, all sourced from GRIT, Gases, Research, Innovation & Technology S.L.U, with a purity level of at least 99.5%.

The DESs experimentally characterized in this study were prepared following the methodology used by Codera et al. [266]. In particular, tetramethylammonium chloride ([N_{1111}]Cl) was combined with ethylene glycol (EG) or glycerol (GL) in an HBA:HBD mole ratio of 1:3. During the preparation of DESs, [Ch]Cl and [N_{1111}]Cl HBAs were placed in a vacuum oven at 343.15 K before use. After the drying process, they were stored in a drying system containing phosphorus pentoxide to avoid any further hydration. The standard procedure established by Moradi et al. [272] and Nkosi *et al.* [273] was followed in all cases. DESs were prepared in a beaker using a Mettler Toledo PM2000 balance with an uncertainty of $\pm$ 0.01 g and heated at 338.15 K for 1 h with continuous stirring until a uniform, transparent liquid was formed. The beaker was sealed during the DES preparation. In the particular case of the aqueous [Ch]Cl:GL (1:3) system, water was added to the DES and controlled gravimetrically, until reaching a 10 wt.% content.

8.2.2. Methods

Determination of DESs density and viscosity

The density and viscosity of DESs were measured using a digital densimeter and viscometer over a temperature range of 293.15 K to 343.15 K, in 5 K increments, under atmospheric pressure. Two

TABLE 8.1: Molecular structures of the considered type III DES precursors.

Name	Structure	Abbreviation
choline chloride	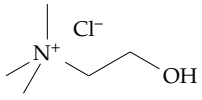	[Ch]Cl
tetramethylammonium chloride	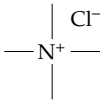	$[N_{1111}]Cl$
ethylene glycol	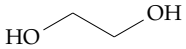	EG
glycerol	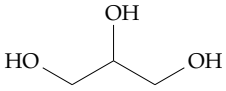	GL

measurements were performed for each DES and property, and the results are expressed as the average, with a measurement uncertainty of 0.0001 g·cm^{-3} for density and ±0.1 mPa·s for viscosity. Detailed information regarding the experimental equipment and setup for density and viscosity measurements can be found in previous work [266].

Determination of hydrofluorocarbon solubility

HFC solubility was determined using an isochoric saturation analytical method with a custom-built apparatus. A known amount of DES (±0.01 g) was introduced into the equilibrium cell, and the entire system was evacuated for 2 h at 300.15 K using a vacuum pump (COMECTA - IVYMEN, model 5900621). Meanwhile, HFC from the commercial bottle was introduced into the gas cylinder of the system, with the temperature set at 300.15 K. Once equilibrium was reached, the vacuum was stopped, and the gas from the cylinder was swiftly transferred into the cell while stirring, causing an initial pressure increase. The system was maintained at 300.15 K, digitally recording the pressure inside the equilibrium cell every second until complete absorption occurred, evidenced by a stable equilibrium pressure persisting for at least 30 min. The uncertainty of gas solubility measurements on a mole fraction basis was determined to be $\pm 5 \cdot 10^{-4}$.

Thermophysical molecular modeling

All considered species were modeled using the soft-SAFT EoS [139, 140] to characterize their thermodynamic behavior. For DESs, the individual component approach [274] was employed, thus requiring independent molecular models for HBAs and HBDs. Following previous works [274, 275], [Ch]Cl and $[N_{1111}]Cl$ were modeled as associating compounds with two association sites each, one positive and one negative, simulating the cation–anion interaction. EG and GL were also

TABLE 8.2: Molecular weight and soft-SAFT molecular parameters for the considered DESs and HFCs. The notation of Huang and Radosz [148] is used to denote the association scheme in each case.

Compound	M_w [g/mol]	$m_{s,i}$	σ_{ii} [Å]	ε_{ii}/k_B [K]	$\varepsilon^{A_iB_i}/k_B$ [K]	$k^{A_iB_i}$ [Å^3]	Assoc. scheme	Source
[Ch]Cl	139.63	5.096	3.401	428.40	3384	2100	2B	[274]
[N_{1111}]Cl	109.60	3.818	3.413	360.80	3384	2100	2B	[275]
EG	62.07	1.751	3.668	326.05	4384	4195	2B	[276]
GL	92.09	2.397	3.638	392.95	4945	2250	2B	[174]
H_2O	18.02	1.000	3.154	365.00	2388	2932	4C	[277]
R32	52.00	1.321	3.529	144.40	1708	24050	2B	[229]
R143a	84.04	1.392	4.103	149.00	1717	24050	2B	[278]
R134a	102.03	1.392	4.166	166.60	1862	24050	2B	[230]
R125	120.02	1.392	4.242	148.80	1685	24050	2B	[229]

modeled following the same association scheme, to mimic the hydroxyl groups present in these molecules [174, 275, 276]. Moreover, water was also included within the analyzed species, given its presence in the [Ch]Cl: GL (1:3) + 10 wt.% H_2O DES. In this work, water is modeled using four association sites, two positive and two negative, parameterized to preserve the tetrahedral structure of the molecule when hydrogen bonding occurs [277].

All HFCs were described as homonuclear chains with two association sites each, one positive and one negative, simulating the dipole moment caused by the electronegativity of the molecule. This model has shown the best performance when describing interactions with ILs and DESs [267, 268]. The complete set of parameters for all compounds is taken from previous works [174, 229, 230, 274–278] and is presented in Table 8.2 for completeness.

Liquid shear viscosity, η^L, of the considered DESs was modeled using the Free Volume Theory (FVT). The required parameters for [Ch]Cl, EG, GL, and H_2O were previously obtained using the spider-web methodology and employing the soft-SAFT EoS for the required modeling of density [274]. Within this approach [279], FVT parameters of pure compounds are regressed through mixtures between them, allowing to parameterize species which are not liquid at normal temperature and pressure conditions, such as [Ch]Cl. The combined use of FVT and the soft-SAFT EoS demonstrated reliable results for the modeling of viscosity in type III DESs, and thus was extended to derive the corresponding parameters for [N_{1111}]Cl. In this work, this HBA was modeled by applying the spider-web methodology to the [N_{1111}]Cl:EG (1:3) and [N_{1111}]Cl:GL (1:3).

8.3. Results and Discussion

8.3.1. Thermophysical characterization of DESs

Experimental measurements of liquid mass density, $\hat{\rho}^L$, and liquid shear viscosity, η^L, for the studied [N_{1111}]Cl:EG (1:3) and [N_{1111}]Cl:GL (1:3) DESs, along with available experimental data for

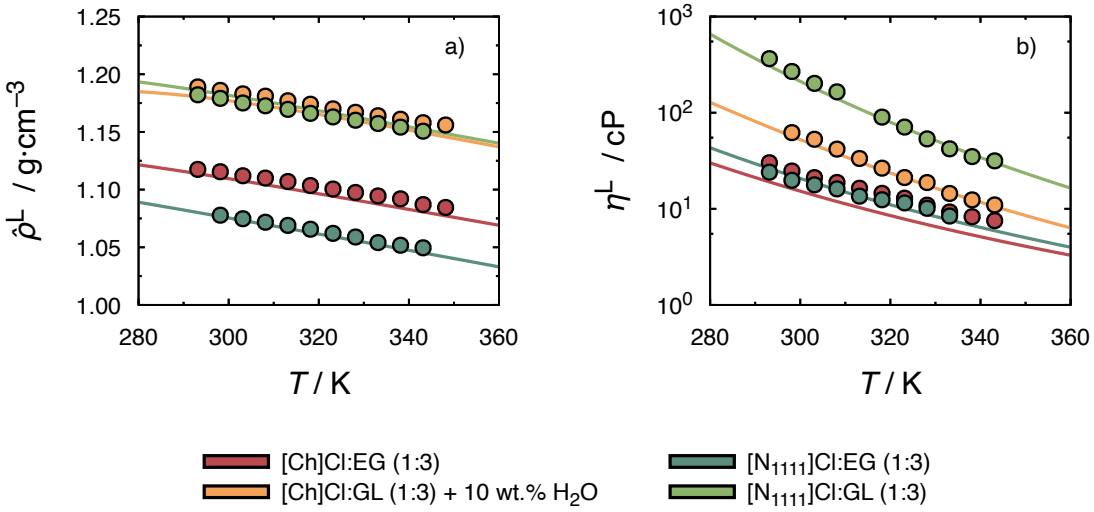

FIGURE 8.1: Liquid mass density (a) and liquid shear viscosity (b) of the considered DESs at different temperatures. Results from the soft-SAFT EoS (—) are shown and compared with available and measured experimental data (○) [67, 266].

[Ch]Cl:EG (1:3) and [Ch]Cl:GL (1:3) + 10 wt.% H_2O, are illustrated in Figure 8.1. As observed, $\hat{\rho}^L$ exhibits a consistent linear decrease with temperature in all cases, consistently with previous reports [67, 266]. Among the evaluated systems, [Ch]Cl:GL (1:3) + 10 wt.% H_2O displays the highest density, although very closely followed by [N_{1111}]Cl:GL (1:3). Moreover, DESs comprising EG show lower densities, especially for [N_{1111}]Cl:EG (1:3). This trend underscores the influence of the DES precursors on density variations, mostly related to molecular size, which is well correlated with $\hat{\rho}^L$. Concerning the HBA influence, [Ch]Cl-based DESs provide higher densities than their [N_{1111}]Cl-based analogues, although to a lesser extent than HBDs.

The performance of the soft-SAFT EoS in describing the density of the investigated DESs is illustrated in Figure 8.1a. To address the minor discrepancies in mixture density predictions from pure compound parameters, binary size parameters of $l_{\text{HBA–HBD}} = -0.023$ for both [N_{1111}]Cl-based DESs were incorporated to the model. This minor correction, with a temperature-independent common coefficient, ensures quantitative agreement across the studied DESs. In general, results from soft-SAFT EoS demonstrate acceptable agreement with experimental data, with an AARD% values of 1.16%, 1.12%, 1.13%, and 1.51% for [Ch]Cl:EG (1:3), [Ch]Cl:GL (1:3) + 10 wt.% H_2O, N_{1111}]Cl:EG (1:3), and [N_{1111}]Cl:GL (1:3), respectively.

In the case of η^L, noticeable differences among DESs were observed. Notably, [N_{1111}]Cl:GL (1:3) exhibited the highest viscosity, surpassing 250 cP. This rise in viscosity is attributed to the more elevated number of hydroxyl groups of GL compared to EG, facilitating enhanced hydrogen bonding interactions with the HBA and, consequently, leading to higher viscosities.

The utilized FVT parameters, including the values for [N_{1111}]Cl regressed in this work, are presented in Table 8.3. As seen from Figure 8.1b, an excellent agreement with viscosity data was

TABLE 8.3: FVT parameters for the DES precursors considered in this work.

Compound	α [J·m^3·mol^{-1}·kg^{-1}]	$B{\cdot}10^2$	$L_v{\cdot}10^2$ [Å]	Source
[Ch]Cl	374.58	0.6867	0.0170	[274]
[N_{1111}]Cl	379.55	0.7920	0.0042	This work
EG	356.55	0.0911	8.5466	[274]
GL	335.74	0.2794	2.9452	[274]
H_2O	485.21	0.1001	1.4239	[274]

found, with an AARD% of 8.11% across all DESs. Consistently with previous works [274, 280], the employed approach offers a poorer performance at low temperatures, which is attributed to the difficulty in capturing the sharp exponential increase in viscosity. However, these deviations only occur at high viscosity values, in a region with lower interest for practical applications. Otherwise, the description of aqueous DESs is remarkable, reconfirming the high versatility of the followed approach in achieving a reliable description of this property at different conditions [274].

8.3.2. Modeling of HFC solubility in type III DESs

Upon characterizing the liquid-phase behavior of the investigated DESs, their capacity to absorb R32, R134a, R143a, and R125 was studied. Solubility isotherms were measured at 300.15 K at pressures up to 6 bar, not to surpass the saturation pressure of R134a, which stands at 7.0 bar at this temperature. The experimental solubility data for the two [N_{1111}]Cl-based DESs studied in this work are provided in Table 8.4.

Figure 8.2 presents the solubility isotherms, at 300.15 K, as a function of the liquid mole fraction of HFC (x_{HFC}) in each studied DES, including the previous results obtained for [Ch]Cl-based DESs [67, 266]. A comprehensive analysis of the results demonstrates a relatively low solubility of HFCs for all investigated DESs, which can be attributed to the absence of fluorine atoms in their chemical structure. Previous works on the solubility of HFCs in fluorinated ILs [66] and DESs [203] has suggested that the presence of fluorine atoms can enhance the F-gases solubility by forming hydrogen bonds (H–F–H). However, this high degree of absorption comes at a cost of a nearly null capacity to selectively separate these HFCs.

In the DESs under investigation in this work, it appears that the primary influence lies on a weak physical absorption dominated by entropic effects, where the volume of the HFC molecules plays a key role. Indeed, R32, the smallest HFC among those studied, being the only single-carbon compound, exhibits the highest solubility. Concerning the two-carbon refrigerants, it may be noted that the amount of fluorine atoms in HFCs do not consistently correlate with enhanced solubility. For instance, while R134a, containing four fluorine atoms, ranks as the second compound with the highest solubility, R125 (with five fluorine atoms) and R143a (with three fluorine atoms) exhibit similar and lower solubility levels compared to other HFCs. In this case, two different effects play a role. On one hand, R125 has a low solubility due to the presence of five fluorine atoms, forming a relatively stable structure of a certain size and leaving low allocation for strong interactions with

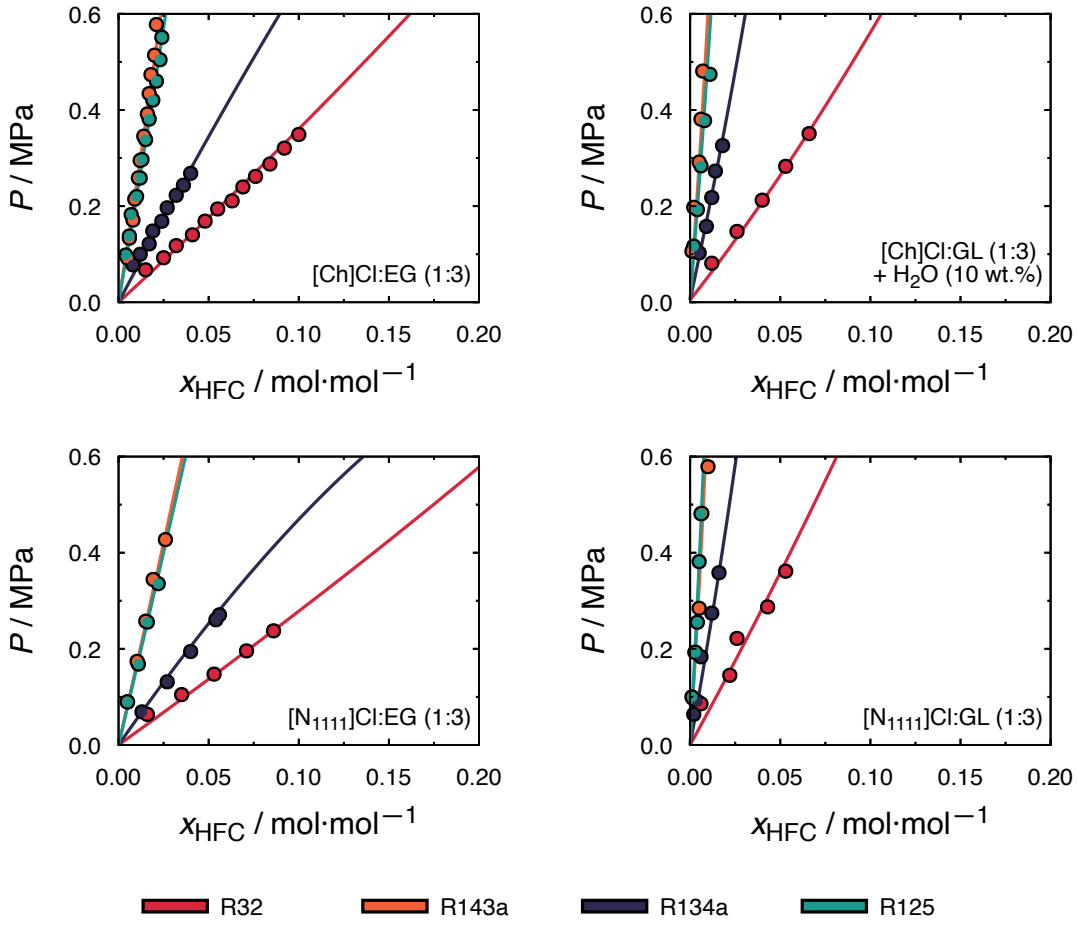

FIGURE 8.2: Solubility isotherms of HFCs in the studied DESs at 300.15 K. Results from the soft-SAFT EoS (—) are shown and compared with available and measured experimental data (○) [67, 266].

TABLE 8.4: Measured solubility isotherms the considered HFCs in [N_{1111}]Cl:EG (1:3) and [N_{1111}]Cl:GL (1:3) at 300.15 K.

x_{R32} [mol·mol^{-1}]	P [MPa]	x_{R143a} [mol·mol^{-1}]	P [MPa]	x_{R134a} [mol·mol^{-1}]	P [MPa]	x_{R125} [mol·mol^{-1}]	P [MPa]
[N_{1111}]Cl:EG (1:3)							
0.016	0.064	0.005	0.090	0.013	0.069	0.005	0.089
0.035	0.105	0.010	0.174	0.027	0.131	0.011	0.168
0.053	0.147	0.015	0.258	0.040	0.194	0.016	0.256
0.071	0.196	0.019	0.344	0.054	0.261	0.022	0.336
0.086	0.237	0.026	0.427	0.056	0.271	-	-
[N_{1111}]Cl:GL (1:3)							
0.006	0.086	0.002	0.096	0.002	0.064	0.001	0.100
0.022	0.145	0.003	0.193	0.004	0.091	0.003	0.193
0.026	0.222	0.005	0.284	0.006	0.183	0.004	0.255
0.043	0.287	0.007	0.482	0.012	0.274	0.005	0.382
0.053	0.362	0.010	0.579	0.016	0.358	0.006	0.481

the DESs. Conversely, the asymmetric R143a, with three fluorine atoms at the same molecule end, exhibits a high dipole moment [281], but lacks the previously mentioned H–F–H structure, resulting in a lower solubility. In any case, this variation in solubility among these HFCs represents an advantage for their separation. Specifically, it suggests that R125 and R143a could potentially be readily separated from mixtures of HFCs containing R134a and R32.

Although qualitative behavior among DESs is similar, it is notable that [N_{1111}]Cl:EG (1:3) exhibits a slightly higher absorption capacity, followed by [Ch]Cl:EG (1:3), [Ch]Cl:GL (1:3) + 10 wt.% H_2O, and finally [N_{1111}]Cl:GL (1:3). The latter seems to be clearly affected by its higher viscosity, possibly affecting mass transfer. In any case, no substantial differences are appreciated among all DESs, suggesting that the influence of the DESs structure on the solubilities of the considered HFCs appears to be modest.

As shown in Figure 8.2, the soft-SAFT EoS provides good agreement with experimental data. Molecular parameters provided in Table 8.2 are used for multicomponent calculations, where each HFC–DES combination is treated as a ternary mixture, except for systems containing [Ch]Cl:GL (1:3) + 10 wt.% H_2O, which are treated as quaternary mixtures. In this regard, binary interaction parameters for dispersive energy, k_{ij}, where employed to correct deviations arising from predictions of HFC solubility. A summary of the utilized values is provided in Table 8.5.

Some remarkable trends emerge from analyzing the values of these parameters and their relevance to the interactions within the mixture. Notably, most cases exhibit $k_{ij} < 0$, indicating that classical Lorentz-Berthelot combining rules underestimate the cross-dispersive energy of the considered systems and suggesting potentially missing interactions within the model. Additionally, consistent

TABLE 8.5: Regressed binary interaction parameters for dispersive energy, k_{ij} for the soft-SAFT EoS.

i	*i*	k_{ij}
[Ch]Cl	R32	–0.2998
[Ch]Cl	R143a	–0.1374
[Ch]Cl	R134a	–0.1450
[Ch]Cl	R125	–0.2103
[Ch]Cl	H_2O	–0.0450
$[N_{1111}]$Cl	R32	–0.3000
$[N_{1111}]$Cl	R143a	–0.0477
$[N_{1111}]$Cl	R134a	–0.0577
$[N_{1111}]$Cl	R125	–0.1278
EG	HFCs	–0.1008
LA	HFCs	–0.2338
GL	HFCs	–0.0532
R143a	H_2O	0.1500
R134a	H_2O	0.1500

[a]Transferred from previous work [273].

$k_{\text{HBD–HFC}}$ could be obtained across all systems, suggesting that the parameter can be transferred among HFCs if no experimental data are available. For the case of [Ch]Cl:GL (1:3) + 10 wt.% H_2O, a $k_{\text{[Ch]Cl–H}_2\text{O}} = -0.045$ parameter was transferred from previous work [273]. In contrast, binary parameters of R32, R143a, and R134a with water were optimized and fixed at $k_{\text{HFC–H}_2\text{O}} = 0.150$. Overall, soft-SAFT EoS effectively describes the solubility of each HFC in the examined DESs, showing good agreement with experimental data.

Finally, dissolution enthalpies of each HFC in HFC + DES mixtures, $\Delta\tilde{H}^{\text{dis}}$, were computed from Eq. 4.46. Calculations were performed at 300.15 K and $x_{\text{HFC}} = 0.0001$, and results are presented in Table 8.6. As can be seen, R32 develops the most negative values of ΔH^{dis}, implying that all investigated DESs have a clearly higher affinity for R32 than for the rest of HFCs.

TABLE 8.6: Dissolution enthalpy, $\Delta\tilde{H}^{\text{dis}}$ (in kJ·mol^{-1}), for HFCs in HFC + DES mixtures at 300.15 K and $x_{\text{HFC}} = 0.0001$, computed using the soft-SAFT EoS.

DES	R32	R143a	R134a	R125
[Ch]Cl:EG (1:3)	–21.51	–11.28	–17.28	–11.60
[Ch]Cl:GL (1:3) + 10 wt.% H_2O	–37.05	–30.00	–34.90	–30.58
$[N_{1111}]$Cl:EG	–21.60	–11.06	–17.13	–11.17
$[N_{1111}]$Cl:GL	–14.15	–8.00	–11.35	–7.55

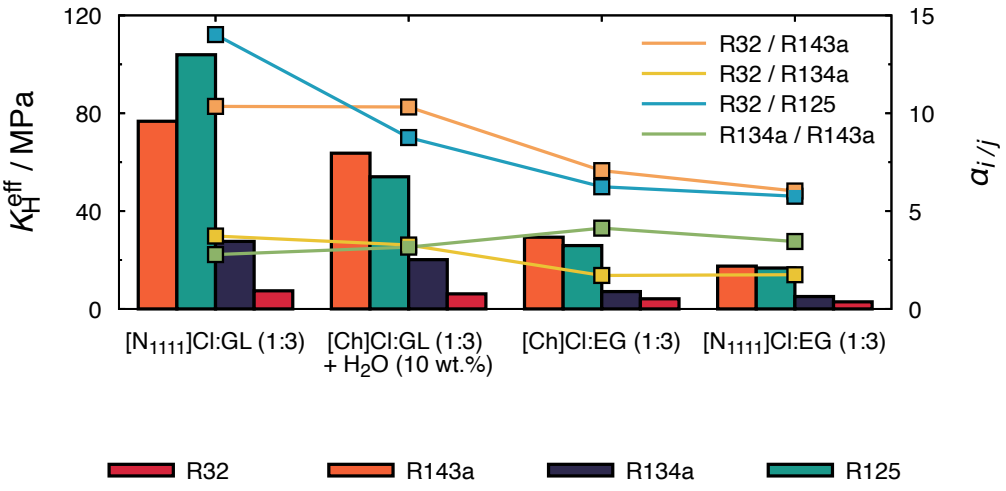

FIGURE 8.3: Effective Henry's constants, K_H^{eff}, (■ , left axis) and ideal selectivity, $\alpha_{i/j}$, (—, right axis) of HFCs in HFC + DES mixtures at 300.15 K. Results from the soft-SAFT EoS are shown.

8.3.3. HFC selectivity in type III assessed from multicomponent mixtures

Figure 8.3 present effective Henry's constants, K_H^{eff}, and ideal selectivities, $\alpha_{i/j}$, of different HFCs in the studied DESs, computed using Eqs. 4.43 and 4.44, respectively. Values for K_H^{eff} are directly linked to results regarding solubility isotherms. $[N_{1111}]$Cl:EG shows the lowest Henry's constants among DESs, indicating the highest absorption capacities. Additionally, it can be noted that R32 shows the lowest K_H^{eff} values in all DESs, followed by R134a, R143a, and R125. This is directly related to values of $\alpha_{i/j}$, displayed for different HFC combinations. Despite lower absorption capacities compared to fluorinated eutectic solvents [203], the studied DESs exhibit commendable selectivities for given HFC mixtures. The highest $\alpha_{i/j}$ values are obtained for the R32/R125 combination, with $[N_{1111}]$Cl:GL (1:3) showing the highest ideal selectivity. In turn, for R134a/R143a, ideal selectivity reaches its highest value with [Ch]Cl:EG (1:3).

Finally, competitive selectivities, $S_{i/j}$, related to the commercial blends R410A (50 wt.% R32 + 50 wt.% R125), R407F (30 wt.% R32 + 30 wt.% R125 + 40 wt.% R134a), and R404A (44 wt.% R125 + 52 wt.% R143a + 4 wt.% R134a) were computed. Eq. 4.45 can be directly applied for the binary R410A blend. However, an expression for the competitive selectivity of an HFC in ternary blends, such as R407F and R404A, must be proposed in an analogous manner. In this work, selectivity of species i from its mixture with species j and k is expressed using Eq. 8.1,

$$S_{i/(j+k)} = \left(\frac{y_j + y_k}{y_i}\right)\left(\frac{x_i}{x_j + x_k}\right). \tag{8.1}$$

Required liquid and vapor mole fractions in the multicomponent systems comprising HFC blends and DESs were obtained through flash calculations at 300.15 K and different pressures. Moreover, the global mole fraction of DES was fixed at a value of $z_{\mathrm{DES}} = 0.7$.

Results are illustrated in Figure 8.4, where the separation of R410A, R407F, and R404 was assessed through the selectivities $S_{\mathrm{R32/R125}}$, $S_{\mathrm{R32/(R125+R134a)}}$, and $S_{\mathrm{R134a/(R125+R143a)}}$, respectively. The analysis reveals a high thermodynamic efficiency in the separation of the R410A for the studied DESs, particularly for $[\mathrm{N}_{1111}]$Cl:GL (1:3). For the separation of R32 from the R407F blend, the same sequence of DES selectivities is obtained, although with generally lower values than those related to R410A. Finally, no significant differences are observed between selectivities for R134a in R404A among the studied DESs. With the lowest values within the considered refrigerant blends, [Ch]Cl:EG (1:3) shows the best performance in this case.

The effect of different pressures in selectivity can also be observed from Figure 8.4, highlighting the alignment with ideal selectivities at conditions of low pressure. While these conditions enhance separation performance, this comes at the cost of a reduced absorption capacity, as presented in Figure 8.2. On the other hand, conditions of higher pressures do not seem attractive, as they almost invariably lead to lower selectivities. Therefore, according to this analysis, operating under moderate pressure is advisable for an efficient HFC separation.

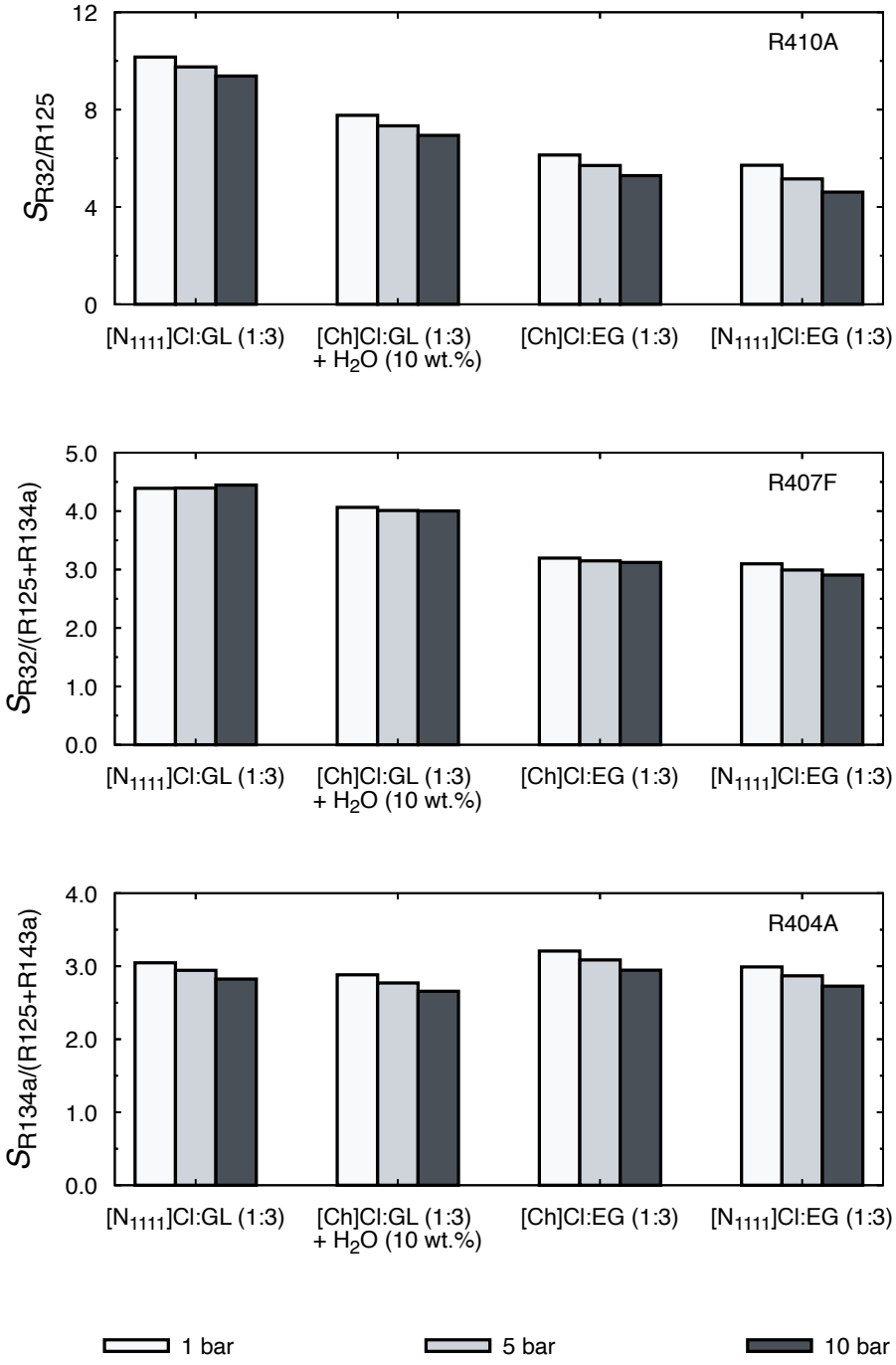

FIGURE 8.4: Selectivity of different HFCs in mixtures of refrigerant blends with DESs at 300.15 K, $x_{\text{DES}} = 0.7$, and different pressures. Results from the soft-SAFT EoS are shown.

8.4. Conclusions

In this work, the solubility of four common HFCs (R32, R143a, R134a, and R125) was investigated using four type III DESs, based on [Ch]Cl and [N_{1111}]Cl as HBAs and employing ethylene glycol and glycerol as HBDs. New experimental data for density, viscosity, and HFC solubilities were measured for the [N_{1111}]Cl-based DESs, at a HBA:HBD mole ratio of 1:3. Subsequently, the soft-SAFT EoS was used to generate molecular models for the considered systems. Moreover, this EoS was combined with FVT to correlate the measured viscosity of [N_{1111}]Cl-based DESs, demonstrating an acceptable performance.

Solubility trend across the DESs was observed as R32 > R134a > R125 > R143a, with [N_{1111}]Cl:EG (1:3) showing a higher solubility capacity. Despite a relatively low absorption, the investigated DESs exhibited promising selectivity for separating HFCs mixtures, particularly those containing R32, thereby suggesting potential applications in separating commercial blends like R410A and R407F.

The detailed thermodynamic modeling further supports the applicability of the soft-SAFT EoS in accurately describing these systems, facilitating the prediction of various crucial properties for process design and scale-up, including density and viscosity of pure DESs, dissolution enthalpy, effective Henry's constants, as well as ideal and competitive selectivity. In particular, the soft-SAFT EoS allowed to study the behavior of competitive selectivity under various operational conditions. This analysis enabled the identification of suitable DES candidates for recovering R32 and R134a from commercial refrigerant blends.

These findings offer a valuable insight into the thermodynamic behavior in mixtures comprised of HFCs and type III DESs. However, the comprehensive development and implementation of an efficient separation process for the recovery of these gases should include additional considerations, such as recycling stability, economic evaluation and life cycle assessment.

9. Assessing the Phase-out of R410A Using Deep Eutectic Solvents

In this chapter, extractive distillation using the [Ch]Cl:EG DES is evaluated as an alternative reclamation route for the R410A refrigerant blend, combining process simulation with life cycle assessment and supply chain optimization within a multiscale framework. The environmental performance of DES-based reclamation is compared with conventional treatment pathways, and its system-level impact is assessed through multiregional projections of R410A consumption and end-of-life management from 2025 to 2050. The environmental advantages of DES-based reclamation depend on the extent to which recovered components supply their demand over fresh production. Moreover, the implementation of DES-based reclamation can reduce cumulative use- and disposal-related CO_2e emissions by 45% relative to destruction-oriented scenarios, with earlier deployment being key to accomplish larger avoided emissions. Emissions associated to the use phase remain a dominant contributor to the overall carbon footprint, limiting the relative benefit of the proposed process.

9.1. Introduction

The limitations of business-as-usual (BAU) reclamation of refrigerant blends is exemplified by R410A. As this equimass blend of R32 and R125 exhibits near-azeotropic behavior, the recovery of its individual components by common distillation methods is heavily impeded [282]. Widely adopted as a replacement for chlorodifluoromethane (R22) [283, 284], R410A remains prevalent in modern refrigeration systems, especially in developing countries. However, its high GWP of 1924 [11] ensures its inclusion in the phase-out schedule of the Kigali Amendment of the Montreal Protocol (KA), demanding the cease of production, consumption, and in-stock quantities in the near future. Thus, to enable a circular management of R410A, the selective recovery of their constituents via extractive distillation emerges as a promising route from an environmental viewpoint.

Type III DESs reported particularly high affinities for R32, with selectivities up to 10 for its separation from R125 [285]. In particular, a DES composed of choline chloride ([Ch]Cl) and ethylene glycol (EG) in a 1:3 molar ratio, [Ch]Cl:EG (1:3), has shown to yield the selective separation of these

components [266]. Thus, the use of this DES as an entrainer for the separation of R410A emerges as a promising alternative for the phase-out of this blend.

DESs are frequently described as green solvents, one of their most attractive features compared to ILs [265]. However, this characterization is highly dependent on the considered application, as well as the production process of its constituents [68]. In this context, life cycle assessment (LCA), as a tool for evaluating and comparing the environmental impacts associated with different process alternatives [185], provides valuable information regarding the sustainability of emerging solvents such as DESs. Previous contributions have applied LCA to the HFC recovery using ILs [66] and DESs [67], based on process simulation as a reliable source of material and energy requirements. In both cases, the studied process was reported to achieve reductions of around 90% in the overall carbon footprint compared to the BAU production of the considered HFCs. In particular, Clinjk et al. [67] evaluated a DES composed of [Ch]Cl and lactic acid for the recovery of R125 from R410A, highlighting this approach as an effective pathway to replace conventional production routes from this blend. These results highlight the importance of further evaluating DES candidates for the reclamation of pure HFCs from refrigerant mixtures. However, within the ongoing phase-out of R410A, DES-based reclamation has yet to be assessed as an effective end-of-life alternative, both relative to BAU treatment pathways and in terms of the environmental implications associated with its deployment.

In this chapter, treatment of R410A by DES-based reclamation, using [Ch]Cl:EG (1:3), is assessed as an alternative route to support the phase-out of this refrigerant blend. The environmental impacts associated to this process are compared to those of chemical destruction as an end-of-life treatment. Moreover, the effect of its deployment are evaluated by incorporating DES-based reclamation into projections of multi-regional consumption and treatment routes of R410A. To this end, a supply chain model is developed to identify environmentally favorable combinations of supply and end-of-life alternatives under different scenarios. Process simulations of DES-based reclamation are used to estimate the material and energy requirements of this technology, relying on previously parameterized thermodynamic models [168, 286, 287] and considerations for transport properties. The provided multiscale framework proved effective for evaluating DES-based reclamation from process to supply chain level, providing insights into the role of novel solvents in a cleaner phase-out of high-GWP refrigerants.

9.2. Methods

The framework applied in this work involves the combined use of the PC-SAFT EoS, process simulation, LCA, and supply chain analysis to holistically study the performance of this DES in the recovery of R32 and R125 from the R410A refrigerant blend.

9.2.1. Thermophysical modeling

The PC-SAFT EoS [141, 142] was selected as the thermodynamic model in this work, given its robust framework and wide implementation in process simulation software. To model the [Ch]Cl:EG (1:3) DES, available molecular parameters for [Ch]Cl and EG were directly applied [168, 286]. Each

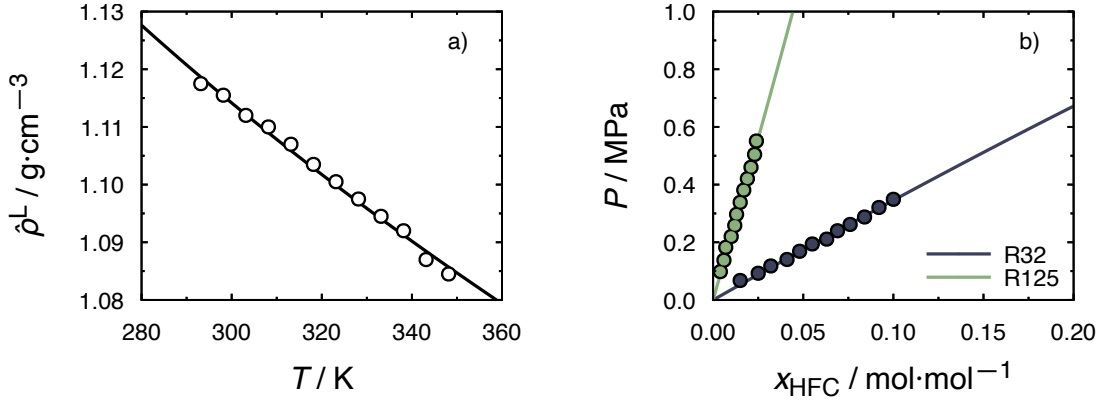

FIGURE 9.1: Liquid mass density of ChCl:EG (1:3) at different temperatures (a) and solubility isotherms of R32 and R125 in ChCl:EG (1:3) (b). Results from the PC-SAFT EoS are shown (—) and compared with available experimental data (○) [266].

compound is considered to present a 2B association scheme [148]. The thermodynamic characterization of the solvent mixture was completed by including a [Ch]Cl–EG binary interaction parameter, $k_{[Ch]Cl–EG}$, previously optimized to experimental density data [288]. Although this parameter was originally fit to [Ch]Cl:EG at a 1:2 mole ratio, direct transfer to the studied 1:3 ratio yields a convincing depiction of available liquid density data, as shown in Figure 9.1a. Values for this binary parameter are presented in Table 9.1.

For R32 and R125, previously optimized, non-associating, parameters were directly applied [287]. Although these parameters are precise in the modeling of pure HFCs, its phase equilibrium with the considered solvents require additional information due to the polarization in the liquid phase. These effects were considered by including cross-association between the HFCs and the DES precursors. This was achieved by fixing the association energy, $\epsilon^{A_iB_i}$, to zero for both HFCs, while considering an association volume of $\kappa^{A_iB_i} = 0.1$ for these species. The association scheme for both HFCs was set to 2B, in order to mimic the generated dipole moment. Additionally, different k_{ij} values were fit to available experimental solubility data, and are presented in Table 9.1. As can be seen from Figure 9.1b, a good depiction of solubility isotherms is provided by the PC-SAFT EoS. Moreover, a R32–R125 binary interaction parameter, also presented in Table 9.1, was included to correctly represent the azeotrope of the R410A blend.

For BAU reclamation, the original PC-SAFT model for decane [141] was used as a surrogate for heavy oils present in used R410A, recovered from refrigeration equipment. No binary interaction parameter was fit in this case. As for R410A destruction, reactants and products of the incineration were obtained from reported combustion schemes for HFCs [289, 290]. Thus, besides R410A, oxygen, water, hydrogen fluoride, carbon monoxide, and carbon dioxide were considered for this process. Water was modeled after the work of Cameretti and Sadowski [291], where a temperature-dependent segment diameter, $\sigma_{T,ii}$, was fit to describe its density at low temperatures. In order to transfer this water model to Aspen Plus simulations, where only scalar segment diameters are

TABLE 9.1: Binary dispersion interaction parameters, k_{ij}, between species related to the DES-based reclamation process.

i	j	k_{ij}
[Ch]Cl	EG	[a]
[Ch]Cl	R32	-0.05199
[Ch]Cl	R125	-0.08581
EG	R32	0.06489
EG	R125	0.07261
R32	R125	0.00649

[a] A temperature dependent binary parameter of $k_{ij} = 0.5169 - 0.001397 \cdot T$ [K] was used [288].

allowed, a mean value was computed following Eq. 9.1,

$$\sigma_{ii} = \frac{1}{T_1 - T_0} \int_{298\,K}^{373\,K} \sigma_{T,ii} dT \,. \tag{9.1}$$

On the other hand, oxygen, carbon monoxide, and carbon dioxide were modeled after their original PC-SAFT parameters [141], while hydrogen fluoride was modeled based on the work by Towne et al. [292]. All parameters for these additional species are presented in Table 9.2.

Transport properties, required for rate-based modeling of the distillation column, were included based on models available in the Aspen Plus suite. Namely, the liquid-phase behavior of viscosity, thermal conductivity, and surface tension must be correlated or predicted to include transport limitations in the absorption process. The DIPPR family of models was used to correlate available experimental data for [Ch]Cl:EG (1:3) and its mixture with R32 and R125. While parameters are available for EG and both HFCs, no parameters are available for [Ch]Cl, as it is not a liquid at atmospheric conditions. To tackle this problem, DIPPR coefficients for [Ch]Cl were regressed based on reported data on viscosity [266], thermal conductivity [293], and surface tension [294] for the [Ch]Cl:EG DES. Resulting parameters are presented in Table 9.3.

For pure species i, liquid viscosity, η_i^{L} and surface tension, ς_i, where computed following Eqs. 9.2 and 9.3, respectively.

$$\ln \eta_i^{\mathrm{L}} = C_{1,i} + \frac{C_{2,i}}{T} + C_{3,i} \ln T + C_{4,i} T^{C_{5,i}} \,; \quad T \in [T_{\min},\, T_{\max}] \,. \tag{9.2}$$

$$\ln \varsigma_i = \ln \left(C_{1,i} [1 - T_{r,i}] \right) \left(C_{2,i} + C_{3,i} T_{r,i} + C_{4,i} T_{r,i}^2 + C_{5,i} T_{r,i}^5 \right) \,; \quad T \in [T_{\min},\, T_{\max}] \,. \tag{9.3}$$

Moreover, liquid thermal conductivity, λ_i^{L} was computed from two different available correlations. For HFCs and DESs precursors, λ_i^{L} was computed from Eqs. 9.4 and 9.5, respectively.

TABLE 9.2: Molecular weight and PC-SAFT molecular parameters for the considered DES, HFCs, and compounds related to R410A destruction and BAU reclamation.

Compound	M_w [g·mol^{-1}]	$m_{s,i}$	σ_{ii} [Å]	ε_{ii}/k_B [K]	$\varepsilon^{A_iB_i}/k_B$ [K]	$\kappa^{A_iB_i}$	Assoc. scheme	Source
[Ch]Cl	139.63	13.020	2.368	228.07	8000.00	0.20000	2B	[168]
EG	62.07	2.437	3.233	344.06	2702.60	0.02216	2B	[286]
R32	52.00	2.554	2.781	181.28	0.00	0.10000	2B	[287]
R125	120.02	3.052	3.148	158.12	0.00	0.10000	2B	[287]
Decane	142.29	4.6627	3.8384	243.87	0	0	-	[141]
Water	18.02	1.205	2.790[a]	353.94	2425.67	0.04509	2B	[291]
Carbon dioxide	28.01	2.0729	2.7852	169.21	0	0	-	[141]
Carbon monoxide	44.01	1.3097	3.2507	92.15	0	0	-	[141]
Hydrogen fluoride	20.01	1.821	2.278	117.8	1791	3.0749	2B	[292]

[a] A mean value for the temperature-dependent collision diameter was used.

$$\lambda_i^{\mathrm{L}} = C_{1,i} + C_{2,i}T + C_{3,i}T^2 + C_{4,i}T^3 + C_{5,i}T^4\,; \quad T \in [T_{\min},\, T_{\max}]\,, \tag{9.4}$$

$$\lambda_i^{\mathrm{L}} = C_{1,i}\left(1 + C_{2,i}T_{r,i}^{1/3} + C_{3,i}T_{r,i}^{2/3} + C_{4,i}T_{r,i}\right)\,. \tag{9.5}$$

Subsequently, liquid viscosity, surface tension, and liquid thermal conductivity of mixtures were obtained following the default models of mixing rules available in Aspen Plus.

9.2.2. Process simulation of the treatment routes of R410A

DES-based reclamation

DES-based reclamation was modeled as the extractive distillation of R410A to obtain high-purity R125, followed by solvent regeneration to obtain high-purity R32, allowing to reuse the DES in a new absorption cycle. The algorithm proposed by Finberg and Shiflett [282] was employed to optimize distillate and bottoms purity obtained from the distillation column. The height of this equipment was constrained to a maximum of 40 stages. Moreover, although DESs are coined with high thermal stability and negligible volatility, previous studies have expanded on the measurable volatility for ethylene glycol-based solvents [45]. As the temperature stability of DESs is inherently lower than ILs previously studied for this application [282], the process was simulated considering a maximum bottoms temperature of 80°C. The distillation column was represented by a rate-based RADFRAC model, with reboiler and condenser, thus accounting for mass transfer limitations in the DES. A packed column was considered, with Sulzer Mellapak 125X structured packing installed in the mass transfer section of the column, *i.e.*, between stages 2 and $N_{\mathrm{T}} - 1$. The packing bed was represented using a height of 0.5 m per theoretical plate and a column diameter of 0.2 m.

TABLE 9.3: Parameters for DIPPR correlations for liquid viscosity, η_i^{L}, surface tension, ς_i, and liquid thermal conductivity, λ_i^{L}, for the species considered in this work.

Property	i	$C_{1,i}$	$C_{2,i}$	$C_{3,i}$	$C_{4,i}$	$C_{5,i}$	$T_{\min}$ [K]	$T_{\max}$ [K]
η_i^{L} [cP]	[Ch]Cl	47.6293	$-1.0518\cdot10^{-2}$	–7.546	$-9.909\cdot10^{-4}$	1	273.15	400.00
	EG	-158.162	10210	22.26	$-1.128\cdot10^{-16}$	6	260.15	470.38
	R32	-10.8152	850.20	1.060	$-1.172\cdot10^{-18}$	7	137.00	343.15
	R125	6.09322	513.94	–1.717	0	0	170.15	333.19
ς_i [mN·m^{-1}]	[Ch]Cl	106.119	0.64808	1.525	$1.090\cdot10^{-2}$	0	273.15	400.00
	EG	50.6810	-0.51224	1.484	0.	0.	260.15	719.00
	R32	69.3620	1.2273	0.	0.	0.	136.95	351.26
	R125	53.6790	1.2463	0.	0.	0.	170.15	339.17
λ_i^{L} [W·m^{-1}·K^{-1}]	[Ch]Cl	–0.594231	–2.9568	–1.845	3.966	0	273.15	400.00
	EG	0.179780	–6.8432	19.54	–12.88	0	260.15	647.10
	R32	0.149778	$-6.4173\cdot10^{-4}$	$2.215\cdot10^{-7}$	0	0	136.95	302.56
	R125	$7.0622\cdot10^{-2}$	$-3.6524\cdot10^{-4}$	$1.962\cdot10^{-8}$	0	0	170.15	333.15

In the optimized process, a flow of 10 kg of R410A at 300.15 K and 2 MPa enters the distillation column on its 14$^{\text{th}}$ stage, while 42 kg of [Ch]Cl:EG (1:3), at the same temperature and pressure, enters through the 2$^{\text{nd}}$ stage of the equipment, taking advantage of its low vapor pressure. From the top of the column, R125 is obtained at 99.6% purity and 15°C, while at the bottoms a mixture of [Ch]Cl:EG (1:3) and R32 at 70°C is brought to a heat exchanger to lower its temperature to 15°C. A flash vessel, operated at 0.01 MPa and 15°C, is used to regenerate the solvent, allowing to obtain R32 with a 99.5% purity and recovering the DES from the liquid phase. The regenerated solvent is transported to a pump to restore its initial pressure and then re-entered to the distillation column. The resulting process is presented in Figure 9.2.

BAU reclamation

BAU reclamation was modeled as a conventional distillation-based purification process. A feed stream of R410A containing 1 wt.% decane as an impurity is introduced into a distillation column simulated using the RADFRAC model with equilibrium considerations only. A total of 10 equilibrium stages were considered, operating at 1.5 MPa as a common operation condition for the effective separation of heavy components. Thus, decane is recovered in the bottoms stream, while R410A is obtained as the distillate with a mass purity of 99.9%. The process was designed to deliver a distillate flow rate of 100 kg·h^{-1} of purified R410A.

R410A destruction

R410A destruction was modeled as high-temperature thermal oxidation, based on the wider availability of this technology compared to emerging pyrolysis-based alternatives [295]. Based on established reaction schemes [289, 290], the process feed consists of R410A, air (21 wt.% O_2, 79 wt.%

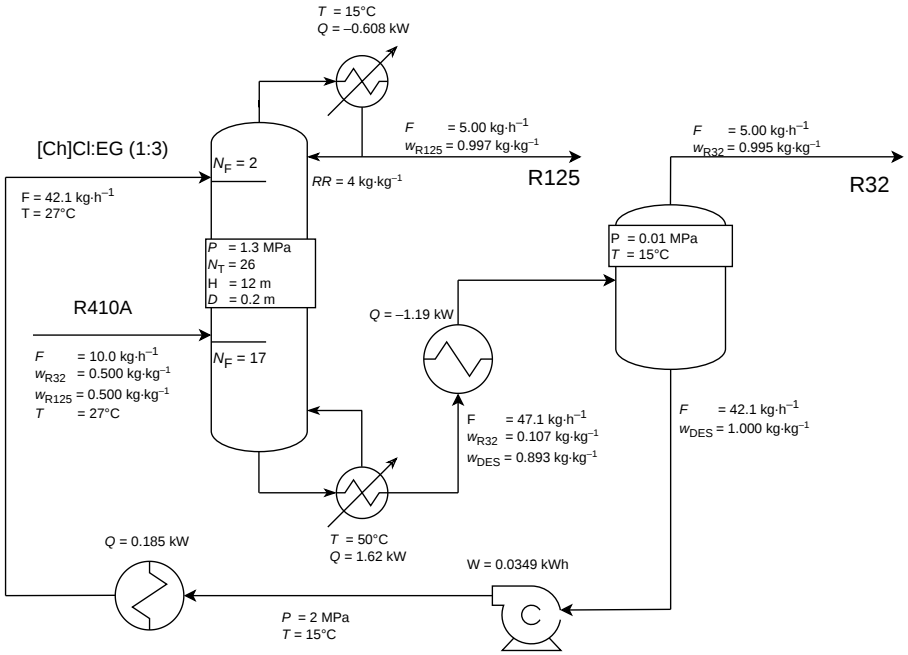

FIGURE 9.2: Extractive distillation process for separating R410A with [Ch]Cl:EG (1:3) as entrainer.

N_2), and water, while the main reaction products are assumed to be hydrogen fluoride, carbon monoxide, carbon dioxide, and water. The reactants are fed into a thermodynamic equilibrium reactor, represented by a RGIBBS model, with a feed of 1 kg·h^{-1} of R410A, 0.2 kg·h^{-1} of water to promote a complete conversion to hydrogen fluoride, and excess air. The reactor operates at 1500 K and 0.01 MPa, representing common operation conditions of high temperature and negative pressure.

9.2.3. Environmental assessment

To quantify the environmental impact of the treatment of R410A by different routes, a consequential LCA was performed following a cradle-to-grave approach with a cutoff approach, under the ISO14040/44 framework [191]. The goal was to compare the treatment of R410A by destruction and DES-based reclamation. To this end, the functional unit was defined as the treatment of 1 kg of used R410A. All computations were performed using the Brightway2 [296] suite.

Life cycle inventories (LCIs) for the foreground system were generated from the background data available in the ecoinvent v3.9 database [192]. DES-based reclamation activity is generated by first applying BAU reclamation to obtain a flow of R410A free of impurities. Then, the clean R410A flow is separated into R32 and R125, both with at least a 99.5% purity, by azeotropic distillation using [Ch]Cl:EG (1:3) as entrainer. The generation of these HFCs was accounted for by crediting

TABLE 9.4: Geographic regions considered in this work, along with their Kigali Amendment consumption baselines and group type.

Region	Abbreviation	KA consumption baseline [Mt_{CO_2e}]	Group type
European Union	EU	184.2	non-A5
China	CN	813.0	A5, group 1
United States	US	302.5	non-A5

their avoided BAU production, for which previously reported inventories [66, 67] were directly applied. The production process of [Ch]Cl was directly taken from the work of Zaib et al. [68], while production of EG was directly taken from the ecoinvent database. For R410A destruction, it was considered that all obtained hydrogen fluoride was converted to fluorine-based salts by using calcium hydroxide at the outlet of the system [290]. The recovery of hydrogen fluoride was accounted for by crediting the avoided production of this compound. The constructed LCIs for R410A destruction, BAU reclamation, and DES-based reclamation are presented in Tables D.1, D.2, and D.3, respectively.

The life cycle impact assessment (LCIA) was done following the ReCiPe 2016 v1.03 methodology [194]. Using the hierarchical approach, six environmental midpoint categories were considered, *i.e.*, global warming potential (GWP), terrestrial acidification potential (TAP), human toxicity potential (HTP), ozone depletion potential (ODP), water consumption potential (WCP), and fossil fuel potential (FFP). Moreover, the tree general endpoint categories, *i.e.*, ecosystem quality (EQ), human health (HH), and natural resources (NR), where also considered.

Uncertainty in environmental impacts was assessed by performing a Monte Carlo sampling of 1200 background inventories. This sampling was stochastically generated from the probability distribution functions characterizing the uncertainty of LCI parameters [297], allowing to determine the frequency, f, of runs related to a given quantity on each environmental impact. For each impact category i, the difference between the score of DES-based reclamation and destruction, ΔEI_i, was computed at each respective run. Then, the probability of burden shifting in DES-based reclamation was estimated as the fraction of runs where $\Delta EI_i > 0$ [298].

9.2.4. Supply chain analysis

To quantify the environmental impact associated to the deployment of DES-based reclamation, the consumption and disposal of R410A was modeled across three geographical regions, namely the European Union, China, and United States, given the availability of supply data. A time horizon of 40 years was considered, spanning from $Y_0 = 2010$ to $Y_2 = 2050$. To this end, the KA phase-down schedule for each region was first determined based on the consumption baselines reported in Table 9.4. According to the group type of each region, different reduction steps on R410A consumption were applied [299].

Regional HFC consumption over this period was then compiled from available historical data and projections [27, 299–302]. For regions lacking full time-series projections, future consumption was estimated by scaling the mean consumption of the last available KA phase-down step, e.g., 2019–2023 for non-A5 regions, according to the phase-down trajectory. In cases where region-specific projections of total HFC demand were unavailable, total HFC consumption was assumed to follow the KA schedule proportionally, using the consumption baseline as reference.

Finally, R410A consumption was derived by assuming that its share of total HFC consumption, expressed in t_{CO_2e}, decreases to zero by year Y_2, consistent with a complete phase-out of high-GWP refrigerants. A linear decrease scheme was adopted as a simple model to represent the progressive reduction in its use, in the absence of region-specific measures. The parameter f^{BL}, with a reference global value of 0.30, was defined as the initial share of R410A in total HFC consumption, evaluated at the last year prior to KA-driven consumption reduction in each region.

Based on the computed R410A consumption projections, annual emissions, in-use stocks, and recoverable end-of-life masses were computed based on the 2006 and 2019 IPCC Guidelines [303, 304], which have proven feasible in the modeling of usage trends for fluorocarbons [299, 305–308]. As a main assumption, initial R410A stocks were considered to be zero, thus ignoring previous years of demand for this compound in the comparative analysis. R410A stocks at year y_i and in region r_j, $\mathrm{ST}_{i,j}$, were computed according to Eq. 9.6,

$$\mathrm{ST}_{i,j} = \begin{cases} 0 & , i = 0 \\ \mathrm{ST}_{i-1,j} + \mathrm{C}_{i,j} - \mathrm{EM}_{i,j} & , i \geq 1 \,, \end{cases} \tag{9.6}$$

where $\mathrm{C}_{i,j}$ and $\mathrm{EM}_{i,j}$ are the R410A consumption and emissions at year y_i and in region r_j, respectively. R410A consumption is divided into initial, $\mathrm{C}^{\mathrm{init}}_{i,j}$, and servicing, $\mathrm{C}^{\mathrm{serv}}_{i,j}$, contributions, which respectively represent the consumption related to initial charging and servicing of equipment. These quantities follow the relationship given by Eq. 9.7,

$$\mathrm{C}_{i,j} = \mathrm{C}^{\mathrm{init}}_{i,j} + \mathrm{C}^{\mathrm{serv}}_{i,j} \,. \tag{9.7}$$

In this work, it was assumed that at the initial year, $Y_0 = 2010$, and in all considered regions, R410A consumption is given solely by initial servicing, and that the fraction of this flow from the total consumption decreases linearly until reaching zero at the year $Y^{\mathrm{serv}} = 2040$. Consequently, the share of servicing demand in the R410A consumption is assumed to grow linearly until representing all R410A demand by year Y^{serv}. On the other hand, R410A emissions were computed following Eq. 9.8,

$$\mathrm{EM}_{i,j} = \mathrm{EM}^{\mathrm{cha}}_{i,j} + \mathrm{EM}^{\mathrm{ope}}_{i,j} + \mathrm{EM}^{\mathrm{dis}}_{i,j} \,, \tag{9.8}$$

where $\mathrm{EM}^{\mathrm{cha}}_{i,j}$, $\mathrm{EM}^{\mathrm{ope}}_{i,j}$, and $\mathrm{EM}^{\mathrm{dis}}_{i,j}$ are the emissions related to the charging, operation, and disposal of the refrigeration equipment, respectively. The charging emissions are computed as shown in Eq. 9.9,

$$\mathrm{EM}_{i,j}^{\mathrm{cha}} = \varepsilon^{\mathrm{cha}}\, \mathrm{C}_{i,j}^{\mathrm{init}}\,, \tag{9.9}$$

where $\varepsilon^{\mathrm{cha}}$ is the emission factor for the charging operation. On the other hand, operational and end-of-life emissions are dependent of the retiring fraction of equipment after i years of use, f_i^{EOL}. As done in previous contributions [306], a Weibull distribution function was used to model this fraction, presented in Eq. 9.10,

$$f_i^{\mathrm{EOL}} = \frac{\beta}{\lambda}\left(\frac{i}{\lambda}\right)^{\beta-1} \exp\left[-\left(\frac{i}{\lambda}\right)^{\beta}\right]\,, \tag{9.10}$$

where λ and β are the scale and shape parameters of the function, respectively, and were fit to data reported by Chen et al. [307] of disposal patterns of commercial air conditioning equipment. Thus, values of $\lambda = 14.73$ and $\beta = 13.96$ were used as default in the model. It is worth noting that, although these values are China-specific, they were applied to all considered regions, in order to define a base-case retirement of R410A-based equipment.

Upon defining the R410A retired fraction for each year, operational emissions were computed as the surviving equipment at each year following Eq. 9.11,

$$\mathrm{EM}_{i,j}^{\mathrm{ope}} = \begin{cases} \varepsilon^{\mathrm{ope}}\left(1 - f_i^{\mathrm{EOL}}\right) Q_{i,j} & ,\, i = 0 \\ \varepsilon^{\mathrm{ope}}\left[\left(1 - \sum_{k=0}^{i} f_k^{\mathrm{EOL}}\right) Q_{0,j} + \sum_{k=1}^{i}\left(1 - \sum_{l=0}^{i-k} f_l^{\mathrm{EOL}}\right)\left(Q_{k,j} - \mathrm{EM}_{k-1,j}^{\mathrm{ope}}\right)\right] & ,\, i \geq 1\,, \end{cases} \tag{9.11}$$

where $Q_{i,j} = \mathrm{C}_{i,j} - \mathrm{EM}_{i,j}^{\mathrm{cha}}$ and $\varepsilon^{\mathrm{ope}}$ is the emission factor of the operation of refrigeration equipment. In turn, disposal emissions are computed as the non-recoverable fraction of the total end-of-life R410A, $\mathrm{EOL}_{i,j}$, following Eq. 9.12,

$$\mathrm{EM}_{i,j}^{\mathrm{dis}} = (1 - \eta^{\mathrm{rec}})\mathrm{EOL}_{i,j}\,, \tag{9.12}$$

where η^{rec} is the recoverable fraction of the end-of-life refrigerant. The $\mathrm{EOL}_{i,j}$ flow is directly obtained from the retirement distribution as shown in Eq. 9.13,

$$\mathrm{EOL}_{i,j} = \begin{cases} f_i^{\mathrm{EOL}}\, Q_{i,j} & ,\, i = 0 \\ f_i^{\mathrm{EOL}}\, Q_{0,j} + \sum_{k=1}^{i} f_{i-k}^{\mathrm{EOL}}\left(Q_{k,j} - \mathrm{EM}_{k-1,j}^{\mathrm{ope}}\right) & ,\, i \geq 1\,. \end{cases} \tag{9.13}$$

Thus, besides disposal emissions, the recoverable end-of-life, $\mathrm{EOL}_{i,j}^{\mathrm{rec}}$ was computed from Eq. 9.14,

$$\mathrm{EOL}_{i,j}^{\mathrm{rec}} = \eta^{\mathrm{rec}}\, \mathrm{EOL}_{i,j}\,. \tag{9.14}$$

All emission factors and recovery efficiency were fixed to the recommended values from the IPCC Guidelines [304], and thus $\varepsilon^{\text{cha}} = 0.05$, $\varepsilon^{\text{ope}} = 0.10$, and $\eta^{\text{rec}} = 0.90$.

Once all required flows were obtained, a supply chain optimization model was constructed to satisfy the projected R410A consumption and manage the end-of-life R410A, for all years $y_i > Y_1 = 2025$ and regions r_j. Thus, R410A supply was established as a combination of fresh production, $\text{F}_{i,j}$, BAU reclamation, $\text{R}_{i,j}^{\text{BAU}}$, imports, $\text{I}_{i,j,j'}$, and exports, $\text{I}_{i,j',j}$, while end-of-life corresponds to either venting, $\text{V}_{i,j}$, destruction, $\text{D}_{i,j}$, BAU reclamation, $\text{R}_{i,j}^{\text{BAU}}$, or DES-based reclamation, $\text{R}_{i,j}^{\text{DES}}$. For each optimization run, the overall global warming impact, GWI (expressed in $\text{t}_{\text{CO}_2\text{e}}$), was minimized subject to the mass balance and capacity constraints, allowing to identify the most environmentally favorable allocation of supply and end-of-life treatment pathways.

The optimization problem is formulated in Eq. 9.15. Here, the $\text{I}_{i,j,j'}$ matrix defines the imports, at year y_i, from region $r_{j'}$ to region r_j, simultaneously defining exports from region r_j to region $r_{j'}$. The characterization factors, cf, for each flow were obtained directly from the performed LCA, and are presented in Table 9.5. The characterization factor for trade flows was computed considering the transport of R410A by sea, and using the mean distance across all regions. Moreover, all decision variables were constrained to be non-negative.

$$
\begin{aligned}
\min \quad & \sum_{i=1}^{n_y}\sum_{j=1}^{n_r} \text{GWI}_{i,j} = \sum_{i=1}^{n_r}\sum_{j=1}^{n_r} cf^{\text{F}}\,\text{F}_{i,j} + cf^{\text{R,BAU}}\,\text{R}_{i,j}^{\text{BAU}} \\
& + cf^{\text{R,DES}}\,\text{R}_{i,j}^{\text{DES}} + cf^{\text{D}}\,\text{D}_{i,j} + cf^{\text{V}}\,\text{V}_{i,j} + \sum_{j'=1}^{n_r} cf_{j,j'}^{\text{I}}\,\text{I}_{i,j,j'} \\
\text{s.t.} \quad & \text{C}_{i,j} - \text{F}_{i,j} - \sum_{j'=1}^{n_r}\left(\text{I}_{i,j,j'} - \text{I}_{i,j',j}\right) - \text{R}_{i,j}^{\text{BAU}} = 0\,, && y \geq Y_1, \forall j \\
& \Theta_{i,j}^{\text{KA}} - \text{F}_{i,j} - \sum_{j'=1}^{n_r}\left(\text{I}_{i,j,j'} - \text{I}_{i,j',j}\right) \geq 0\,, && y \geq Y_1, \forall j \\
& \text{I}_{i,j,j} = 0\,, && y \geq Y_1, \forall j \\
& \text{EOL}_{i,j}^{\text{rec}} - \text{D}_{i,j} - \text{V}_{i,j} - \text{R}_{i,j}^{\text{BAU}} - \text{R}_{i,j}^{\text{DES}} = 0\,, && y \geq Y_1, \forall j \\
& f_j^{\text{IC,D}}\,\text{EOL}_{i,j}^{\text{rec}}\,\left((1+\xi)^{y_i - Y_1}\right) - \text{D}_{i,j} \geq 0\,, && y \geq Y_1, \forall j \\
& f_j^{\text{IC,R}}\,\text{EOL}_{i,j}^{\text{rec}}\,\left((1+\xi)^{y_i - Y_1}\right) - \text{R}_{i,j}^{\text{BAU}} \geq 0\,, && y \geq Y_1, \forall j \\
& \text{R}_{i,j}^{\text{DES}} = 0\,, && y_i < Y^{\text{RDES,0}}, \forall j \\
& f_j^{\text{IC,R}}\,\text{EOL}_{i,j}^{\text{rec}}\,\left((1+\xi)^{y_i - Y^{\text{RDES,0}}}\right) f^{\text{RDES}} - \text{R}_{i,j}^{\text{DES}} \geq 0\,, && y_i \geq Y^{\text{RDES,0}}, \forall j
\end{aligned}
\tag{9.15}
$$

In Equation 9.15, the first constraint ensures that R410A consumption is satisfied through production, net trade (imports minus exports), and BAU reclamation. The second constraint limits its production plus net trade according to the maximum allowed consumption under the Kigali Amendment, $\Theta_{i,j}^{\text{KA}}$, for each year and region. The third constraint prohibits trades within the same

TABLE 9.5: Characterization factors for each flow considered in the supply chain model.

Flow	F	I	R^{BAU}	R^{DES}	D	V
cf / $kg_{CO_2e} \cdot kg_{R410A}^{-1}$	8.986	0.083	2.454	-8.402	4.294	2254

TABLE 9.6: Parameters related to the supply chain model for the multi-regional use and treatment of R410A.

Parameter	Definition	Reference value	Uncertainty
f^{BL}	Share of R410A of the total HFC consumption, in tCO_2e, in the last year without consumption reduction according to the KA (2018 for A5 regions, 2024 for non-A5 regions)	0.30	±0%
$f_j^{IC,D}$	Initial capacity, relative to the total recoverable end-of-life R410A at year Y_1, of destruction for region j	0.10 (A5 regions) 0.20 (non-A5 regions)	±35% (A5 regions) ±25% (non-A5 regions)
$f_j^{IC,R}$	Initial capacity, relative to the total recoverable end-of-life R410A at year Y_1, of BAU reclamation for region j	0.10 (A5 regions) 0.50 (non-A5 regions)	±35% (A5 regions) ±30% (non-A5 regions)
ξ	Annual growth rate of end-of-life technologies (destruction, BAU reclamation and DES-based reclamation)	0.05	±30%

region. The fourth constraint represents the mass balance for the recoverable end-of-life R410A, distributing this flow among destruction, venting, BAU reclamation, and DES-based reclamation.

The fifth and sixth constraints describe the available treatment capacities for destruction and BAU reclamation. The parameters $f_j^{IC,D}$ and $f_j^{IC,R}$ represent the fractions of recoverable end-of-life R410A that can be treated via destruction and BAU reclamation in the initial year Y_1, respectively. To model the development of these technologies over time, both capacities were assumed to increase according to a given compound annual growth rate, ξ.

The seventh constraint introduces the parameter $Y^{RDES,0}$, representing the year of initial deployment of DES-based reclamation. Finally, the eight constraint models the capacity growth of this technology, analogously to the other end-of-life treatments, and includes the parameter f^{RDES}, which defines the initial capacity of DES-based reclamation relative to the BAU reclamation capacity. The reference values for all the considered parameters are listed in Table 9.6.

Two main scenarios, namely the baseline and proposed scenarios, were defined by respectively prohibiting and allowing the deployment of DES-based reclamation in the supply chain model.

The global warming impacts at year y_i and region r_j for each case, $\mathrm{GWI}_{i,j}|_{\mathrm{Baseline}}$ and $\mathrm{GWI}_{i,j}|_{\mathrm{Proposed}}$, were then used to compute the multi-regional relative reduction in cumulative carbon footprint at year y_i, $\Delta\mathrm{GWI}_i$, as shown in Eq. 9.16,

$$\Delta\mathrm{GWI}_i = \frac{\sum_{j=1}^{n_r} \mathrm{GWI}_{i,j}|_{\mathrm{Proposed}} - \mathrm{GWI}_{i,j}|_{\mathrm{Baseline}}}{\sum_{j=1}^{n_r} \mathrm{GWI}_{i,j}|_{\mathrm{Baseline}}}. \tag{9.16}$$

Moreover, reduction in carbon footprint including system-level emissions, $\mathrm{E}_{i,j}$, was also considered by defining $\Delta\mathrm{GWI}'_i$ by Eq. 9.17,

$$\Delta\mathrm{GWI}'_i = \frac{\sum_{j=1}^{n_r} \mathrm{GWI}_{i,j}|_{\mathrm{Proposed}} - \mathrm{GWI}_{i,j}|_{\mathrm{Baseline}}}{\sum_{j=1}^{n_r} \mathrm{GWI}_{i,j}|_{\mathrm{Baseline}} + \mathrm{EM}_{i,j}}. \tag{9.17}$$

A sensitivity analysis was performed to quantify the uncertainty associated to the parameters presented in Table 9.6, which are related to the deploy and growth of destruction and BAU reclamation. The assumed share of R410A of the total HFC consumption, f^{BL}, demonstrated no effect on the relative difference ΔGWI, and thus was not varied across the different runs. A Monte Carlo analysis was done by conducting a latin hypercube sampling to generate different samples from the combination of these parameters, which were varied according to the different standard deviations also presented in Table 9.6. The minimization problem from Equation 9.15 was solved for both scenarios and for the 2000 iterations to generate a distribution for $\Delta\mathrm{GWI}_i$ and $\Delta\mathrm{GWI}'_i$. Uncertainty in each one of these computed quantities was then assessed by obtaining the 2.5^{th}–97.5^{th} percentile range in each case. Additionally, the 25^{th}–75^{th} percentile range was also computed to obtain information on the shape of the obtained distributions.

9.3. Results and Discussion

9.3.1. Environmental impacts of HFC reclamation

Figure 9.3 compares the GWP of destruction and DES-based reclamation (RDES) as two alternative end-of-life treatments for R410A. As shown, the lower carbon footprint of DES-based reclamation suggests a remarkable potential as a preferable end-of-life route for the studied refrigerant. Additionally, for both processes, fugitive emissions account for an important part of the global warming impact. For destruction, these emissions account for more than half of the overall GWP, with the remaining environmental impact primarily being associated to lime production and heat requirements. On the other hand, the positive GWP contributions of DES-based reclamation can be roughly divided into fugitive emissions, BAU reclamation, production of [Ch]Cl:EG (1:3), and heat

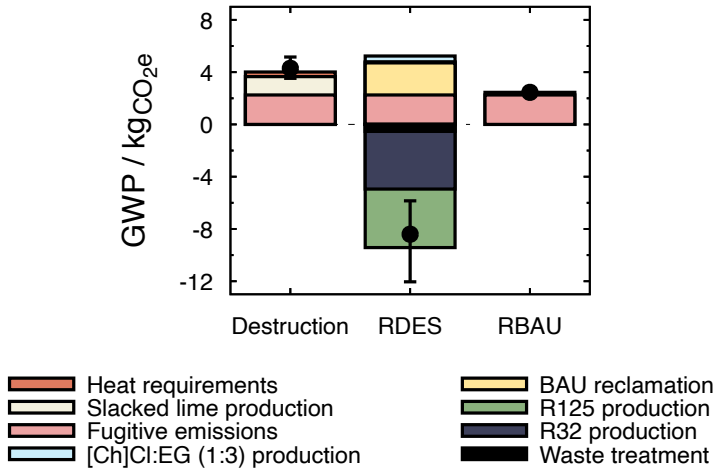

FIGURE 9.3: GWP associated to the treatment of 1 kg of R410A for alternative end-of-life routes. Contributions of individual processes (▭) and total GWP (●) are presented. Error bars represent the 5th–95th percentile range from Monte Carlo simulations.

requirements. Figure 9.3 also includes the main contributions for the GWP of BAU reclamation (RBAU), showing that its carbon footprint is almost completely controlled by fugitive emissions. Importantly, the avoided production of R32 and R125 is what enables the DES-based reclamation to reach a lower GWP than destruction. This suggests that the environmental benefit of this end-of-life route is subjected to its capacity to displace conventional production of these HFCs, and thus to the existing demand for these compounds.

To evaluate the presence of burden shifting in DES-based reclamation, different midpoint and endpoint indicators were also compared with the destruction treatment. Figure 9.4 summarizes the distribution of impacts of the two end-of-life routes over the sampled background scenarios. The difference between the environmental impact of DES-based reclamation and destruction, δEI is also shown to directly point the probability of burden shifting. Within the uncertainty range, most midpoint categories display a lower environmental impact for DES-based reclamation, suggesting that no marked burden shifting is present. The exception to this is the human toxicity potential category, for which a markedly low environmental impact is observed for the destruction process, while DES-based reclamation shows a higher uncertainty and burden shifting in 75% of the runs. As for the endpoint indicators, human health is the only one displaying an important probability of burden shifting, with a 50%. These results highlight that, within the uncertainty range, there is a non-negligible probability of burden shifting towards health-related impacts upon the implementation of DES-based reclamation.

9.3.2. Implementation of DES-based reclamation

Upon assessing the environmental impacts associated to the DES-based reclamation process, its impact in the carbon footprint of R410A usage over time was studied by performing a supply

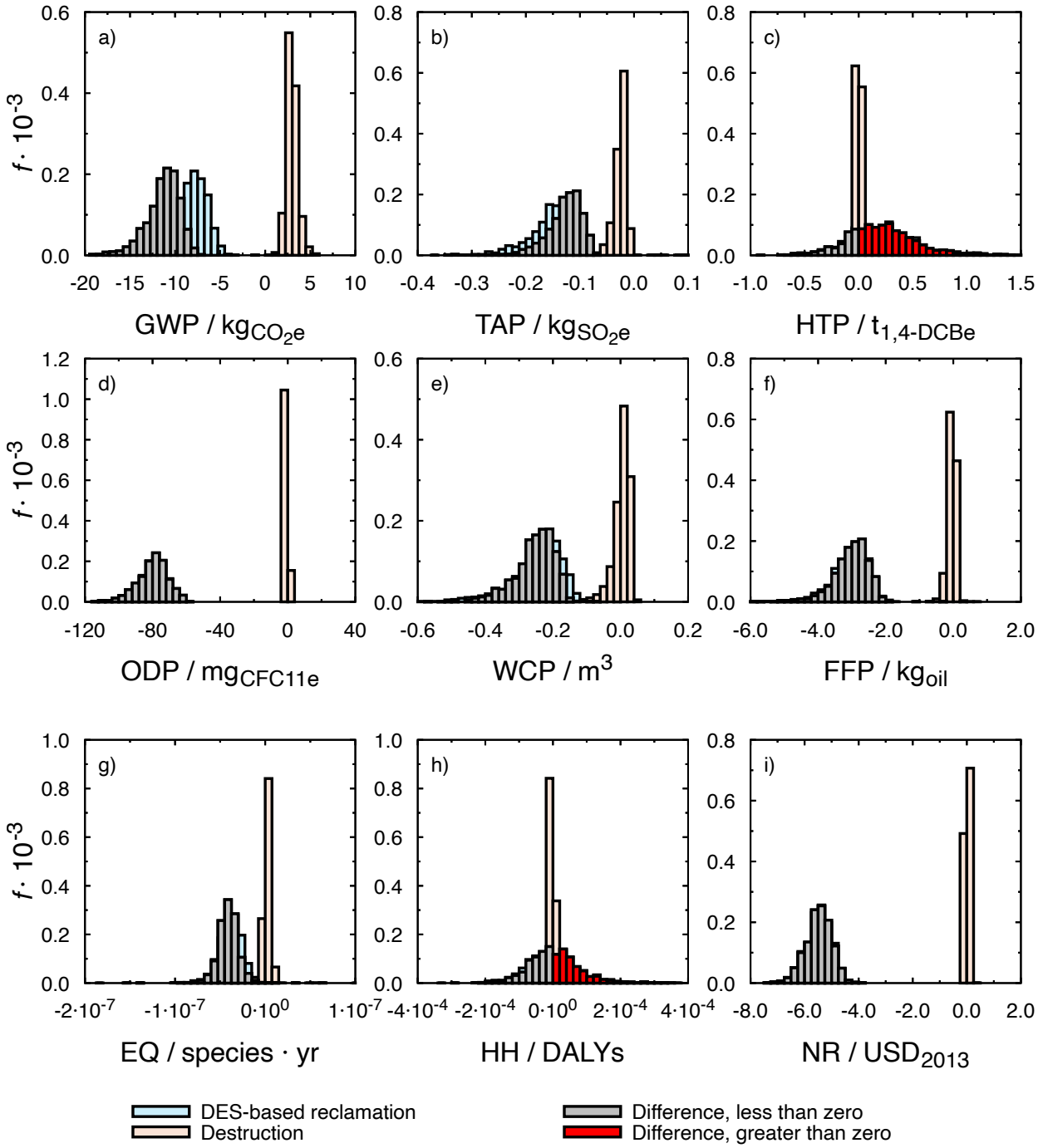

FIGURE 9.4: Distributions of midpoint and endpoint environmental categories from the ReCiPe 2016 v1.03 methodology [194], obtained from Monte Carlo simulations, for the treatment of 1 kg of R410A via DES-based reclamation and destruction. Differences between both routes are also shown, and the cases where DES-based reclamation leads to higher impacts are highlighted in red. The probability of burden shifting is reflected by the fraction of the difference distribution exceeding zero [298].

chain analysis. This effect was assessed by comparing the two considered scenarios, i.e., the baseline scenario, where no DES-based reclamation is allowed, and the proposed scenario, where this technology is implemented. Figure 9.5 shows the results of the minimized carbon footprint for both studied cases, reporting the different pathways for the end of life and supply of R410A, and additionally displaying the relative reduction in the overall global warming impact. Figures 9.5a and 9.5b compare the end-of-life treatment in both scenarios, first showing that early years are characterized by higher venting rates, consistently with a lower development of phase-out technologies. With the progressive reduction of end-of-life R410A, and the increase in destruction and reclamation capacity over time, both scenarios show a shift to a more environmentally friendly treatment of this refrigerant. In the baseline scenario, it can be seen that, at the end of the considered time period, a shift to the destruction of R410A is observed, driven by the drop in R410A consumption, shown in Figure 9.5c. On the other hand, for the proposed scenario, the addition of DES-based reclamation mainly reduces the share of R410A venting, and its development yields to almost the total replacement of destruction by the end of the period.

The distribution of consumption of R410A in both scenarios is almost unchanged, and is shown in Figure 9.5c for the baseline scenario. As can be seen, an important part of the demand is supplied by fresh production, given that projected R410A consumption is lower than maximum consumption allowed by the Kigali Amendment in all considered regions. Fresh R410A production is mainly controlled by China, given its historical role as the main producer of this refrigerant. Additionally, projections also show that a faster development of BAU reclamation is a key feature to reach lower a carbon footprint in the worldwide supply of R410A. For both scenarios, a full deployment of BAU reclamation for the end-of-life treatment of R410A in early years could ensure that around two thirds of the R410A demand is reached from a circular economy framework, avoiding larger amounts of fresh production. As previously observed [307], the underdevelopment of reclamation, especially in China, is a key barrier in the reduction of GHG emissions in the following years. By the end of the analyzed time period, and across all considered regions, R410A consumption and end-of-life management yield a total of 1.16 $GtCO_2e$ and 0.79 $GtCO_2e$ in the baseline and proposed scenarios, respectively. On the other hand, system-level emissions yield a total of 2.43 $GtCO_2e$, and its aggregation by equipment charging, operation, and disposal over time and across all regions is presented in Figure 9.6. Here, it is clear that operational emissions are the main contributors to this net value, highlighting the importance in the management of the use phase of R410A in the relative impact of deploying DES-based reclamation.

Finally, Figure 9.5d compares the relative reduction in global warming impact, ΔGWI, between both scenarios. To observe the avoided GHG emissions with respect to the overall usage of R410A, this avoided impact was computed including and omitting emissions steaming from charging, use, and disposal of refrigeration equipment. Thus, ΔGWI and $\Delta GWI'$, respectively defined in Equations 9.16 and 9.17, are simultaneously presented. As can be seen, avoided GHG emissions can amount for almost the half of the emissions steaming from the baseline scenario, with a steep early drop related to the start of the deployment of DES-based reclamation. Computed uncertainty in this case is relatively high, suggesting that relative differences at the end of the period can vary from 18.4% to 66.7%, with a mean value of 45.4%, and with a distribution suggesting a shift into lower values of ΔGWI. On the other hand, the reduction in carbon footprint relative to the

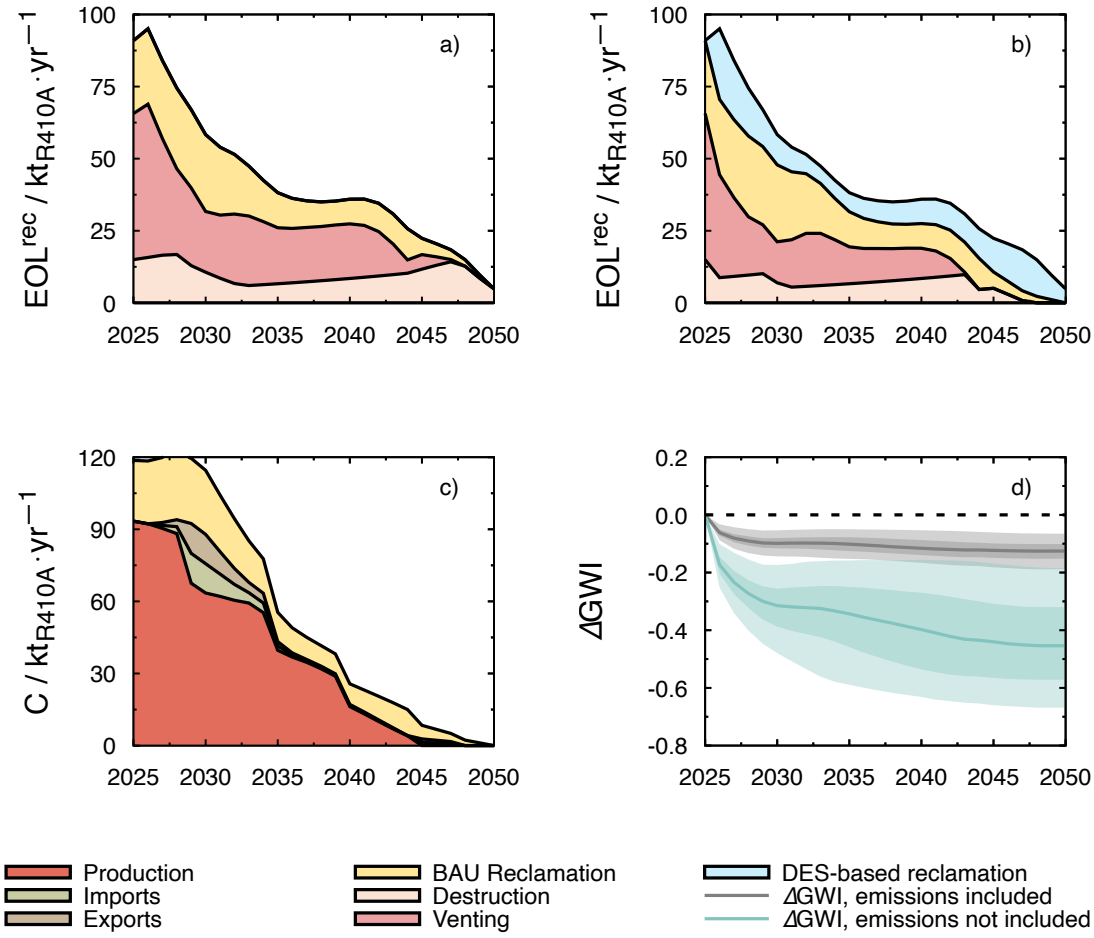

FIGURE 9.5: Projected evolution of recoverable end-of-life, consumption, and relative reduction in cumulative global warming impact associated to the use of R410A across all considered regions, under baseline and proposed scenarios. (a) Contributions to the projected recoverable end-of-life in the baseline (no DES-based reclamation allowed) scenario. (b) Contributions to the projected recoverable end-of-life in the proposed (DES-based reclamation allowed) scenario. (c) Contributions to the projected consumption. (d) Relative reduction in global warming impact of the proposed scenario compared to the baseline scenario, with and without accounting for system-level emissions; light- and dark-shaded areas represent the 2.5th-97.5th and 25th-75th percentile ranges, respectively, obtained from Monte Carlo simulations.

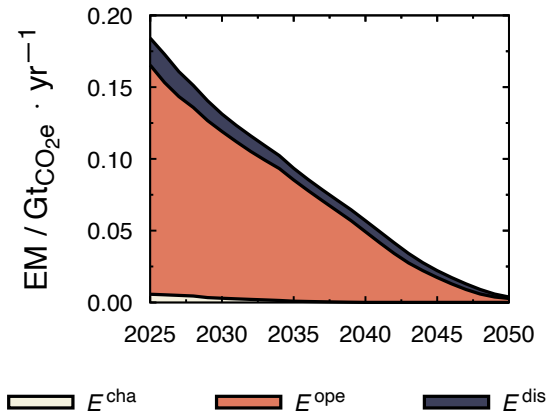

FIGURE 9.6: Aggregation of system-level emissions related to the use of R410A across the considered regions.

whole emission scheme is considerably lower and less uncertain, with reductions between 6.5% and 18.8%, with a mean value of 12.5%, by the end of the period. This estimation corroborates that the climate benefits steaming from implementing DES-based reclamation are greatly influenced by the characteristic emissions of refrigeration equipment.

To explore the effect of different deployment schemes of DES-based reclamation, a sensitivity analysis conveying the year of initial implementation, $Y^{\mathrm{RDES},0}$, and relative initial capacity, f^{RDES}, was performed. Results are presented in Figure 9.7, where the relative difference in carbon footprint between both scenarios without system-level emissions, ΔGWI, is shown for different combinations among these parameters. As expected, higher initial capacities, coupled with an earlier implementation, are the ideal cases for a lower environmental impact. Moreover, the mitigation by DES-based reclamation is strongly influenced by this latter parameter, showing that deploying this technology later than 2040 heavily hinders reductions in carbon footprint, Thus, relative initial capacity shows an overall lesser influence in GWI reductions, suggesting that a higher mitigation can be achieved by prioritizing an early deployment of DES-based reclamation. More precisely, implementation in early years with the same initial capacity as the BAU reclamation can reduce emissions in about a 36%, while doubling this capacity yields reductions of a 61%.

The influence of alternative phase-out schemes for R410A on avoided GHG emissions was assessed by varying the scale, λ, and shape, β, parameters of the retirement function defined in Equation 9.10. Here, λ governs the timing of equipment retirement, shifting decommissioning towards earlier or later years of operation, while β represents the spread of retirement over time, with lower values indicating more gradual phase-out profiles. For each λ–β combination, ΔGWI, as defined in Equation 9.16, was evaluated. Additionally, the change in total system-level emissions over the 2025-2050 period, EM, was analyzed by computing their relative difference with respect to the base case ($\lambda = \lambda_0 = 14.73$, $\beta = \beta_0 = 13.96$) as

$$\Delta_{\lambda,\beta}\mathrm{EM} = \frac{\mathrm{EM}\left(\lambda,\beta\right) - \mathrm{EM}\left(\lambda_0,\beta_0\right)}{\mathrm{EM}\left(\lambda_0,\beta_0\right)}\,. \tag{9.18}$$

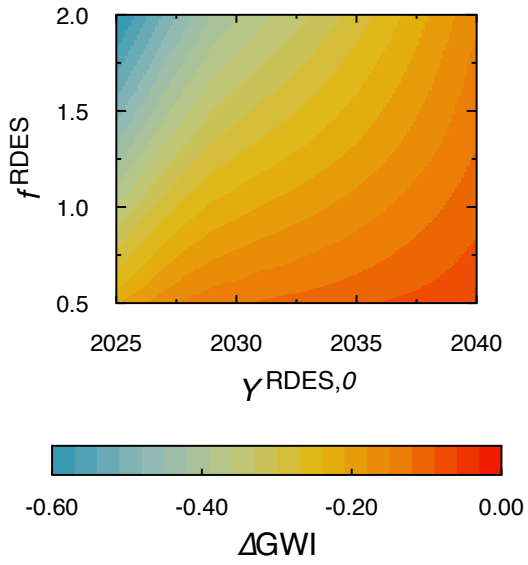

FIGURE 9.7: Effect of implementation year, $Y^{RDES,0}$, and initial capacity relative to BAU reclamation, f^{RDES}, of DES-based reclamation in the relative reduction in global warming impact of the proposed scenario compared to the baseline scenario.

Moreover, as initial capacities for destruction and BAU reclamation were defined as fixed shares of the end-of-life R410A flow (parameter f^{BL} in Table 9.6), they were additionally constrained to avoid unrealistically large values under scenarios of increased end-of-life flows. Thus, for each λ–β combination, capacities were limited to the minimum between the scaled end-of-life flow and their correspondent base case value (λ_0, β_0).

Results for the avoided carbon footprint due to DES-based reclamation are shown in Figure 9.8a. Here, larger relative reductions in carbon footprint are obtained by combinations of larger λ with lower β values, corresponding to higher equipment mean lifetimes and more gradual retirement profiles, respectively. Under these conditions, the model predicts potential relative reductions of up to 56.4%, equivalent to a net reduction of 0.43 Gt_{CO_2e}. The mechanisms underlying this behavior are illustrated in Figure 9.9, which reports the contributions to the end-of-life R410A over time for the case of $\lambda = 24$ and $\beta = 5$. In this system, the delayed phase-out of R410A allows end-of-life technologies to progressively scale up before peak flows are reached. The deployment of DES-based reclamation is further enhanced by this, thus amplifying the reduction in overall carbon footprint.

Results for the relative difference in system-level emissions are presented in Figure 9.8b. In contrast to the trends observed for ΔGWI, shorter equipment lifetimes (lower λ values) consistently lead to lower cumulative emissions compared to the base case. Moreover, the largest reductions are obtained for lower β values, reaching relative differences of up to 78.4% (equivalent to 1.91 Gt_{CO_2e}). This behavior can be explained by the contributions to system-level emissions over time presented in Figure 9.10. For a fixed β, increasing λ leads to higher emissions related to equipment use,

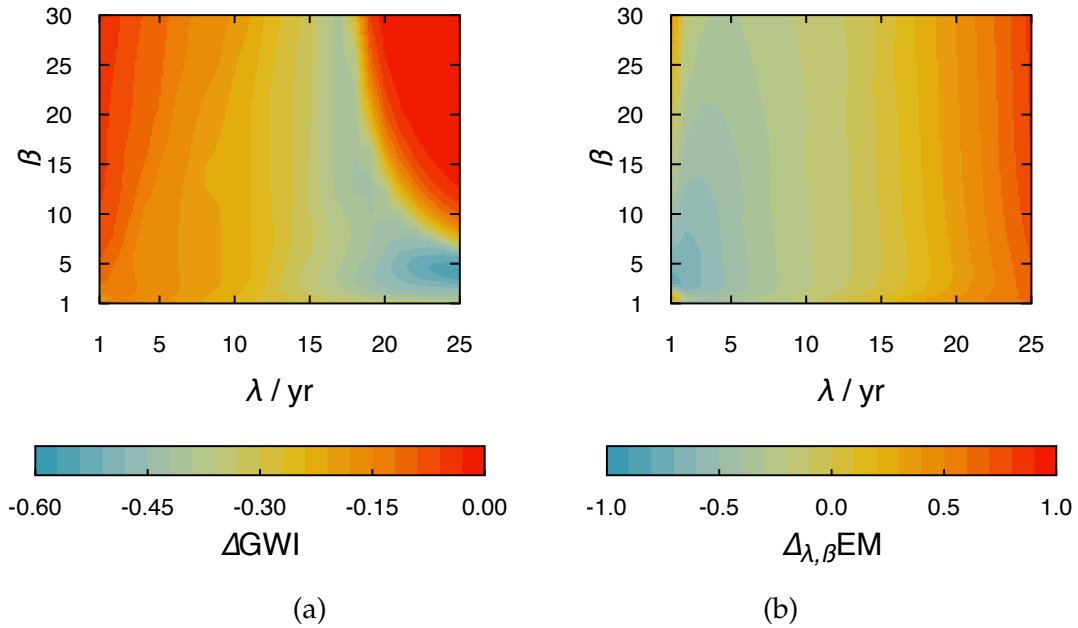

FIGURE 9.8: Effect of equipment lifetime parameters, λ and β, on the environmental performance of R410A usage. (a) Relative difference in cumulative GWI between the proposed and baseline scenarios, ΔGWI (see Figure 9.5), evaluated across λ–β combinations and expressed in difference to the base case ($\lambda = \lambda_0 = 14.73$, $\beta = \beta_0 = 13.96$). (b) Corresponding difference in total system-level emissions, for the period of 2025 to 2050, relative to the same base case.

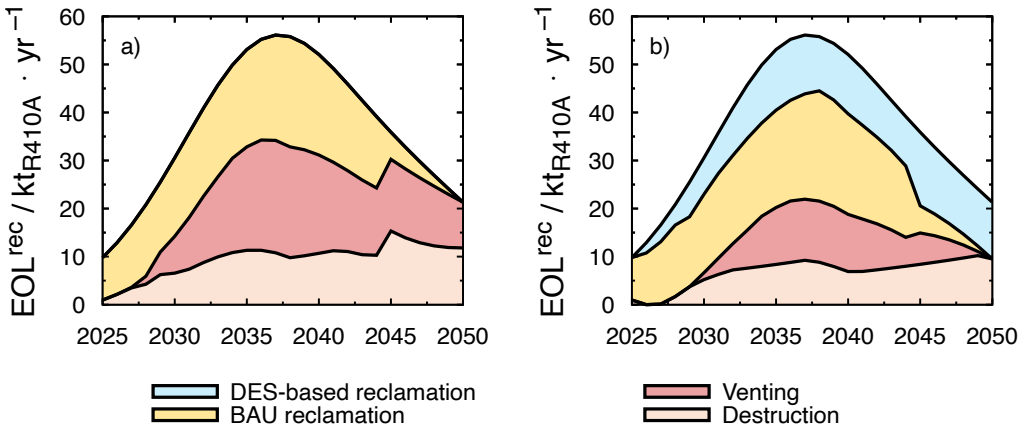

FIGURE 9.9: Contributions to the projected recoverable end-of-life R410A in the baseline (no DES-based reclamation allowed) (a) and proposed (DES-based reclamation allowed) (b) scenarios using parameters of the retirement distribution function of $\lambda = 24$ and $\beta = 5$.

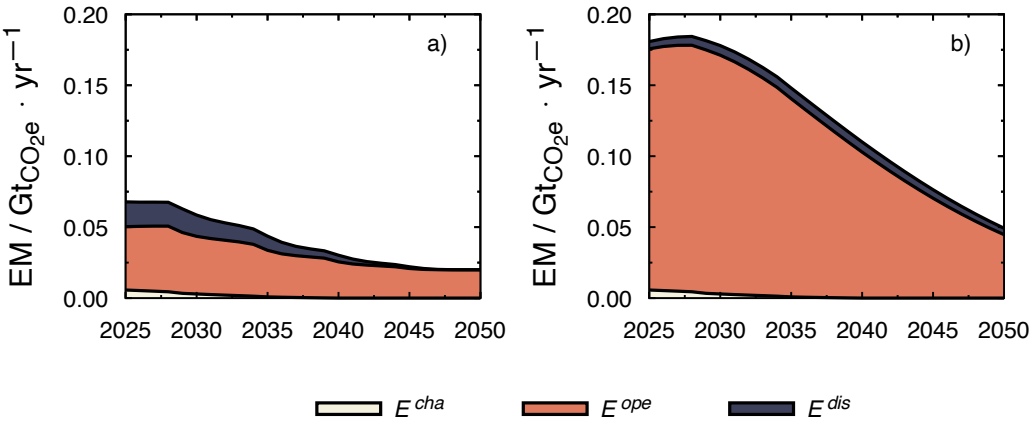

FIGURE 9.10: Contributions to system-level emissions related to the use of R410A across the considered regions, considering parameters of the retirement function (Equation 9.10) of $\beta = 2$ and (a) $\lambda = 2$ and (b) $\lambda = 24$.

highlighting that operational emissions dominate the emissions of the system.

These results highlight the trade-off between system-level emissions and the avoided carbon footprint associated to the implementation of DES-based reclamation. Equipment mean lifetime is the dominant parameter, and exhibits opposite effects on the two metrics. While longer lifetimes enhance the reduction in GWI by enabling a higher deployment of management technologies, they also increase emissions due to prolonged use-phase operation. The magnitude of the increase on potential emissions suggests that strategies promoting shorter equipment lifetimes are more effective for reducing the overall environmental impact than those aimed at optimizing the deployment of DES-based reclamation.

9.4. Conclusions

In this work, a combined methodology of LCA and supply chain analysis was applied to study the reach of DES-based reclamation of R410A. Process simulations of destruction, BAU reclamation, and DES-based reclamation of R410A were performed to obtain the material and energy requirements in each case, considering for the latter the characteristic transport limitations in the absorption capabilities of the considered solvent.

LCA of the considered end-of-life routes for R410A showed that DES-based reclamation is a feasible alternative to reduce the carbon footprint of the treatment of this refrigerant, serving as a route to avoid the fresh production of R32 and R125. Following the ReCiPe methodology, midpoint and endpoint indicators were computed to corroborate burden shifting in the proposed process. As could be seen, the only observed burden shifting is related to human toxicity potential and general human health, which, within the observed uncertainty, yields a non-negligible overlap between both treatment options, suggesting possibly higher values for DES-based reclamation.

A further assessment of the proposed reclamation process was performed by creating a supply chain model for the multiregional usage of R410A over time. A comparative between scenarios with and without the deployment of DES-based reclamation showed that GHG emissions related to the use and disposal of R410A could be reduced between 18% and 67% by 2050 with an early implementation of this technology. However, emissions related to charging, operation, and disposal of refrigerant equipment heavily influence the overall carbon footprint, bringing the reductions in carbon footprint of DES-based reclamation between 7% and 19%. The R410A supply route with lower environmental impact showed a strong tendency to fresh production, given that projections for consumption generally satisfied the consumption limits given by the Kigali Amendment to the Montreal Protocol. As expected, China arises as the most critical region in the management of R410A stocks, given its higher volume of consumption and thus end-of-life flows.

A sensitivity analysis of year of initial implementation and relative initial capacity of DES-based reclamation showed that the latter parameter effects a lower influence on the avoided GWI, highlighting its secondary role in the climate benefits of the proposed technology, subjected to the year of initial implementation. Similarly, the analysis of different phase-out schemes shows the trade-off between higher available end-of-life R410A for DES-based reclamation and higher emissions due to a prolonged use-phase.

This work assesses the importance of a modeling of the general usage of R410A in the framework of its certain future phase-out. While DES-based reclamation is a promising solution to tackle both the end-of-life treatment of this compound and the supply of its constituents to the market, emissions steaming from the use-phase of R410A exert a heavy influence on the overall carbon footprint. The proposed multiscale approach to the use of DESs for R410A separation grants a feasible route for the search of pathways in the phase-out of refrigerant mixtures with high global warming potentials.

10. Conclusions and Outlook

10.1. Dissertation conclusions

The multiscale framework developed in this thesis has provided a comprehensive strategy in the understanding of eutectic solvents applied to the separation and recovery of fluorinated greenhouse gases. The integration of COSMO-RS, molecular dynamics simulations, and SAFT-based equations of state allowed to connect molecular insights with desirable thermophysical behavior for the absorption of hydrofluorocarbons (HFCs). The integration of process simulation coupled and life cycle assessment revealed further insights into the decision-making for the implementation of extractive distillation utilizing novel solvents.

The study in Chapter 6 focused on fluorinated eutectic solvents, in an attempt to understand the molecular features driving their high HFC solubility capacities. The suitability of COSMO-RS and MD simulations in the study of these solvents was assessed by characterizing their deviation from ideal-solution behavior. Results showed a qualitative correspondence between both theories and the expected behavior of eutectic solvents, validating their use for the considered systems. COSMO-RS reproduced experimental solubility trends with reasonable accuracy, while MD simulations provided qualitative predictions of the phase equilibrium. Further microscopic insights were obtained from MD simulations, and were used to explain the observed behavior on HFC absorption. Results revealed the importance of multiple physical effects on the solvation of the considered gases, including localized solute–solvent interactions, dispersive forces, and the disruption of HFC clusters in the liquid phase. In particular, solvents containing Br^- showed a marked affinity for reducing R32 aggregation and increasing its solubility with respect to solvents based on bulkier ionic precursors. However, for fluorinated ethanes such as R134a and R125, van der Waals interactions became more relevant in the solvation process.

In Chapter 7, quaternary phosphonium-based ionic liquids (PILs) were evaluated as potential entrainers for the separation of commercial refrigerant blends. Using $[P_{666,14}]$Cl as a reference, new soft-SAFT molecular models were developed for $[P_{666,14}]$[GLY] and $[P_{666,14}]$[TMPP]. COSMO-RS and DFT calculations were used to define the association scheme and derive its parameters for these solvents, reducing the empirical parameter degeneracy. The resulting soft-SAFT parameterization yield an accurate modeling of solubility isotherms for HFCs and hydrofluoroolefins (HFOs), particularly under low-pressure conditions. The subsequent extension to ternary vapor–liquid equilibria allowed to evaluate the performance of PILs for the separation of HFC- and HFO-based

blends. The effect of temperature, pressure, and the interaction between solutes showed important effects on selectivity, granting insights of suitable conditions for an enhanced separation. Particularly, [$P_{666,14}$][TMPP] showed potential as entrainer for R410A, while [$P_{666,14}$]Cl proved feasible for the treatment of R451A. Thus, obtained results provided insights for the design of PIL-based DESs for separation applications.

Chapter 8 further expanded the analysis toward type III deep eutectic solvents (DESs), based on quaternary ammonium salts and polyol hydrogen bond donors. New experimental HFC solubility data was generated for DESs based on [N_{1111}]Cl, complementing previous information for [Ch]Cl-based DESs. The soft-SAFT equation of state provided accurate representations of solvent density and solubility isotherms through the individual-component approach applied to DES precursors. Moreover, its combination with Free Volume Theory enabled the characterization of viscosity. The thermodynamic evaluation of these solvents, through the calculation of Henry's constants and dissolution enthalpies, evidenced a particular affinity for R32, leading to favorable ideal selectivities for this HFC. This potential was subsequently analyzed by the characterization of competitive selectivity at non-diluted conditions and different pressures. Results revealed that the separation capabilities of the considered solvents is not reduced under less favorable conditions for selective absorption. Thus, type III DESs provide suitable thermodynamic characteristics for the extractive distillation of commercial refrigerant blends such as R410A and R407F.

Finally, DES-based reclamation of refrigerant blends was evaluated at a process- and system-level in Chapter 9. Extractive distillation of R410A, the [Ch]Cl:EG (1:3) DES, was modeled using process simulation. The quantified material and energy requirements were used to compare the environmental impact of DES-based reclamation against the conventional destruction route. Results from process simulation showed that R32 and R125 are obtained at high purities, even when considering characteristic transport limitations of DESs. Furthermore, the life cycle assessment (LCA) demonstrated that DES-based reclamation can reduce the carbon footprint of the end-of-life treatment of R410A by replacing fresh production of R32 and R125. However, burden shifting in impact indicators related to human toxicity was also observed, highlighting the need for further uncertainty assessment in the considered environmental impact categories. The environmental effects of the deployment of DES-based reclamation were analyzed through a supply chain model for the multiregional usage of R410A over time. Carbon footprint results revealed that cumulative emissions related to the use and disposal of this refrigerant blend could be greatly reduced by 2050 with an early implementation of this technology. Nevertheless, emissions associated with the use-phase of R410A remain a dominant contributor to the overall carbon footprint, limiting the relative effectiveness of DES-based reclamation. Therefore, an adequate management of R410A supply can be achieved only if a circular economy framework is complemented by improvements on operational emissions.

Across Chapters 6–9, this thesis demonstrates that multiscale solvent design is a robust framework for developing separation technologies for refrigerant blends. The characterization of microscopic solvation phenomena towards the design of new absorption units proves the effectivity of molecular modeling techniques in this application. Further considerations for the development of SAFT models yields predictive models capable of granting key thermodynamic information to evaluate the reliability of new absorption units. Moreover, LCA provides fundamental information

in the decision-making of these new processes, highlighting the potential and limitations of new technologies. The integration of these computational tools establishes a scalable methodology for identifying promising solvents, evaluating their thermodynamic performance, and assessing their contribution to the phase-out of high-GWP fluorinated greenhouse gases.

10.2. Outlook

Although the methodology developed in this thesis provides a strong basis for the design of solvents for F-gas recovery, several opportunities remain for future research. First, additional experimental measurements of properties relevant to process design are required to validate promising solvent candidates. This need is particularly evident for eutectic solvents and ionic liquids, which often exhibit high viscosities that limit their performance in separation applications. Furthermore, properties such as thermal conductivity, heat capacity, and surface tension are essential for process simulations involving rate-based modeling. Thus, a comprehensive characterization of thermophysical properties beyond thermodynamic equilibrium constitutes a mandatory step toward the rational design of novel entrainers.

Second, the solvent design space should be expanded toward emerging formulations of deep eutectic solvents. In particular, Type V eutectic solvents, formed from non-ionic precursors, represent a promising alternative from an environmental perspective. The insights and methodological framework developed throughout this thesis can serve as a basis for the screening and evaluation of these systems. This includes localized interactions, free volume, and competitive selectivity.

Third, theoretical developments not considered within the scope of this thesis may provide powerful tools for the study of advanced entrainers. In the first place, the implementation of polarizable force fields in molecular dynamics simulations can provide a more accurate description of intermolecular interactions, especially considering the well documented polarity of fluorinated gases in liquid phases. Moreover, these approaches improve the prediction of transport properties in transport-limited systems, without requiring corrective strategies such as the rescaling of point charges. In the second place, machine learning techniques, now a considerably expanding topic in the literature, can be integrated with all computational techniques employed in this thesis. Potential applications include the use of COSMO-derived descriptors for an extensive exploration of the chemical space, the parameterization of SAFT models and molecular simulation force fields, and the prediction of life cycle inventory data for novel compounds not included in common databases. The combined implementation of both theoretical developments offers promising routes toward a more comprehensive and precise exploration of solvents.

Finally, future studies should combine life cycle assessment with techno-economic analysis to evaluate the practical deployment potential of new reclamation technologies. By incorporating an economic dimension, an additional balance between alternative end-of-life management routes for refrigerant blends can be included. Such analysis could provide a more realistic assessment of the opportunities and limitations of a large-scale implementation of separation approaches based on emerging solvents.

Bibliography

[1]United Nations, *The 17 goals (https://sdgs.un.org/goals)*.

[2]IPCC, *Climate change 2023: synthesis report. contribution of working groups i, II and III to the sixth assessment report of the intergovernmental panel on climate change*, tech. rep. (IPCC, Geneva, Switzerland, 2023).

[3]D. I. V. Domeisen, E. A. B. Eltahir, E. M. Fischer, R. Knutti, S. E. Perkins-Kirkpatrick, C. Schär, S. I. Seneviratne, A. Weisheimer, and H. Wernli, "Prediction and projection of heatwaves", Nature Reviews Earth & Environment **4**, 36–50 (2023).

[4]J. C. Orr, V. J. Fabry, O. Aumont, L. Bopp, S. C. Doney, R. A. Feely, A. Gnanadesikan, N. Gruber, A. Ishida, F. Joos, R. M. Key, K. Lindsay, E. Maier-Reimer, R. Matear, P. Monfray, A. Mouchet, R. G. Najjar, G.-K. Plattner, K. B. Rodgers, C. L. Sabine, J. L. Sarmiento, R. Schlitzer, R. D. Slater, I. J. Totterdell, M.-F. Weirig, Y. Yamanaka, and A. Yool, "Anthropogenic ocean acidification over the twenty-first century and its impact on calcifying organisms", Nature **437**, 681–686 (2005).

[5]R. A. Wiebe and D. S. Wilcove, "Global biodiversity loss from outsourced deforestation", Nature **639**, 389–394 (2025).

[6]S. Kang, Q. Zhang, Y. Qian, Z. Ji, C. Li, Z. Cong, Y. Zhang, J. Guo, W. Du, J. Huang, Q. You, A. K. Panday, M. Rupakheti, D. Chen, O. Gustafsson, M. H. Thiemens, and D. Qin, "Linking atmospheric pollution to cryospheric change in the third pole region: current progress and future prospects", National Science Review **6**, 796–809 (2019).

[7]J. Rockstroem, W. Steffen, K. Noone, A. Persson, F. S. Chapin, E. F. Lambin, T. M. Lenton, M. Scheffer, C. Folke, H. J. Schellnhuber, B. Nykvist, C. A. d. Wit, T. Hughes, S. v. d. Leeuw, H. Rodhe, S. Soerlin, P. K. Snyder, R. Costanza, U. Svedin, M. Falkenmark, L. Karlberg, R. W. Corell, V. J. Fabry, J. Hansen, B. Walker, D. Liverman, K. Richardson, P. Crutzen, and J. A. Foley, "A safe operating space for humanity", Nature **461**, 472–475 (2009).

[8]K. Richardson, W. Steffen, W. Lucht, J. Bendtsen, S. E. Cornell, J. F. Donges, M. Drüke, I. Fetzer, G. Bala, W. v. Bloh, G. Feulner, S. Fiedler, D. Gerten, T. Gleeson, M. Hofmann, W. Huiskamp, M. Kummu, C. Mohan, D. Nogués-Bravo, S. Petri, M. Porkka, S. Rahmstorf, S. Schaphoff, K. Thonicke, A. Tobian, V. Virkki, L. Wang-Erlandsson, L. Weber, and J. Rockstroem, "Earth beyond six of nine planetary boundaries", Science Advances **9**, eadh2458 (2023).

[9]PBScience, *Planetary health check (https://www.planetaryhealthcheck.org).*

[10]H. S. Findlay, R. A. Feely, L. Jiang, G. Pelletier, and N. Bednaršek, "Ocean acidification: another planetary boundary crossed", Global Change Biology **31**, e70238 (2025).

[11]IPCC, "Anthropogenic and natural radiative forcing", *Climate change 2013: the physical science basis* (Cambridge University Press, Cambridge, United Kingdom and New York, NY, USA, 2013) Chap. 8, 659–740.
[12]United Nations, *United nations framework convention on climate change (UNFCCC)*, 1992.
[13]United Nations, *Kyoto protocol to the united nations framework convention on climate change*, 1997.
[14]United Nations, *Paris agreement to the united nations framework convention on climate change*, 2015.
[15]M. T. McCulloch, A. Winter, C. E. Sherman, and J. A. Trotter, "300 years of sclerosponge thermometry shows global warming has exceeded 1.5 °c", Nature Climate Change **14**, 171–177 (2024).
[16]M. Filonchyk, M. P. Peterson, L. Zhang, V. Hurynovich, and Y. He, "Greenhouse gases emissions and global climate change: examining the influence of CO2, CH4, and n2o", Science of The Total Environment **935**, 173359 (2024).
[17]IPCC, "Emissions trends and drivers", *Climate change 2022: mitigation of climate change*, edited by P. R. Shukla and J. Skea (IPCC, 2022) Chap. 2, 215–294.
[18]G. J. M. Velders, D. W. Fahey, J. S. Daniel, M. McFarland, and S. O. Andersen, "The large contribution of projected HFC emissions to future climate forcing", Proceedings of the National Academy of Sciences **106**, 10949–10954 (2009).
[19]M. O. McLinden and M. L. Huber, "(r)evolution of refrigerants", Journal of Chemical & Engineering Data **65**, 4176–4193 (2020).
[20]United Nations Environment Programme (UNEP), *The montreal protocol on substances that deplete the ozone layer*, 1987.
[21]M. J. Molina and F. S. Rowland, "Stratospheric sink for chlorofluoromethanes: chlorine atom-catalysed destruction of ozone", Nature **249**, 810–812 (1974).
[22]A. J. Sicard and R. T. Baker, "Fluorocarbon refrigerants and their syntheses: past to present", Chemical Reviews **120**, 9164–9303 (2020).
[23]B. K. Sovacool, S. Griffiths, J. Kim, and M. Bazilian, "Climate change and industrial f-gases: a critical and systematic review of developments, sociotechnical systems and policy options for reducing synthetic greenhouse gas emissions", Renewable and Sustainable Energy Reviews **141**, 110759 (2021).
[24]G. J. Velders, D. W. Fahey, J. S. Daniel, S. O. Andersen, and M. McFarland, "Future atmospheric abundances and climate forcings from scenarios of global and regional hydrofluorocarbon (HFC) emissions", Atmospheric Environment **123**, 200–209 (2015).
[25]United Nations Environment Programme (UNEP), *Amendment to the montreal protocol on substances that deplete the ozone layer*, 2016.
[26]Institute for Governance & Sustainable Development (IGSD), *China issues national plan to strengthen the management of ozone-depleting substances and climate-polluting hydrofluorocarbons*, Apr. 2025.
[27]S. Ludig, W. Jörß, and V. Brebeck, *ETC CM report 2025/05: fluorinated greenhouse gases 2025*, tech. rep. (European Environment Agency, 2025).
[28]Environmental Protection Agency (EPA), *Regulatory actions for managing HFC use and reuse*, 2025.
[29]X. Zhang and Y. Li, "A review of recent research on hydrofluoroolefin (HFO) and hydrochlorofluoroolefin (HCFO) refrigerants", Energy **311**, 133423 (2024).

[30]P. J. Castro, J. M. M. Aráujo, G. Martinho, and A. B. Pereiro, "Waste management strategies to mitigate the effects of fluorinated greenhouse gases on climate change", Applied Sciences **11**, 4367 (2021).
[31]D. J. Sheldon and M. R. Crimmin, "Repurposing of f-gases: challenges and opportunities in fluorine chemistry", Chemical Society Reviews **51**, 4977–4995 (2022).
[32]T. Wang, J. Li, D. Xie, H. Miao, L. Shi, and X. Dai, "A novel photo-thermal synergistic catalytic method for degradation of waste hydrofluorocarbons as greenhouse gases", Applied Thermal Engineering **270**, 126211 (2025).
[33]I. I. I. Alkhatib, C. G. Albà, Y. Li, S. Stephan, F. Llovell, and L. F. Vega, "Molecular origin of interfacial anomalies in azeotropic refrigerant mixtures", The Journal of Physical Chemistry C **129**, 14622–14637 (2025).
[34]American Society of Heating, Refrigerating and Air-Conditioning Engineers (ASHRAE), *ASHRAE refrigerant designations*, 2021.
[35]M. F. Doherty and J. P. Knapp, "Distillation, azeotropic, and extractive", *Kirk-othmer encyclopedia of chemical technology*, Vol. 8, 5th ed. (John Wiley & Sons, 2004), 786–852.
[36]V. Gerbaud, I. Rodriguez-Donis, L. Hegely, P. Lang, F. Denes, and X. You, "Review of extractive distillation. process design, operation, optimization and control", Chemical Engineering Research and Design **141**, 229–271 (2019).
[37]H. Iwasaki, N. Hoshiya, Y. Kishikawa, J. Escorihuela, and N. Shibata, "Repurposing HFC-125 to tetrafluoroethylene: a step toward a more sustainable fluoropolymer feedstock strategy", iScience **28**, 112580 (2025).
[38]M. F. Doherty and M. F. Malone, "Homogeneous azeotropic distillation", *Conceptual design of distillation systems*, edited by E. M. Munson, 1st ed. (McGraw-Hill Higher Education, New York, 2001) Chap. 5, 183–241.
[39]Z. Lei, C. Dai, J. Zhu, and B. Chen, "Extractive distillation with ionic liquids: a review", AIChE Journal **60**, 3312–3329 (2014).
[40]M. Neubauer, T. Wallek, and S. Lux, "Deep eutectic solvents as entrainers in extractive distillation – a review", Chemical Engineering Research and Design **184**, 402–418 (2022).
[41]R. D. Rogers and K. R. Seddon, "Ionic liquids–solvents of the future?", Science **302**, 792–793 (2003).
[42]D. R. MacFarlane and K. R. Seddon, "Ionic liquids—progress on the fundamental issues", Australian Journal of Chemistry **60**, 3–5 (2007).
[43]K. R. Baca, K. Al-Barghouti, N. Wang, M. G. Bennett, L. M. Valenciano, T. L. May, I. V. Xu, M. Cordry, D. M. Haggard, A. G. Haas, A. Heimann, A. N. Harders, H. G. Uhl, D. T. Melfi, A. D. Yancey, R. Kore, E. J. Maginn, A. M. Scurto, and M. B. Shiflett, "Ionic liquids for the separation of fluorocarbon refrigerant mixtures", Chemical Reviews **124**, 5167–5226 (2024).
[44]S. Asensio-Delgado, F. Pardo, G. Zarca, and A. Urtiaga, "Absorption separation of fluorinated refrigerant gases with ionic liquids: equilibrium, mass transport, and process design", Separation and Purification Technology **276**, Lots of experimental solubilities for IL+HFCs, 119363 (2021).
[45]D. O. Abranches and J. A. Coutinho, "Everything you wanted to know about deep eutectic solvents but were afraid to be told", Annual Review of Chemical and Biomolecular Engineering **14**, 141–163 (2023).

[46]E. L. Smith, A. P. Abbott, and K. S. Ryder, "Deep eutectic solvents (DESs) and their applications", Chemical Reviews **114**, 11060–11082 (2014).

[47]B. B. Hansen, S. Spittle, B. Chen, D. Poe, Y. Zhang, J. M. Klein, A. Horton, L. Adhikari, T. Zelovich, B. W. Doherty, B. Gurkan, E. J. Maginn, A. Ragauskas, M. Dadmun, T. A. Zawodzinski, G. A. Baker, M. E. Tuckerman, R. F. Savinell, and J. R. Sangoro, "Deep eutectic solvents: a review of fundamentals and applications", Chemical Reviews **121**, 1232–1285 (2021).

[48]S. Shan, I. B. Jovein, P. Figiel, B. Chen, G. Sadowski, C. Held, and G. Yu, "Selective absorption of fluorinated gases by natural deep eutectic solvents: PC-SAFT modeling and mechanistic insights", AIChE Journal, 10.1002/aic.70457 (2026).

[49]D. O. Abranches, M. A. R. Martins, L. P. Silva, N. Schaeffer, S. P. Pinho, and J. A. P. Coutinho, "Phenolic hydrogen bond donors in the formation of non-ionic deep eutectic solvents: the quest for type v DES", Chemical Communications **55**, 10253–10256 (2019).

[50]G. M. Kontogeorgis and G. K. Folas, "Thermodynamics for process and product design", *Thermodynamic models for industrial applications: from classical and advanced mixing rules to association theories*, 1st ed. (John Wiley & Sons, United Kingdom, 2010) Chap. 1, 3–14.

[51]W. Chapman, K. Gubbins, G. Jackson, and M. Radosz, "SAFT: equation-of-state solution model for associating fluids", Fluid Phase Equilibria **52**, 31–38 (1989).

[52]I. G. Economou, "Statistical associating fluid theory: a successful model for the calculation of thermodynamic and phase equilibrium properties of complex fluid mixtures", Industrial & Engineering Chemistry Research **41**, 953–962 (2002).

[53]C. S. Beraldo, L. A. Follegatti-Romero, G. M. Kontogeorgis, and X. Liang, "Modeling CO2 solubility in deep eutectic solvents using the saft-vr mie and pc-saft equations of state", Fluid Phase Equilibria **598**, 114479 (2025).

[54]D. Frenkel and B. Smit, *Understanding molecular simulation: from algorithms to applications*, 2nd ed. (Elsevier, 2002).

[55]S. A. Hollingsworth and R. O. Dror, "Molecular dynamics simulation for all", Neuron **99**, 1129–1143 (2018).

[56]S. Asensio-Delgado, M. Viar, A. A. Pádua, G. Zarca, and A. Urtiaga, "Understanding the molecular features controlling the solubility differences of r-134a, r-1234ze(e), and r-1234yf in 1-alkyl-3-methylimidazolium tricyanomethanide ionic liquids", ACS Sustainable Chemistry & Engineering **10**, 15124–15134 (2022).

[57]J. N. C. Lopes and A. A. H. Pádua, "CL&p: a generic and systematic force field for ionic liquids modeling", Theoretical Chemistry Accounts **131**, 1129 (2012).

[58]K. G. Sprenger, V. W. Jaeger, and J. Pfaendtner, "The general AMBER force field (GAFF) can accurately predict thermodynamic and transport properties of many ionic liquids", The Journal of Physical Chemistry B **119**, 5882–5895 (2015).

[59]D. P. Kovács, J. H. Moore, N. J. Browning, I. Batatia, J. T. Horton, Y. Pu, V. Kapil, W. C. Witt, I.-B. Magdău, D. J. Cole, and G. Csányi, "MACE-OFF: short-range transferable machine learning force fields for organic molecules", Journal of the American Chemical Society **147**, 17598–17611 (2025).

[60]A. Szabo and N. S. Ostlund, *Modern quantum chemistry: introduction to advanced electronic structure theory* (Dover Publications, New York, July 1996).

[61]A. Klamt, F. Eckert, and W. Arlt, "COSMO-RS: an alternative to simulation for calculating thermodynamic properties of liquid mixtures", Annual Review of Chemical and Biomolecular Engineering **1**, 101–122 (2010).
[62]A. Klamt, "The COSMO and COSMO-RS solvation models", Wiley Interdisciplinary Reviews: Computational Molecular Science **1**, 699–709 (2011).
[63]H. Qin, J. Cheng, H. Yu, T. Zhou, and Z. Song, "Hierarchical ionic liquid screening integrating COSMO-RS and aspen plus for selective recovery of hydrofluorocarbons and hydrofluoroolefins from a refrigerant blend", Industrial & Engineering Chemistry Research **61**, 4083–4094 (2022).
[64]Z. Zuo, M. Cao, W. Mu, I. B. Jovein, C. Held, B. Chen, and G. Yu, "Selective absorption of fluorinated gases by deep eutectic solvents: thermodynamics and molecular insights", Separation and Purification Technology **364**, 132342 (2025).
[65]J. Kleinekorte, L. Fleitmann, M. Bachmann, A. Katelhon, A. Barbosa-Póvoa, N. von der Assen, and A. Bardow, "Life cycle assessment for the design of chemical processes, products, and supply chains", Annual Review of Chemical and Biomolecular Engineering **11**, 1–31 (2020).
[66]D. Jovell, J. O. Pou, F. Llovell, and R. Gonzalez-Olmos, "Life cycle assessment of the separation and recycling of fluorinated gases using ionic liquids in a circular economy framework", ACS Sustainable Chemistry & Engineering **10**, 71–80 (2022).
[67]D. Clijnk, V. Codera, J. Pou, J. Fernandez-Garcia, and R. Gonzalez-Olmos, "Enhancing circular economy of waste refrigerants management using deep eutectic solvents", Sustainable Materials and Technologies **41**, e01062 (2024).
[68]Q. Zaib, M. J. Eckelman, Y. Yang, and D. Kyung, "Are deep eutectic solvents really green?: a life-cycle perspective", Green Chemistry **24**, 7924–7930 (2022).
[69]N. Winterton, "The green solvent: a critical perspective", Clean Technologies and Environmental Policy **23**, 2499–2522 (2021).
[70]V. Hessel, N. N. Tran, M. R. Asrami, Q. D. Tran, N. V. D. Long, M. Escribà-Gelonch, J. O. Tejada, S. Linke, and K. Sundmacher, "Sustainability of green solvents – review and perspective", Green Chemistry **24**, 410–437 (2021).
[71]B. Huang and O. A. v. Lilienfeld, "Ab initio machine learning in chemical compound space", Chemical Reviews **121**, 10001–10036 (2021).
[72]C. Bilodeau, W. Jin, T. Jaakkola, R. Barzilay, and K. F. Jensen, "Generative models for molecular discovery: recent advances and challenges", Wiley Interdisciplinary Reviews: Computational Molecular Science **12**, `10.1002/wcms.1608` (2022).
[73]M. Sumita, S. Ishida, K. Yoshizoe, R. Tamura, K. Terayama, and K. Tsuda, "Molecular design with artificial intelligence: progress and perspectives for small molecules", Chemical Reviews **126**, 3007–3054 (2026).
[74]J. Tomasi and M. Persico, "Molecular interactions in solution: an overview of methods based on continuous distributions of the solvent", Chemical Reviews **94**, 2027–2094 (1994).
[75]J. Tomasi, B. Mennucci, and R. Cammi, "Quantum mechanical continuum solvation models", Chemical Reviews **105**, 2999–3094 (2005).
[76]A. Klamt, "Conductor-like screening model for real solvents: a new approach to the quantitative calculation of solvation phenomena", The Journal of Physical Chemistry **99**, 2224–2235 (1995).
[77]F. Eckert and A. Klamt, "Fast solvent screening via quantum chemistry: COSMO-RS approach", AIChE Journal **48**, 369–385 (2002).

[78]L. Onsager, "Electric moments of molecules in liquids", Journal of the American Chemical Society **58**, 1486–1493 (1936).
[79]L. Pauling, *The nature of the chemical bond: an introduction to modern structural chemistry*, 3rd ed. (Cornell University Press, New York, 1960).
[80]A Bondi, "Van der waals volumes and radii", The Journal of Physical Chemistry **68**, 441–451 (1964).
[81]A. Klamt, V. Jonas, T. Bürger, and J. C. W. Lohrenz, "Refinement and parametrization of COSMO-RS", The Journal of Physical Chemistry A **102**, 5074–5085 (1998).
[82]S. Miertuš, E. Scrocco, and J. Tomasi, "Electrostatic interaction of a solute with a continuum. a direct utilizaion of AB initio molecular potentials for the prevision of solvent effects", Chemical Physics **55**, 117–129 (1981).
[83]A. Klamt and G. Schüürmann, "COSMO: a new approach to dielectric screening in solvents with explicit expressions for the screening energy and its gradient", Journal of the Chemical Society, Perkin Transactions 2 **0**, 799–805 (1993).
[84]Dassault Systèmes, *BIOVIA COSMOtherm*, 2024.
[85]S. G. Balasubramani, G. P. Chen, S. Coriani, M. Diedenhofen, M. S. Frank, Y. J. Franzke, F. Furche, R. Grotjahn, M. E. Harding, C. Hättig, A. Hellweg, B. Helmich-Paris, C. Holzer, U. Huniar, M. Kaupp, A. M. Khah, S. K. Khani, T. Müller, F. Mack, B. D. Nguyen, S. M. Parker, E. Perlt, D. Rappoport, K. Reiter, S. Roy, M. Rückert, G. Schmitz, M. Sierka, E. Tapavicza, D. P. Tew, C. v. Wüllen, V. K. Voora, F. Weigend, A. Wodynski, and J. M. Yu, "TURBOMOLE: modular program suite for ab initio quantum-chemical and condensed-matter simulations", The Journal of Chemical Physics **152**, 184107 (2020).
[86]R. Sander, W. E. Acree, A. D. Visscher, S. E. Schwartz, and T. J. Wallington, "Henry's law constants (IUPAC recommendations 2021)", Pure and Applied Chemistry **94**, 71–85 (2022).
[87]M. P. Allen and D. J. Tildesley, *Computer simulation of liquids*, 2nd ed. (Oxford University Press, 2017).
[88]G. Battimelli and G. Ciccotti, "Berni alder and the pioneering times of molecular simulation", The European Physical Journal H **43**, 303–335 (2018).
[89]W. L. Jorgensen, D. S. Maxwell, and J. Tirado-Rives, "Development and testing of the OPLS all-atom force field on conformational energetics and properties of organic liquids", Journal of the American Chemical Society **118**, 11225–11236 (1996).
[90]B. R. Brooks, R. E. Bruccoleri, B. D. Olafson, D. J. States, S. Swaminathan, and M. Karplus, "CHARMM: a program for macromolecular energy, minimization, and dynamics calculations", Journal of Computational Chemistry **4**, 187–217 (1983).
[91]P. K. Weiner and P. A. Kollman, "AMBER: assisted model building with energy refinement. a general program for modeling molecules and their interactions", Journal of Computational Chemistry **2**, 287–303 (1981).
[92]M. G. Martin and J. I. Siepmann, "Transferable potentials for phase equilibria. 1. united-atom description of n-alkanes", The Journal of Physical Chemistry B **102**, 2569–2577 (1998).
[93]S. J. Marrink, H. J. Risselada, S. Yefimov, D. P. Tieleman, and A. H. d. Vries, "The MARTINI force field: coarse grained model for biomolecular simulations", The Journal of Physical Chemistry B **111**, 7812–7824 (2007).

[94]P. C. T. Souza, R. Alessandri, J. Barnoud, S. Thallmair, I. Faustino, F. Grünewald, I. Patmanidis, H. Abdizadeh, B. M. H. Bruininks, T. A. Wassenaar, P. C. Kroon, J. Melcr, V. Nieto, V. Corradi, H. M. Khan, J. Domański, M. Javanainen, H. Martinez-Seara, N. Reuter, R. B. Best, I. Vattulainen, L. Monticelli, X. Periole, D. P. Tieleman, A. H. d. Vries, and S. J. Marrink, "Martini 3: a general purpose force field for coarse-grained molecular dynamics", Nature Methods **18**, 382–388 (2021).

[95]W. C. Swope, H. C. Andersen, P. H. Berens, and K. R. Wilson, "A computer simulation method for the calculation of equilibrium constants for the formation of physical clusters of molecules: application to small water clusters", The Journal of Chemical Physics **76**, 637–649 (1982).

[96]R. Hockney, S. Goel, and J. Eastwood, "Quiet high-resolution computer models of a plasma", Journal of Computational Physics **14**, 148–158 (1974).

[97]J.-P. Ryckaert, G. Ciccotti, and H. J. Berendsen, "Numerical integration of the cartesian equations of motion of a system with constraints: molecular dynamics of n-alkanes", Journal of Computational Physics **23**, 327–341 (1977).

[98]S. Miyamoto and P. A. Kollman, "Settle: an analytical version of the SHAKE and RATTLE algorithm for rigid water models", Journal of Computational Chemistry **13**, 952–962 (1992).

[99]B. Hess, H. Bekker, H. J. C. Berendsen, and J. G. E. M. Fraaije, "LINCS: a linear constraint solver for molecular simulations", Journal of Computational Chemistry **18**, 1463–1472 (1997).

[100]L. Verlet, "Computer "experiments" on classical fluids. i. thermodynamical properties of lennard-jones molecules", Physical Review **159**, 98–103 (1967).

[101]H. J. C. Berendsen, J. P. M. Postma, W. F. v. Gunsteren, A DiNola, and J. R. Haak, "Molecular dynamics with coupling to an external bath", The Journal of Chemical Physics **81**, 3684–3690 (1984).

[102]G. Bussi, D. Donadio, and M. Parrinello, "Canonical sampling through velocity rescaling", The Journal of Chemical Physics **126**, 014101 (2007).

[103]S. Nosé, "A molecular dynamics method for simulations in the canonical ensemble", Molecular Physics **52**, 255–268 (1984).

[104]W. G. Hoover, "Canonical dynamics: equilibrium phase-space distributions", Physical Review A **31**, 1695–1697 (1985).

[105]M Parrinello and A Rahman, "Polymorphic transitions in single crystals: a new molecular dynamics method", Journal of Applied Physics **52**, 7182–7190 (1981).

[106]S. Nosé and M. Klein, "Constant pressure molecular dynamics for molecular systems", Molecular Physics **50**, 1055–1076 (1983).

[107]L. Martínez, R. Andrade, E. G. Birgin, and J. M. Martínez, "PACKMOL: a package for building initial configurations for molecular dynamics simulations", Journal of Computational Chemistry **30**, 2157–2164 (2009).

[108]B. Hess, "Determining the shear viscosity of model liquids from molecular dynamics simulations", The Journal of Chemical Physics **116**, 209–217 (2002).

[109]E. J. Maginn, R. A. Messerly, D. J. Carlson, D. R. Roe, and J. R. Elliot, "Best practices for computing transport properties 1. self-diffusivity and viscosity from equilibrium molecular dynamics [article v1.0]", Living Journal of Computational Molecular Science **1**, 6324 (2018).

[110]I.-C. Yeh and G. Hummer, "System-size dependence of diffusion coefficients and viscosities from molecular dynamics simulations with periodic boundary conditions", The Journal of Physical Chemistry B **108**, 15873–15879 (2004).

[111]C. Chipot and A. Pohorille, "Calculating free energy differences using perturbation theory", *Free energy calculations, theory and applications in chemistry and biology*, edited by C. Chipot and A. Pohorille, 1st ed., Springer Series in Chemical Physics (Springer, Berlin, Heidelberg, 2007), 33–75.
[112]D. Wu and D. A. Kofke, "Phase-space overlap measures. i. fail-safe bias detection in free energies calculated by molecular simulation", The Journal of Chemical Physics **123**, 054103 (2005).
[113]P. Kollman, "Free energy calculations: applications to chemical and biochemical phenomena", Chemical Reviews **93**, 2395–2417 (1993).
[114]R. W. Zwanzig, "High-temperature equation of state by a perturbation method. i. nonpolar gases", The Journal of Chemical Physics **22**, 1420–1426 (1954).
[115]C. H. Bennett, "Efficient estimation of free energy differences from monte carlo data", Journal of Computational Physics **22**, 245–268 (1976).
[116]M. R. Shirts and J. D. Chodera, "Statistically optimal analysis of samples from multiple equilibrium states", The Journal of Chemical Physics **129**, 124105 (2008).
[117]A. S. J. S. Mey, B. K. Allen, H. E. B. Macdonald, J. D. Chodera, D. F. Hahn, M. Kuhn, J. Michel, D. L. Mobley, L. N. Naden, S. Prasad, A. Rizzi, J. Scheen, M. R. Shirts, G. Tresadern, and H. Xu, "Best practices for alchemical free energy calculations [article v1.0]", Living Journal of Computational Molecular Science **2**, `10.33011/livecoms.2.1.18378` (2020).
[118]Y. Matsunaga, M. Kamiya, H. Oshima, J. Jung, S. Ito, and Y. Sugita, "Use of multistate bennett acceptance ratio method for free-energy calculations from enhanced sampling and free-energy perturbation", Biophysical Reviews **14**, 1503–1512 (2022).
[119]G. Bussi, "Hamiltonian replica exchange in GROMACS: a flexible implementation", Molecular Physics **112**, 379–384 (2014).
[120]N. Metropolis, A. W. Rosenbluth, M. N. Rosenbluth, A. H. Teller, and E. Teller, "Equation of state calculations by fast computing machines", The Journal of Chemical Physics **21**, 1087–1092 (1953).
[121]J. M. Prausnitz, R. N. Lichtenhaler, and E. Gomes de Azevedo, "The phase-equilibrium problem", *Molecular thermodynamics of fluid-phase equilibria*, 3rd ed. (Prentice Hall PTR, New Jersey, 1999) Chap. 1, 1–4.
[122]J. D. van der Waals, "The equation of state for gases and liquids", *Nobel lectures in physics 1901-1921*, Vol. 1 (Elsevier Publishing Company, 1967).
[123]J. O. Valderrama, "The state of the cubic equations of state", Industrial & Engineering Chemistry Research **42**, 1603–1618 (2003).
[124]O. Redlich and J. Kwong, "On the thermodynamics of solutions. v. an equation of state. fugacities of gaseous solutions.", Chemical Reviews **44**, 233–244 (1949).
[125]G. Soave, "Equilibrium constants from a modified redlich-kwong equation of state", Chemical Engineering Science **27**, 1197–1203 (1972).
[126]D.-Y. Peng and D. B. Robinson, "A new two-constant equation of state", Industrial & Engineering Chemistry Fundamentals **15**, 59–64 (1976).
[127]G. M. Kontogeorgis and G. K. Folas, "Cubic equations of state: the classical mixing rules", *Thermodynamic models for industrial applications: from classical and advanced mixing rules to association theories*, 1st ed. (John Wiley & Sons, United Kingdom, 2010) Chap. 3, 41–74.

[128]E. A. Müller and K. E. Gubbins, "Associating fluids and fluid mixtures", *Experimental thermodynamics*, Vol. 5, edited by J. V. Sengers, R. F. Kayser, C. J. Peters, and H. J. W. Jr., Experimental Thermodynamics (International Union of Pure and Applied Chemistry, 2000) Chap. 12, 435–477.
[129]G. Jackson, W. G. Chapman, and K. E. Gubbins, "Phase equilibria of associating fluids: spherical molecules with multiple bonding sites", Molecular Physics **65**, 1–31 (1988).
[130]W. G. Chapman, G. Jackson, and K. E. Gubbins, "Phase equilibria of associating fluids: chain molecules with multiple bonding sites", Molecular Physics **65**, 1057–1079 (1988).
[131]W. G. Chapman, K. E. Gubbins, G. Jackson, and M. Radosz, "New reference equation of state for associating liquids", Industrial & Engineering Chemistry Research **29**, 1709–1721 (1990).
[132]M. S. Wertheim, "Fluids with highly directional attractive forces. i. statistical thermodynamics", Journal of Statistical Physics **35**, 19–34 (1984).
[133]M. S. Wertheim, "Fluids with highly directional attractive forces. II. thermodynamic perturbation theory and integral equations", Journal of Statistical Physics **35**, 35–47 (1984).
[134]M. S. Wertheim, "Fluids with highly directional attractive forces. III. multiple attraction sites", Journal of Statistical Physics **42**, 459–476 (1986).
[135]M. S. Wertheim, "Fluids with highly directional attractive forces. IV. equilibrium polymerization", Journal of Statistical Physics **42**, 477–492 (1986).
[136]A. Gil-Villegas, A. Galindo, P. J. Whitehead, S. J. Mills, G. Jackson, and A. N. Burgess, "Statistical associating fluid theory for chain molecules with attractive potentials of variable range", The Journal of Chemical Physics **106**, 4168–4186 (1997).
[137]C. McCabe, A. Galindo, A. Gil-Villegas, and G. Jackson, "Predicting the high-pressure phase equilibria of binary mixtures of perfluoro-n-alkanes + n-alkanes using the SAFT-VR approach", The Journal of Physical Chemistry B **102**, 8060–8069 (1998).
[138]T. Lafitte, A. Apostolakou, C. Avendaño, A. Galindo, C. S. Adjiman, E. A. Müller, and G. Jackson, "Accurate statistical associating fluid theory for chain molecules formed from mie segments", The Journal of Chemical Physics **139**, 154504 (2013).
[139]F. J. Blas and L. F. Vega, "Thermodynamic behaviour of homonuclear and heteronuclear lennard-jones chains with association sites from simulation and theory", Molecular Physics **92**, 135–150 (1997).
[140]F. J. Blas and L. F. Vega, "Prediction of binary and ternary diagrams using the statistical associating fluid theory (SAFT) equation of state", Industrial & Engineering Chemistry Research **37**, 660–674 (1998).
[141]J. Gross and G. Sadowski, "Perturbed-chain SAFT: an equation of state based on a perturbation theory for chain molecules", Industrial & Engineering Chemistry Research **40**, 1244–1260 (2001).
[142]J. Gross and G. Sadowski, "Application of the perturbed-chain SAFT equation of state to associating systems", Industrial & Engineering Chemistry Research **41**, 5510–5515 (2002).
[143]E. A. Müller and K. E. Gubbins, "Molecular-based equations of state for associating fluids: a review of SAFT and related approaches", Industrial & Engineering Chemistry Research **40**, 2193–2211 (2001).
[144]S. P. Tan, H. Adidharma, and M. Radosz, "Recent advances and applications of statistical associating fluid theory", Industrial & Engineering Chemistry Research **47**, 8063–8082 (2008).

[145]C. McCabe and A. Galindo, "SAFT associating fluids and fluid mixtures", *Applied thermodynamics of fluids*, edited by A. R. Goodwin, J. Sengers, and C. J. Peters (RSC Publishing, 2010) Chap. 8, 215–279.
[146]S. P. Tan, H. Adidharma, and M. Radosz, "Generalized procedure for estimating the fractions of nonbonded associating molecules and their derivatives in thermodynamic perturbation theory", Industrial & Engineering Chemistry Research **43**, 203–208 (2004).
[147]J. P. Wolbach and S. I. Sandler, "Using molecular orbital calculations to describe the phase behavior of cross-associating mixtures", Industrial & Engineering Chemistry Research **37**, 2917–2928 (1998).
[148]S. H. Huang and M. Radosz, "Equation of state for small, large, polydisperse, and associating molecules", Industrial & Engineering Chemistry Research **29**, 2284–2294 (1990).
[149]A. M. Georgoulaki, l. V. Ntouros, D. P. Tassios, and A. Z. Panagiotopoulos, "Phase equilibria of binary lennard-jones mixtures: simulation and van der waals l-fluid theory", Fluid Phase Equilibria **100**, 153–170 (1994).
[150]H. A. Lorentz, "Ueber die anwendung des satzes vom virial in der kinetischen theorie der gase", Annalen der Physik **248**, 127–136 (1881).
[151]B. Berthelot, "Sur le mélange des gaz", C. R. Hebd. Seances Acad. Sci. **126**, 1703–1706 (1898).
[152]J. K. Johnson, J. A. Zollweg, and K. E. Gubbins, "The lennard-jones equation of state revisited", Molecular Physics **78**, 591–618 (1993).
[153]M. S. Wertheim, "Fluids of dimerizing hard spheres, and fluid mixtures of hard spheres and dispheres", The Journal of Chemical Physics **85**, 2929–2936 (1986).
[154]M. S. Wertheim, "Thermodynamic perturbation theory of polymerization", The Journal of Chemical Physics **87**, 7323–7331 (1987).
[155]J. K. Johnson, E. A. Mueller, and K. E. Gubbins, "Equation of state for lennard-jones chains", The Journal of Physical Chemistry **98**, 6413–6419 (1994).
[156]E. A. Müller and K. E. Gubbins, "An equation of state for water from a simplified intermolecular potential", Industrial & Engineering Chemistry Research **34**, 3662–3673 (1995).
[157]S. S. Chen and A. Kreglewski, "Applications of the augmented van der waals theory of fluids.: i. pure fluids", Berichte der Bunsengesellschaft für physikalische Chemie **81**, 1048–1052 (2010).
[158]T. Boublík, "Hard-sphere equation of state", The Journal of Chemical Physics **53**, 471–472 (1970).
[159]G. A. Mansoori, N. F. Carnahan, K. E. Starling, and T. W. Leland, "Equilibrium thermodynamic properties of the mixture of hard spheres", The Journal of Chemical Physics **54**, 1523–1525 (1971).
[160]N. F. Carnahan and K. E. Starling, "Equation of state for nonattracting rigid spheres", The Journal of Chemical Physics **51**, 635–636 (1969).
[161]J. A. Barker and D Henderson, "Perturbation theory and equation of state for fluids: the square-well potential", The Journal of Chemical Physics **47**, 2856–2861 (1967).
[162]J. A. Barker and D Henderson, "Perturbation theory and equation of state for fluids. II. a successful theory of liquids", The Journal of Chemical Physics **47**, 4714–4721 (1967).
[163]J. M. L. Sengers, "Mean-field theories, their weaknesses and strength", Fluid Phase Equilibria **158**, 3–17 (1999).
[164]M. A. Anisimov and J. V. Sengers, "Critical and crossover phenomena in fluids and fluid mixtures", *Supercritical fluids: fundamentals and applications*, edited by E. Kiran, P. G. Debenedetti, and C. J. Peters (Springer Netherlands, 2000), 89–121.

[165]F. Llovell, J. C. Pàmies, and L. F. Vega, "Thermodynamic properties of lennard-jones chain molecules: renormalization-group corrections to a modified statistical associating fluid theory", The Journal of Chemical Physics **121**, 10715–10724 (2004).
[166]M. Yang, T. Zhan, Y. Su, A. Dong, M. He, and Y. Zhang, "Crossover PC-SAFT equations of state based on white's method for the thermodynamic properties of CO2, n-alkanes and n-alkanols", Fluid Phase Equilibria **564**, 113610 (2023).
[167]C. Held and G. Sadowski, "Compatible solutes: thermodynamic properties relevant for effective protection against osmotic stress", Fluid Phase Equilibria **407**, 224–235 (2016).
[168]L. F. Zubeir, C. Held, G. Sadowski, and M. C. Kroon, "PC-SAFT modeling of CO2 solubilities in deep eutectic solvents", The Journal of Physical Chemistry B **120**, 2300–2310 (2016).
[169]J. M. Prausnitz, R. N. Lichtenhaler, and E. G. d. Azevedo, "Classical thermodynamics of phase equilibria", *Molecular thermodynamics of fluid-phase equilibria*, 3rd ed. (Prentice Hall {PTR}, New Jersey, 1999) Chap. 2, 9–26.
[170]M. L. Michelsen, "The isothermal flash problem. part i. stability", Fluid Phase Equilibria **9**, 1–19 (1982).
[171]J. M. Prausnitz, R. N. Lichtenthaler, and E. Gomes de Azevedo, "Solubilities of gases in liquids", *Molecular thermodynamics of fluid-phase equilibria*, 3rd ed. (Prentice Hall PTR, New Jersey, 1999) Chap. 10, 583–634.
[172]C. Cadena, J. L. Anthony, J. K. Shah, T. I. Morrow, J. F. Brennecke, and E. J. Maginn, "Why is CO2 so soluble in imidazolium-based ionic liquids?", Journal of the American Chemical Society **126**, 5300–5308 (2004).
[173]A. Allal, C. Boned, and A. Baylaucq, "Free-volume viscosity model for fluids in the dense and gaseous states", Physical Review E **64**, 011203 (2001).
[174]E. A. Crespo, L. P. Silva, J. O. Lloret, P. J. Carvalho, L. F. Vega, F. Llovell, and J. A. P. Coutinho, "A methodology to parameterize SAFT-type equations of state for solid precursors of deep eutectic solvents: the example of cholinium chloride", Physical Chemistry Chemical Physics **21**, 15046–15061 (2019).
[175]S. Chapman, "VI. on the law of distribution of molecular velocities, and on the theory of viscosity and thermal conduction, in a non-uniform simple monatomic gas", Philosophical Transactions of the Royal Society of London. Series A, Containing Papers of a Mathematical or Physical Character **216**, 279–348 (1916).
[176]T. H. Chung, M. Ajlan, L. L. Lee, and K. E. Starling, "Generalized multiparameter correlation for nonpolar and polar fluid transport properties", Industrial & Engineering Chemistry Research **27**, 671–679 (1988).
[177]P. D. Neufeld, A. R. Janzen, and R. A. Aziz, "Empirical Equations to Calculate 16 of the Transport Collision Integrals Ω(l, s)* for the Lennard-Jones (12–6) Potential", The Journal of Chemical Physics **57**, 1100–1102 (1972).
[178]C. R. Wilke, "A viscosity equation for gas mixtures", The Journal of Chemical Physics **18**, 517–519 (1950).
[179]World Commission on Environment and Development (WCED), *Our common future* (Oxford University Press, Oxford, 1987).
[180]J. F. Jenck, F. Agterberg, and M. J. Droescher, "Products and processes for a sustainable chemical industry: a review of achievements and prospects", Green Chemistry **6**, 544–556 (2004).

[181]M. K. v. d. Hulst, M. A. J. Huijbregts, N. v. Loon, M. Theelen, L. Kootstra, J. D. Bergesen, and M. Hauck, "A systematic approach to assess the environmental impact of emerging technologies: a case study for the GHG footprint of CIGS solar photovoltaic laminate", Journal of Industrial Ecology **24**, 1234–1249 (2020).

[182]G. Rebitzer, T. Ekvall, R. Frischknecht, D. Hunkeler, G. Norris, T. Rydberg, W.-P. Schmidt, S. Suh, B. Weidema, and D. Pennington, "Life cycle assessment part 1: framework, goal and scope definition, inventory analysis, and applications", Environment International **30**, 701–720 (2004).

[183]A. Bjørn, M. Owsianiak, C. Molin, and M. Z. Hauschild, "LCA history", *Life cycle assessment, theory and practice*, edited by M. Z. Hauschild, R. K. Rosenbaum, and S. I. Olsen (Springer, Switzerland, 2018) Chap. 3, 17–30.

[184]G. Finnveden, M. Z. Hauschild, T. Ekvall, J. Guinée, R. Heijungs, S. Hellweg, A. Koehler, D. Pennington, and S. Suh, "Recent developments in life cycle assessment", Journal of Environmental Management **91**, 1–21 (2009).

[185]A. Bjørn, M. Owsianiak, C. Molin, and A. Laurent, "Main characteristics of LCA", *Life cycle assessment: theory and practice*, edited by M. Z. Hauschild, R. K. Rosenbaum, and S. I. Olsen (Springer, Switzerland, 2018) Chap. 2, 9–16.

[186]R. Heijungs and S. Suh, *The computational structure of life cycle assessment*, 1st ed. (Springer Dordrecht, 2013).

[187]A. Ciroth, F. Recanati, and R. Arvidsson, "Principles of life cycle inventory modeling: the basic model, extensions, and conventions", *Life cycle inventory analysis, methods and data*, edited by A. Ciroth and R. Arvidsson, LCA Compendium – The Complete World of Life Cycle Assessment (Springer Cham, 2021).

[188]J. B. Guinée, *Life cycle assessment – an operational guideline to the ISO standards – parts 1–3*, tech. rep. (Ministry of Housing, Spatial Planning, the Environment, and the Centre of Environmental Science, 2001).

[189]O. Jolliet, M. Margni, R. Charles, S. Humbert, J. Payet, G. Rebitzer, and R. Rosenbaum, "IMPACT 2002+: a new life cycle impact assessment methodology", The International Journal of Life Cycle Assessment **8**, 324–330 (2003).

[190]M. A. J. Huijbregts, Z. J. N. Steinmann, P. M. F. Elshout, G. Stam, F. Verones, M. D. M. Vieira, A. Hollander, M. Zijp, and R. van Zelm, *ReCiPe 2016 a harmonized life cycle impact assessment method at midpoint and endpoint level report i: characterization. RIVM report 2016-0104*, tech. rep. (National Institute of Public Health and the Environment, Bilthoven, 2016).

[191]M. Finkbeiner, "Background and future prospects in life cycle assessment – the complete world of life cycle assessment", *The international standards as the constitution of life cycle assessment: the ISO 14040 series and its offspring*, edited by W. Klöpffer, LCA Compendium – The Complete World of Life Cycle Assessment (Springer, 2014), 85–106.

[192]G. Wernet, C. Bauer, B. Steubing, J. Reinhard, E. Moreno-Ruiz, and B. Weidema, "The ecoinvent database version 3 (part i): overview and methodology", The International Journal of Life Cycle Assessment **21**, 1218–1230 (2016).

[193]I. T. Herrmann and A. Moltesen, "Does it matter which life cycle assessment (LCA) tool you choose? – a comparative assessment of SimaPro and GaBi", Journal of Cleaner Production **86**, 163–169 (2015).

[194]M. A. J. Huijbregts, Z. J. N. Steinmann, P. M. F. Elshout, G. Stam, F. Verones, M. Vieira, M. Zijp, A. Hollander, and R. v. Zelm, "ReCiPe2016: a harmonised life cycle impact assessment method at midpoint and endpoint level", The International Journal of Life Cycle Assessment **22**, 138–147 (2017).

[195]A. B. Pereiro, M. J. Pastoriza-Gallego, K. Shimizu, I. M. Marrucho, J. N. C. Lopes, M. M. Piñeiro, and L. P. N. Rebelo, "On the formation of a third, nanostructured domain in ionic liquids", The Journal of Physical Chemistry B **117**, 10826–10833 (2013).

[196]A. B. Pereiro, J. M. M. Araújo, S. Martinho, F. Alves, S. Nunes, A. Matias, C. M. M. Duarte, L. P. N. Rebelo, and I. M. Marrucho, "Fluorinated ionic liquids: properties and applications", ACS Sustainable Chemistry & Engineering **1**, 427–439 (2013).

[197]L. F. Lepre, D. Andre, S. Denis-Quanquin, A. Gautier, A. A. H. Pádua, and M. C. Gomes, "Ionic liquids can enable the recycling of fluorinated greenhouse gases", ACS Sustainable Chemistry & Engineering **7**, 16900–16906 (2019).

[198]J. E. Sosa, R. P. P. L. Ribeiro, P. J. Castro, J. P. B. Mota, J. M. M. Araújo, and A. B. Pereiro, "Absorption of fluorinated greenhouse gases using fluorinated ionic liquids", Industrial & Engineering Chemistry Research **58**, 20769–20778 (2019).

[199]C. Maton, N. D. Vos, and C. V. Stevens, "Ionic liquid thermal stabilities: decomposition mechanisms and analysis tools", Chemical Society Reviews **42**, 5963–5977 (2013).

[200]A. Bhattacharjee, J. A. Lopes-da Silva, M. G. Freire, J. A. Coutinho, and P. J. Carvalho, "Thermophysical properties of phosphonium-based ionic liquids", Fluid Phase Equilibria **400**, 103–113 (2015).

[201]Y. Sun, Q. Wei, X. Wang, X. Wang, and M. He, "Absorption separation of hydrofluorocarbon/hydrofluoroolefin refrigerant mixtures using ionic liquids", Industrial & Engineering Chemistry Research **61**, HFC solubility data in [P66614][Cl], 12787–12796 (2022).

[202]A. R. R. Teles, H. Correia, G. J. Maximo, L. P. N. Rebelo, M. G. Freire, A. B. Pereiro, and J. A. P. Coutinho, "Solid–liquid equilibria of binary mixtures of fluorinated ionic liquids", Physical Chemistry Chemical Physics **18**, 25741–25750 (2016).

[203]P. J. Castro, A. E. Redondo, J. E. Sosa, M. E. Zakrzewska, A. V. M. Nunes, J. M. M. Araújo, and A. B. Pereiro, "Absorption of fluorinated greenhouse gases in deep eutectic solvents", Industrial & Engineering Chemistry Research **59**, 13246–13259 (2020).

[204]Y. Ainai, A. Taniguchi, T. Kuramochi, C. Yokoyama, and D. Kodama, "Density, viscosity, and CO2 solubility of deep eutectic solvents comprising tetrabutylammonium or phosphonium bromide and ethylene glycol", Fluid Phase Equilibria **584**, 114122 (2024).

[205]Y. Zhao, J. Dou, A. Wei, S. Khoshkrish, and J. Yu, "Highly efficient and reversible low-concentration SO2 absorption in flue gas using novel phosphonium-based deep eutectic solvents with different substituents", Journal of Molecular Liquids **340**, 117228 (2021).

[206]I. Wazeer, I. M. AlNashef, A. A. Al-Zahrani, and M. K. Hadj-Kali, "The subtle but substantial distinction between ammonium- and phosphonium-based deep eutectic solvents", Journal of Molecular Liquids **332**, 115838 (2021).

[207]A. Al-Ghamdi, D. Saini, M. Singh, and N. I. Malek, "Nonideal behavior of aqueous deep eutectic solvents based on tetrabutylphosphonium bromide and ethylene glycol/glycerol", Journal of Chemical & Engineering Data **67**, 2963–2973 (2022).

[208]Z. Ge, H. Cheng, G. Zhang, L. Wang, and Z. Qi, "Mechanism of extractive separation of light cycle oil using a deep eutectic solvent composed of tetrabutylphosphonium bromide and levulinic acid", Energy & Fuels **36**, 1854–1862 (2022).
[209]D. V. D. Spoel, E. Lindahl, B. Hess, G. Groenhof, A. E. Mark, and H. J. C. Berendsen, "GROMACS: fast, flexible, and free", Journal of Computational Chemistry **26**, 1701–1718 (2005).
[210]J. N. C. Lopes and A. A. H. Pádua, "Molecular force field for ionic liquids composed of triflate or bistriflylimide anions", The Journal of Physical Chemistry B **108**, 16893–16898 (2004).
[211]J. N. C. Lopes, J. Deschamps, and A. A. H. Pádua, "Modeling ionic liquids using a systematic all-atom force field", The Journal of Physical Chemistry B **108**, 2038–2047 (2004).
[212]J. N. C. Lopes and A. A. H. Pádua, "Molecular force field for ionic liquids III: imidazolium, pyridinium, and phosphonium cations; chloride, bromide, and dicyanamide anions", The Journal of Physical Chemistry B **110**, 19586–19592 (2006).
[213]A. S. L. Gouveia, C. E. S. Bernardes, L. C. Tomé, E. I. Lozinskaya, Y. S. Vygodskii, A. S. Shaplov, J. N. C. Lopes, and I. M. Marrucho, "Ionic liquids with anions based on fluorosulfonyl derivatives: from asymmetrical substitutions to a consistent force field model", Physical Chemistry Chemical Physics **19**, 29617–29624 (2017).
[214]L. A. M. Pereira, L. F. G. Martins, J. R. Ascenso, P. Morgado, J. P. P. Ramalho, and E. J. M. Filipe, "Diffusion coefficients of fluorinated surfactants in water: experimental results and prediction by computer simulation", Journal of Chemical & Engineering Data **59**, 3151–3159 (2014).
[215]S. C. Potter, D. J. Tildesley, A. Burgess, and S. C. Rogers, "A transferable potential model for the liquid-vapour equilibria of fluoromethanes", Molecular Physics **92**, 825–834 (1997).
[216]R. P. S. Peguin, G. Kamath, J. J. Potoff, and S. R. P. d. Rocha, "All-atom force field for the prediction of vapor-liquid equilibria and interfacial properties of HFA134a", The Journal of Physical Chemistry B **113**, 178–187 (2009).
[217]T. Darden, D. York, and L. Pedersen, "Particle mesh ewald: an n log(n) method for ewald sums in large systems", The Journal of Chemical Physics **98**, 10089–10092 (1993).
[218]N. Wang, Y. Zhang, K. S. Al-Barghouti, R. Kore, A. M. Scurto, and E. J. Maginn, "Structure and dynamics of hydrofluorocarbon/ionic liquid mixtures: an experimental and molecular dynamics study", The Journal of Physical Chemistry B **126**, 8309–8321 (2022).
[219]E. J. Maginn, "Molecular simulation of ionic liquids: current status and future opportunities", Journal of Physics: Condensed Matter **21**, 373101 (2009).
[220]J. A. Lemkul, J. Huang, B. Roux, and A. D. MacKerell, "An empirical polarizable force field based on the classical drude oscillator model: development history and recent applications", Chemical Reviews **116**, 4983–5013 (2016).
[221]E. N. Sinitsyn, L. A. Mikhalevich, L. V. Biryukova, N. N. Danilov, G. N. Muratov, and A. P. Fedorov, "Saturated vapor pressure, vapor and liquid densities at saturation line, and critical parameters of perfluorovaleric acid and of its fluoro- and chloroanhydrides", VINITI, 1516–80 (1980).
[222]Y. Zhang, H. Squire, B. Gurkan, and E. J. Maginn, "Refined classical force field for choline chloride and ethylene glycol mixtures over wide composition range", Journal of Chemical & Engineering Data **67**, 1864–1871 (2022).
[223]S. Hempel, J. Fischer, D. Paschek, and G. Sadowski, "Activity coefficients of complex molecules by molecular simulation and gibbs-duhem integration", Soft Materials **10**, 26–41 (2012).

[224]P. V. Klimovich, M. R. Shirts, and D. L. Mobley, "Guidelines for the analysis of free energy calculations", Journal of Computer-Aided Molecular Design **29**, 397–411 (2015).
[225]Z. Wu, D. L. Dotson, I. Alibay, B. K. Allen, M. S. Barhaghi, J. Hénin, T. T. Joseph, I. M. Kenney, H. Lee, H. Li, V. Lim, S. Liu, D. Marson, P. T. Merz, A. Schlaich, D. Mobley, M. R. Shirts, and O. Beckstein, "Alchemlyb: the simple alchemistry library", Journal of Open Source Software **9**, 6934 (2024).
[226]W. F. V. Gunsteren and H. J. C. Berendsen, "A leap-frog algorithm for stochastic dynamics", Molecular Simulation **1**, 173–185 (1988).
[227]N. Goga, A. J. Rzepiela, A. H. d. Vries, S. J. Marrink, and H. J. C. Berendsen, "Efficient algorithms for langevin and DPD dynamics", Journal of Chemical Theory and Computation **8**, 3637–3649 (2012).
[228]N. Wang, R. S. DeFever, and E. J. Maginn, "Alchemical free energy and hamiltonian replica exchange molecular dynamics to compute hydrofluorocarbon isotherms in imidazolium-based ionic liquids", Journal of Chemical Theory and Computation **19**, 3324–3335 (2023).
[229]S. Asensio-Delgado, D. Jovell, G. Zarca, A. Urtiaga, and F. Llovell, "Thermodynamic and process modeling of the recovery of R410A compounds with ionic liquids", International Journal of Refrigeration **118**, 365–375 (2020).
[230]C. G. Albà, L. F. Vega, and F. Llovell, "A consistent thermodynamic molecular model of n-hydrofluoroolefins and blends for refrigeration applications", International Journal of Refrigeration **113**, 145–155 (2020).
[231]M. A. Cuendet and W. F. v. Gunsteren, "On the calculation of velocity-dependent properties in molecular dynamics simulations using the leapfrog integration algorithm", The Journal of Chemical Physics **127**, 184102 (2007).
[232]M. Brehm and B. Kirchner, "TRAVIS - a free analyzer and visualizer for monte carlo and molecular dynamics trajectories", Journal of Chemical Information and Modeling **51**, 2007–2023 (2011).
[233]M. Brehm, M. Thomas, S. Gehrke, and B. Kirchner, "TRAVIS—a free analyzer for trajectories from molecular simulation", The Journal of Chemical Physics **152**, 164105 (2020).
[234]A. Klamt, "COSMO-RS for aqueous solvation and interfaces", Fluid Phase Equilibria **407**, 152–158 (2016).
[235]J. E. Sosa, R. Santiago, A. E. Redondo, J. Avila, L. F. Lepre, M. C. Gomes, J. M. M. Araújo, J. Palomar, and A. B. Pereiro, "Design of ionic liquids for fluorinated gas absorption: COSMO-RS selection and solubility experiments", Environmental Science & Technology **56**, 5898–5909 (2022).
[236]K. Goloviznina, Z. Gong, and A. A. H. Padua, "The CL&pol polarizable force field for the simulation of ionic liquids and eutectic solvents", Wiley Interdisciplinary Reviews: Computational Molecular Science **12**, 10.1002/wcms.1572 (2022).
[237]D. v. d. Spoel, P. J. v. Maaren, P. Larsson, and N. Tîmneanu, "Thermodynamics of hydrogen bonding in hydrophilic and hydrophobic media", The Journal of Physical Chemistry B **110**, 4393–4398 (2006).
[238]C. A. Pena, A. Soto, and H. Rodríguez, "Tetrabutylphosphonium acetate and its eutectic mixtures with common-cation halides as solvents for carbon dioxide capture", Chemical Engineering Journal **409**, 128191 (2021).

[239]D. Hospital-Benito, J. Lemus, C. Moya, R. Santiago, and J. Palomar, "Process analysis overview of ionic liquids on CO2 chemical capture", Chemical Engineering Journal **390**, 124509 (2020).
[240]K. R. Baca, G. M. Olsen, L. M. Valenciano, M. G. Bennett, D. M. Haggard, B. J. Befort, A. Garciadiego, A. W. Dowling, E. J. Maginn, and M. B. Shiflett, "Phase equilibria and diffusivities of HFC-32 and HFC-125 in ionic liquids for the separation of R-410A", ACS Sustainable Chemistry & Engineering **10**, 816–830 (2022).
[241]X. Liu, N. Lv, C. Su, and M. He, "Solubilities of r32, r245fa, r227ea and r236fa in a phosphonium-based ionic liquid", Journal of Molecular Liquids **218**, HFC solubility data in [P66614][TMPP], 525–530 (2016).
[242]X. Liu, X. Qi, N. Lv, and M. He, "Gaseous absorption of fluorinated ethanes by ionic liquids", Fluid Phase Equilibria **405**, HFC solubility data in [P66614][TMPP], 1–6 (2015).
[243]V. Ermolaev, V. Miluykov, I. Rizvanov, D. Krivolapov, E. Zvereva, S. Katsyuba, O. Sinyashin, and R. Schmutzler, "Phosphonium ionic liquids based on bulky phosphines: synthesis, structure and properties", Dalton Transactions **39**, 5564–5571 (2010).
[244]L. Tan, J. Zhu, M. Zhou, X. He, and S. Zhang, "The effect of imidazolium and phosphonium ionic liquids on toluene absorption studied by a molecular simulation", Journal of Molecular Liquids **298**, 112054 (2020).
[245]Y. Chen, F. Mutelet, and J.-N. Jaubert, "Solubility of CO2 in 1-butyl-3-methylimidazolium diethyleneglycolmonomethylethersulfate and trihexyl(tetradecyl)phosphonium dodecyl-benzenesulfonate", Fluid Phase Equilibria **354**, 191–198 (2013).
[246]R. I. Canales, C. Held, M. J. Lubben, J. F. Brennecke, and G. Sadowski, "Predicting the solubility of CO2 in toluene + ionic liquid mixtures with PC-SAFT", Industrial & Engineering Chemistry Research **56**, 9885–9894 (2017).
[247]M. Bülow, M. Ascani, and C. Held, "ePC-SAFT advanced - part i: physical meaning of including a concentration-dependent dielectric constant in the born term and in the debye-hückel theory", Fluid Phase Equilibria **535**, 112967 (2021).
[248]M. Bülow, M. Ascani, and C. Held, "ePC-SAFT advanced – part II: application to salt solubility in ionic and organic solvents and the impact of ion pairing", Fluid Phase Equilibria **537**, 112989 (2021).
[249]X. Ji and C. Held, "Modeling the density of ionic liquids with ePC-SAFT", Fluid Phase Equilibria **410**, 9–22 (2016).
[250]G. Alonso, P. Gamallo, R. Sayós, and F. Llovell, "Combining soft-SAFT and COSMO-RS modeling tools to assess the CO2–SO2 separation using phosphonium-based ionic liquids", Journal of Molecular Liquids **297**, 111795 (2020).
[251]S. B. Rodriguez-Reartes and F. Llovell, "Characterizing the potential of phosphonium-based ionic liquids for CO2 capture via multiscale modeling", Industrial & Engineering Chemistry Research **64**, 17878–17891 (2025).
[252]S. Grimme, J. Antony, S. Ehrlich, and H. Krieg, "A consistent and accurate ab initio parametrization of density functional dispersion correction (DFT-d) for the 94 elements h-pu", The Journal of Chemical Physics **132**, 154104 (2010).
[253]F. Neese, F. Wennmohs, U. Becker, and C. Riplinger, "The ORCA quantum chemistry program package", The Journal of Chemical Physics **152**, 224108 (2020).

[254]S. Simon, M. Duran, and J. J. Dannenberg, "How does basis set superposition error change the potential surfaces for hydrogen-bonded dimers?", The Journal of Chemical Physics **105**, 11024–11031 (1996).

[255]S. Boys and F. Bernardi, "The calculation of small molecular interactions by the differences of separate total energies. some procedures with reduced errors", Molecular Physics **19**, 553–566 (1970).

[256]A. B. Pereiro, F. Llovell, J. M. M. Araújo, A. S. S. Santos, L. P. N. Rebelo, M. M. Piñeiro, and L. F. Vega, "Thermophysical characterization of ionic liquids based on the perfluorobutanesulfonate anion: experimental and soft-SAFT modeling results", ChemPhysChem **18**, 2012–2023 (2017).

[257]B. F. Goodrich, J. C. d. l. Fuente, B. E. Gurkan, D. J. Zadigian, E. A. Price, Y. Huang, and J. F. Brennecke, "Experimental measurements of amine-functionalized anion-tethered ionic liquids with carbon dioxide", Industrial & Engineering Chemistry Research **50**, 111–118 (2011).

[258]C. M. Neves, P. J. Carvalho, M. G. Freire, and J. A. Coutinho, "Thermophysical properties of pure and water-saturated tetradecyltrihexylphosphonium-based ionic liquids", The Journal of Chemical Thermodynamics **43**, 948–957 (2011).

[259]Y. Sun, G. Di, J. Wang, Y. Hu, X. Wang, and M. He, "Gaseous solubility and thermodynamic performance of absorption system using r1234yf/IL working pairs", Applied Thermal Engineering **172**, R1234yf solubility data in [P66614][Cl], 115161 (2020).

[260]T. Jiang, X. Meng, Y. Sun, L. Jin, Q. Wei, J. Wang, X. Wang, and M. He, "Absorption behavior for r1234ze(e) and r1233zd(e) in [p66614][cl] as working fluids in absorption refrigeration systems", International Journal of Refrigeration **131**, R1234ze(E) in [P66614][Cl], 178–185 (2021).

[261]Z. Wang, H. Mou, X. Nie, M. Chen, C. Xu, and G. Li, "Separation of hydrofluorocarbons using ionic liquids: a state-of-the-art review on molecular interactions, phase equilibria, and industrial process design", Separation and Purification Technology **393**, 137229 (2026).

[262]C. G. Albà, L. F. Vega, and F. Llovell, "Assessment on separating hydrofluoroolefins from hydrofluorocarbons at the azeotropic mixture r513a by using fluorinated ionic liquids: a soft-SAFT study", Industrial & Engineering Chemistry Research **59**, 13315–13324 (2020).

[263]A. R. C. Morais, A. N. Harders, K. R. Baca, G. M. Olsen, B. J. Befort, A. W. Dowling, E. J. Maginn, and M. B. Shiflett, "Phase equilibria, diffusivities, and equation of state modeling of HFC-32 and HFC-125 in imidazolium-based ionic liquids for the separation of R-410A", Industrial & Engineering Chemistry Research **59**, 18222–18235 (2020).

[264]S. Asensio-Delgado, M. Viar, F. Pardo, G. Zarca, and A. Urtiaga, "Gas solubility and diffusivity of hydrofluorocarbons and hydrofluoroolefins in cyanide-based ionic liquids for the separation of refrigerant mixtures", Fluid Phase Equilibria **549**, 113210 (2021).

[265]A. Prabhune and R. Dey, "Green and sustainable solvents of the future: deep eutectic solvents", Journal of Molecular Liquids **379**, 121676 (2023).

[266]V. Codera, D. Clijnk, J. Pou, J. Fernandez-Garcia, F. Llovell, and R. Gonzalez-Olmos, "Process design for the recovery of waste refrigerants using deep eutectic solvents", Journal of Environmental Chemical Engineering **11**, 110255 (2023).

[267]M. G. Demirbek, S. B. R. Reartes, and F. Llovell, "Thermodynamic analysis of the absorption of common refrigerants in fluorinated deep eutectic solvents", Fluid Phase Equilibria **581**, 114077 (2024).

[268]D. Jovell, S. B. Gómez, M. E. Zakrzewska, A. V. M. Nunes, J. M. M. Araújo, A. B. Pereiro, and F. Llovell, "Insight on the solubility of r134a in fluorinated ionic liquids and deep eutectic solvents", Journal of Chemical & Engineering Data **65**, 4956–4969 (2020).

[269]C. G. Albà, I. I. I. Alkhatib, F. Llovell, and L. F. Vega, "Assessment of low global warming potential refrigerants for drop-in replacement by connecting their molecular features to their performance", ACS Sustainable Chemistry & Engineering **9**, 17034–17048 (2021).

[270]I. I. I. Alkhatib, C. G. Albà, A. S. Darwish, F. Llovell, and L. F. Vega, "Searching for sustainable refrigerants by bridging molecular modeling with machine learning", Industrial & Engineering Chemistry Research **61**, 7414–7429 (2022).

[271]C. Albà, I. Alkhatib, F. Llovell, and L. Vega, "Hunting sustainable refrigerants fulfilling technical, environmental, safety and economic requirements", Renewable and Sustainable Energy Reviews **188**, 113806 (2023).

[272]H. Moradi and N. Farzi, "Experimental and computational assessment of the physicochemical properties of choline chloride/ethylene glycol deep eutectic solvent in 1:2 and 1:3 mole fractions and 298.15–398.15 k", Journal of Molecular Liquids **339**, 116669 (2021).

[273]N. Nkosi, K. Tumba, and S. Ramsuroop, "Measurements of activity coefficient at infinite dilution for organic solutes in tetramethylammonium chloride + ethylene glycol deep eutectic solvent using gas-liquid chromatography", Fluid Phase Equilibria **462**, 31–37 (2018).

[274]L. Alencar, S. Rodriguez-Reartes, F. Tavares, and F. Llovell, "A consistent framework to characterize the impact of co-solvents in the key process thermophysical properties of choline chloride-based DESs", Journal of Industrial and Engineering Chemistry **132**, 279–290 (2024).

[275]J. Lloret, L. F. Vega, and F. Llovell, "Accurate description of thermophysical properties of tetraalkylammonium chloride deep eutectic solvents with the soft-SAFT equation of state", Fluid Phase Equilibria **448**, 81–93 (2017).

[276]N. Pedrosa, J. C. Pàmies, J. A. P. Coutinho, I. M. Marrucho, and L. F. Vega, "Phase equilibria of ethylene glycol oligomers and their mixtures", Industrial & Engineering Chemistry Research **44**, 7027–7037 (2005).

[277]L. F. Vega, F. Llovell, and F. J. Blas, "Capturing the solubility minima of n-alkanes in water by soft-SAFT", The Journal of Physical Chemistry B **113**, 7621–7630 (2009).

[278]O. Vilaseca, F. Llovell, J. Yustos, R. Marcos, and L. F. Vega, "Phase equilibria, surface tensions and heat capacities of hydrofluorocarbons and their mixtures including the critical region", The Journal of Supercritical Fluids **55**, 755–768 (2010).

[279]E. Cané, F. Llovell, and L. F. Vega, "Accurate viscosity predictions of linear polymers from n-alkanes data", Journal of Molecular Liquids **243**, 115–123 (2017).

[280]M. B. Oliveira, S. V. Freitas, F. Llovell, L. F. Vega, and J. A. Coutinho, "Development of simple and transferable molecular models for biodiesel production with the soft-SAFT equation of state", Chemical Engineering Research and Design **92**, 2898–2911 (2014).

[281]W. A. Fouad and L. F. Vega, "Next generation of low global warming potential refrigerants: thermodynamic properties molecular modeling", AIChE Journal **64**, 250–262 (2018).

[282]E. A. Finberg and M. B. Shiflett, "Process designs for separating R-410A, R-404A, and R-407C using extractive distillation and ionic liquid entrainers", Industrial & Engineering Chemistry Research **60**, 16054–16067 (2021).

[283]L. Zhao, W. Zeng, and Z. Yuan, "Reduction of potential greenhouse gas emissions of room air-conditioner refrigerants: a life cycle carbon footprint analysis", Journal of Cleaner Production **100**, 262–268 (2015).

[284]Y. Zhang, Z. Yang, Y. Chen, H. He, and Y. Zhao, "Life cycle climate performance of R410A and its environmentally friendly alternative working fluids in a heat pump system", Sustainable Energy Technologies and Assessments **71**, 104020 (2024).

[285]L. Alencar, B. González-Barramuño, S. Rodriguez-Reartes, H. Quinteros-Lama, J. M. Garrido, V. Codera, J. Pou, F. Tavares, R. Gonzalez-Olmos, and F. Llovell, "Thermophysical characterization of sustainable pathways for hydrofluorocarbons separation utilizing deep eutectic solvents", Journal of Industrial and Engineering Chemistry **146**, 788–799 (2025).

[286]E. A. Crespo, J. M. Costa, A. M. Palma, B. Soares, M. C. Martín, J. J. Segovia, P. J. Carvalho, and J. A. Coutinho, "Thermodynamic characterization of deep eutectic solvents at high pressures", Fluid Phase Equilibria **500**, 112249 (2019).

[287]K. Li, Z. Ye, and X. Liang, "Comparative study of phase equilibrium modeling with cubic and association equations of state", Journal of Chemical & Engineering Data **69**, 4261–4279 (2024).

[288]E. Cea-Klapp, I. Polishuk, R. I. Canales, H. Quinteros-Lama, and J. M. Garrido, "Estimation of thermodynamic properties and phase equilibria in systems of deep eutectic solvents by PC-SAFT EoS", Industrial & Engineering Chemistry Research **59**, 22292–22300 (2020).

[289]S. Takahashi, H. Nakamura, T. Tezuka, S. Hasegawa, and K. Maruta, "Multi-stage oxidation of a CH2f2/air mixture examined by weak flames in a micro flow reactor with a controlled temperature profile", Combustion and Flame **201**, 140–147 (2019).

[290]S. Takahashi, H. Nakamura, T. Tezuka, and K. Maruta, "Oxidation of a c2hf5/air mixture examined by weak flames in a micro flow reactor with a controlled temperature profile", Combustion and Flame **217**, 12–20 (2020).

[291]L. F. Cameretti and G. Sadowski, "Modeling of aqueous amino acid and polypeptide solutions with PC-SAFT", Chemical Engineering and Processing: Process Intensification **47**, 1018–1025 (2008).

[292]J. Towne, X. Liang, and G. M. Kontogeorgis, "Application of quantum chemistry insights to the prediction of phase equilibria in associating systems", Industrial & Engineering Chemistry Research **60**, HF parameters PC-SAFT, 5992–6005 (2021).

[293]H. H. Al-Kayiem, T. L. Oladosu, S. I. Gilani, and A. T. Baheta, "Molecular dynamics of binary deep eutectic solvents as biocompatible working fluids in heat and mass transfer systems", Journal of Molecular Liquids **342**, 117493 (2021).

[294]P. Aravena, E. Cea-Klapp, N. F. Gajardo-Parra, A. F. Olea, H. Carrasco, J. M. Garrido, and R. I. Canales, "Influence of hydrogen bond acceptors and water content on surface tension in glycol-based eutectic mixtures", Industrial & Engineering Chemistry Research **63**, 11184–11195 (2024).

[295]Y. Yasaka, S. Karkour, K. Shobatake, N. Itsubo, and F. Yakushiji, "Life-cycle assessment of refrigerants for air conditioners considering reclamation and destruction", Sustainability **15**, 473 (2022).

[296]C. Mutel, "Brightway: an open source framework for life cycle assessment", The Journal of Open Source Software **2**, 236 (2017).

[297]E. Groen, R. Heijungs, E. Bokkers, and I. d. Boer, "Methods for uncertainty propagation in life cycle assessment", Environmental Modelling & Software **62**, 316–325 (2014).

[298]R. K. Rosenbaum, S. Georgiadis, and P. Fantke, "Uncertainty management and sensitivity analysis", *Life cycle assessment: theory and practice*, edited by M. Z. Hauschild, R. K. Rosenbaum, and S. I. Olsen (Springer, Switzerland, 2018) Chap. 11, 271.
[299]F. Bai, M. An, J. Wu, X. Fang, P. Jiang, B. Yao, X. Zhao, X. Xiang, Z. Chen, and J. Hu, "Pathway and cost-benefit analysis to achieve china's zero hydrofluorocarbon emissions", Environmental Science & Technology **57**, 6474–6484 (2023).
[300]Environmental Protection Agency (EPA), *2022 expanded HFC data*.
[301]Environmental Protection Agency (EPA), *2023 expanded HFC data*.
[302]Environmental Protection Agency (EPA), *Expanded HFC data*.
[303]Intergovernmental Panel on Climate Change (IPCC), "Emissions of fluorinated substitutes for ozone depleting substances", *IPCC guidelines for national greenhouse gas inventories*, Vol. 3 (IPCC, 2006) Chap. 7.
[304]Intergovernmental Panel on Climate Change (IPCC), "Emissions of fluorinated substitutes for ozone depleting substances", *2019 refinement to the 2006 IPCC guidelines for national greenhouse gas inventories*, Vol. 3 (IPCC, 2019) Chap. 7.
[305]Y.-X. Li, Z.-Y. Zhang, M.-D. An, D. Gao, L.-Y. Yi, and J.-X. Hu, "The estimated schedule and mitigation potential for hydrofluorocarbons phase-down in china", Advances in Climate Change Research **10**, 174–180 (2019).
[306]H. Liu, H. Duan, N. Zhang, Y. Ma, G. Liu, T. R. Miller, R. Mao, M. Xu, J. Li, and J. Yang, "Rethinking time-lagged emissions and abatement potential of fluorocarbons in the post-kigali amendment era", Nature Communications **15**, 6687 (2024).
[307]Z. Chen, P. Purohit, F. Bai, T. Gasser, Y. He, L. Höglund-Isaksson, P. Jiang, J. Wu, and J. Hu, "Sustainable management of banked fluorocarbons as a cost-effective climate action", Environmental Science & Technology **59**, 16356–16367 (2025).
[308]P. Jiang, P. Purohit, X. Xiang, Z. Chen, F. Bai, X. Zhao, X. Zhang, and J. Hu, "Cooling china without warming the planet: climate and co-benefits of HFC phase-down", npj Climate and Atmospheric Science **9**, 10.1038/s41612-025-01289-1 (2026).
[309]L. E. Chirlian and M. M. Francl, "Atomic charges derived from electrostatic potentials: a detailed study", Journal of Computational Chemistry **8**, 894–905 (1987).
[310]C. M. Breneman and K. B. Wiberg, "Determining atom-centered monopoles from molecular electrostatic potentials. the need for high sampling density in formamide conformational analysis", Journal of Computational Chemistry **11**, 361–373 (1990).
[311]E. A. Muller, A. Ervik, and A. Mejía, "A guide to computing interfacial properties of fluids from molecular simulations [article v1.0]", Living Journal of Computational Molecular Science **2**, 10.33011/livecoms.2.1.21385 (2020).
[312]E. W. Lemmon and R. T. Jacobsen, "A new functional form and new fitting techniques for equations of state with application to pentafluoroethane (HFC-125)", Journal of Physical and Chemical Reference Data **34**, 69–108 (2005).
[313]J. H. Irving and J. G. Kirkwood, "The statistical mechanical theory of transport processes. IV. the equations of hydrodynamics", The Journal of Chemical Physics **18**, 817–829 (1950).
[314]M Nagel and K Bier, "Vapour-liquid equilibrium of ternary mixtures of the refrigerants R32, R125 and R134a", International Journal of Refrigeration **18**, 534–543 (1995).

[315]L. Kou, Z. Yang, X. Tang, W. Zhang, and J. Lu, "Experimental measurements and correlation of isothermal vapor-liquid equilibria for HFC-32 + HFO-1234ze (e) and HFC-134a + HFO-1234ze(E) binary systems", The Journal of Chemical Thermodynamics **139**, 105798 (2019).

[316]T. Kamiaka, C. Dang, and E. Hihara, "Vapor-liquid equilibrium measurements for binary mixtures of r1234yf with r32, r125, and r134a", International Journal of Refrigeration **36**, 965–971 (2013).

A. Parameterization of molecular dynamics force field for R125

Parameterization of R125 for MD simulations was done on the basis of its similarity with R134a, which only replaces one fluorine atom for a hydrogen atom in its chemical structure. All bonded and non-bonded parameters for R125 were directly transferred from the work of Peguin et al. on R134a [216]. To represent the charge transfer across the molecule, upon the replacement of one hydrogen atom for a fluorine atom, point charges were recalculated using the CHELPG scheme [309, 310]. A geometry optimization using the MP2/6-31+g(d,p) level of theory was performed to obtain a minimum energy structure for R125. Then, a single point calculation at the MP2/aug-cc-pVTZ level of theory was done to generate the required wave function information and the subsequent CHELPG calculation. All computations were done using the ORCA software [253], and obtained charges are listed in Table A.1.

To validate the obtained FF for R125, its phase equilibrium was characterized using the direct coexistence method at three selected temperatures of 250 K, 280 K, and 300 K. In this method, the VLE condition is emulated by joining two separate homogeneous simulations representing the liquid and vapor phases, whose sizes and number of molecules are set to meet the expected equilibrium densities at each temperature. Box length in the x and y axes were set to $L_x = L_y =$ 5.0 nm, to avoid finite-size effects in the computation of equilibrium properties [311]. Meanwhile, box lengths in the z axis were set to $L_z = 12.5$ nm, to ensure a sufficiently elongated initial box for both phases. Thus, at each considered temperature, the number of R125 molecules in the liquid,

TABLE A.1: Computed point charges for the different sites in R125.

Atom	q [e]
C, CF_3	0.5322
C, CF_2H	0.2993
F	-0.1935
H	0.1360

TABLE A.2: Initial configuration of the considered systems for the computation of the VLE of R125.

T [K]	n^{L}	n^{V}	P^{sat} [bar]
250	2230	30	3.00
280	2010	95	8.47
300	1810	170	14.61

n^{L}, and vapor, n^{V}, phases were computed from available conditions of phase equilibrium [312]. Initial configurations for the studied systems are summarized in Table A.2.

R125 molecules were randomly inserted in each simulation box using PACKMOL [107], and an energy minimization was performed to eliminate possible overlaps between atoms. Then, NP_zAT equilibration runs were performed for each phase, running for 30 ns and 10 ns for the liquid and vapor phases, respectively. The Berendsen thermostat and isotropic barostat [101] were used to respectively fix the desired temperature and saturation pressures, the latter being obtained from available VLE data [312]. Time constants for the thermostat and barostat were set to 1.5 ps and 2.5 ps, respectively. All force field configurations were analogous to those of systems studied in Chapter 6. After properly equilibrating both phases, the configuration of the liquid phase was put between two copies of the vapor phase, explicitly defining the interface of the system. Then, a 60 ns NVT production run was performed using the Nosé-Hoover thermostat [104] with a time constant of 1.5 ps.

To compute the surface tension, γ, of each system, the Irving-Kirkwood relationship [313] was directly applied following Eq. A.1,

$$\gamma = \frac{L_z}{2}\left(P_{zz} - \frac{P_{xx} + P_{yy}}{2}\right), \tag{A.1}$$

where P_{xx}, P_{yy}, and P_{zz} are the diagonal components of the pressure tensor. Thus, in each case, γ was obtained by the averaging of the last 30 ns of the production run.

Density of each phase was computed from density profiles, obtained using the same time interval. Results are shown in Figure A.1, where it is clear that the parameterized model for R125 is able to follow the behavior of both the coexistence curve and interfacial tension at the intended temperatures.

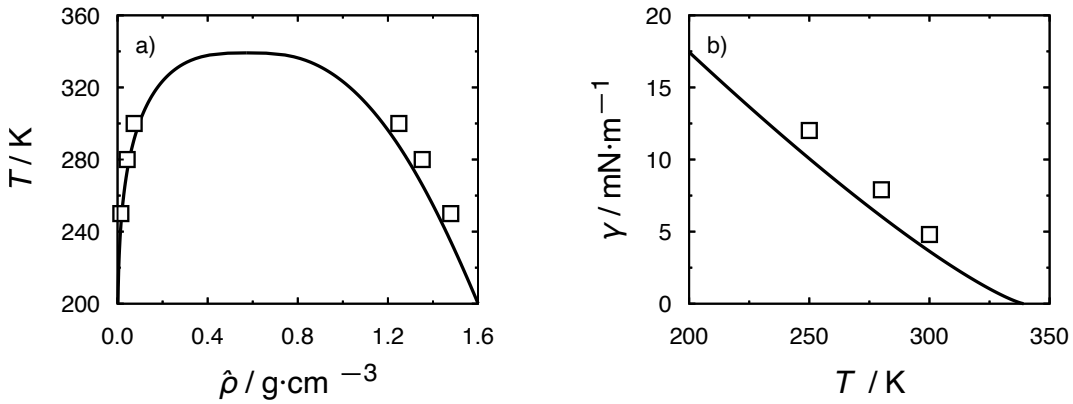

FIGURE A.1: Vapor-liquid coexistence curve (a) and surface tension, γ, as a function of temperature (b) for R125. MD simulation results (□) are shown and compared with available data from NIST (—) [312].

B. Validation of molecular dynamics force fields for FESs

The employed MD FF for PFPA was validated by computing its liquid mass density, $\hat{\rho}^{\mathrm{L}}$, at 1 bar and temperatures of 303 K, 313 K, and 333 K, selected based on available experimental data [221]. 1000 PFPA molecules were inserted in cubic simulation boxes of dimensions $L_x = L_y = L_z = 6.5$ nm using PACKMOL [107]. A further energy optimization run was performed to eliminate possible overlaps between atoms. A subsequent 0.5 ns NPT equilibration run was performed to bring the system at the desired conditions. The Berendsen thermostat and isotropic barostat [101] were employed, with coupling constants of 1.5 ps and 2.5 ps, respectively. All force field configurations were analogous to those of systems studied in Chapter 6. Finally, a 5 ns NPT equilibration run was performed to compute the density of the system. The Nosé-Hoover thermostat [104] and Parrinello-Rahman barostat [105] were applied with coupling constants of 1.5 ps and 3.5 ps.

The last 3 ns of each production run were used to compute $\hat{\rho}^{\mathrm{L}}$. Results are shown in Figure B.1, where it is clear that the parameters transferred from the models for perfluoroalkylated species [214] yields an overestimation of density. To enhance the capability of the model to depict the density of PFPA, the procedure proposed by Zhang et al. [222] was employed. Here, LJ parameters for all sites present in the molecule are scaled by empirical factors, allowing to optimize the description of target properties. Thus, simulations for liquid density at the three selected temperatures were performed at varying scaling factors of collision diameter and dispersive energy in the PFPA molecule, allowing to find the combination yielding the lowest deviation from experimental densities. Scaling factors for collision diameter and dispersive energy of 1.04 and 0.89 were able to minimize such deviations, as shown in Figure B.1. Values of these factors suggest an overestimation of dispersive energy upon transfer of the more general parameters for perfluoroalkylated species [214].

Upon validating the model for PFPA, the performance of the FFs for FESs was assessed by computing $\hat{\rho}^{\mathrm{L}}$ at 1 bar, different temperatures, and different HBA:HBD mole ratios. Based on available experimental data [203], temperatures of 293.15 K, 303.15 K, and 313.15 K were considered, along with HBA:HBD mole ratios of 2:1, 1:1, and 1:2. For each simulation, the number of HBA molecules was fixed to 400, *i.e.*, 400 cation and anion components. Thus, the number of PFPA molecules was set in each case to the value required to obtain the proper ratio between both components. For initial configurations, simulation boxes of 7.0 nm were used in all cases. An analogous procedure than that of MD simulations of PFPA was followed for every system. Results of these calculations

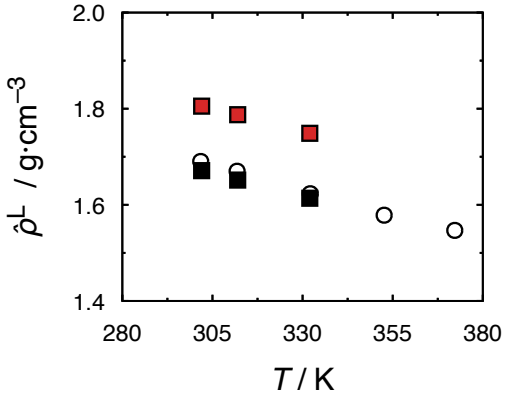

FIGURE B.1: Liquid mass density, $\hat{\rho}^L$, for PFPA at different temperatures. Results from MD simulations with unscaled (■) and scaled (■) Lennard-Jones parameters are shown and compared with available experimental data (○) [221].

are presented in Figure B.2, where it can be seen that the considered molecular dynamics models are able to reproduce the behavior of density of the studied FESs. It is important to note that the $[HDFS]^-$ cation required a scaling of its LJ parameters to yield a better correspondence with experimental data. For this species, collision diameter and dispersive energy of every site were scaled by 1.04 and 0.97, respectively. This represents a small correction for the deviations due to the direct transfer of its parameters from the $[NFS]^-$ model.

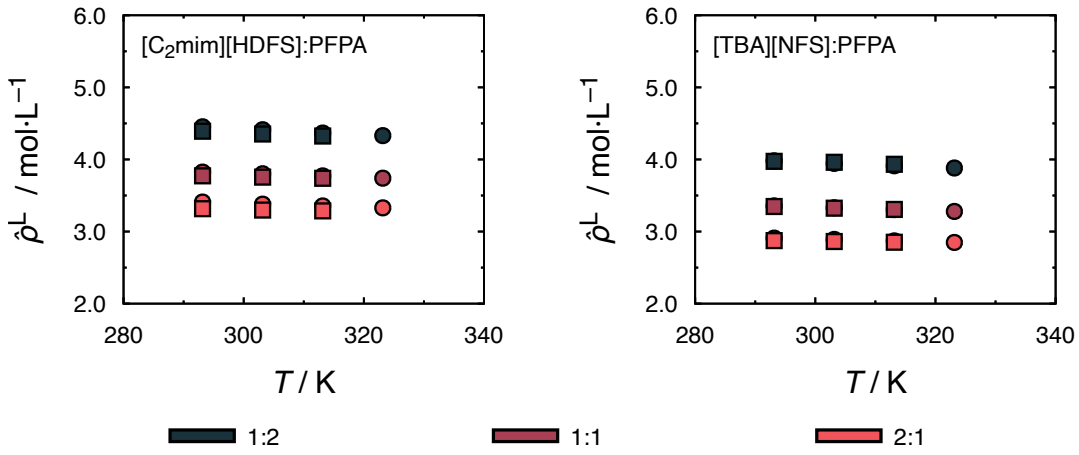

FIGURE B.2: Liquid mass density, $\hat{\rho}^L$, for the considered FESs at different temperatures and HBA:HBD mole ratios. MD simulation results (□) are shown and compared with available experimental data (○) [203].

C. Modeling of F-gases using COSMO-RS and SAFT-based EoS

Different HFCs and HFOs were characterized using COSMO-RS, implemented in the COSMOtherm software [84]. Analogously to other studied species, the BP-TZVP parameterization was selected to optimize their molecular structures and obtain their respective $p_S(\sigma)$ and $\mu_S(\sigma)$. Results of this analysis are presented in Figure C.1 for selected HFCs (R32, R152a, R134a, and R125) and HFOs (R1234yf and R1234ze(E)).

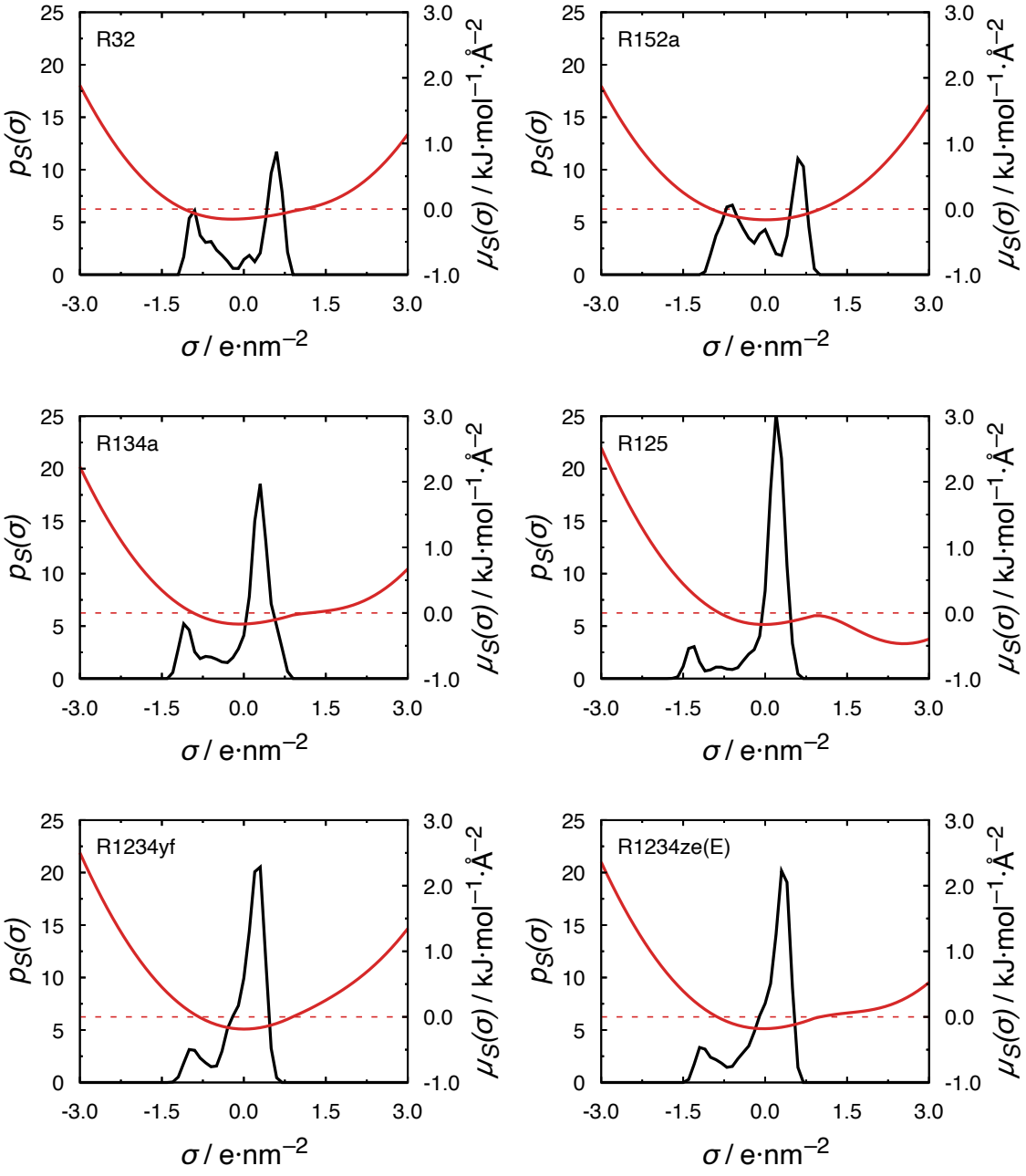

FIGURE C.1: σ-profiles, $p_S(\sigma)$, (——, left axis) and σ-potentials, $\mu_S(\sigma)$, at 303.15 K (——, right axis), obtained using COSMO-RS at the BP-TZVP parameterization, for the considered F-gases. The $y = 0$ line is included in the right axis (- - -) for guiding purposes.

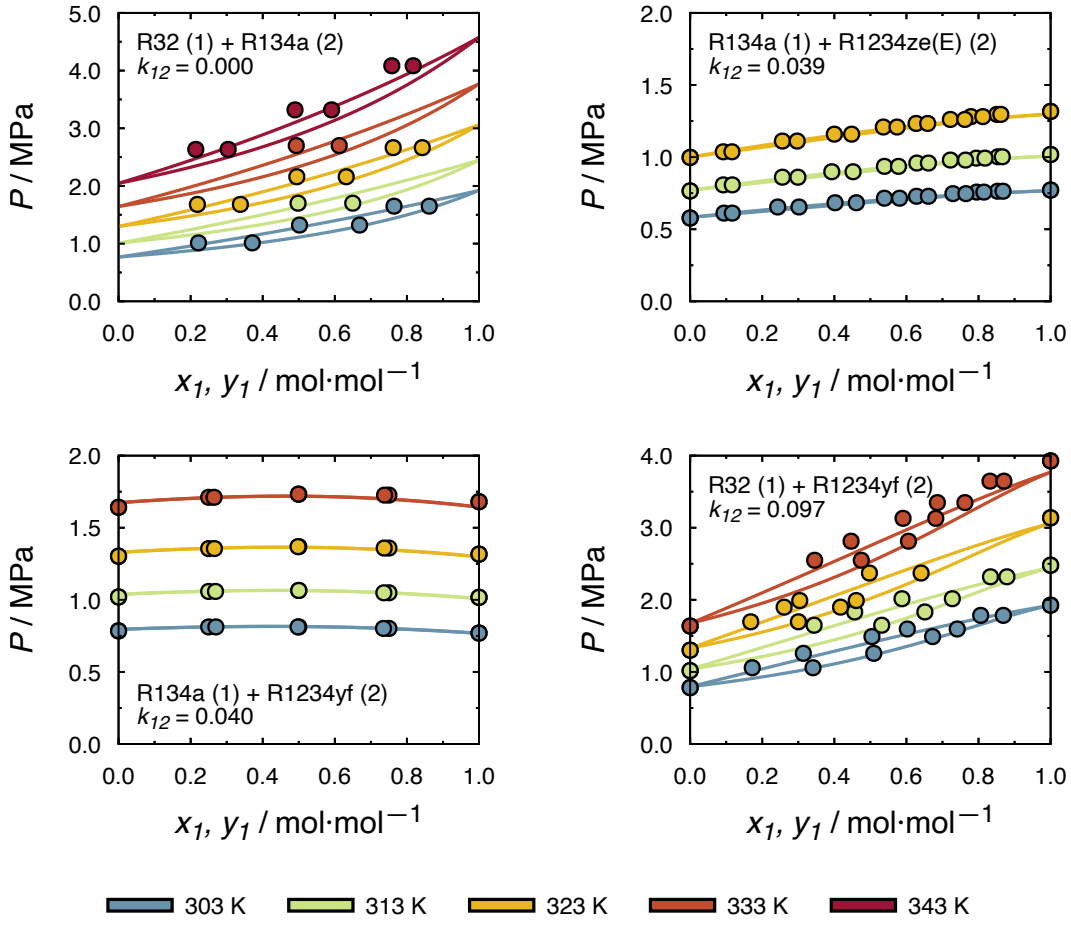

FIGURE C.2: VLE of selected refrigerant blends. Results from soft-SAFT EoS (—) are shown and compared with available experimental data (○) [314–316]. Binary interaction parameters for dispersive energy in the soft-SAFT EoS, k_{12}, are shown in each case.

D. Life cycle inventories for environmental assessment

TABLE D.1: LCI for the destruction of 1 kg of R410A by incineration.

Activity	Amount	Unit	Location
market for water, deionised	0.200	[kg]	RoW
market for lime, hydrated, packed	1.403	[kg]	RoW
market for heat, district or industrial, natural gas	9.052	[MJ]	RoW
market for chemical factory, organics	10^{-12}	[unit]	GLO
market for limestone residue	–1.403	[kg]	RoW
hydrogen fluoride production	–0.758	[kg]	RER
oxygen emission	1.659	[kg]	-
nitrogen emission	7.900	[kg]	-
carbon dioxide emission	0.790	[kg]	-
carbon monoxide emission	$2{\cdot}10^{-5}$	[kg]	-
water emission	0.050	[m^3]	-
R32 emission	0.001	[kg]	-
R125 emission	0.001	[kg]	-

TABLE D.2: LCI for the reclamation of 1 kg of R410A by conventional distillation.

Activity	Amount	Unit	Location
market for heat, from steam, in chemical industry	0.549	[MJ]	RoW
market for electricity, high voltage	0.105	[kw·h]	CH
treatment of waste mineral oil, hazardous waste incineration	0.007	[kg]	RoW
transport, freight, aircraft, all distances to generic market for transport, freight, aircraft, unspecified	0.100	[t·km]	GLO
market for chemical factory, organics	10^{-12}	[unit]	GLO
R32 emission	0.001	[kg]	-
R125 emission	0.001	[kg]	-

TABLE D.3: LCI for the treatment of 1 kg of R410A using extractive distillation with [Ch]Cl:EG (1:3) as entrainer. Inventories for the production of [Ch]Cl, R32, and R125 were obtained from previous work [66–68].

Activity	Amount	Unit	Location
refrigerant R410A obtained from BAU reclamation	1.000	[kg]	RoW
choline chloride : ethylene glycol (1:3) production	0.211	[kg]	RoW
market for heat, from steam, in chemical industry	0.649	[MJ]	RoW
market for electricity, high voltage	0.183	[kw·h]	CH
transport, freight, aircraft, all distances to generic market for transport, freight, aircraft, unspecified	0.100	[t·km]	GLO
market for hazardous waste, for incineration	0.211	[kg]	RoW
market for chemical factory, organics	10^{-12}	[unit]	GLO
refrigerant R32 production	–0.500	[kg]	RoW
refrigerant R125 production	–0.500	[kg]	RoW
R32 emission	0.001	[kg]	-
R125 emission	0.001	[kg]	-

E. List of Publications

Publications included in this thesis

[1]B. González-Barramuño, E. Cea-Klapp, N. F. Gajardo-Parra, R. I. Canales, H. Quinteros-Lama, and J. M. Garrido, "Unveiling molecular features controlling the solubility of hydrofluorocarbons in fluorine-based eutectic solvents", Industrial & Engineering Chemistry Research **64**, 22400–22412 (2025).

[2]B. González-Barramuño, H. Quinteros-Lama, J. M. Garrido, F. Llovell, and S. B. Rodriguez-Reartes, "Selective recovery of fluorinated gases from commercial refrigerants using phosphonium-based ionic liquids", Industrial & Engineering Chemistry Research, 10.1021/acs.iecr.6c00635 (2026).

[3]L. Alencar, B. González-Barramuño, S. Rodriguez-Reartes, H. Quinteros-Lama, J. Garrido, V. Codera, J. Pou, F. Tavares, R. Gonzalez-Olmos, and F. Llovell, "Thermophysical characterization of sustainable pathways for hydrofluorocarbons separation utilizing deep eutectic solvents", Journal of Industrial and Engineering Chemistry **146**, 788–799 (2025).

Publications not included in this thesis

[1]B. González-Barramuño, E. Cea-Klapp, S. Cerda, I. Polishuk, M. M. Piñeiro, H. Quinteros-Lama, and J. M. Garrido, "Scaling theories for predicting the viscosity of binary and ternary refrigerant mixtures", International Journal of Refrigeration **155**, 73–80 (2023).

[2]B. González-Barramuño, E. Cea-Klapp, I. Polishuk, H. Quinteros-Lama, M. M. Piñeiro, and J. M. Garrido, "Molecular insights into the wettability and adsorption of acid gas–water mixture", The Journal of Physical Chemistry B **128**, 3764–3774 (2024).

[3]E. Cea-Klapp, B. González-Barramuño, N. F. Gajardo-Parra, A. Karelovic, H. Quinteros-Lama, R. I. Canales, and J. M. Garrido, "Assessing thermodynamics models for phase equilibria and interfacial properties relevant to the hydrogenation of carbon dioxide", Industrial & Engineering Chemistry Research **63**, 12235–12249 (2024).

[4]E. Porter, B. González-Barramuño, S. Schmidt, E. Cea-Klapp, N. Gajardo-Parra, H. Quinteros-Lama, R. I. Canales, and J. M. Garrido, "Thermophysical characterization of tetraethylammonium chloride-based eutectic solvents for carbon capture", Journal of Chemical & Engineering Data, 10.1021/acs.jced.6c00016 (2026).